Multiscale Investigations of Mechanobiology

in vitro Observations and Computational Modeling

Vom Promotionsausschuss der
Technischen Universität Hamburg
zur Erlangung des akademischen Grades

Doktor-Ingenieur (Dr.-Ing.)

genehmigte Dissertation (kumulativ)

von
Daniel Paukner

aus
Eberbach

2025

Reviewers: Prof. Dr. Christian J. Cyron
Prof. Jay D. Humphrey, Ph.D.
Prof. Dr. Roland C. Aydin

Chair of the Board of Examiners: Prof. Dr. Juergen Grabe

Date of Oral Examination: 30.01.2025

Acknowledgements

There are so many people who made the past five years truly unforgettable and I thank each and everyone of them. In particular, I would like to express my deepest gratitude to my advisor, Prof. Christian Cyron, for granting me the freedom to pursue my own path. This independence allowed me to discover my strengths, talents, and motivation, while always knowing that guidance and support were available when needed.

I am also sincerely grateful to my second advisor, Prof. Jay Humphrey. I deeply admire you not only for your remarkable scientific contributions but also for the person you are. You have been a true inspiration to me, and I am beyond grateful for the opportunity to visit your lab multiple times.

During my time at Yale, I had the privilege of working with an incredibly talented group of people in Prof. Humphrey's lab. I sincerely thank everyone I met there – it was a pleasure to collaborate with and learn from all of you. In particular, I would like to thank Jason and Ramak, who played a crucial role during my first visit by teaching me the fundamentals of lab work and assisting in building the device that enabled parts of this work. Additionally, I am grateful to Iva, who provided invaluable support and taught me so much about cell culture. Beyond our work in the lab, I truly enjoyed our conversations and the time spent together, whether chatting about life outside of academia or sharing good food.

A special thanks goes to Abhay, with whom I spent countless hours in the lab discussing science and many other things. Your insights and enthusiasm were always appreciated, as were our squash matches. I still don't know how you always managed to show up while I was at the most challenging step of my experiments, but your presence and support meant a lot to me.

I would also like to thank my colleagues in Hamburg, particularly Kian, Marius, and Vasu. It has been a lot of fun discussing both work and other topics with you, and I have learned so much from our conversations. I am also grateful to Bettina and Stephanie for their continuous support in so many situations.

To my family – your support has been my foundation. To my parents, thank you for supporting me throughout all of my academic endeavors. To my sister and her

husband, thank you for always being there for me. To my niece Luisa and nephew Benjamin, your curiosity and challenging questions have been a constant source of joy and inspiration.

Finally, I want to express my deepest appreciation to my best friend Timo and my partner Isabella. I could not have completed this work without your constant encouragement, patience, and belief in me. It all paid off in the end, and I am forever grateful for your support during this time.

Neunkirchen, January 2025 Daniel Paukner

Abstract

Mechanobiology, an interdisciplinary field that explores the relationship between mechanical forces and biological processes, has gained growing interest in the past decades. It focuses on understanding how mechanical signals influence the behavior, structure, and function of biological systems at various levels, from molecules and cells to tissues and organs. Integrating mechanics and biology is crucial for gaining insights into fundamental (mechanobiological) mechanisms underlying processes like cell migration and tissue homeostasis in health and disease.

Cell migration, for example, plays a critical role in wound healing and cancer. To examine the mechanical mechanisms of cell migration in realistic three-dimensional fiber networks, a computational model capturing the micromechanical behavior of these networks was combined with a simplified model of a cell. This helped identify a limited set of mechanical mechanisms that can reproduce experimentally observed cell migration patterns, including complex phenomena such as durotaxis – the preferred migration towards stiffer regions. In addition, a biphasic relation between migration efficiency and fiber stiffness or contraction rate was discovered. The results suggest a crucial role of adhesion stability in determining migration behavior, which aligns with previous experimental observations.

Mechanical homeostasis is an essential concept in mechanobiology and describes how cells actively try to establish and maintain a preferred mechanical state to promote tissue homeostasis. Cell-seeded tissue equivalents are often used as a reduced model system to study soft tissue adaptation in response to mechanical perturbations. However, no quantitative data are available on adaptation processes under dynamic biaxial loading, which represents the most common loading condition *in vivo*. To close this gap, vascular smooth muscle cells embedded in collagen gels were subjected to various kinds of dynamic biaxial loading. The data showed that regardless of loading amplitude or boundary condition, the cells established and maintained a preferred force or stress, which was similar in all conditions. The results suggest that forces or stresses play a critical role in regulating the mechanical adaptation of vascular smooth muscle cells.

Computational models of soft tissue adaptation in response to mechanical perturbations have proven particularly useful in hypothesis testing and predicting disease progression. To understand better how intracellular signal processing and cell-cell communication affect tissue homeostasis, a novel multiscale finite element model was developed by combining existing models of macroscopic growth and remodeling, intracellular signaling, and reaction-diffusion equations. This *in silico* tool facilitates studying the effects of disrupted intracellular signaling processing on macroscopic tissue adaptation processes and could assist in designing artificial tissues or identifying novel pharmacological treatment strategies.

In summary, the projects covered in this thesis aim to improve the understanding of different mechanobiological processes on various scales, ranging from individual cells to entire tissues. Through novel experimental methods and computational models, it was possible to confirm or identify key quantities and processes that are essential in regulating cell behavior and tissue adaptation. An improved understanding of mechanobiological mechanisms can have important implications for tissue engineering, regenerative medicine, and the development of novel therapeutic strategies for various diseases.

Table of contents

List of figures

Nomenclature

Acronyms / Abbreviations

AngII	Angiotensin II
EC	Endothelial cell
ECM	Extracellular matrix
G&R	Growth and remodeling
GAG	Glycosaminoglycan
GPCR	G protein-coupled receptor
MMP	Matrix metalloproteinase
MSC	Mesenchymal stem cell
ODE	Ordinary differential equation
PG	Proteoglycan
RTK	Receptor tyrosine kinase
SMC	Smooth muscle cell

Chapter 1

Introduction

1.1 Overview

More than one billion people are affected by hypertension worldwide [158], accounting for roughly 30-45% of adults [20]. In the U.S. alone, more than 100 million adults have been diagnosed with hypertension, nearly half of the adult population [76]. High blood pressure is a major risk factor for many cardiovascular diseases, including heart failure and atrial fibrillation; additionally, chronic kidney disease, peripheral artery disease, and cognitive decline have also been associated with chronically elevated blood pressure [143]. While numerous drugs exist to treat hypertension, less than a third of patients achieve adequate blood pressure control with a single drug [90]. Hence, current guidelines recommend initiating treatments with a combination of two drugs – with increasing dosages or potentially adding a third drug if blood pressure does not reach target values [143]. However, given the number of drugs available, the optimal combination is challenging to obtain and impractical to assess.

To improve future treatments not only of hypertension but also other diseases, a better understanding of the involved biological processes is essential. Importantly, it is increasingly appreciated that mechanical factors play a critical role in regulating these processes in health and disease [68, 159]. Hypertension, for example, alters the mechanical environment cells experience, primarily cells in the cardiovascular system. It has been observed that these cells respond to altered mechanical stimuli, such as forces or stresses, by inducing vascular remodeling that mediates homeostasis, a process aimed at maintaining key quantities within a preferred range to ensure proper tissue form and function [64]. Hence, there is a pressing need to understand better how changes in the mechanical environment affect homeostasis – in health as well as in disease.

The discipline studying the interaction of mechanics and biology is called mechanobiology, which has gained growing interest over the past decades. Mechanobiology is an inherently multiscale discipline, ranging from tissues to cells to individual molecules, and is as complex as it is fascinating. A major challenge is how mechanobiological mechanisms on the molecular and cellular scale manifest as changes on the tissue level and, conversely, how mechanical loads at the tissue level are sensed by molecular structures and processed by cells to induce a response.

To address these challenges, this thesis explores different aspects of mechanobiology using novel experimental as well as computational tools spanning multiple length and time scales. The aim is to improve the understanding of how mechanical stimuli affect biological processes, which is relevant for informing future experimental studies and improving therapeutic strategies.

1.2 Aims and objectives

This thesis covers different aspects of mechanobiology, aiming to improve our understanding of how mechanics influences diverse biological processes. The thesis is based on three projects, with individual aims and objectives described below.

Project 1: Cell migration in three-dimensional fiber networks

Aim Cell migration plays an important role in health and disease, however, the underlying mechanisms of cell migration in three-dimensional environments are not well understood. The aim of project 1 is to identify mechanical mechanisms underlying adhesion-mediated cell migration in realistic three-dimensional fiber networks using computational modeling.

Objectives

1. Apply a micromechanical computational finite element model to recreate realistic three-dimensional fiber networks
2. Include a simplified cell model based on two assumptions: experimentally observed integrin (un-)binding behavior and cytoskeletal contraction
3. Compare model predictions with experimental results and draw conclusions on key mechanical mechanisms involved in cell migration

Project 2: Dynamic biaxial loading of tissue equivalents

Aim Soft tissues *in vivo* are most commonly subjected to multiaxial loading, however, only few quantitative data have been reported. Project 2 aims to investigate how cell-seeded tissue equivalents adapt to different biaxial mechanical stimuli of physiological relevance by measuring cell-generated forces in response to various dynamic loading and boundary conditions.

Objectives

1. Isolate vascular smooth muscle cells from mice and perform experiments with cell-seeded tissue equivalents using a previously developed bioreactor
2. Examine the influence of different dynamic biaxial loading and boundary conditions on the mechanical adaptation of cells and assess (evolving) mechanical properties by force-extension tests
3. Draw conclusions on mechanical adaptation of vascular smooth muscle cells subjected to dynamic biaxial loading, in particular, on tensional homeostasis

Project 3: Multiscale model of soft tissue growth and remodeling

Aim Macroscopic adaptations of soft tissue in response to mechanical perturbations are driven by cellular responses on the microscale. To better understand how intracellular signaling processes and cell-cell communication affect macroscopic tissue adaptation, project 3 aims to develop a multiscale finite element model of soft tissue growth and remodeling.

Objectives

1. Combine homogenized constrained mixture model with intracellular signaling network based on ordinary differential equations to replace phenomenological gain parameters
2. Include reaction-diffusion equations to allow cell-cell communication via diffusion of signaling molecules
3. Simulate the adaptation of the thoracic aorta in response to mechanical perturbations and compare with previous models and experimental results

Figure 1.1 illustrates the different length and time scales involved in mechanobiology as well as the scales covered by the projects listed above.

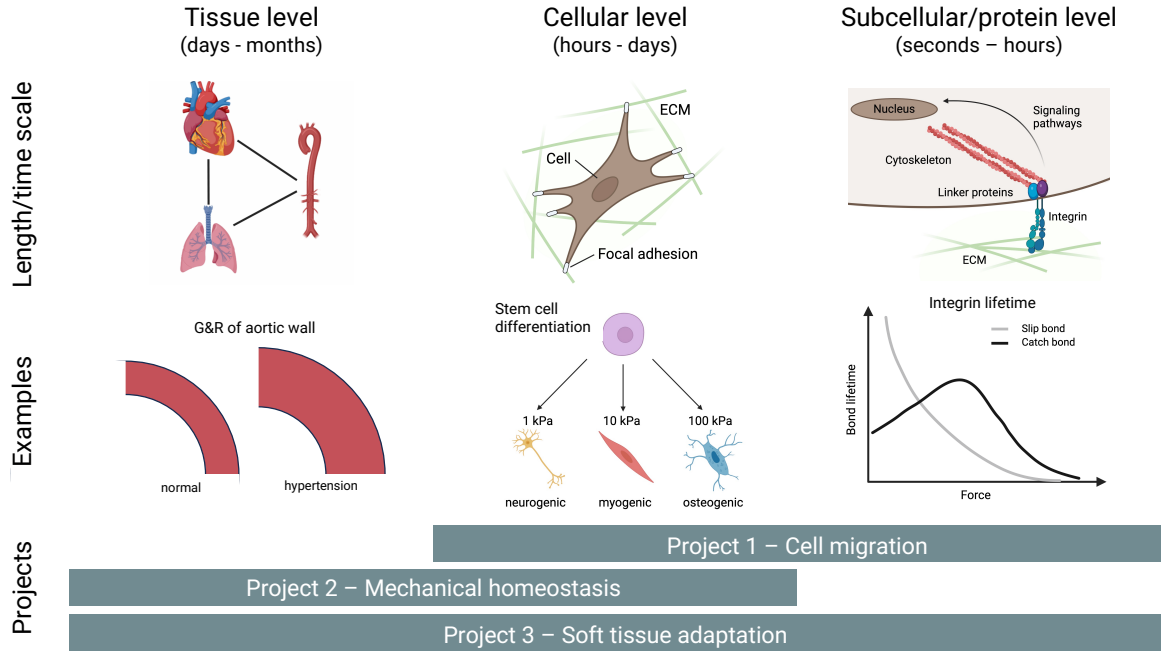

Figure 1.1 Schematic illustration of the length and time scales covered by the projects in this thesis. On the tissue scale, adaptation processes usually take several days to months. For example, the adaptation of a blood vessel in response to elevated blood pressure usually takes several weeks. Zooming in on the cellular level, adaptation processes take hours to days. For example, cell migration can be observed over the course of hours. Further zooming into an individual cell, subcellular structures and proteins become visible, which are key in sensing and processing signals from the environment and usually adjust within seconds to hours. The projects combine different scales to improve the understanding of mechanobiological processes. (Created with BioRender.com)

1.3 Outline

Since the common theme of all projects constituting this thesis is mechanobiology, chapter 2 gives a brief introduction to the field and describes mechanobiological processes on different length and time scales. While a detailed description of the entire field is beyond the scope of this thesis, the chapter is intended to provide sufficient background information for the following chapters. They present the three core projects of this thesis, ranging from computational modeling of cell migration (chapter 3, Paper A) to experiments with cell-seeded tissue equivalents (chapter 4, Paper B) to a multiscale model of soft tissue growth and remodeling (chapter 5, Paper C). Chapter 6 discusses the results, and chapter 7 concludes with a summary.

Chapter 2

A brief introduction to mechanobiology

2.1 Overview

As mentioned in chapter 1, diseases such as hypertension, chronic inflammation, and cardiovascular fibrosis affect large parts of our society, regardless of age, gender, or socio-economic background. Despite being different in their macroscopic manifestations, many of these diseases can have a common cause: impaired cellular signal sensing and processing. The two most common signals nearly every cell experiences are biochemical and mechanical stimuli. Even though it has been known since the late 19th century that a dynamic relationship exists between mechanical loading and growth and remodeling in living biological tissues [23, 147], most research in the last decades has focused on biochemical signaling.

However, advances in experimental, theoretical, and computational techniques have made it possible to study the complex underlying mechanisms of cellular mechanosensing, transduction, and processing in detail. This has given rise to the emerging field of mechanobiology, which explores the influence of mechanical stimuli on biological processes at different length and time scales. One of the main difficulties in studying mechanobiology is its inherent multiscale character, illustrated in Figure 2.1. To reduce the complexity of this multiscale system consisting of molecules, cells, and tissues, most studies have focused on specific aspects, which has led to valuable insights and helped identify individual mechanobiological relevant components, such as stretch-sensitive proteins. However, due to the pluralism of causes and effects in biological systems, this approach offers a limited understanding of how system properties emerge and how the system behaves in its entirety. To overcome the limitations of the reductionist

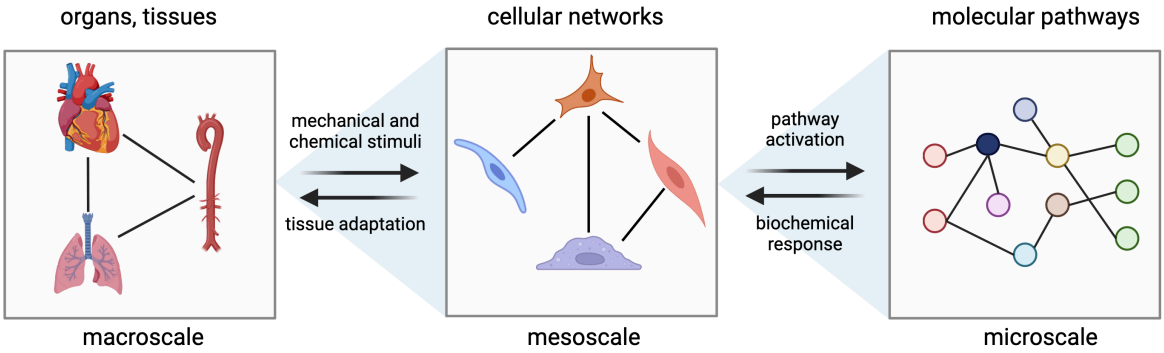

Figure 2.1 Schematic illustration of the multiscale structure of soft tissue. Each tissue in the body comprises different cell types, closely working together and communicating with each other. Every cell has an internal network of signaling pathways that process the numerous mechanical and biochemical inputs a cell receives from its environment and produce a specific biochemical response. This response feeds back into the multicellular network, where it can influence other cells, and the resulting collective response can, in turn, lead to macroscopic tissue adaptation, for example, by cell proliferation or matrix synthesis. In an optimal setting, this control loop leads to appropriate tissue adaptation in response to a changed environment to promote homeostasis. (Created with BioRender.com)

approach, a more holistic view of the system is required by combining processes at different length and time scales.

An essential emergent behavior of many biological systems is homeostasis. Healthy living organisms, or their subunits, such as organs, tissues, or cells, tend to maintain a homeostatic equilibrium, a preferred mechanical and biochemical state. The process of maintaining the homeostatic equilibrium is called homeostasis. This is an active process that, in healthy organisms, is dynamically stable and ultimately aims to ensure tissues maintain their form and function by appropriately adapting to changes in the chemical and mechanical environment.

A critical step in this process is mechanotransduction – how cells convert mechanical stimuli into (intracellular) biochemical signals [63]. In the healthy case, tissue-resident cells constantly sense and integrate signals from their environment and respond to promote homeostasis. However, in the case of malfunctioning mechanotransduction, mechanical cues are not correctly sensed or processed by the cells, potentially leading to improper tissue adaptation. Importantly, while the mechanical state of the tissue is crucial as it might determine mechanical failure once stresses exceed strength, the mechanotransduction process is regulated by what cells perceive as the current mechanical state and how this compares to desired setpoints [65].

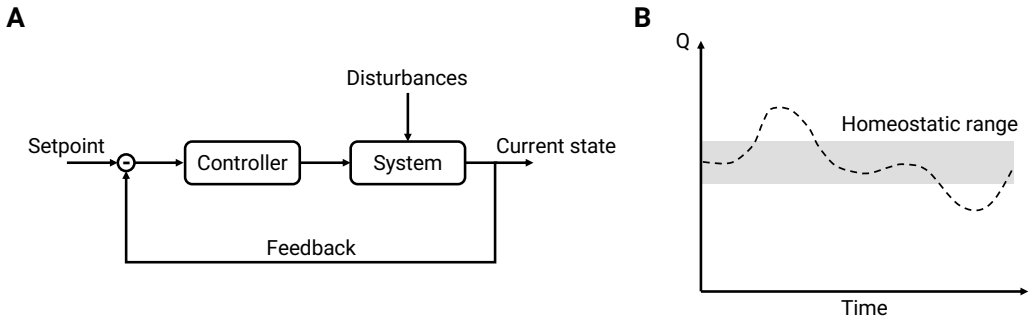

Figure 2.2 Schematic illustration of a generic negative feedback loop and homeostasis. A) The current state of the system under control is compared to a setpoint to compute an error signal, which is fed into the controller. The controller determines an appropriate control signal to regulate the system, which might be affected by external disturbances. Applied to the case of soft tissue, the system could be identified as the combination of cells and ECM that are subjected to mechanical perturbations, such as stretch or flow. At the same time, cells act as controllers of the system by sensing its mechanical state and comparing it to a reference setpoint. Deviations from the preferred state will lead to cellular responses, such as changes in phenotype or ECM modification, to return the system back to normal. B) Evolution of a quantity Q regulated by negative feedback to remain within a homeostatic range (gray area). Note that the homeostatic range might shift with time (adaptive homeostasis), potentially in response to disease (see, for example, Ezra *et al.* [38]).

A key role in homeostasis can be attributed to negative feedback loops, which ensure that deviations from a preferred setpoint are countered by a response that returns perturbed values toward their target state (Fig. 2.2A). Note that homeostasis does not necessarily require that target values be exactly restored but only within a certain range (Fig. 2.2B). By contrast, positive feedback loops can have a detrimental effect by amplifying a perturbation, leading to unstable behavior and moving further and further away from the preferred setpoint.

To illustrate the importance of proper feedback systems, consider the effects of dysregulated tissue growth. Tissue growth, either by matrix deposition, especially collagen, or by cell proliferation, is an important tool for tissue homeostasis. However, sustained collagen deposition and uncontrolled cell proliferation can have detrimental effects, as observed in fibrosis. In cardiovascular fibrosis, excessive collagen deposition leads to a stiffened aortic wall, reducing the energy-storing capability of the aorta and thereby increasing the pulsatile mechanical load on the heart permanently. This is often associated with severe cardiovascular diseases [17]. On the other hand, sustained atrophy (negative growth), for example, through secretion of matrix metalloproteinases (MMPs) or apoptosis of cells, can weaken tissue and subsequently result in mechanical failure of soft tissues. Hence, functioning mechanotransduction is key to ensuring

tissue homeostasis by providing the correct response to perturbations – in direction and magnitude.

In summary, mechanobiology is a multidisciplinary field investigating mechanisms by which cells sense, process, and respond to mechanical signals from their surroundings. The resulting cellular responses and adaptations can manifest at multiple scales ranging from the subcellular level to the cell level to the tissue or organ level. From a clinical perspective, one is often interested in the adaptations on the tissue level as these are more easily observed and measured. However, it is crucial to study cellular and subcellular processes if one seeks to understand the underlying mechanisms and how disturbances propagate from the micro- to the macroscale and vice versa. By understanding how mechanical forces induce changes at the molecular, cellular, and tissue levels, mechanobiology tries to provide meaningful insights into tissue physiology and disease development. An improved understanding can potentially lead to advancements in designing engineered tissues and organs, repairing and regenerating damaged tissue, and providing therapy for diseases.

2.2 Mechanobiology on different scales

The following sections describe a few examples of mechanobiological processes on different length and time scales to provide some context for and facilitate the understanding of the results presented in chapters 3, 4, and 5.

2.2.1 Tissue level

The influence of mechanics on the tissue level is probably the most studied, likely because it is more accessible to (experimental) observation than the cellular and subcellular scales. This might be especially relevant for early research in the field.

Already more than 150 years ago, Henry Gassett Davis observed that tissue can adapt to changes in its mechanical environment [23]: he observed that an increased load caused soft tissue to lengthen due to the addition of mass, while a reduced load caused tissue to shorten due to mass removal. This is termed Davis' law. Shortly after Davis' discovery, Julius Wolff discovered a similar phenomenon in bones, called Wolff's law [147]: if loads on a bone increase, it will remodel over time and become stronger to resist that sort of loading. The inverse is true as well, and continued immobilization leads to a loss of bone mass [130]. These two observations suggest an important role of

mechanical stimuli in maintaining tissue function, which applies to both soft and hard tissue despite their different structures and functions.

The mechanical cues the cells respond to are, at least in the case of soft tissue, provided by the extracellular matrix (ECM), which is schematically illustrated in Fig. 2.3. The ECM consists of hundreds of proteins, glycoproteins, and proteoglycans (PGs); however, the gross mechanical properties are primarily governed by elastic fibers, fibrillar collagens, and glycosaminoglycans (GAGs) [63]. Elastin, the main component of elastic fibers, is primarily produced and deposited during development, and with a half-life of around 70 years (in humans [117]), it is very stable compared to other constituents. It can withstand large stretches and endows the tissue with the ability to store elastic energy. Since elastin is not produced in adulthood, any damage, fatigue, or degradation leads to irrecoverable changes that can affect tissue form and function. For example, age-related loss of elastic fiber integrity and normal degradation causes wrinkling of the skin as well as stiffening of elastic arteries. Collagen is the most abundant protein in mammals, and more than 25 different collagen types are known to date, with type I and III collagens being the most common [112]. While the exact process of collagen fiber formation is still an active field of research, it is known that fibrillar collagen has a hierarchical structure where individual collagen molecules (1.5 nm in diameter) assemble and cross-link into microfibrils and fibrils (20-100 nm in diameter), which in turn form collagen fibers (0.5-20 μm in diameter) [12, 56]. Compared to elastin, collagen has a short half-life of around 10 - 100 days (in the vasculature [101]) and can be synthesized by interstitial cells such as fibroblasts and smooth muscle cells (SMCs). These cells cannot only produce collagen but also degrade it via the secretion of matrix metalloproteinases (MMPs) of various types. MMPs accelerate the breakdown and degradation of collagen and other extracellular matrix constituents and are essential in cell-driven matrix remodeling [100]. Finally, GAGs and PGs are highly hydrated molecules that contribute to the compressive stiffness of connective tissues [69, 153]. In addition, they can sequester growth factors, which are important for cell signaling [109]. These and other structural constituents undergo continuous turnover (deposition and degradation) and remodeling (change in structure), which is mediated by interstitial cells. Indeed, the balance of deposition and degradation rates regulates tissue homeostasis and can change in response to disease or injury. Notably, even when maintaining a steady state, cells are actively synthesizing and removing matrix constituents to regulate the mechanical properties of the ECM. An often overlooked but highly important aspect is that this constant turnover occurs while the ECM is mechanically stressed [63].

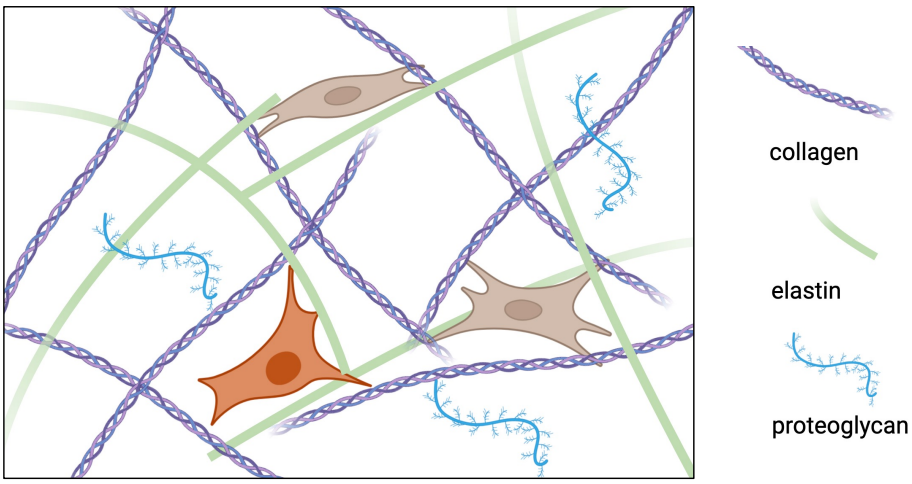

Figure 2.3 Schematic illustration of the extracellular matrix (ECM). The ECM is a fibrous network of collagen and elastin fibers that provides structural support to tissue and cells. While elastin fibers endow tissues with a certain degree of elasticity, collagen fibers endow tissues with mechanical strength. In addition to sequestering signaling molecules, proteoglycans can bind a significant amount of water and contribute to the compressive stiffness of tissue. (Created with BioRender.com)

To study how mechanical cues provided by the ECM affect cell behavior, many experimental approaches have focused on so-called tissue equivalents. This eliminates the complexity of native tissue, which contains many constituents potentially influencing each other. Tissue equivalents represent simplified model systems and are most commonly based on collagen (specifically type I). One of the first to use collagen-based tissue equivalents was Bell *et al.* [11], who studied the compaction of free-floating cell-seeded collagen gels. Different variations of studies have evolved over the past decades, starting with relatively simple, free-floating gels and turning into more sophisticated devices that can measure cell-generated forces and apply external mechanical perturbations [14, 31, 62]. In their seminal paper, Brown *et al.* [14] used such a device to subject uniaxial cell-seeded collagen gels to positive and negative static stretches. They found that the embedded cells regulated the tissue stresses/forces to maintain a certain homeostatic setpoint when the samples were mechanically perturbed (Fig. 2.4). This behavior was termed *tensional homeostasis* and is an essential concept in mechanobiology. However, a more accurate description of the phenomenon might be *mechanical homeostasis*, as it is still unclear which quantity might be regulated on the macroscale [33, 63].

The adaption of tissue *in vivo* is more challenging to study, but Matsumoto and Hayashi [93] showed that the thoracic aorta of rats is capable to mechano-adapt to increased mechanical loads induced by hypertension. They observed that the aortic

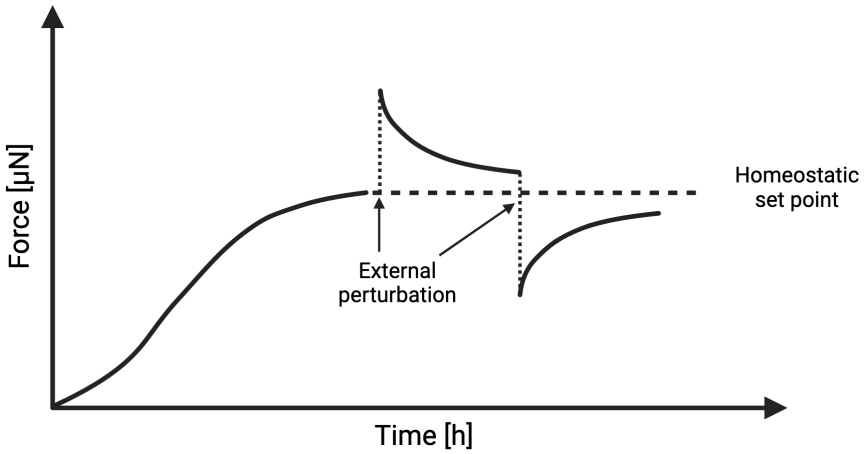

Figure 2.4 Schematic illustration of tensional homeostasis. In uniaxial experiments with cell-seeded collagen gels, Brown *et al.* [14] observed that once cells have established a preferred mechanical force, they try to restore this homeostatic state after external perturbations. The external perturbations are usually applied as positive or negative stretches.

wall adapts in a way that maintains a specific circumferential stress by increasing its thickness. This adaptation occurred rapidly within a few weeks after hypertension was induced. Additionally, they showed that on longer time scales (16 weeks), the elastic properties of the aortic wall were also restored. More recent studies showed how various disorders could affect the mechano adaptability of the vasculature [16, 138] as well as different adaptations based on regional differences in the aorta [13].

Theoretical concepts in line with the observed tendency of cells to maintain a preferred mechanical state allow a relatively simple mathematical description of the adaptation processes but provide considerable insight [60]. Assuming an idealized cylinder is a good first approximation of a blood vessel, one can use Laplace's law to compute the mean circumferential stress (σ_θ) in the vessel wall

$$\sigma_\theta = \frac{Pa}{h} \tag{2.1}$$

while the mean axial stress (σ_z) is given by

$$\sigma_z = \frac{f}{\pi h(2a+h)}. \tag{2.2}$$

Here, P is the transmural pressure, f the applied axial load, and a and h are the deformed inner radius and wall thickness of the cylinder. Hypertension, for example, leads to an increased transmural pressure P, which increases the circumferential stresses. To compensate for the elevated stress, the wall thickness h has to increase, which has

been observed experimentally [93, 149] and is schematically illustrated in Fig. 2.5. Conversely, a reduced transmural pressure caused a thinning of the wall to restore circumferential stresses [10]. These adaptations occurred over a period of a few weeks to months.

In addition to the regulation of the circumferential stress via adaptation of the thickness, it appears that the vessel diameter is regulated to maintain a certain wall shear stress [82]. Theoretically, this can be understood by assuming a steady, fully developed, laminar, one-dimensional, incompressible flow of a Newtonian fluid within a rigid circular tube (again, a rough approximation of a blood vessel) [60]. In this case, the mean wall shear stress (τ_w) is given by

$$\tau_w = 4\frac{\mu Q}{\pi a^3} \tag{2.3}$$

with μ the viscosity, Q the flow rate, and a is again the deformed luminal radius. If the flow rate Q increases, assuming a constant viscosity, the inner radius a has to increase to restore a preferred wall shear stress.

Taken together, idealized adaptations of luminal radius and wall thickness in response to changed mechanical loads are given by

$$a = \left(\frac{Q}{Q_0}\right)^{1/3} a_0 \qquad \text{and} \qquad h = \left(\frac{P}{P_0}\right)\left(\frac{Q}{Q_0}\right)^{1/3} h_0, \tag{2.4}$$

where P/P_0 and Q/Q_0 are the ratios of current to initial transmural pressure and flow rate and a_0 and h_0 initial luminal radius and wall thickness, respectively. Additionally, axial stress (eq. (2.2)) has also been reported to play a crucial role in the adaptation of arteries [61]. Despite the simplifying assumptions, the above equations provide a good qualitative and quantitative prediction of (ideal) tissue adaptation.

While tissue stress has proven to be a good metric to describe and predict the homeostatic adaptation processes, it is unlikely that it can be sensed by cells directly since it is a macroscopic quantity (in addition to being a man-made concept) [33]. Note, too, that other quantities, such as strain, force, or stiffness, might be potential target variables that are conserved by homeostasis.

2.2.2 Cell level

Similar to the previous section about soft tissue adaptation in response to varying mechanical loads, individual cell behavior has been observed to change based on mechanical cues from the cellular microenvironment.

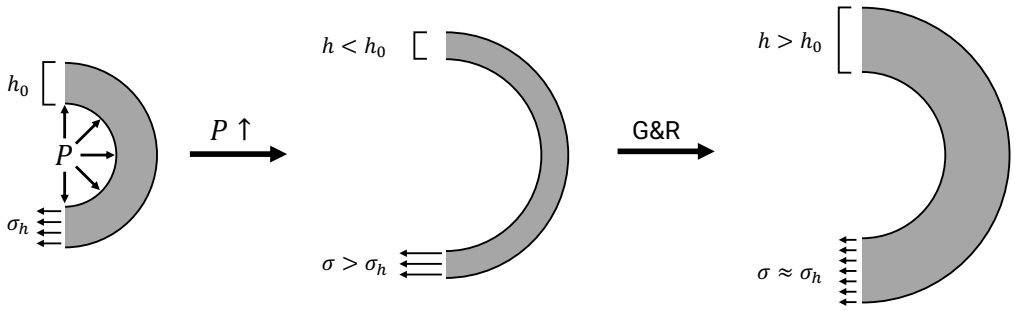

Figure 2.5 Schematic illustration of the adaptation process of an idealized blood vessel in response to a sudden increase in transmural pressure P. Right after the pressure increase, wall thickness h is lower than its initial thickness h_0, and circumferential stresses σ increase above the homeostatic value σ_h. Growth and remodeling (G&R) return circumferential stresses to the homeostatic value by increasing the thickness of the vessel above its initial value.

For example, a seminal study by Engler *et al.* [37] showed that stem cell differentiation could be affected by substrate stiffness (Fig. 2.6A). They cultured mesenchymal stem cells (MSCs) on two-dimensional polyacrylamide gels of different levels of stiffness. After several days of culture, the MSCs showed a specific phenotype based on substrate stiffness. Cells on soft substrates, mimicking brain tissue, became neurogenic, while cells on intermediate stiffnesses, mimicking muscle tissue, became myogenic, and cells on stiff substrates, mimicking collagenous bone, became osteogenic. Interestingly, this stiffness-directed lineage specification could be blocked by inhibiting nonmuscle myosin II, an actin-binding protein with an essential role in regulating cell adhesions [132]. Its inhibition only seemed to affect the differentiation process without significantly influencing other aspects, such as cell shape and function.

In another interesting study, Bangasser *et al.* [9] showed that substrate stiffness influences cell migration in a cell-type-dependent manner. By tracking embryonic forebrain neurons (ECFNs) and U251 glioma cells migrating on substrates of varying stiffnesses, they identified a biphasic relationship between migration efficiency and substrate stiffness (Fig. 2.6B). ECFNs showed optimal migration, in terms of area covered in a certain time interval (similar to a diffusion coefficient), on substrates with a stiffness of $\sim$ 1 kPA, while U251 glioma cells showed optimal migration on substrates with a stiffness of $\sim$ 100 kPA. Using computational modeling, they also identified myosin II and cell-matrix adhesions as key regulators, which was experimentally verified by simultaneous inhibition of both mechanisms. This resulted in a decrease in the substrate stiffness where migration was optimal.

Besides reacting to substrate stiffness, cells have been observed to follow signals of various kinds through directed migration [116]. These signals include, for example,

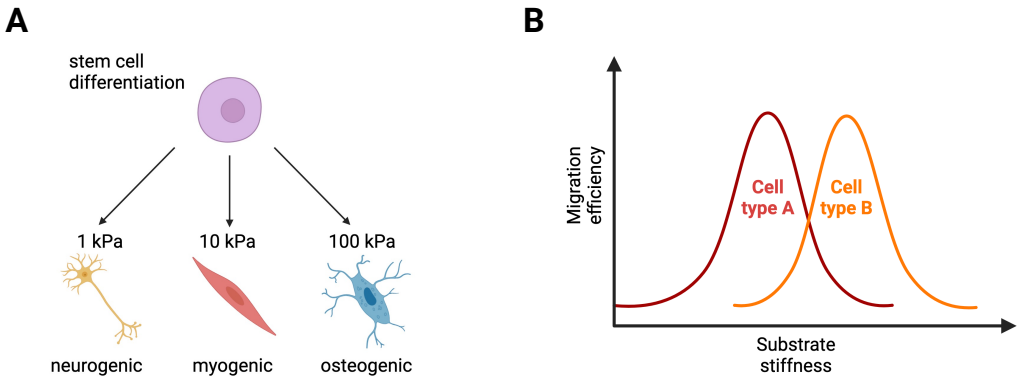

Figure 2.6 Schematic illustration of the potential influence of substrate stiffness on cell behavior. A) Engler *et al.* [37] showed how substrate stiffness could guide stem cell differentiation with stem cells cultured on soft substrates becoming neurogenic, on intermediate stiffnesses they became myogenic, and on stiff substrates they become osteogenic. B) Bangasser *et al.* [9] identified a biphasic relationship between migration efficiency and substrate stiffness, which is cell-type dependent and can be modulated by inhibiting integrin binding and cytoskeletal contraction. (Created with BioRender.com)

chemical (chemotaxis), mechanical (durotaxis), or topological (topotaxis/contact guidance) signals and usually lead to the migration of cells along the gradients of these signals. Chemical signals are usually sensed by receptors on the cell surface, such as G protein-coupled receptors (GPCRs) or receptor tyrosine kinases (RTKs), while mechanical and topological signals are usually sensed via cell-matrix adhesions (so-called integrins and focal adhesions, see next section). How these signals are transmitted and finally executed to result in directed migration is still ongoing research.

While the studies mentioned above focused on the behavior of individual cells, it is often a collection of various cell types that interact to promote tissue homeostasis and proper tissue function. In many tissues, the relevant cell types include organ-specific parenchymal cells (for example, SMCs in the aorta or hepatocytes in the liver), fibroblasts, macrophages, and endothelial cells, which can be summarized as a basic tissue unit [1]. The communication between cells is often mediated by the secretion of signaling molecules, such as growth factors, from one cell, which then diffuse through the tissue and are sensed by other cells. This is called paracrine signaling. Alternatively, if the source of the signaling molecule is the cell itself, this is called autocrine signaling. A third mode of signaling is called endocrine signaling, where signaling molecules, often hormones, are released into the bloodstream and received by distant target cells. Instead of communicating via diffusion of signaling molecules, cells can also exchange signals via direct physical connections. This can be subdivided into biochemical signaling through gap junctions, which allow the passage of small

molecules from cell to cell, and mechanical signaling by so-called adherens junctions, which connect the cytoskeleton of neighboring cells and facilitate the transmission of (mechanical) forces and stresses [3]. Both methods are especially important for epithelial tissue, such as the monolayer of endothelial cells lining the luminal wall of blood vessels.

The interactions of several cell types can lead to complex cell-cell communication patterns, potentially involving numerous signaling molecules. These networks of cells can be challenging to comprehend but are important if one seeks to understand tissue behavior in health and disease. For example, endothelial cells (ECs), which line the interior surface of blood vessels, can sense and respond to changes in shear stresses caused by variations in blood flow. ECs play an important role in regulating the diameter of muscular arteries by releasing vasoconstrictors such as endothelin-1 (ET1) or vasodilators such as nitric oxide (NO). Both can be sensed by SMCs in the vessel wall and cause contraction or relaxation, respectively. Functioning cell-cell communication plays a critical role in many more processes ranging from tissue development and homeostasis to immune responses to carcinogenesis [6, 121].

In summary, many observations have been made describing the response of individual cells to their mechanical microenvironment and the interaction of different cell types. While these findings help improve the understanding of specific aspects of cell behavior, it is less well understood if and how they combine into macroscopic responses of soft tissue, especially when subjected to mechanical perturbations.

2.2.3 Subcellular and molecular level

The observed cell behaviors described in the previous section are primarily governed by cell-matrix interactions, which in turn are regulated by processes on the subcellular and molecular scale.

To be able to respond to mechanical perturbations, cells need to assess the mechanical properties of the ECM. Transmembrane proteins, so-called integrins, allow cells to attach to different ECM constituents, thereby physically linking fibers of the ECM outside the cell to the cytoskeleton inside the cell (Fig. 2.7). Integrins consist of an α and β subunit, and the combination of the subunits determines the affinity of the integrin to ECM components such as collagens (for example, $\alpha_2\beta_1$) or fibronectins (for example, $\alpha_5\beta_1$). Binding and unbinding of integrins to ECM ligands is a stochastic process, and the applied force can modulate the unbinding probability. Two types of bonds have been identified: slip bonds are characterized by a continuously decreasing bond lifetime with increased force, whereas catch bonds have been observed to stabilize

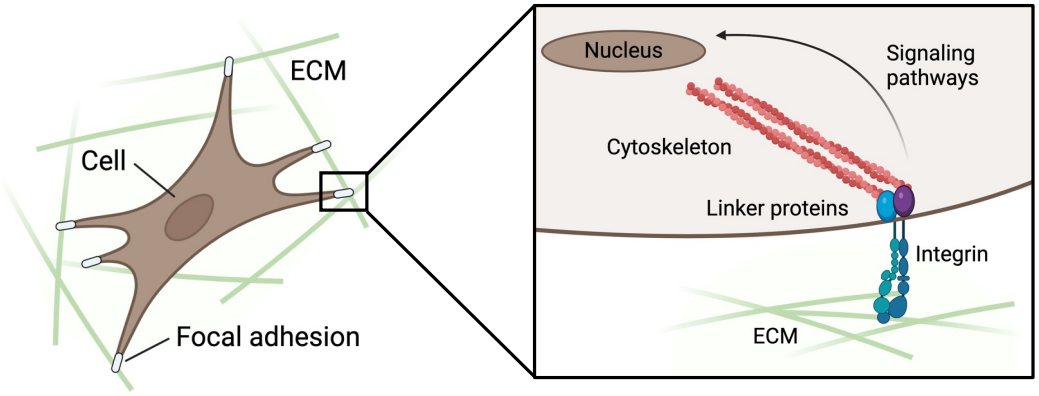

Figure 2.7 Schematic illustration of key subcellular structures and molecules of mechanobiology. Cells attach to the ECM via focal adhesions, which contain several integrins. Within the cell, the cytoskeleton connects the cytoplasmic site of the focal adhesions to the cell nucleus. Focal adhesions have been identified as a major signaling hub that can activate different signaling pathways affecting cell behavior. (Created with BioRender.com)

with applied load before bond lifetime decreases once a certain threshold is exceeded [78], see Fig. 2.8.

Focal adhesions form through the clustering of several integrins and other cytoplasmic proteins, such as vinculin, talin, and paxillin [92]. They provide a more stable connection between the cytoskeleton and the ECM, allowing force transmission from the ECM into the cell or vice versa. Additionally, they have been identified as a major signaling hub. In particular, focal adhesion kinase (FAK) is a key signaling molecule with many downstream effects that are triggered by intracellular signaling pathways that mediate cellular processes such as cell cycle progression or cytoskeletal reorganization [67, 92, 135].

The cytoskeleton is a dynamic and constantly remodeling structure consisting mainly of actin filaments, intermediate filaments, and microtubules. Various proteins have been identified in regulating the dynamics of the cytoskeleton, such as Arp2/3 [15] or cofilin [141]. Besides providing structural integrity to the cell, the cytoskeleton can actively contract to generate tension and exert forces on the surrounding ECM, which are transmitted via focal adhesions. The cytoskeletal contraction is mainly mediated by the interaction of actin filaments and the motor protein myosin II [122] and can be altered through intracellular signaling processes such as the Rho/ROCK pathway [45]. Force transmission can also occur in the other direction, with focal adhesions transferring forces from the ECM to the cytoskeleton. In fact, focal adhesions and the cytoskeleton interact with each other via the recruitment of proteins such as vinculin [39] or zyxin [152].

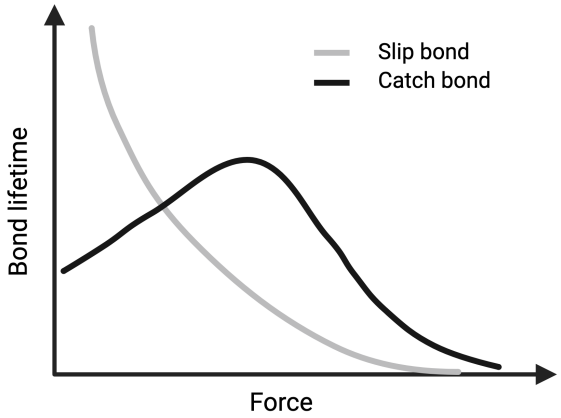

Figure 2.8 Schematic illustration of slip and catch bonds. Slip bonds show a decreasing lifetime with an increased applied force, whereas catch bonds initially get more stable before the bond lifetime decreases above a certain threshold.

This system consisting of the contractile cytoskeleton, integrins/focal adhesion, and ECM is also called a molecular clutch [36, 98]. In particular, Elosegui-Artola *et al.* [36] suggested that the key regulator of the molecular clutch is the force loading rate and not necessarily the force *per se*. According to [36], a typical cycle of the clutch mechanism is initiated by the engagement of the clutches through binding to the ECM substrate with a specific binding rate. Continuous contraction of the cytoskeleton through myosin motors starts loading the engaged clutches and deforms the substrate depending on substrate stiffness. As forces continue to increase, bonds eventually fail, which can lead to a rapid disengagement of the clutches, and the cycle starts again. They also highlight the importance of substrate stiffness in regulating the molecular clutch. Very stiff substrates cause a rapid loading of the clutches, leading to destabilization and preventing additional clutches from engaging. Substrates that are too compliant don't load the clutches fast enough, again leading to destabilization. This mechanism might help to understand cell responses to different substrate rigidities as described in the previous section (cell differentiation and migration). Note that besides ECM stiffness, other factors can also affect the loading rate, such as myosin contractility or integrin binding dynamics [9].

Integrins and focal adhesions have both been identified as important signaling hubs associated with transducing signals originating from mechanical perturbations of the cell environment [47, 148]. Note, though, that cells also sense other signals, such as the concentrations of growth factors or hormones, via numerous receptors on the cell membrane. All these signals are integrated by intracellular signaling pathways, which are usually a complex cascade of chemical reactions that eventually influence

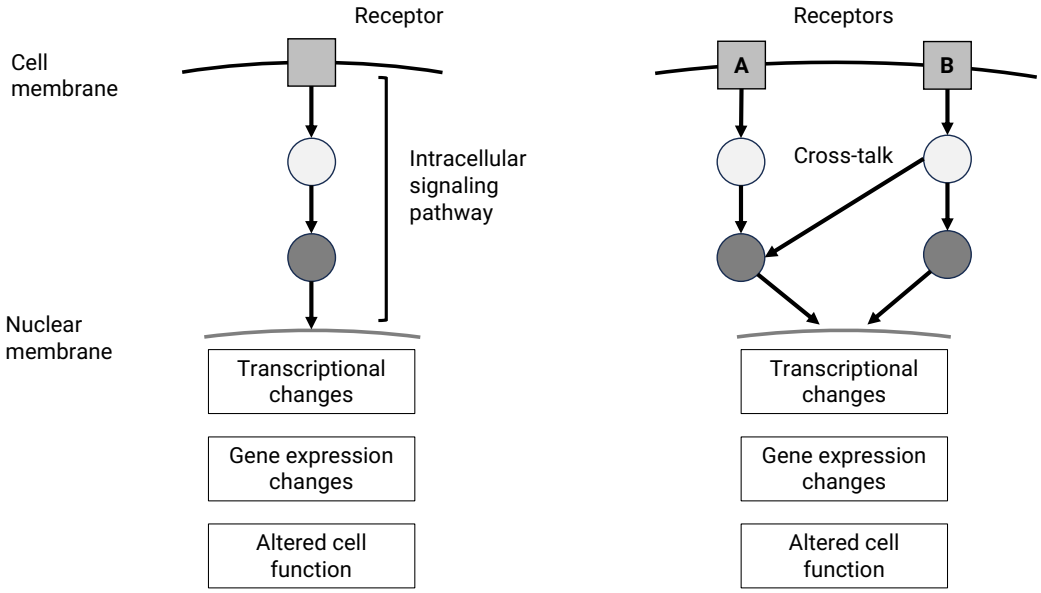

Figure 2.9 Schematic illustration of intracellular signaling pathways. Receptors on the cell membrane sense external stimuli, which can be biochemical or mechanical. This triggers a cascade of intracellular reactions that ultimately lead to altered cell function and behavior through transcriptional changes and associated changes in gene expression. A set of reactions originating from a receptor and causing changes in cell function is often called a signaling pathway. However, individual pathways often interact with each other through cross-talk, such as through shared components that are part of either pathway.

cell behavior and function via the modulation of gene expression, see Fig. 2.9. For example, individual pathways have been identified to regulate or influence cytoskeletal reorganization, migration, proliferation, or differentiation. Oftentimes, however, there is cross-talk between two or more pathways, which makes it difficult to precisely determine which reactions are involved in specific cellular behavior. Nevertheless, recent advances in obtaining and analyzing 'omics' data, that is, genomics, proteomics, and transcriptomics, have helped to generate maps or networks of interactions that likely regulate or at least play a prominent role in specific cellular processes. For example, the Rho/ROCK pathway has been identified as a major regulator of cytoskeletal dynamics, including cell adhesion, motility, and contraction [5], whereas the MAPK (Mitogen-activated protein kinase) pathway has been linked to cell proliferation, differentiation, and development [157].

Interestingly, the cell nucleus has also been identified as a mechanoregulator. For example, mechanical stimuli from the ECM perceived by the focal adhesions and propagated to the cytoskeleton can induce conformational changes of cytoplasmic proteins and subsequent shuttling to the nucleus. These mechano-actuated proteins include, for

example, paxilin [158] or YAP/TAZ [35]. In addition to proteins translocating to the nucleus in response to mechanical cues, the cell nucleus can 'sense' forces through the nucleus-cytoskeletal-integrin coupling. In particular, the nuclear membrane has been identified as a critical component associated with the so-called Linker of Nucleoskeleton and Cytoskeleton (LINC) complex. Nesprins, a protein, are part of the cytoplasmic side of the LINC complex and connect the nucleus to the fibers of the cytoskeleton, while SUN proteins connect the nesprins to the nuclear lamina through lamin A, a nuclear scaffolding protein. This connection into the cell nucleus can then affect the chromatin – a compact package of DNA and proteins – resulting in modulated transcriptional activity [129].

In summary, subcellular structures and molecules are directly involved in mechanosensing and mechanotransduction. While significant progress has been made in uncovering the mechanisms and functions of these components, further studies are still needed to understand better how they interact to regulate cell behavior and how this leads to the observations mentioned previously on the cellular and tissue scales.

2.3 Contributions of this work

As illustrated in the previous sections, mechanobiology is an inherently multiscale discipline involving different length and time scales with cells as the primary mediators. However, cells rarely act in isolation but form a system with their surrounding ECM based on mutual interactions and modifications. Given the multiscale nature of this system, computational modeling at different scales has and will continue to provide meaningful insights into the underlying mechanism of tissue homeostasis and disease. These models range from gene regulatory networks to cell-cell communication to phenomenological models of soft tissue growth and remodeling. Multiscale models that are based on microscale mechanisms and can predict observed adaptations on the macroscale could prove particularly insightful [65].

This thesis aims to advance the understanding of some of the aforementioned mechanobiological processes by using novel computational and experimental tools. In particular, the computational models try to reflect the multiscale nature by including mechanistic approaches on the cellular and subcellular level and linking them to observations/manifestations on larger length and time scales (Papers A and C). The experimental contributions of this work are highly relevant for improving our understanding of mechanical homeostasis, especially under dynamic biaxial loading

of physiological relevance (Paper B). The following publications form the core of the presented work.

Paper A – Integrin-mediated cell migration in three-dimensional fiber networks

Key contributions and findings

- cellular contractility and catch bond integrin behavior is sufficient to reproduce cell migration in realistic three-dimensional fiber networks
- model predicts a constant integrin turnover, with steady-state values depending on cellular contractility and fiber stiffness
- model predicts a biphasic relationship between migration efficiency and fiber stiffness/contraction rate
- durotaxis can arise from purely mechanical interactions without a need to prescribe cell polarization

Paper B – Dynamic biaxial loading of cell-seeded tissue equivalents

Key contributions and findings

- vascular SMCs can establish and maintain a preferred mechanical state under dynamic biaxial loading regardless of external strains up to 10%
- mechanical adaptation of vascular SMCs appears independent of applied loading and boundary conditions within tested range of strains
- study suggests a critical role of forces/stresses in regulating cell behavior consistent with prior studies
- first quantification and comparison of physiologically relevant cyclic loading conditions with implications on multiaxial tensional homeostasis

Paper C – Multiscale model of soft tissue growth and remodeling

Key contributions and findings

- efficient finite element model combining intracellular signaling on the subcellular level, cell-cell communication on the cell level, and mechanics on the tissue level

- first homogenized constrained mixture model to include effects of wall shear stress on G&R
- *in silico* tool to examine effects of disrupted intracellular signal processing and cell-cell communication on tissue adaptation
- identified long-term instabilities in the homogenized constrained mixture model, which could indicate missing assumptions in the theory

Chapter 3

Integrin-mediated cell migration in three-dimensional fiber networks

3.1 Introduction

Cell migration plays an essential role in numerous processes, including development, immune response, wound healing, and cancer [26, 40, 94, 154]. Wound healing, for example, is a complicated multi-step process that relies on the migration of cells (usually fibroblasts) towards and into the injured tissue to deposit new ECM through the secretion of collagen and fibronectin [50]. Additionally, myofibroblasts – a fibroblast phenotype with increased contractility – can assist in closing the wound through contraction [96]. Over time, the cells deposit and remodel the ECM and are removed once the healing process is complete.

Another important example of cell migration is cancer. Cancer cells are highly motile, which allows them to migrate and invade other tissues or organs distant from the primary site of the tumor by entering the circulation through blood or lymphatic vessels [18]. While cancer cells use the same mechanisms as other cells to migrate, it seems like they can transition between different migration modes, thereby retaining an invasive phenotype and potentially rendering therapeutic strategies ineffective [42].

The two most well-characterized modes of migration are amoeboid and mesenchymal migration, and their effectiveness depends on the cell's (mechanical) environment. For example, amoeboid migration is characterized by a more rounded cell morphology and very low cell adhesion to the environment. High rates of polymerization and

contraction of the actin cytoskeleton drive cell body deformations and bleb formation, which move the cell body [81]. This form of migration is often rapid and avoids proteolytic degradation of ECM barriers by circumnavigating obstacles using the high deformability of the cell body. Leukocytes have been observed to use this type of migration [41].

On the other hand, mesenchymal migration depends on cell-matrix adhesions via integrins and is usually associated with high proteolytic activity. This integrin-mediated mode of migration can be described by a 5-step process [86, 119]. It starts with the growth of actin filaments, which push the cell membrane outward, forming pseudopod extensions and the leading edge. This involves numerous proteins that regulate actin cytoskeleton polymerization, such as the ARP2/3 complex. In the second step, integrins interact with the ECM ligands to form cell-matrix interactions. Integrin clustering leads to the formation of stable focal adhesions, which are linked to the actin cytoskeleton through recruited adaptor proteins such as talin or vinculin. Next, surface proteases concentrate near substrate binding sites, cleaving ECM components like collagen or fibronectin. In the fourth step, myosin II binds to actin filaments, generating contraction of the cytoskeleton, which is modulated by the Rho/ROCK pathway. In the last step, focal adhesions disassemble through actin binding and severing proteins, such as cofilin. Following the disassembly of the focal adhesions, integrins detach from the substrate and are recycled towards the leading edge or deposited back onto the substrate. This migration mode is primarily used by mesenchymal cells, such as fibroblasts [29]. Figure 3.1 illustrates the process for migration on a two-dimensional substrate where the third step, protease activity, can be neglected, resulting in a 4-step process.

It has been observed that cells, in particular tumor cells, can switch between mesenchymal migration and amoeboid migration if the internal or external environment changes, which is called mesenchymal-amoeboid transition or amoeboid-mesenchymal transition [103]. For example, if the proteolytic activity of HT-1080 fibrosarcoma cells, which is associated with mesenchymal migration, is inhibited, they transition to protease-independent amoeboid migration [146]. Alternatively, if adhesion to the substrate is inhibited via disruption of integrins, tumor cells migrating in three-dimensional matrices can compensate for the loss of adhesion by transitioning to amoeboid migration, which does not require substantial cell-matrix connections [42]. Importantly, this cannot be achieved when cells migrate on two-dimensional substrates, as a loss of adhesion leads to the detachment of the cell from the substrate. This already highlights a subtle but key difference between migration in 2D and migration

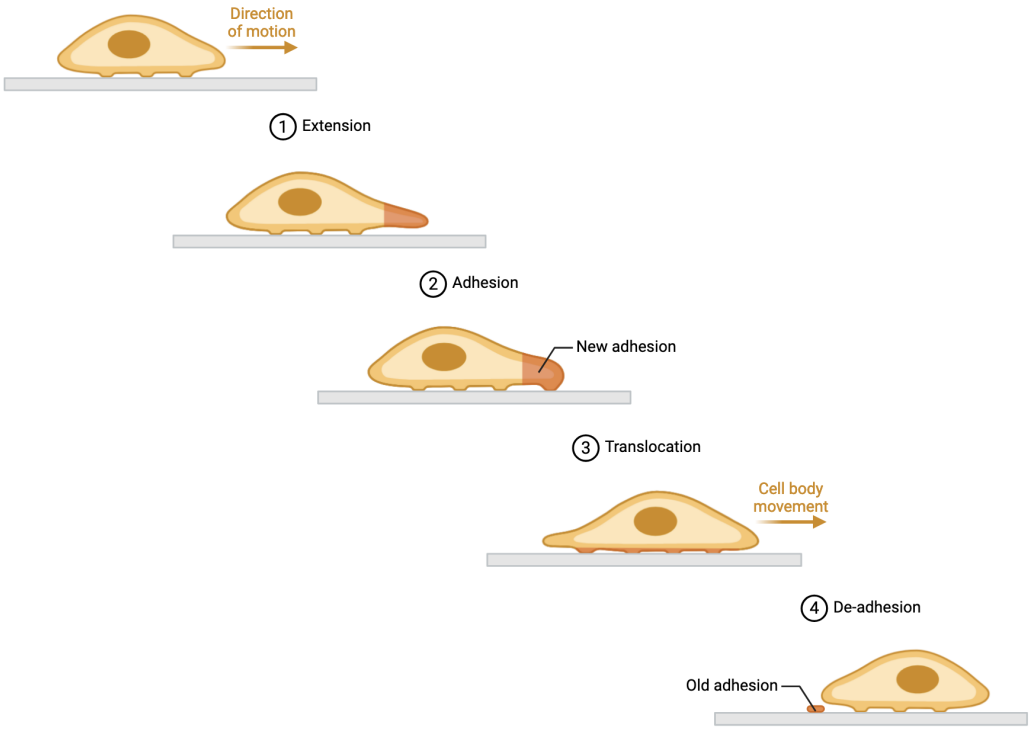

Figure 3.1 Schematic illustration of cell migration process on a two-dimensional substrate. In this case, proteolytic activity can be neglected, and the 5-step process described in [86, 119] turns into a 4-step process. (Created with BioRender.com)

in 3D. The challenges of cell migration in three-dimensional fiber networks, for the cell as well as for experimental observations, will be discussed in the next section.

3.2 Challenges of cell migration in 3D fiber networks

Cell migration has been studied extensively in two dimensions [104, 113]. For example, migration speeds of different cell types have been compared by Friedl *et al.* [43] and Bangasser *et al.* [9] investigated migration on substrates of different stiffnesses. While these findings have improved the understanding of certain molecular and biophysical mechanisms involved in cell migration, it is unclear if they also apply to three-dimensional migration, which is the most common *in vivo*. In fact, Cukierman *et al.* [21], Doyle *et al.* [28], and Yamada *et al.* [150] describe in their review articles how cell migration and cell-matrix interactions can significantly depend on dimensionality.

Regardless of the mode of migration, mesenchymal or amoeboid, complex three-dimensional fiber networks present many additional physical challenges to the cell, which are not present when migrating on two-dimensional substrates. For example, dense

ECM fibers might lead to cell confinement, which requires proteolytic modification or transient or permanent remodeling of the ECM via active contractile forces to continue moving. This is usually a characteristic of mesenchymal cell migration, whereas amoeboid migration exploits pores in the ECM to squeeze through using the cell nucleus as a mechanical gauge [111]. Additionally, different local mechanical properties might guide cell migration, including topological cues, spatially varying concentrations of ECM constituents, or ECM crosslinking. In particular, it is important to consider the local rather than the global mechanical properties of the ECM. While individual collagen fibers possess a relatively high Young's modulus of around 1 MPa [72], the bulk Young's modulus of a reconstituted collagen gel is typically on the order of 1 Pa to 1 kPa [4, 73]. This discrepancy between bulk mechanical properties and micromechanical properties, which are likely more important to the individual cell [27], is challenging to investigate and control in experiments. Besides these external challenges, the cell nucleus is the greatest internal physical limitation for a cell migrating in three-dimensional fiber networks. Since it is the least deformable part of a cell, it is often a limiting factor when small pore sizes confine cell movement [145].

From an experimental point of view, performing cell migration experiments is challenging because it is difficult to precisely modulate individual parameters of the ECM or fibrous scaffolds. For example, increasing the collagen concentration of reconstituted hydrogels leads to a reduced pore size [145]. At the same time, however, this can change the fiber diameters and the bulk mechanical properties. Changing the polymerization temperature or the source of collagen can also have a significant influence on the resulting fiber network and affect pore size as well as fiber diameter [145]. Furthermore, the plasticity of cells to transition to different migration modes can make it difficult to uncover the underlying mechanisms one is interested in. Many of these compensatory effects, such as switching to different integrin types if the primary type is blocked [128], complicate experimental studies even though they might be beneficial *in vivo*. Hence, systematically studying cell migration in three-dimensional fiber networks is challenging, as it requires precise control of the network architecture and properties on the micro- and macroscale as well as the mechanisms involved in cell migration.

3.3 Summary and contribution of paper A

To overcome the challenges associated with experimentally investigating cell migration in three-dimensional fiber networks, a previously developed finite element model of

cell-matrix interactions was used [32]. This model can recreate realistic biological fiber networks based on key descriptors such as free fiber length, valency, and fiber orientation correlation. Moreover, the model can capture the multiscale mechanics inherent to these networks with individual fibers having a stiffness on the order of MPa, whereas the hydrogel itself has a stiffness on the order of $1\ Pa - 1\ kPa$.

This study focuses on mesenchymal migration, which depends on integrins to form cell-matrix adhesions and active cytoskeletal contraction to move the cell body. The integrins are modeled as springs, which can transiently bind to fibers of the ECM and cluster into focal adhesions. Similar to what has been observed experimentally (see chapter 2.2.3), integrin dynamics are modeled as catch bonds with an initially increasing bond lifetime as force is applied before destabilizing once a threshold force is exceeded [78, 140]. Cytoskeletal contraction, mediated by contractile stress fibers, is included via rods that connect the cell nucleus to the integrins and that can change their length based on a constant, predefined contraction rate. In doing so, the stress fibers exert forces on the integrins and, in turn, on the fibers of the ECM. The translocation of the nucleus is then determined by the force balance of the attached stress fibers. Importantly, the focus is on integrin-mediated migration in non-confining networks, i.e., networks where the pore size is larger than the size of the cell nucleus so that proteolytic activity plays no significant role. Hence, the cell nucleus is not modeled explicitly but instead represented by a single point. This reduced model offers precise control over three key mechanical constituents of migration, namely cellular contractility, focal adhesions based on integrins, and the fibrous network.

After verifying the simulations based on experimental results from other studies [27, 29, 145], variations of various network and fiber parameters were studied. In particular, how the collagen concentration, the fibers' Young's modulus, and cytoskeletal contraction rates influence cell migration. In all simulations, the number of integrins reaches a steady state, albeit at different levels, mainly depending on collagen concentration and fiber stiffness. Note, though, that this state is dynamic, and integrins continuously bind and disengage.

Similar to the results described by Bangasser *et al.* [9], the simulations showed a biphasic relationship between migration efficiency and fiber stiffness as well as between migration efficiency and cytoskeletal contraction rate. Here, migration efficiency is defined as the mean squared displacement (MSD), which gives a statistical measure of how effectively a random walker, in this case the cell, can explore its surroundings.

Furthermore, a stiffness gradient can be introduced by prescribing a gradient in fiber diameter along one direction of the simulation domain, which permits the study

of directed cell migration based on external signals. These simulations showed that the included micromechanical mechanisms appear sufficient to reproduce durotaxis, the tendency of cells to migrate toward stiffer regions. Interestingly, a steady state number of integrins was also observed in this case, which was very similar to the homogeneous networks studied before. Moreover, higher collagen concentrations and higher cytoskeletal contraction rates seemed to improve gradient detection and subsequent movement along the gradient.

In summary, the results showed that the combination of realistic (micro)mechanics of a fiber network, cell-matrix interactions via catch bonds, and contraction of cytoskeletal stress fibers appear sufficient to reproduce cell migration in three-dimensional fiber networks. Notably, no other assumptions, such as how cell polarization occurs or how local stiffness is sensed, were required. Yet, the model was able to reproduce realistic migration speeds and capture more complex phenomena such as durotaxis.

3.4 Future perspectives

Multicellular migration In many cases *in vivo*, cells do not migrate in isolation but could be affected by other cells in the vicinity. This is especially important for tumor cells. Using the presented model, it could be studied how two migrating cells influence each other, potentially affecting migration speed, efficiency, or persistence.

Contact guidance By modifying the fiber networks, it is possible to introduce topological cues into the ECM, such as a preferred fiber alignment. This so-called contact guidance presents an oriented signal to the cell, which has been observed to promote directional cell migration along the fibers [30, 139]. According to Provenzano *et al.* [108], contact guidance could play an important role in cancer cell invasion by exploiting aligned ECM to rapidly migrate and invade tissue.

Modified integrin dynamics Another interesting study would be to examine the influence of different integrin dynamics. This could potentially affect migration speeds and shift the stiffness at which optimal migration efficiency was observed. Modified integrin dynamics could be interpreted as a different integrin type (especially if experimental data are available), a diseased case, or modifications by a pharmacological treatment.

Chapter 4

Dynamic biaxial loading of cell-seeded tissue equivalents

4.1 Introduction

Cell-matrix interactions are not only important for cell migration but also play a significant role in tissue development, health, and disease [24]. As mentioned in chapter 2, cell-matrix interactions provide a mechanism for cells to regulate the ECM (inside-out signaling) as well as to receive biomechanical signals from the surrounding ECM (outside-in signaling).

To maintain a preferred mechanical state, cells can regulate the composition, structure, and mechanical properties of the ECM, which is referred to as mechanical homeostasis [14, 63]. On short time scales of several hours, cells likely adjust their contractile forces to maintain a preferred mechanical state according to Eichinger *et al.* [34]. On longer time scales, cells might adjust ECM turnover via increased production and removal to restore a preferred mechanical state. Importantly, in this case newly deposited ECM must be incorporated within existing ECM under load, which requires that newly synthesized ECM constituents must have the same mechanical properties as the degraded ones. Thus, proper regulation of ECM turnover is essential to maintain tissue form and function.

On the other hand, cell behavior is influenced by ECM constituents, organization, and mechanical properties. As mentioned previously, ECM stiffness can have significant effects on cell differentiation, migration, and survival. In fact, cell-matrix interactions

are vital for adherent cells as they need to be anchored to the ECM or otherwise undergo anoikis, a form of programmed cell death that occurs when cell-matrix interactions are disrupted [44]. Moreover, forces in the ECM, transmitted to the cell via attachments to the ECM, can result in changes in cell behavior, often indicated by altered gene expression. For example, cyclic stretching of cell-seeded tissue equivalents has been shown to affect expression levels of collagens, MMPs, and signaling molecules, such as transforming growth factor-β [51]. However, this is dependent on the cell type as well as the applied strain magnitude and frequency.

To understand better how ECM composition, structure, and mechanical properties affect cell behavior or vice versa, how cell behavior affects ECM properties, experiments with cell-seeded tissue equivalents have proven useful. They represent a simple model system of native tissue but remove a lot of complexity and are easier to modulate. Controlled mechanical testing of these simpler model systems can help to get a better understanding of the reciprocal nature of cell-matrix interactions, including underlying mechanisms of mechanotransduction. It is important to precisely quantify and compare cellular adaptations in response to various external loading and boundary conditions, particularly to physiologically relevant conditions. This typically excludes uniaxial testing as most tissues *in vivo* are subjected to multiaxial loading.

4.2 Limitations of mechanical testing devices for cell-seeded tissue equivalents

To study how cells react to mechanical stimuli, different experimental devices and approaches have been developed in the past decades. For example, the FlexCell device provides a relatively simple 2D culture system in which a monolayer of cells grown on an elastic membrane can be stretched by applying a vacuum. Possible dynamic loading conditions include uniaxial as well as equibiaxial stretching. This device has been used successfully in a variety of studies, for example, examining inflammatory or fibrotic responses to mechanical strain [2, 156]. However, the FlexCell device has several limitations. First, it is a 2D culture system, and as mentioned in previous chapters, cell behavior can be significantly different in 2D and 3D, which is the predominant environment for cells *in vivo* [21, 28, 150]. Second, it does not permit the application of non-equibiaxial or strip-biaxial loading, which is often what cells experience in the body. Third, the device is not able to measure the cell-generated forces, which is required to study phenomena such as *tensional homeostasis*.

To resolve the first limitation and study cell-matrix interactions in three-dimensional environments, including cellular behavior in response to mechanical perturbations, so-called tissue equivalents, introduced in the late 1970s [11], can be used. They represent a simplified version of the highly complex extracellular matrix by reducing the myriad constituents usually present in the ECM to a single fibrillar protein, such as collagen or fibrin, thereby omitting confounding factors. Collagen-based tissue equivalents (also called hydrogels due to a high content of bound water) are most common as collagen is the predominant structural protein in mammals.

Initially, unconstrained and free-floating gels were used to study how cells compact and remodel the ECM [11, 120]. Later studies introduced more capable devices (or bioreactors) that were able to subject the gels – often rectangular or ring-shaped – to static or dynamic (uniaxial) strains [14, 133]. Some of these devices could also measure the cell-generated forces and mechanical adaptations in response to externally applied loads. This led to the seminal discovery that cells tend to maintain and restore a preferred mechanical state even when subjected to external mechanical perturbations, which was termed *tensional homeostasis* [14].

Despite the significant insights gained through these experiments, the devices were not able to subject the tissue equivalents to realistic biaxial loads and boundary conditions. Further developments were necessary to introduce biaxial bioreactors that allowed to mimic *in vivo* conditions more closely. For example, Hu *et al.* [58] used a custom biaxial bioreactor based on [62] to study the effects of static equibiaxial and strip-biaxial loading on the mechanical properties of tissue equivalents. Lee *et al.* [87] performed similar investigations but with dynamic cyclic equibiaxial loading. Other studies focused on the influence of stretch on fiber and cell alignment [19, 49] or tried to enhance the mechanical properties of tissue-engineered constructs [99, 115, 118]. However, only few studies report forces cells establish and maintain in collagen-based tissue equivalents under dynamic loading. Additionally, most previous studies focused on uniaxial studies, even though most soft tissues are subjected to multiaxial loading *in vivo*.

4.3 Summary and contribution of paper B

To address the limitations mentioned above, we used a previously developed biaxial bioreactor that can measure cell-generated forces while subjecting the tissue equivalents to various static or dynamic loading conditions [31]. These conditions include uniaxial, equibiaxial, non-equibiaxial, and strip-biaxial stretching (Fig. 4.1).

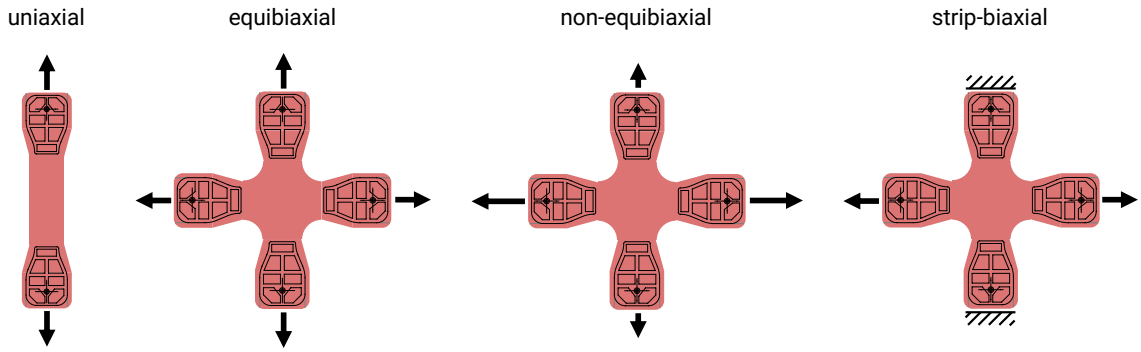

Figure 4.1 Schematic illustration of possible experimental setups using the bioreactor described in [31]. In particular, the biaxial experiments are relevant since most tissues *in vivo* are subjected to multiaxial loading conditions.

To mimic *in vivo* loading conditions, especially the latter three conditions are relevant. For instance, strip-biaxial loading is characterized by holding the sample at a constant overall stretch along one axis while cyclically stretching in the orthogonal axis. This represents a highly physiologically relevant loading condition as, for example, vascular SMCs of the aorta are subjected to cyclic stretching in the circumferential direction, while there is little to no axial stretch during a cardiac cycle [7].

In this study, primary aortic SMCs were isolated from the descending thoracic aorta, suprarenal abdominal aorta, and infrarenal abdominal aorta of mice. After culturing under standard cell culture conditions, the cells were embedded in collagen gels and tested using our custom bioreactor. Different loading protocols were used to (1) assess the effects of increased equibiaxial loading amplitudes and (2) examine the effects of different boundary conditions (strip- vs. equibiaxial) while keeping the stretch amplitude the same. All loading protocols consisted of the same three phases: (i) a 15-hour initialization phase to allow cells to attach to the collagen matrix and establish preferred forces, (ii) a quasi-static force-extension test, (iii) seven hours of cyclic loading (either equibiaxial or strip-biaxial stretching). Phases (ii) and (iii) formed an interval that was repeated seven times, resulting in a total duration of the experiment of approximately 66 hours.

The results suggest that the mechanical adaptation of the cells was largely independent of the applied loading and boundary conditions. This was shown by nearly identical mean steady-state forces during all cyclic loading intervals regardless of loading amplitude (equibiaxial 5% vs. 10%) and boundary condition (equi- vs. strip-biaxial at 5%). These results align with previous experiments on ring-shaped tissue equivalents [142], and the authors hypothesized that cells adapt the stiffness of their actin

cytoskeleton to maintain a preferred range of stresses. Recent experiments by Walker *et al.* [134] confirmed this hypothesis by inhibiting cytoskeletal remodeling of the actin cytoskeleton, which abolished the ability of cells to adjust their stiffness and hence maintain a preferred mechanical load.

Moreover, stiffness-force plots from the force-extensions tests showed a remarkable similarity for all loading conditions for the forces the cells adapted to. This could suggest that cells not only try to maintain a preferred force or stress but also a preferred stiffness-force relationship. However, further experiments are necessary to explore and validate this hypothesis and find the direction of influence.

In summary, the study showed that vascular SMCs can establish and maintain a preferred mechanical state under dynamic biaxial loading regardless of external strains of up to 10%. Overall, the study highlighted the important role of force, stress, or tension in regulating cell behavior and is consistent with prior studies [74, 75, 88]. This was the first quantification and comparison of diverse types of cyclic loading of vascular SMC-seeded tissue equivalents, particularly using *in vivo* relevant conditions having implications on multiaxial tensional homeostasis.

4.4 Future perspectives

Cell types and knockouts To examine if the observed behavior is specific to vascular SMCs or a generic mechanical homeostatic process, additional cell types, such as adventitial aortic fibroblasts, could be tested. Moreover, to probe the underlying subcellular or molecular mechanisms of the observed behavior, cells with genetic defects in mechanosensory proteins, such as in the focal adhesions complex (cf. section 2.2.3), could be tested and potentially provide valuable insights.

Histology and gene expression Adding histological analysis could prove helpful in studying effects such as cell or fiber (re-)alignment and provide deeper insight into micromechanical changes, potentially relevant for computational modeling. A more involved addition would be to examine gene expression (via qPCR or gene sequencing) under the different loading conditions, which could provide valuable insights into subcellular processes and signaling pathways responsible for the observed behaviors. For example, specific contractile proteins might be differentially regulated under different loading amplitudes, potentially even showing spatial differences (for example, static vs. cycled arms in strip-biaxial experiments).

Chapter 5

Multiscale model of soft tissue growth and remodeling

5.1 Introduction

Given the complexity of soft tissue growth and remodeling and the associated experimental difficulties, computational modeling is indispensable to increase the understanding of the underlying mechanisms. Besides facilitating systematic hypothesis testing, these models can be used to predict tissue adaptation under various conditions.

For example, Taber and Humphrey [125] have shown that for arteries, growth correlates better with stress than with strain, leading to the often used hypothesis that arterial growth is stress-regulated [8, 57, 80], and in particular, regulated by deviations of stress from a preferred setpoint [65]. Note, though, that while stress is a convenient metric for modeling purposes, it remains unclear which quantity serves as a target variable for mechanical homeostasis, thereby driving G&R [33].

These models have also been used to study disease progression. For example, the evolution of cerebral [8] or aortic aneurysms [83, 89, 144], which are local dilatations of a blood vessel and can lead to fatal consequences due to rupture or dissection. Other examples include vascular aging [131], hypertension [84, 85], or thrombus formation [25]. The latter can, among other conditions, lead to myocardial infarction or pulmonary embolism.

In addition to hypothesis testing and modeling disease progression, these models allow researchers to optimize artificially engineered tissue in a cost- and time-effective

way. For example, they have been used to optimize the (mechanical) properties of tissue-engineered vascular grafts (TEVGs) [97, 124], while others have highlighted the critical role of the immune response during vascular graft degradation [123].

Importantly, those modeling approaches are not limited to the vasculature but can also be used to gain insight into adaptation processes of cardiac tissue [46, 102], pattern formation in the brain [55], or skin mechanics [126]. Computational modeling, as a general tool in biomechanics and mechanobiology, can thus help better understand how changes in the mechanical environment affect tissue adaptation and potentially lead to the development of new therapeutic strategies or assist in developing artificial tissue constructs.

5.2 Missing inter- and intracellular signaling in current G&R models

Two major theoretical frameworks have been developed in the past decades to model the adaptation of soft tissues in response to changes in their mechanical environment. The first is the kinematic growth model developed by Rodriguez *et al.* [114], which shares similarities with mathematical models of plasticity and viscoelasticity. This theory is based on a multiplicative split of the total deformation gradient at G&R time s into an elastic part and an inelastic growth part,

$$\mathbf{F}(s) = \mathbf{F}_e(s)\mathbf{F}_g(s). \tag{5.1}$$

$\mathbf{F}_g$ deforms the stress-free reference configuration to an intermediate configuration, also stress-free but generally geometrically incompatible. The subsequent elastic deformation $\mathbf{F}_e$ maps the intermediate configuration to the current configuration, which is geometrically compatible and in mechanical equilibrium. To compute the elastic part of the deformation, a mechanobiological constitutive equation for $\mathbf{F}_g$ is required since the total deformation $\mathbf{F}$ is known. Different approaches exist to define an appropriate constitutive equation, for example, via the definition of a linear evolution equation for $\dot{\mathbf{F}}_g$ or via directly specifying an equation for $\mathbf{F}_g$. Regardless of the approach, the constitutive equation must fulfill the assumption that no growth takes place in the homeostatic state. The advantage of the kinematic growth model is its mathematical simplicity, which allows an efficient computational implementation. However, the model cannot accommodate different constituents with different natural stress-free configurations and growth characteristics. In addition to focusing on growth (changes

in tissue mass) and not remodeling (changes in tissue microstructure), the model is mainly focused on the consequences of G&R and not on biological or micromechanical processes.

The second framework is the constrained mixture theory developed by Humphrey and Rajagopal [59]. Here, an infinitesimal volume element is assumed to consist of n structurally significant constituents such as elastin, collagen, and smooth muscle. The key assumption is that all constituents ($i \in \{1, 2, ..., n\}$) experience the same total deformation $\mathbf{F}$ with respect to a reference configuration – they are constrained to deform together.

During growth and remodeling, different individual mass increments of each constituent i can be deposited at times $\tau \geq 0$ with an elastic prestretch $\mathbf{F}_{pre}^{i(\tau)}$ with respect to a fictitious stress-free natural configuration $\kappa_n^{i(\tau)}$. Importantly, while the total deformation gradient $\mathbf{F}$ is the same for all volume elements, the elastic and inelastic parts vary for each constituent. Thus, the current elastic part of the deformation gradient of constituent i at time s, which was deposited at time τ, is then given by

$$\mathbf{F}_e^i(s,\tau) = \mathbf{F}(s)\mathbf{F}(\tau)^{-1}\mathbf{F}_{pre}^{i(\tau)} \tag{5.2}$$

with $\mathbf{F}(s)$ the deformation gradient of the whole mixture, $\mathbf{F}(\tau)$ the deformation gradient of the mixture at deposition time τ, and $\mathbf{F}_{pre}^{i(\tau)}$ the above described prestretch. Note that $\mathbf{F}_{pre}^{i(\tau)}$ is often assumed to be constant, i.e., independent of deposition time τ.

Since the deposited mass increments have finite half-lives, they degrade over time, affecting the mass density $\rho_0^i(s)$ of constituent i at time s. The mass density of constituent i per unit reference volume is then given by

$$\rho_0^i(s) = \rho_0^i(0)Q^i(s) + \int_0^s \dot{\rho}_{0+}^i(\tau)q^i(s,\tau)d\tau \tag{5.3}$$

where $\rho_0^i(0)$ is the intial density of consitituent i and $Q^i(s)$ its remaining fraction at time s. The true (local) mass production rate at time τ is given by $\dot{\rho}_{0+}^i(\tau)$ and $q^i(s,\tau) \in [0,1]$ represents the fraction of the mass deposited at time τ that survives at time s. The mass density of the entire mixture is the sum of the individual mass densities, $\rho_0(s) = \sum \rho_0^i(s)$. Similarly, the strain energy of the mixture is given by the sum of the individual strain energies, $\Psi(s) = \sum \Psi^i(s)$, where the individual strain energy of constituent i is given by

$$\Psi^i(s) = \rho_0^i(0)Q^i(s)W^i(\mathbf{F}_e^i(s,0)) + \int_0^s \dot{\rho}_{0+}^i(\tau)q^i(s,\tau)W^i(\mathbf{F}_e^i(s,\tau))d\tau \tag{5.4}$$

with W^i the strain energy per unit reference mass of constituent i, which is a function of the elastic part of the deformation gradient $\mathbf{F}_e^i(s,\tau)$. To close the system of equations, constitutive equations for the mass production, $\dot{\rho}_{0+}^i(\tau)$, and removal, $q^i(s,\tau)$, need to be defined.

While the constrained mixture theory is based on realistic micromechanical processes of G&R – the continuous production and removal of constituents in potentially different stressed configurations – its mathematical theory is complex, and simulations are computationally expensive since a large number of evolving natural configurations have to be tracked for each constituent.

To overcome this complexity, Cyron *et al.* [22] introduced the homogenized constrained mixture model, which combines the efficiency and simplicity of the kinematic growth model with the micromechanical foundations of the constrained mixture model. The key idea is to replace computationally expensive evaluations of history integrals, such as in equation (5.4), with a temporal homogenization over all mass increments deposited at different times τ. In this way, the effect of growth and remodeling can be represented by an averaged inelastic deformation gradient $\mathbf{F}_{gr}^i(s)$ that is independent of the deposition time τ of individual mass increments of constituent i. The elastic part of the deformation gradient for constituent i is then given by

$$\mathbf{F}_e^i(s) = \mathbf{F}(s)\mathbf{F}_{gr}^i(s)^{-1} = \mathbf{F}(s)\mathbf{F}_g(s)^{-1}\mathbf{F}_r^i(s)^{-1} \tag{5.5}$$

where $\mathbf{F}_g(s)$ captures the inelastic change of geometry due to growth of all constituents together (change of tissue mass), and $\mathbf{F}_r^i(s)$ captures the inelastic part of the deformation gradient resulting from remodeling due to mass turnover of each constituent i. Both $\mathbf{F}_g$ and $\mathbf{F}_r^i$ have to be defined via evolution equations.

Regardless of using the original constrained mixture model or the homogenized version, both rely on constitutive equations to determine growth. Mass production is often defined based on an average deviation of a scalarized metric of the Cauchy stress from a preferred state σ_h,

$$\dot{\rho}_{0+}^i(s) = \frac{\rho_0^i(s)}{T^i}\left[1 + k_\sigma \frac{\sigma^i(s) - \sigma_h^i}{\sigma_h^i}\right] \tag{5.6}$$

with T^i a characteristic decay time of constituent i, and k_σ a dimensionless gain parameter. Note though that other definitions of $\dot{\rho}_{0+}^i(s)$ are possible.

While this definition allows a simple and efficient implementation to simulate tissue adaptation, it does not allow detailed studies of subcellular processes. Especially the

macroscopic consequences of disturbed intracellular signal processing are difficult to include in this case since it might not be apparent *a priori* how disrupted cell signaling affects the gain parameter.

In recent years, numerous intracellular signaling pathways have been identified as mechanosensitive and potentially affecting growth and remodeling. Additionally, (biochemical) cell-cell communication, which can play a significant role in tissue homeostasis and disease, for example, in the case of inflammation, has been studied in more detail. These studies greatly benefited from recent advancements in generating and analyzing 'omics' data, such as proteomics and transcriptomics, resulting in vast amounts of data giving insight into subcellular processes.

Thus, there has been an increased interest in more mechanistic models that focus on cells (including intracellular signaling and cell-cell communication) as the main mediators of tissue growth and remodeling. Both of these aspects are important if one seeks to understand the complex multiscale nature of mechanobiological adaptation processes in health and disease.

5.3 Summary and contribution of paper C

Building on previous works of Irons *et al.* [71] and Marino *et al.* [91], a homogenized constrained mixture model of soft tissue growth and remodeling that includes intracellular signaling as well as biochemical cell-cell communication was developed.

Instead of using a phenomenological gain parameter in equation (5.6), the output of a cell signaling model governs growth. This intracellular signaling model is based on a logic-gated system of ordinary differential equations (ODEs) that represent the biochemical reactions that occur within the cell during signal processing. The underlying framework has been introduced by Kraeutler *et al.* [79] and, despite its simplicity compared to other modeling approaches, showed remarkable results in various studies [48, 155].

The model can accommodate several cell types, each with their own intracellular signaling pathways. In combination with standard reaction-diffusion equations, this allows biochemical cell-cell communication via autocrine or paracrine signaling. This is achieved through the secretion of different signaling molecules (again regulated by the output of intracellular signaling pathways) by the cell types included in the simulation, which subsequently diffuse through the tissue to reach their target cells. This approach also allows the addition of external substances, such as possible time-

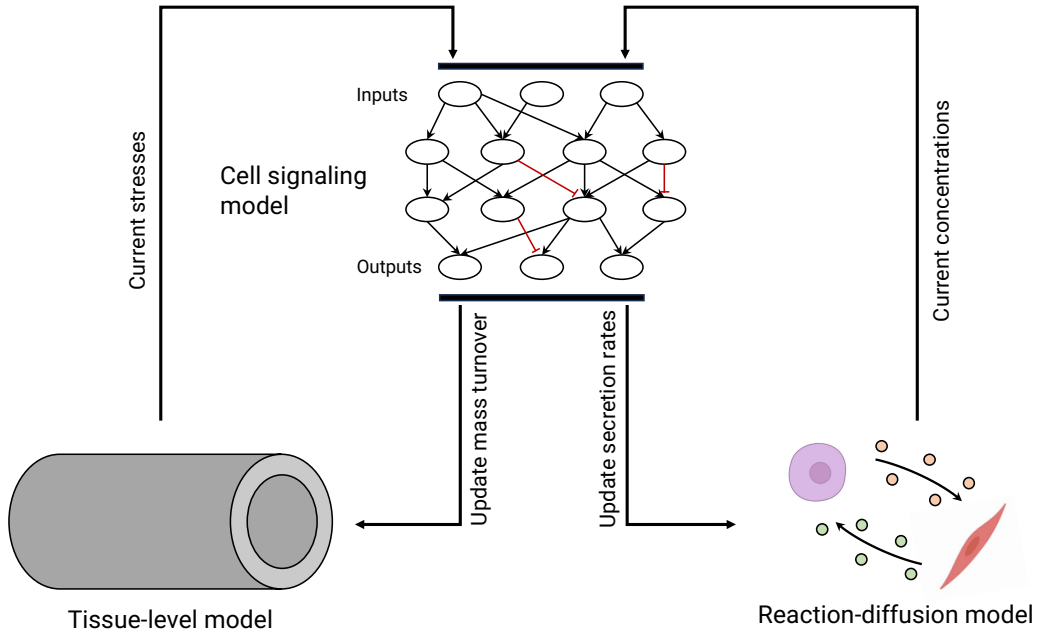

Figure 5.1 Schematic illustration of the multiscale model. Key mediators of the tissue adaptation process are the intramural cells, which are represented by the cell signaling model. The current mechanical state, e.g., transmural stresses, and current concentrations of signaling molecules, serve as input to the intracellular signaling network. Solving the cell signaling model leads to updated mass turnover and secretion rates, which affect the tissue-level mechanical model and the reaction-diffusion model, which capture cell-cell communication.

dependent pharmacological treatments or endocrine signals. The coupled multiscale model is schematically illustrated in Fig. 5.1.

Using the model, it could be shown that the presence of exogenous angiotensin II (AngII), a hormone involved in blood pressure regulation [95], does affect the time course of tissue adaptation by increasing collagen turnover. Additionally, including the effects of biochemical cell-cell communication between endothelial cells (responding to changes in wall shear stress) and intramural cells (SMCs and fibroblasts) can significantly influence the outcome of the G&R process. Importantly, homogenized constrained mixture models have so far neglected the influence of wall shear stress-mediated growth and remodeling.

While these results are promising, the simulations showed long-term instabilities when there was rapid growth, occurring when parameter values representing the sensitivity to changes in stress were large. Notably, these instabilities were not limited to the newly introduced coupled model but also appeared in the standard version of the homogenized constrained mixture model. The reasons for the instabilities are unclear and could indicate missing assumptions or mechanisms in the model. Interestingly,

these instabilities could be resolved if diffusion of the intramural cells was included, which could be interpreted as a form of cell migration. However, this lacks physiological foundations.

5.4 Future perspectives

Genetic disorders and pharmacological treatments Very low sensitivities to stress could be interpreted as a compromised (stress) receptor, potentially leading to maladaptive adaptations in response to changes in the mechanical environment. However, these kinds of defects, possibly caused by a genetic disorder, can show at any node in the network. If the disturbed node leads to a maladaptive response might not be immediately apparent since compensatory mechanisms, such as alternative paths in the signaling networks, could still ensure homeostasis. These disturbances in the network, often in the form of knockdowns/knockouts or overexpressions, can be easily included in the logic-gated signaling pathways to probe potential compensatory mechanisms.

Related to this kind of study might be the identification of potential pharmacological targets to rescue maladaptive behavior caused by compromised intracellular signaling. A separate network analysis could prove useful in quantifying or ranking the importance of nodes, for example, by the number of connections (total, incoming, or outgoing). The combination of theoretical network analysis and simulations could potentially help identify possible targets, which might not necessarily be the affected node itself, that could lead to a compensatory adaptive response.

Cell heterogeneity It is known that not all cells of the same type are identical, and there is usually a certain degree of variation between cells. For example, the same cell type can express different phenotypes to establish several distinct subpopulations, such as synthetic or contractile SMCs. In other cases, only a certain percentage of a cell population might be affected by a genetic disorder.

This kind of variation in cell behavior can be included in the model by creating several signaling networks with different parameters for each subpopulation of interest. The total pathway output for a given cell type is then computed as the outputs of the individual cell signaling networks weighted by the relative contribution of the subpopulation

$$\psi^i(s) = \sum_{j=1}^{k} w_j \cdot \psi_j^i(s), \tag{5.7}$$

with $\psi^i(s)$ being the total output of node i at time s, w_j the weight of subpopulation j, and $\psi^i_j(t)$ the output of node i of the signaling network of subpopulation j. Note that the weights are constrained by $\sum_j^k w_j = 1$ with k the number of subpopulations. Currently, we assume a constant, relative distribution of the subpopulations. This is a simplification that might not hold true in reality as it is possible that one subpopulation might outgrow the others significantly, leading to a change in the relative distribution. If this is the case, it would be more appropriate to model each subpopulation as an individual constituent so that their mass densities can evolve independently.

Cellular networks The study presented the case of EC-intramural cell communication via nitric oxide and endothelin-1. However, there are many more potential cell combinations that could be studied in the future. For example, inflammation has been associated with hypertension, particularly mediated by the accumulation of immune cells in the vasculature and even other organs [53, 54]. Using the proposed model could help identify key mechanisms regulating the inflammatory response in soft tissues.

Chapter 6

Discussion

As described in chapter 2, mechanobiology is an inherently multiscale phenomenon. The incomplete understanding of mechanobiological systems as a whole, such as the reciprocal relationship of cells embedded in ECM, makes it difficult to translate findings on the molecular or cell level directly to adaptations on the macroscopic tissue scale. However, this is often the goal, for example, for tissue-engineered constructs. This work investigated different aspects of mechanobiological systems to improve the understanding of (emergent) system properties spanning multiple length and time scales to explain experimental observations and provide insight into underlying mechanisms. The projects ranged from cell migration in three-dimensional fiber networks to dynamic biaxial testing of cell-seeded tissue equivalents to multiscale modeling of soft tissue growth and remodeling. The following section reviews the results of these projects by highlighting their importance and discussing limitations.

Cell migration – Paper A This study examined micromechanical mechanisms underlying cell migration in realistic three-dimensional fiber networks characterized by a multiscale mechanical behavior. The study was able to reproduce realistic cell migration speeds observed experimentally as well as more complex phenomena such as durotaxis. This was achieved by introducing a simple set of subcellular and molecular mechanisms: (i) cell-matrix interactions based on catch bonds and (ii) a constant contraction rate of the stress fibers connecting integrins to the cell nucleus.

During integrin-dependent migration, cell-matrix adhesions are essential for allowing efficient cell movement. In particular, Doyle *et al.* [27] have shown that the local stiffness perceived by an individual adhesion in combination with applied forces governs adhesion stability. This observation could be key for interpreting the simulation results.

For example, the results showed that after an initialization phase, the number of bound integrins stabilized and reached a dynamic steady state, meaning there was a constant turnover of integrins. This is an important finding since a balanced turnover of adhesions is required to allow cell migration [52, 66, 137]. If adhesions are too stable, the cell will not be able to detach from the matrix, whereas if adhesions are not stable enough, the cell can not apply forces to the ECM to move the cell body. Interestingly, we found that the steady state level of integrins depends on the contraction rate as well as the fiber stiffness. This could result from the catch bond behavior where a higher contraction rate or, similarly, a higher fiber stiffness leads to a more rapid loading of the integrins, resulting in increased adhesion stability, thereby allowing more integrins to bind. However, there might be an upper limit for both fiber stiffness and contraction rate, which leads to a saturation behavior above which integrins are loaded too rapidly and become unstable.

Additionally, the results revealed a biphasic relationship between fiber stiffness and migration efficiency in terms of mean squared displacement. A similar observation has been made by Bangasser *et al.* [9] in experiments on two-dimensional substrates. Again, this could result from adhesion stability, where a specific combination of ECM fiber stiffness and contraction rate leads to an optimal range of adhesion stability (neither too stable nor too unstable), allowing more efficient migration. To verify this hypothesis, future simulations could vary the integrin binding dynamics (particularly, the force at which bond lifetime is maximal) to examine if that shifts the optimal fiber stiffness or contraction rate to different values.

Compared to other three-dimensional models of cell migration [77], the presented model does not prescribe any specific mechanisms to drive cell polarization. Instead, the simple set of mechanisms listed above is sufficient to recreate durotaxis, the tendency of cells to migrate towards stiffer regions. In the model, durotaxis could arise due to spatially varying adhesion stability. Integrins attached to stiffer fibers are loaded more rapidly and are more stable, whereas integrins attached to softer substrates are less stable and detach more easily. Effectively, this leads to cell movement towards the stiffer region.

While the findings provide meaningful insights into which mechanical mechanisms could explain cell migration in three-dimensional fiber networks, the study was limited in the possible cell migration modes by focusing exclusively on integrin-mediated migration. Furthermore, the study focused on cell migration in non-impeding networks, i.e., networks of low fiber density and large pore sizes. In this case, migration is primarily protease-independent, which means no matrix degradation via MMPs occurs. This

limitation can be attributed to the computational challenges that would be introduced by allowing the degradation of fibers, which are modeled as discrete finite beam elements. Moreover, the focus on non-impeding networks also means that the physical effects of the nucleus are neglected. However, the nucleus is often the limiting factor due to its limited deformability [145] and regulates intracellular signaling processes and morphology as well as influences the migration mode [151]. Additionally, due to the focus on mechanical mechanisms, the study neglected biochemical signaling in general, which influences focal adhesion (dis-)assembly and stability [66, 110] and cytoskeletal contraction [127, 136].

In summary, the computational model successfully reproduced experimentally observed cell migration speeds and more complex phenomena such as durotaxis. This was achieved by combining a realistic micromechanical fiber network with two simple assumptions of cell migration: cell-matrix adhesions based on catch bonds and cytoskeletal contraction. Taken together, the results suggest that adhesion stability plays an essential role in regulating cell migration, including balanced adhesion turnover, migration efficiency, and durotaxis.

Biaxial experiments – Paper B Using a previously developed biaxial bioreactor [31], this study presents the first quantitative analysis of biaxial tensional homeostasis in cell-seeded tissue equivalents under dynamic loading. Compared to previous experiments, this study subjected the tissue equivalents to physiologically relevant loading conditions while measuring cell-generated forces. These conditions included equi- as well as strip-biaxial boundary conditions. While the former is characterized by equal stretches along the primary directions, the latter is characterized by keeping one of the primary axes at a constant length while the perpendicular axis is cyclically stretched. Under idealized conditions, strip-biaxial loading leads to stresses but no strains in the static axis, while the cycled axis experiences stresses and strains [62].

While idealized biaxial loading conditions are easy to analyze and interpret, the stress and strain distributions in cruciform samples are much more complex, resulting from a combination of uniaxial stress/strain states in the arms and more biaxial stress/strain states towards the central region. This was revealed by finite element simulations of cruciform acellular gels, which showed spatially nonuniform stress and strain distributions, especially in the strip-biaxial case. This makes the interpretation of the experimental results less straightforward, but nevertheless, spatially averaged quantities of stress and strain along the two primary axes align with expected values from idealized biaxial conditions and theoretical considerations. Despite this agreement

of average quantities, cells likely respond to local stimuli, not global stress or strain averages. Notwithstanding these caveats, the experimentally measured cell-generated forces represent an integrated response of all the cells, that is, cells experiencing different local stimuli. Thus, the integrated response is expected to reflect an average of all cells over the entire experimental domain.

With these considerations in mind, a key cellular mechanism relevant for interpreting the observations of this study could be the results by Wille *et al.* [142] and Walker *et al.* [134]. Taken together, they suggest that stiffness adaptations of the cellular cytoskeleton via rapid actin depolymerization play an important role in maintaining a preferred range of forces independent of the applied dynamic stretch.

For example, in each of the seven cyclic loading intervals – separated by intermittent force-extension tests – the cells were able to establish and maintain a preferred mechanical state in terms of mean force. Interestingly, this was independent of the applied loading and boundary conditions, which led to significantly different amplitudes. In particular, for the strip-biaxial case this means that while the mean forces are similar in both primary directions and comparable to the equibiaxial case, a differential adaptation of the cells to local stimuli along the two primary directions appears necessary to establish the same forces. Overall, this aligns with the adaption process described above and is similar to previous uniaxial experiments where dynamic loading with different amplitudes led to similar steady-state forces [142].

Similar adaptations were observed during the force-extension tests, which revealed a remarkable similarity in the stiffness-force relationship for all loading conditions. This was valid for the force range the cells experienced during the previous cyclic loading interval, whereas above this range, the similarity diminished. Importantly, this also applied to the loading protocol with the highest cyclic amplitude, even though the force-extension tests showed a decreased stiffness in this case.

In the cases where the stretch amplitude of the force-extension test was higher than the amplitude of cyclic loading, the force-extension test also seemed to induce an initial active cellular adaptation when cyclic loading resumed. Again, potentially triggered by cellular stiffness adaptations in response to the higher forces experienced during the force-extension test compared to the cyclic loading intervals.

In summary, the study showed that vascular SMCs embedded in collagen-based tissue equivalents adapt to maintain a preferred range of biaxial forces independent of the applied loading condition. This suggests a critical role of stress or force in regulating the mechanical adaptation of vascular SMCs.

Multiscale model – Paper C This project introduced a novel multiscale finite element model of soft tissue growth and remodeling by combining the homogenized constrained mixture model with intracellular signaling and biochemical cell-cell communication.

Using the outputs from intracellular signaling networks in the equations governing growth allows a more transparent study of how intracellular processes affect tissue adaptation under various conditions. While the presented results should be considered as a proof of concept, they show how the presence of exogenous AngII accelerates collagen remodeling and leads to a different adaption over time. The signaling pathways can also be used to study the effects of genetic disorders, the impact of which might be challenging to include in a heuristic gain parameter *a priori*. Moreover, a genetic disorder might not necessarily cause a maladaptive tissue response, as compensatory mechanisms can still lead to proper adaptations. Indeed, this robustness could be a desired feature of biological signaling networks, given their noisy environments. Additionally, this could also explain why a unique parametrization of the signaling networks is difficult to obtain and, at the same time, might not be necessary to permit stable adaptations [70].

By including cell-cell communication between endothelial cells and intramural cells, the effects of changes in wall shear stress on cell behavior could be included. This is the first time these effects were included in the homogenized constrained mixture model. Importantly, this also required the addition of appropriate boundary conditions based on previous experimental and computational studies to obtain realistic distributions of signaling molecules (in this case, nitric oxide and endothelin-1) in the vessel wall. While this was an illustrative example of the potential of the model to account for biochemical cell-cell communication, it can be extended to other cell types. For example, the interaction of intramural cells and macrophages could also be modeled in a similar way.

Including cellular signaling networks offers a greater amount of detail but, at the same time, increases the complexity of the model; instead of estimating a single gain parameter per constituent, one needs to parameterize an entire system of equations. However, the logic-gated system of ODEs used in this study showed remarkable results even when default parameters were used. In many cases, finding parameter values for the key parameters governing the system of equations (EC_{50}, W, n) and the initial values of the input nodes might be sufficient. To facilitate network creation, online databases provide curated pathways that could be used as a starting point and further refined to fit the specific needs of a study. Additionally, more sequencing data are becoming available that could be used to generate or parameterize the signaling networks.

An important observation was the instabilities when high sensitivities to stress were used. Importantly, this was not limited to the coupled model but also observed in the standard implementation of the homogenized constrained mixture model for large gain parameters. In both cases, the instabilities were independent of the applied pressure perturbations. Radially varying mass production rates, caused by transmural stress gradients arising from the applied pressure perturbations, could potentially lead to these instabilities.

Interestingly, when diffusion of cells was included, which could be interpreted as cell migration and essentially smooths out transmural gradients, the simulations remained stable. However, this lacks biological justification since radial migration of cells has not been observed and is likely limited due to the elastic laminae in the aorta. Different discretizations and time step sizes were tested to examine if the instabilities were numerical, but the instabilities remained. Thus, the homogenized constrained mixture model seems unable to homogenize transmural stress gradients over longer simulation times. The underlying reason for this is unclear and could be inherent to the model, due to accumulating numerical errors, or based on missing assumptions in the theory. Transmural stress gradients and their homogenization have been studied in the literature, and different mechanisms have been identified that influence these gradients. These mechanisms range from radially varying material parameters to gradients in proteoglycan concentrations to the bilayered structure of the aorta. Hence, there is a need to examine and understand better the underlying cause of these instabilities in the homogenized constrained mixture model.

In summary, the computational model can serve as an *in silico* tool to study how disorders in intracellular signaling pathways and cell-cell communication affect tissue adaptation in response to changes in mechanical loading. However, more work is needed to examine the long-term instabilities.

Chapter 7

Conclusion

While covering various topics, the projects presented in this thesis share a common theme: the importance of mechanics in regulating biological systems. As mentioned in chapter 2, mechanobiology is an inherently multiscale discipline, and mechanobiological processes can manifest at different length and time scales, adding a significant amount of complexity. Hence, to address this complexity and to better understand underlying mechanisms, dedicated computational models and experimental setups are necessary to uncover the influence of the mechanical environment on biological processes across various scales.

In particular, computational models that capture mechanisms as well as manifestations can be especially instructive. However, developing a unifying model that captures all processes from the micro- to the macroscale in detail is often unfeasible. Instead, specialized models that focus on selected mechanisms are necessary, with the key challenge being to identify which mechanisms and assumptions to include. Here, experimental data can prove invaluable to inform these modeling approaches. Similarly, experimental studies can benefit from computational modeling to guide experimental design and determine which experiments to focus on. This is especially important for experiments that are time-consuming, expensive, or dangerous to perform. In fact, computational modeling should go hand in hand with experimental studies and lead to a continuous cycle of model refinement and subsequent experimental verification.

This thesis covered different aspects of this cycle of model development and experimental data collection. By using available experimental measurements of the binding and unbinding kinetics of cell-matrix adhesions, a computational model of cell migration in realistic three-dimensional fiber networks was developed. The model contributed to the understanding of mechanical mechanisms that can explain complex cell migration phenomena in realistic environments, which might now be tested experimentally. In a

similar manner, the novel multiscale model introduced intracellular signaling pathways and cell-cell communication to inform G&R processes on the tissue scale. This can help guide new experimental studies to explore how disorders in intracellular signal processing manifest during macroscopic tissue adaptation. This model can potentially be used as an *in silico* tool to develop new therapeutic strategies or improve the design of artificial tissue constructs. The experimental study focused on cellular behavior on the tissue scale under different biaxial loading and boundary conditions. The study showed that tensional homeostasis is also observed under dynamic biaxial loading and unaffected by different boundary conditions and strain amplitudes. It highlighted the critical role of stresses and forces as regulators of cellular mechanical adaptation, potentially providing valuable information for future modeling approaches.

References

[1] M. Adler, A. Mayo, X. Zhou, R. A. Franklin, J. B. Jacox, R. Medzhitov, and U. Alon, "Endocytosis as a stabilizing mechanism for tissue homeostasis," *Proceedings of the National Academy of Sciences*, vol. 115, no. 8, pp. 1926–1935, 2018. DOI: 10.1073/pnas.1714377115.

[2] S. Agarwal, P. Long, S. Al, N. Piesco, A. Shree, and R. Gassner, "A central role for the nuclear factor-kappaB pathway in anti-inflammatory and proinflammatory actions of mechanical strain," *FASEB journal : official publication of the Federation of American Societies for Experimental Biology*, vol. 17, no. 8, pp. 1–15, 2003. DOI: 10.1096/FJ.02-0901FJE.

[3] B. Alberts, A. Johnson, J. Lewis, D. Morgan, M. Raff, K. Roberts, and P. Walter, *Molecular Biology of the Cell*, J. Wilson and T. Hunt, Eds. New York: W.W. Norton & Company, 2017. DOI: 10.1201/9781315735368.

[4] J. Alcaraz, H. Mori, C. M. Ghajar, D. Brownfield, R. Galgoczy, and M. J. Bissell, "Collective epithelial cell invasion overcomes mechanical barriers of collagenous extracellular matrix by a narrow tube-like geometry and MMP14-dependent local softening," *Integrative Biology*, vol. 3, no. 12, p. 1153, 2011. DOI: 10.1039/c1ib00073j.

[5] M. Amano, M. Nakayama, and K. Kaibuchi, "Rho-kinase/ROCK: A key regulator of the cytoskeleton and cell polarity," *Cytoskeleton*, vol. 67, no. 9, pp. 545–554, 2010. DOI: 10.1002/cm.20472.

[6] E. Armingol, A. Officer, O. Harismendy, and N. E. Lewis, "Deciphering cell–cell interactions and communication from gene expression," *Nature Reviews Genetics*, vol. 22, no. 2, pp. 71–88, 2021. DOI: 10.1038/s41576-020-00292-x.

[7] M. Bäck, T. C. Gasser, J.-B. Michel, and G. Caligiuri, "Biomechanical factors in the biology of aortic wall and aortic valve diseases," *Cardiovascular Research*, vol. 99, no. 2, pp. 232–241, 2013. DOI: 10.1093/cvr/cvt040.

[8] S. Baek, K. R. Rajagopal, and J. D. Humphrey, "A theoretical model of enlarging intracranial fusiform aneurysms," *Journal of Biomechanical Engineering*, vol. 128, no. 1, pp. 142–149, 2006. DOI: 10.1115/1.2132374.

[9] B. L. Bangasser, G. A. Shamsan, C. E. Chan, K. N. Opoku, E. Tüzel, B. W. Schlichtmann, J. A. Kasim, B. J. Fuller, B. R. McCullough, S. S. Rosenfeld, and D. J. Odde, "Shifting the optimal stiffness for cell migration," *Nature Communications*, vol. 8, no. 1, p. 15 313, 2017. DOI: 10.1038/ncomms15313.

[10] I. M. Bayer, S. L. Adamson, and B. L. Langille, "Atrophic Remodeling of the Artery-Cuffed Artery," *Arteriosclerosis, Thrombosis, and Vascular Biology*, vol. 19, no. 6, pp. 1499–1505, 1999. DOI: 10.1161/01.ATV.19.6.1499.

[11] E. Bell, B. Ivarsson, and C. Merrill, "Production of a tissue-like structure by contraction of collagen lattices by human fibroblasts of different proliferative potential in vitro.," *Proceedings of the National Academy of Sciences*, vol. 76, no. 3, pp. 1274–1278, 1979. DOI: 10.1073/pnas.76.3.1274.

[12] J. Bella and D. J. Hulmes, "Fibrillar collagens," *Subcellular Biochemistry*, vol. 82, pp. 457–490, 2017. DOI: 10.1007/978-3-319-49674-0_14.

[13] M. R. Bersi, R. Khosravi, A. J. Wujciak, D. G. Harrison, and J. D. Humphrey, "Differential cell-matrix mechanoadaptations and inflammation drive regional propensities to aortic fibrosis, aneurysm or dissection in hypertension," *Journal of the Royal Society Interface*, vol. 14, no. 136, 2017. DOI: 10.1098/rsif.2017.0327.

[14] R. A. Brown, R. Prajapati, D. A. McGrouther, I. V. Yannas, and M. Eastwood, "Tensional homeostasis in dermal fibroblasts: Mechanical responses to mechanical loading in three-dimensional substrates," *Journal of Cellular Physiology*, vol. 175, no. 3, pp. 323–332, 1998. DOI: 10.1002/(SICI)1097-4652(199806)175:3<323::AID-JCP10>3.0.CO;2-6.

[15] B. Bugyi and M.-F. Carlier, "Control of Actin Filament Treadmilling in Cell Motility," *Annual Review of Biophysics*, vol. 39, no. 1, pp. 449–470, 2010. DOI: 10.1146/annurev-biophys-051309-103849.

[16] C. Cavinato, M. Chen, D. Weiss, M. J. Ruiz-Rodríguez, M. A. Schwartz, and J. D. Humphrey, "Progressive Microstructural Deterioration Dictates Evolving Biomechanical Dysfunction in the Marfan Aorta," *Frontiers in Cardiovascular Medicine*, vol. 8, p. 800 730, 2021. DOI: 10.3389/fcvm.2021.800730.

[17] M. Cecelja and P. Chowienczyk, "Role of arterial stiffness in cardiovascular disease," *JRSM Cardiovascular Disease*, vol. 1, no. 4, pp. 1–10, 2012. DOI: 10.1258/cvd.2012.012016.

[18] A. F. Chambers, A. C. Groom, and I. C. MacDonald, "Dissemination and growth of cancer cells in metastatic sites," *Nature Reviews Cancer*, vol. 2, no. 8, pp. 563–572, 2002. DOI: 10.1038/nrc865.

[19] K. Chen, A. Vigliotti, M. Bacca, R. M. McMeeking, V. S. Deshpande, and J. W. Holmes, "Role of boundary conditions in determining cell alignment in response to stretch," *Proceedings of the National Academy of Sciences*, vol. 115, no. 5, pp. 986–991, 2018. DOI: 10.1073/pnas.1715059115.

[20] C. K. Chow, K. K. Teo, S. Rangarajan, S. Islam, R. Gupta, A. Avezum, A. Bahonar, J. Chifamba, G. Dagenais, R. Diaz, K. Kazmi, F. Lanas, L. Wei, P. Lopez-Jaramillo, L. Fanghong, N. H. Ismail, T. Puoane, A. Rosengren, A. Szuba, A. Temizhan, A. Wielgosz, R. Yusuf, A. Yusufali, M. McKee, L. Liu, P. Mony, and S. Yusuf, "Prevalence, Awareness, Treatment, and Control of Hypertension in Rural and Urban Communities in High-, Middle-, and Low-Income Countries," *JAMA*, vol. 310, no. 9, pp. 959–968, 2013. DOI: 10.1001/jama.2013.184182.

[21] E. Cukierman, R. Pankov, D. R. Stevens, and K. M. Yamada, "Taking cell-matrix adhesions to the third dimension," *Science*, vol. 294, no. 5547, pp. 1708–1712, 2001. DOI: 10.1126/science.1064829.

[22] C. J. Cyron, R. C. Aydin, and J. D. Humphrey, "A homogenized constrained mixture (and mechanical analog) model for growth and remodeling of soft tissue," *Biomechanics and Modeling in Mechanobiology*, vol. 15, no. 6, pp. 1389–1403, 2016. DOI: 10.1007/s10237-016-0770-9.

[23] H. G. Davis, *Conservative surgery*. New York: Appleton, 1867.

[24] X. Di, X. Gao, L. Peng, J. Ai, X. Jin, S. Qi, H. Li, K. Wang, and D. Luo, "Cellular mechanotransduction in health and diseases: from molecular mechanism to therapeutic targets," *Signal Transduction and Targeted Therapy*, vol. 8, no. 1, p. 282, 2023. DOI: 10.1038/s41392-023-01501-9.

[25] P. Di Achille, G. Tellides, C. A. Figueroa, and J. D. Humphrey, "A haemodynamic predictor of intraluminal thrombus formation in abdominal aortic aneurysms," *Proceedings of the Royal Society A: Mathematical, Physical and Engineering Sciences*, vol. 470, no. 2172, p. 20 140 163, 2014. DOI: 10.1098/rspa.2014.0163.

[26] Y. Ding, J. Xu, and J. S. Bromberg, "Regulatory T cell migration during an immune response," *Trends in Immunology*, vol. 33, no. 4, pp. 174–180, 2012. DOI: 10.1016/j.it.2012.01.002.

[27] A. D. Doyle, N. Carvajal, A. Jin, K. Matsumoto, and K. M. Yamada, "Local 3D matrix microenvironment regulates cell migration through spatiotemporal dynamics of contractility-dependent adhesions," *Nature Communications*, vol. 6, no. 1, p. 8720, 2015. DOI: 10.1038/ncomms9720.

[28] A. D. Doyle, R. J. Petrie, M. L. Kutys, and K. M. Yamada, "Dimensions in cell migration," *Current Opinion in Cell Biology*, vol. 25, no. 5, pp. 642–649, 2013. DOI: 10.1016/j.ceb.2013.06.004.

[29] A. D. Doyle, D. J. Sykora, G. G. Pacheco, M. L. Kutys, and K. M. Yamada, "3D mesenchymal cell migration is driven by anterior cellular contraction that generates an extracellular matrix prestrain," *Developmental Cell*, vol. 56, no. 6, pp. 826–841, 2021. DOI: 10.1016/j.devcel.2021.02.017.

[30] A. D. Doyle, F. W. Wang, K. Matsumoto, and K. M. Yamada, "One-dimensional topography underlies three-dimensional fibrillar cell migration," *Journal of Cell Biology*, vol. 184, no. 4, pp. 481–490, 2009. DOI: 10.1083/jcb.200810041.

[31] J. F. Eichinger, D. Paukner, J. M. Szafron, R. C. Aydin, J. D. Humphrey, and C. J. Cyron, "Computer-controlled biaxial bioreactor for investigating cell-mediated homeostasis in tissue equivalents," *Journal of Biomechanical Engineering*, vol. 142, no. 7, 2020. DOI: 10.1115/1.4046201.

[32] J. F. Eichinger, M. J. Grill, I. D. Kermani, R. C. Aydin, W. A. Wall, J. D. Humphrey, and C. J. Cyron, "A computational framework for modeling cell–matrix interactions in soft biological tissues," *Biomechanics and Modeling in Mechanobiology*, vol. 20, no. 5, pp. 1851–1870, 2021. DOI: 10.1007/s10237-021-01480-2.

[33] J. F. Eichinger, L. J. Haeusel, D. Paukner, R. C. Aydin, J. D. Humphrey, and C. J. Cyron, "Mechanical homeostasis in tissue equivalents: a review," *Biomechanics and Modeling in Mechanobiology*, vol. 20, no. 3, pp. 833–850, 2021. DOI: 10.1007/s10237-021-01433-9.

[34] J. F. Eichinger, D. Paukner, R. C. Aydin, W. A. Wall, J. D. Humphrey, and C. J. Cyron, "What do cells regulate in soft tissues on short time scales?" *Acta Biomaterialia*, vol. 134, pp. 348–356, 2021. DOI: 10.1016/j.actbio.2021.07.054.

[35] A. Elosegui-Artola, I. Andreu, A. E. Beedle, A. Lezamiz, M. Uroz, A. J. Kosmalska, R. Oria, J. Z. Kechagia, P. Rico-Lastres, A.-L. Le Roux, C. M. Shanahan, X. Trepat, D. Navajas, S. Garcia-Manyes, and P. Roca-Cusachs, "Force Triggers YAP Nuclear Entry by Regulating Transport across Nuclear Pores," *Cell*, vol. 171, no. 6, pp. 1397–1410, 2017. DOI: 10.1016/j.cell.2017.10.008.

[36] A. Elosegui-Artola, X. Trepat, and P. Roca-Cusachs, "Control of Mechanotransduction by Molecular Clutch Dynamics," *Trends in Cell Biology*, vol. 28, no. 5, pp. 356–367, 2018. DOI: 10.1016/j.tcb.2018.01.008.

[37] A. J. Engler, S. Sen, H. L. Sweeney, and D. E. Discher, "Matrix elasticity directs stem cell lineage specification," *Cell*, vol. 126, no. 4, pp. 677–689, 2006. DOI: 10.1016/j.cell.2006.06.044.

[38] D. G. Ezra, J. S. Ellis, M. Beaconsfield, R. Collin, and M. Bailly, "Changes in fibroblast mechanostat set point and mechanosensitivity: an adaptive response to mechanical stress in floppy eyelid syndrome," *Investigative Opthalmology & Visual Science*, vol. 51, no. 8, p. 3853, 2010. DOI: 10.1167/iovs.09-4724.

[39] B. Fabry, A. H. Klemm, S. Kienle, T. E. Schäffer, and W. H. Goldmann, "Focal Adhesion Kinase Stabilizes the Cytoskeleton," *Biophysical Journal*, vol. 101, no. 9, pp. 2131–2138, 2011. DOI: 10.1016/j.bpj.2011.09.043.

[40] C. M. Franz, G. E. Jones, and A. J. Ridley, "Cell migration in development and disease.," *Developmental cell*, vol. 2, no. 2, D. Wedlich, Ed., pp. 153–8, 2002. DOI: 10.1016/s1534-5807(02)00120-x.

[41] P. Friedl and B. Weigelin, "Interstitial leukocyte migration and immune function," *Nature Immunology 2008 9:9*, vol. 9, no. 9, pp. 960–969, 2008. DOI: 10.1038/ni.f.212.

[42] P. Friedl and K. Wolf, "Tumour-cell invasion and migration: diversity and escape mechanisms," *Nature Reviews Cancer*, vol. 3, no. 5, pp. 362–374, 2003. DOI: 10.1038/nrc1075.

[43] P. Friedl, K. S. Zänker, and E.-B. Bröcker, "Cell migration strategies in 3-D extracellular matrix: Differences in morphology, cell matrix interactions, and integrin function," *Microscopy Research and Technique*, vol. 43, no. 5, pp. 369–378, 1998. DOI: 10.1002/(SICI)1097-0029(19981201)43:5<369::AID-JEMT3>3.0.CO;2-6.

[44] S. M. Frisch and R. A. Screaton, "Anoikis mechanisms," *Current Opinion in Cell Biology*, vol. 13, no. 5, pp. 555–562, 2001. DOI: 10.1016/S0955-0674(00)00251-9.

[45] Y. Fukata, K. Kaibuchi, M. Amano, and K. Kaibuchi, "Rho–Rho-kinase pathway in smooth muscle contraction and cytoskeletal reorganization of non-muscle cells," *Trends in Pharmacological Sciences*, vol. 22, no. 1, pp. 32–39, 2001. DOI: 10.1016/S0165-6147(00)01596-0.

[46] A. M. Gebauer, M. R. Pfaller, F. A. Braeu, C. J. Cyron, and W. A. Wall, "A homogenized constrained mixture model of cardiac growth and remodeling: analyzing mechanobiological stability and reversal," *Biomechanics and Modeling in Mechanobiology*, vol. 22, no. 6, pp. 1983–2002, 2023. DOI: 10.1007/s10237-023-01747-w.

[47] B. Geiger, J. P. Spatz, and A. D. Bershadsky, "Environmental sensing through focal adhesions," *Nature Reviews Molecular Cell Biology*, vol. 10, no. 1, pp. 21–33, 2009. DOI: 10.1038/nrm2593.

[48] C. M. Gorick, J. J. Saucerman, and R. J. Price, "Computational model of brain endothelial cell signaling pathways predicts therapeutic targets for cerebral pathologies," *Journal of Molecular and Cellular Cardiology*, vol. 164, pp. 17–28, 2022. DOI: 10.1016/j.yjmcc.2021.11.005.

[49] R. A. Gould, K. Chin, T. P. Santisakultarm, A. Dropkin, J. M. Richards, C. B. Schaffer, and J. T. Butcher, "Cyclic strain anisotropy regulates valvular interstitial cell phenotype and tissue remodeling in three-dimensional culture," *Acta Biomaterialia*, vol. 8, no. 5, pp. 1710–1719, 2012. DOI: 10.1016/j.actbio.2012.01.006.

[50] S. Guo and L. A. DiPietro, "Factors affecting wound healing," *Journal of Dental Research*, vol. 89, no. 3, pp. 219–229, 2010. DOI: 110.1177/0022034509359125.

[51] V. Gupta and K. J. Grande-Allen, "Effects of static and cyclic loading in regulating extracellular matrix synthesis by cardiovascular cells," *Cardiovascular Research*, vol. 72, no. 3, pp. 375–383, 2006. DOI: 10.1016/j.cardiores.2006.08.017.

[52] S. L. Gupton and C. M. Waterman-Storer, "Spatiotemporal Feedback between Actomyosin and Focal-Adhesion Systems Optimizes Rapid Cell Migration," *Cell*, vol. 125, no. 7, pp. 1361–1374, 2006. DOI: 10.1016/j.cell.2006.05.029.

[53] D. G. Harrison, T. J. Guzik, H. E. Lob, M. S. Madhur, P. J. Marvar, S. R. Thabet, A. Vinh, and C. M. Weyand, "Inflammation, Immunity, and Hypertension," *Hypertension*, vol. 57, no. 2, pp. 132–140, 2011. DOI: 10.1161/HYPERTENSIONAHA.110.163576.

[54] D. G. Harrison, P. J. Marvar, and J. M. Titze, "Vascular Inflammatory Cells in Hypertension," *Frontiers in Physiology*, vol. 3, 2012. DOI: 10.3389/fphys.2012.00128.

[55] M. Holland, S. Budday, A. Goriely, and E. Kuhl, "Symmetry Breaking in Wrinkling Patterns: Gyri Are Universally Thicker than Sulci," *Physical Review Letters*, vol. 121, no. 22, p. 228 002, 2018. DOI: 10.1103/PhysRevLett.121.228002.

[56] D. F. Holmes, Y. Lu, T. Starborg, and K. E. Kadler, "Collagen Fibril Assembly and Function," *Current Topics in Developmental Biology*, vol. 130, pp. 107–142, 2018. DOI: 10.1016/BS.CTDB.2018.02.004.

[57] N. Horvat, L. Virag, G. A. Holzapfel, J. Sorić, and I. Karšaj, "A finite element implementation of a growth and remodeling model for soft biological tissues: Verification and application to abdominal aortic aneurysms," *Computer Methods in Applied Mechanics and Engineering*, vol. 352, pp. 586–605, 2019. DOI: 10.1016/J.CMA.2019.04.041.

[58] J.-J. Hu, Y.-C. Liu, G.-W. Chen, M.-X. Wang, and P.-Y. Lee, "Development of fibroblast-seeded collagen gels under planar biaxial mechanical constraints: a biomechanical study," *Biomechanics and Modeling in Mechanobiology*, vol. 12, no. 5, pp. 849–868, 2013. DOI: 10.1007/s10237-012-0448-x.

[59] J. D. Humphrey and K. R. Rajagopal, "A constrained mixture model for growth and remodeling of soft tissues," *Mathematical Models and Methods in Applied Sciences*, vol. 12, no. 3, pp. 407–430, 2002. DOI: 10.1142/S0218202502001714.

[60] J. D. Humphrey, "Vascular Adaptation and Mechanical Homeostasis at Tissue, Cellular, and Sub-cellular Levels," *Cell Biochemistry and Biophysics*, vol. 50, no. 2, pp. 53–78, 2008. DOI: 10.1007/s12013-007-9002-3.

[61] J. D. Humphrey, J. F. Eberth, W. W. Dye, and R. L. Gleason, *Fundamental role of axial stress in compensatory adaptations by arteries*, 2009. DOI: 10.1016/j.jbiomech.2008.11.011.

[62] J. D. Humphrey, P. B. Wells, S. Baek, J.-J. Hu, K. McLeroy, and A. T. Yeh, "A theoretically-motivated biaxial tissue culture system with intravital microscopy," *Biomechanics and Modeling in Mechanobiology*, vol. 7, no. 4, pp. 323–334, 2008. DOI: 10.1007/s10237-007-0099-5.

[63] J. D. Humphrey, E. R. Dufresne, and M. A. Schwartz, "Mechanotransduction and extracellular matrix homeostasis," *Nature Reviews Molecular Cell Biology*, vol. 15, no. 12, pp. 802–812, 2014. DOI: 10.1038/nrm3896.

[64] J. D. Humphrey, "Mechanisms of Arterial Remodeling in Hypertension," *Hypertension*, vol. 52, no. 2, pp. 195–200, 2008. DOI: 10.1161/HYPERTENSIONAHA.107.103440.

[65] J. D. Humphrey and M. A. Schwartz, "Vascular Mechanobiology: Homeostasis, Adaptation, and Disease," *Annual Review of Biomedical Engineering*, vol. 23, no. 1, pp. 1–27, 2021. DOI: 10.1146/annurev-bioeng-092419-060810.

[66] A. Huttenlocher and A. R. Horwitz, "Integrins in Cell Migration," *Cold Spring Harbor Perspectives in Biology*, vol. 3, no. 9, a005074–a005074, 2011. DOI: 10.1101/cshperspect.a005074.

[67] D. Ilić, C. H. Damsky, and T. Yamamoto, "Focal adhesion kinase: at the crossroads of signal transduction," *Journal of Cell Science*, vol. 110, no. 4, pp. 401–407, 1997. DOI: 10.1242/JCS.110.4.401.

[68] D. Ingber, "Mechanobiology and diseases of mechanotransduction," *Annals of Medicine*, vol. 35, no. 8, pp. 564–577, 2003. DOI: 10.1080/07853890310016333.

[69] R. V. Iozzo and L. Schaefer, "Proteoglycan form and function: A comprehensive nomenclature of proteoglycans," *Matrix Biology*, vol. 42, pp. 11–55, 2015. DOI: 10.1016/j.matbio.2015.02.003.

[70] L. Irons, A. C. Estrada, and J. D. Humphrey, "Intracellular signaling control of mechanical homeostasis in the aorta," *Biomechanics and Modeling in Mechanobiology*, vol. 21, no. 5, pp. 1339–1355, 2022. DOI: 10.1007/s10237-022-01593-2.

[71] L. Irons, M. Latorre, and J. D. Humphrey, "From Transcript to Tissue: Multiscale Modeling from Cell Signaling to Matrix Remodeling," *Annals of Biomedical Engineering*, vol. 49, no. 7, pp. 1701–1715, 2021. DOI: 10.1007/s10439-020-02713-8.

[72] K. A. Jansen, A. J. Licup, A. Sharma, R. Rens, F. C. MacKintosh, and G. H. Koenderink, "The Role of Network Architecture in Collagen Mechanics," *Biophysical Journal*, vol. 114, no. 11, pp. 2665–2678, 2018. DOI: 10.1016/j.bpj.2018.04.043.

[73] J. Joshi, G. Mahajan, and C. R. Kothapalli, "Three-dimensional collagenous niche and azacytidine selectively promote time-dependent cardiomyogenesis from human bone marrow-derived MSC spheroids," *Biotechnology and Bioengineering*, vol. 115, no. 8, pp. 2013–2026, 2018. DOI: 10.1002/bit.26714.

[74] K. Kanda and T. Matsuda, "Mechanical stress-induced orientation and ultrastructural change of smooth muscle cells cultured in three-dimensional collagen lattices," *Cell Transplantation*, vol. 3, no. 6, pp. 481–492, 1994. DOI: 10.1177/096368979400300605.

[75] A. A. Karkhaneh Yousefi, C. Petit, A. Ben Hassine, and S. Avril, "Stiffness sensing by smooth muscle cells: Continuum mechanics modeling of the actomyosin role," *Journal of the Mechanical Behavior of Biomedical Materials*, vol. 144, p. 105 990, 2023. DOI: 10.1016/j.jmbbm.2023.105990.

[76] M. E. Katz, R. Mszar, A. A. Grimshaw, C. G. Gunderson, O. K. Onuma, Y. Lu, and E. S. Spatz, "Digital Health Interventions for Hypertension Management in US Populations Experiencing Health Disparities," *JAMA Network Open*, vol. 7, no. 2, e2356070, 2024. DOI: 10.1001/jamanetworkopen.2023.56070.

[77] M.-C. Kim, Y. R. Silberberg, R. Abeyaratne, R. D. Kamm, and H. H. Asada, "Computational modeling of three-dimensional ECM-rigidity sensing to guide directed cell migration," *Proceedings of the National Academy of Sciences*, vol. 115, no. 3, E390–E399, 2018. DOI: 10.1073/pnas.1717230115.

[78] F. Kong, A. J. García, A. P. Mould, M. J. Humphries, and C. Zhu, "Demonstration of catch bonds between an integrin and its ligand," *Journal of Cell Biology*, vol. 185, no. 7, pp. 1275–1284, 2009. DOI: 10.1083/jcb.200810002.

[79] M. J. Kraeutler, A. R. Soltis, and J. J. Saucerman, "Modeling cardiac β-adrenergic signaling with normalized-Hill differential equations: comparison with a biochemical model," *BMC Systems Biology*, vol. 4, no. 1, p. 157, 2010. DOI: 10.1186/1752-0509-4-157.

[80] E. Kuhl, R. Maas, G. Himpel, and A. Menzel, "Computational modeling of arterial wall growth : Attempts towards patient-specific simulations based on computer tomography," *Biomechanics and Modeling in Mechanobiology*, vol. 6, no. 5, pp. 321–331, 2007. DOI: 10.1007/s10237-006-0062-x.

[81] T. Lämmermann and M. Sixt, "Mechanical modes of 'amoeboid' cell migration," *Current Opinion in Cell Biology*, vol. 21, no. 5, pp. 636–644, 2009. DOI: 10.1016/j.ceb.2009.05.003.

[82] B. L. Langille, "Blood Flow-Induced Remodeling of the Artery Wall," in *Flow-Dependent Regulation of Vascular Function*, New York, NY: Springer New York, 1995, pp. 277–299. DOI: 10.1007/978-1-4614-7527-9_13.

[83] M. Latorre and J. D. Humphrey, "Numerical knockouts–In silico assessment of factors predisposing to thoracic aortic aneurysms," *PLOS Computational Biology*, vol. 16, no. 10, A. Marsden, Ed., e1008273, 2020. DOI: 10.1371/journal.pcbi.1008273.

[84] M. Latorre, M. R. Bersi, and J. D. Humphrey, "Computational modeling predicts immuno-mechanical mechanisms of maladaptive aortic remodeling in hypertension," *International Journal of Engineering Science*, vol. 141, pp. 35–46, 2019. DOI: 10.1016/J.IJENGSCI.2019.05.014.

[85] M. Latorre and J. D. Humphrey, "Modeling mechano-driven and immuno-mediated aortic maladaptation in hypertension," *Biomechanics and Modeling in Mechanobiology*, vol. 17, no. 5, pp. 1497–1511, 2018. DOI: 10.1007/s10237-018-1041-8.

[86] D. A. Lauffenburger and A. F. Horwitz, "Cell Migration: A Physically Integrated Molecular Process," *Cell*, vol. 84, no. 3, pp. 359–369, 1996. DOI: 10.1016/S0092-8674(00)81280-5.

[87] P.-Y. Lee, Y.-C. Liu, M.-X. Wang, and J.-J. Hu, "Fibroblast-seeded collagen gels in response to dynamic equibiaxial mechanical stimuli: A biomechanical study," *Journal of Biomechanics*, vol. 78, pp. 134–142, 2018. DOI: 10.1016/j.jbiomech.2018.07.030.

[88] C. Li and Q. Xu, "Mechanical stress-initiated signal transductions in vascular smooth muscle cells," *Cellular Signalling*, vol. 12, no. 7, pp. 435–445, 2000. DOI: 10.1016/S0898-6568(00)00096-6.

[89] D. S. Li, C. Cavinato, M. Latorre, and J. D. Humphrey, "Computational modelling distinguishes diverse contributors to aneurysmal progression in the Marfan aorta," *Proceedings of the Royal Society A: Mathematical, Physical and Engineering Sciences*, vol. 479, no. 2276, 2023. DOI: 10.1098/rspa.2023.0116.

[90] G. Mancia, F. Rea, G. Corrao, and G. Grassi, "Two-Drug Combinations as First-Step Antihypertensive Treatment," *Circulation Research*, vol. 124, no. 7, pp. 1113–1123, 2019. DOI: 10.1161/CIRCRESAHA.118.313294.

[91] M. Marino, G. Pontrelli, G. Vairo, and P. Wriggers, "A chemo-mechano-biological formulation for the effects of biochemical alterations on arterial mechanics: the role of molecular transport and multiscale tissue remodelling," *Journal of The Royal Society Interface*, vol. 14, no. 136, p. 20 170 615, 2017. DOI: 10.1098/rsif.2017.0615.

[92] F. Martino, A. R. Perestrelo, V. Vinarský, S. Pagliari, and G. Forte, "Cellular Mechanotransduction: From Tension to Function," *Frontiers in Physiology*, vol. 9, 2018. DOI: 10.3389/fphys.2018.00824.

[93] T. Matsumoto and K. Hayashi, "Mechanical and Dimensional Adaptation of Rat Aorta to Hypertension," *Journal of Biomechanical Engineering*, vol. 116, no. 3, pp. 278–283, 1994. DOI: 10.1115/1.2895731.

[94] A. J. McKenzie, S. R. Hicks, K. V. Svec, H. Naughton, Z. L. Edmunds, and A. K. Howe, "The mechanical microenvironment regulates ovarian cancer cell morphology, migration, and spheroid disaggregation," *Scientific Reports*, vol. 8, no. 1, pp. 1–20, 2018. DOI: 10.1038/s41598-018-25589-0.

[95] P. K. Mehta and K. K. Griendling, "Angiotensin II cell signaling: physiological and pathological effects in the cardiovascular system.," *American journal of physiology. Cell physiology*, vol. 292, no. 1, pp. 82–97, 2007. DOI: 10.1152/ajpcell.00287.2006.

[96] K. S. Midwood, L. V. Williams, and J. E. Schwarzbauer, "Tissue repair and the dynamics of the extracellular matrix," *The International Journal of Biochemistry & Cell Biology*, vol. 36, no. 6, pp. 1031–1037, 2004. DOI: 10.1016/J.BIOCEL.2003.12.003.

[97] K. S. Miller, R. Khosravi, C. K. Breuer, and J. D. Humphrey, "A hypothesis-driven parametric study of effects of polymeric scaffold properties on tissue engineered neovessel formation," *Acta Biomaterialia*, vol. 11, no. 1, pp. 283–294, 2015. DOI: 10.1016/J.ACTBIO.2014.09.046.

[98] T. Mitchison and M. Kirschner, "Cytoskeletal dynamics and nerve growth," *Neuron*, vol. 1, no. 9, pp. 761–772, 1988. DOI: 10.1016/0896-6273(88)90124-9.

[99] A. Mol, N. J. B. Driessen, M. C. M. Rutten, S. P. Hoerstrup, C. V. C. Bouten, and F. P. T. Baaijens, "Tissue engineering of human heart valve leaflets: a novel bioreactor for a strain-based conditioning approach," *Annals of Biomedical Engineering*, vol. 33, no. 12, pp. 1778–1788, 2005. DOI: 10.1007/s10439-005-8025-4.

[100] G. Murphy and H. Nagase, "Progress in matrix metalloproteinase research," *Molecular Aspects of Medicine*, vol. 29, no. 5, pp. 290–308, 2008. DOI: 10.1016/J.MAM.2008.05.002.

[101] R. Nissen, G. J. Cardinale, and S. Udenfriend, "Increased turnover of arterial collagen in hypertensive rats.," *Proceedings of the National Academy of Sciences*, vol. 75, no. 1, pp. 451–453, 1978. DOI: 10.1073/PNAS.75.1.451.

[102] P. J. Oomen, M. A. Holland, C. V. Bouten, E. Kuhl, and S. Loerakker, "Growth and remodeling play opposing roles during postnatal human heart valve development," *Scientific Reports 2018 8:1*, vol. 8, no. 1, pp. 1–13, 2018. DOI: 10.1038/s41598-018-19777-1.

[103] K. Paňková, D. Rösel, M. Novotný, and J. Brábek, "The molecular mechanisms of transition between mesenchymal and amoeboid invasiveness in tumor cells," *Cellular and Molecular Life Sciences*, vol. 67, no. 1, pp. 63–71, 2010. DOI: 10.1007/s00018-009-0132-1.

[104] J. T. Parsons, A. R. Horwitz, and M. A. Schwartz, "Cell adhesion: integrating cytoskeletal dynamics and cellular tension," *Nature Reviews Molecular Cell Biology*, vol. 11, no. 9, pp. 633–643, 2010. DOI: 10.1038/nrm2957.

[105] D. Paukner, J. F. Eichinger, and C. J. Cyron, "What are the key mechanical mechanisms governing integrin-mediated cell migration in three-dimensional fiber networks?" *Biomechanics and Modeling in Mechanobiology*, vol. 22, no. 4, pp. 1177–1192, 2023. DOI: 10.1007/s10237-023-01709-2.

[106] D. Paukner, J. D. Humphrey, and C. J. Cyron, "Multiscale homogenized constrained mixture model of the bio-chemo-mechanics of soft tissue growth and remodeling," *Biomechanics and Modeling in Mechanobiology*, 2024. DOI: 10.1007/s10237-024-01884-w.

[107] D. Paukner, I. R. Jennings, C. J. Cyron, and J. D. Humphrey, "Dynamic biaxial loading of vascular smooth muscle cell seeded tissue equivalents," *Journal of the Mechanical Behavior of Biomedical Materials*, vol. 157, 2024. DOI: 10.1016/j.jmbbm.2024.106639.

[108] P. P. Provenzano, D. R. Inman, K. W. Eliceiri, S. M. Trier, and P. J. Keely, "Contact Guidance Mediated Three-Dimensional Cell Migration is Regulated by Rho/ROCK-Dependent Matrix Reorganization," *Biophysical Journal*, vol. 95, no. 11, pp. 5374–5384, 2008. DOI: 10.1529/BIOPHYSJ.108.133116.

[109] R. Raman, V. Sasisekharan, and R. Sasisekharan, "Structural Insights into Biological Roles of Protein-Glycosaminoglycan Interactions," *Chemistry & Biology*, vol. 12, no. 3, pp. 267–277, 2005. DOI: 10.1016/j.chembiol.2004.11.020.

[110] X. Ren, W. Kiosses, D. Sieg, C. Otey, D. Schlaepfer, and M. Schwartz, "Focal adhesion kinase suppresses Rho activity to promote focal adhesion turnover," *Journal of Cell Science*, vol. 113, no. 20, pp. 3673–3678, 2000. DOI: 10.1242/jcs.113.20.3673.

[111] J. Renkawitz, A. Kopf, J. Stopp, I. de Vries, M. K. Driscoll, J. Merrin, R. Hauschild, E. S. Welf, G. Danuser, R. Fiolka, and M. Sixt, "Nuclear positioning facilitates amoeboid migration along the path of least resistance," *Nature*, vol. 568, no. 7753, pp. 546–550, 2019. DOI: 10.1038/s41586-019-1087-5.

[112] S. Ricard-Blum, "The Collagen Family," *Cold Spring Harbor Perspectives in Biology*, vol. 3, no. 1, a004978–a004978, 2011. DOI: 10.1101/cshperspect.a004978.

[113] A. J. Ridley, M. A. Schwartz, K. Burridge, R. A. Firtel, M. H. Ginsberg, G. Borisy, J. T. Parsons, and A. R. Horwitz, "Cell Migration: Integrating Signals from Front to Back," *Science*, vol. 302, no. 5651, pp. 1704–1709, 2003. DOI: 10.1126/science.1092053.

[114] E. K. Rodriguez, A. Hoger, and A. D. McCulloch, "Stress-dependent finite growth in soft elastic tissues," *Journal of Biomechanics*, vol. 27, no. 4, pp. 455–467, 1994. DOI: 10.1016/0021-9290(94)90021-3.

[115] D. Seliktar, R. M. Nerem, and Z. S. Galis, "The role of matrix metalloproteinase-2 in the remodeling of cell-seeded vascular constructs subjected to cyclic strain," *Annals of Biomedical Engineering*, vol. 29, no. 11, pp. 923–934, 2001. DOI: 10.1114/1.1415522.

[116] S. SenGupta, C. A. Parent, and J. E. Bear, "The principles of directed cell migration," *Nature Reviews Molecular Cell Biology*, vol. 22, no. 8, pp. 529–547, 2021. DOI: 10.1038/s41580-021-00366-6.

[117] S. D. Shapiro, S. K. Endicott, M. A. Province, J. A. Pierce, and E. J. Campbell, "Marked longevity of human lung parenchymal elastic fibers deduced from prevalence of D-aspartate and nuclear weapons-related radiocarbon.," *Journal of Clinical Investigation*, vol. 87, no. 5, pp. 1828–1834, 1991. DOI: 10.1172/JCI115204.

[118] J. T. Shearn, N. Juncosa-Melvin, G. P. Boivin, M. T. Galloway, W. Goodwin, C. Gooch, M. G. Dunn, and D. L. Butler, "Mechanical stimulation of tendon tissue engineered constructs: effects on construct stiffness, repair biomechanics, and their correlation," *Journal of Biomechanical Engineering*, vol. 129, no. 6, pp. 848–854, 2007. DOI: 10.1115/1.2800769.

[119] M. P. Sheetz, D. Felsenfeld, C. G. Galbraith, and D. Choquet, "Cell migration as a five-step cycle.," *Biochemical Society symposium*, vol. 65, pp. 233–43, 1999.

[120] D. Simon, L. Niklason, and J. Humphrey, "Tissue transglutaminase, not lysyl oxidase, dominates early calcium-dependent remodeling of fibroblast-populated collagen lattices," *Cells Tissues Organs*, vol. 200, no. 2, pp. 104–117, 2014. DOI: 10.1159/000381015.

[121] D. Song, D. Yang, C. A. Powell, and X. Wang, "Cell-cell communication: old mystery and new opportunity.," *Cell biology and toxicology*, vol. 35, no. 2, pp. 89–93, 2019. DOI: 10.1007/s10565-019-09470-y.

[122] T. Svitkina, "The Actin Cytoskeleton and Actin-Based Motility," *Cold Spring Harbor Perspectives in Biology*, vol. 10, no. 1, a018267, 2018. DOI: 10.1101/cshperspect.a018267.

[123] J. M. Szafron, R. Khosravi, J. Reinhardt, C. A. Best, M. R. Bersi, T. Yi, C. K. Breuer, and J. D. Humphrey, "Immuno-driven and Mechano-mediated Neotissue Formation in Tissue Engineered Vascular Grafts," *Annals of Biomedical Engineering*, vol. 46, no. 11, pp. 1938–1950, 2018. DOI: 10.1007/S10439-018-2086-7/FIGURES/5.

[124] J. M. Szafron, A. B. Ramachandra, C. K. Breuer, A. L. Marsden, and J. D. Humphrey, "Optimization of Tissue-Engineered Vascular Graft Design Using Computational Modeling," *Tissue Engineering. Part C, Methods*, vol. 25, no. 10, p. 561, 2019. DOI: 10.1089/TEN.TEC.2019.0086.

[125] L. A. Taber and J. D. Humphrey, "Stress-Modulated Growth, Residual Stress, and Vascular Heterogeneity," *Journal of Biomechanical Engineering*, vol. 123, no. 6, pp. 528–535, 2001. DOI: 10.1115/1.1412451.

[126] A. B. Tepole, M. Gart, A. K. Gosain, and E. Kuhl, "Characterization of living skin using multi-view stereo and isogeometric analysis," *Acta Biomaterialia*, vol. 10, no. 11, pp. 4822–4831, 2014. DOI: 10.1016/J.ACTBIO.2014.06.037.

[127] M. Tozluoğlu, A. L. Tournier, R. P. Jenkins, S. Hooper, P. A. Bates, and E. Sahai, "Matrix geometry determines optimal cancer cell migration strategy and modulates response to interventions," *Nature Cell Biology*, vol. 15, no. 7, pp. 751–762, 2013. DOI: 10.1038/ncb2775.

[128] H. Truong and E. H. J. Danen, "Integrin switching modulates adhesion dynamics and cell migration.," *Cell adhesion & migration*, vol. 3, no. 2, pp. 179–81, 2009. DOI: 10.4161/cam.3.2.8036.

[129] C. Uhler and G. V. Shivashankar, "Regulation of genome organization and gene expression by nuclear mechanotransduction," *Nature Reviews Molecular Cell Biology*, vol. 18, no. 12, pp. 717–727, 2017. DOI: 10.1038/nrm.2017.101.

[130] H. Uhthoff and Z. Jaworski, "Bone loss in response to long-term immobilisation," *The Journal of Bone and Joint Surgery. British volume*, vol. 60-B, no. 3, pp. 420–429, 1978. DOI: 10.1302/0301-620X.60B3.681422.

[131] A. Valentín, J. D. Humphrey, and G. A. Holzapfel, "A multi-layered computational model of coupled elastin degradation, vasoactive dysfunction, and collagenous stiffening in aortic aging.," *Annals of biomedical engineering*, vol. 39, no. 7, pp. 2027–45, 2011. DOI: 10.1007/s10439-011-0287-4.

[132] M. Vicente-Manzanares, X. Ma, R. S. Adelstein, and A. R. Horwitz, "Non-muscle myosin II takes centre stage in cell adhesion and migration," *Nature Reviews Molecular Cell Biology*, vol. 10, no. 11, pp. 778–790, 2009. DOI: 10.1038/nrm2786.

[133] J. E. Wagenseil, T. Wakatsuki, R. J. Okamoto, G. I. Zahalak, and E. L. Elson, "One-dimensional viscoelastic behavior of fibroblast populated collagen matrices," *Journal of Biomechanical Engineering*, vol. 125, no. 5, pp. 719–725, 2003. DOI: 10.1115/1.1614818.

[134] M. Walker, P. Rizzuto, M. Godin, and A. E. Pelling, "Structural and mechanical remodeling of the cytoskeleton maintains tensional homeostasis in 3D microtissues under acute dynamic stretch," *Scientific Reports*, vol. 10, no. 1, p. 7696, 2020. DOI: 10.1038/s41598-020-64725-7.

[135] H. B. Wang, M. Dembo, S. K. Hanks, and Y. Wang, "Focal adhesion kinase is involved in mechanosensing during fibroblast migration.," *Proceedings of the National Academy of Sciences of the United States of America*, vol. 98, no. 20, pp. 11 295–300, 2001. DOI: 10.1073/pnas.201201198.

[136] T. Wang, S. Hamilla, M. Cam, H. Aranda-Espinoza, and S. Mili, "Extracellular matrix stiffness and cell contractility control RNA localization to promote cell migration," *Nature Communications*, vol. 8, no. 1, p. 896, 2017. DOI: 10.1038/s41467-017-00884-y.

[137] D. J. Webb, J. T. Parsons, and A. F. Horwitz, "Adhesion assembly, disassembly and turnover in migrating cells – over and over and over again," *Nature Cell Biology*, vol. 4, no. 4, E97–E100, 2002. DOI: 10.1038/ncb0402-e97.

[138] D. Weiss, M. Latorre, B. V. Rego, C. Cavinato, B. J. Tanski, A. G. Berman, C. J. Goergen, and J. D. Humphrey, "Biomechanical consequences of compromised elastic fiber integrity and matrix cross-linking on abdominal aortic aneurysmal enlargement," *Acta biomaterialia*, vol. 134, p. 422, 2021. DOI: 10.1016/J.ACTBIO.2021.07.059.

[139] P. Weiss and B. Garber, "Shape and Movement of Mesenchyme Cells as Functions of the Physical Structure of the Medium: Contributions to a Quantitative Morphology," *Proceedings of the National Academy of Sciences of the United States of America*, vol. 38, no. 3, pp. 264–280, 1952. DOI: 10.1073/PNAS.38.3.264.

[140] S. Weng, Y. Shao, W. Chen, and J. Fu, "Mechanosensitive subcellular rheostasis drives emergent single-cell mechanical homeostasis," *Nature Materials*, vol. 15, no. 9, pp. 961–967, 2016. DOI: 10.1038/nmat4654.

[141] O. Wiggan, A. E. Shaw, J. G. DeLuca, and J. R. Bamburg, "ADF/Cofilin Regulates Actomyosin Assembly through Competitive Inhibition of Myosin II Binding to F-Actin," *Developmental Cell*, vol. 22, no. 3, pp. 530–543, 2012. DOI: 10.1016/j.devcel.2011.12.026.

[142] J. J. Wille, E. L. Elson, and R. J. Okamoto, "Cellular and matrix mechanics of bioartificial tissues during continuous cyclic stretch," *Annals of Biomedical Engineering*, vol. 34, no. 11, pp. 1678–1690, 2006. DOI: 10.1007/s10439-006-9153-1.

[143] B. Williams, G. Mancia, W. Spiering, E. Agabiti Rosei, M. Azizi, M. Burnier, D. L. Clement, A. Coca, G. de Simone, A. Dominiczak, T. Kahan, F. Mahfoud, J. Redon, L. Ruilope, A. Zanchetti, M. Kerins, S. E. Kjeldsen, R. Kreutz, S. Laurent, G. Y. Lip, R. McManus, K. Narkiewicz, F. Ruschitzka, R. E. Schmieder, E. Shlyakhto, C. Tsioufis, V. Aboyans, and I. Desormais, "2018 ESC/ESH Guidelines for the management of arterial hypertension," *Journal of Hypertension*, vol. 36, no. 10, pp. 1953–2041, 2018. DOI: 10.1097/HJH.0000000000001940.

[144] J. S. Wilson, S. Baek, and J. D. Humphrey, "Importance of initial aortic properties on the evolving regional anisotropy, stiffness and wall thickness of human abdominal aortic aneurysms," *Journal of The Royal Society Interface*, vol. 9, no. 74, pp. 2047–2058, 2012. DOI: 10.1098/rsif.2012.0097.

[145] K. Wolf, M. te Lindert, M. Krause, S. Alexander, J. te Riet, A. L. Willis, R. M. Hoffman, C. G. Figdor, S. J. Weiss, and P. Friedl, "Physical limits of cell migration: Control by ECM space and nuclear deformation and tuning by proteolysis and traction force," *Journal of Cell Biology*, vol. 201, no. 7, pp. 1069–1084, 2013. DOI: 10.1083/jcb.201210152.

[146] K. Wolf, I. Mazo, H. Leung, K. Engelke, U. H. von Andrian, E. I. Deryugina, A. Y. Strongin, E.-B. Bröcker, and P. Friedl, "Compensation mechanism in tumor cell migration," *The Journal of Cell Biology*, vol. 160, no. 2, pp. 267–277, 2003. DOI: 10.1083/jcb.200209006.

[147] J. Wolff, "Das Gesetz der Transformation der Knochen," *Verlag von August Hirschwald*, 1892.

[148] M. A. Wozniak, K. Modzelewska, L. Kwong, and P. J. Keely, "Focal adhesion regulation of cell behavior.," *Biochimica et biophysica acta*, vol. 1692, no. 2-3, pp. 103–19, 2004. DOI: 10.1016/j.bbamcr.2004.04.007.

[149] C. Xu, C. K. Zarins, H. S. Bassiouny, W. H. Briggs, C. Reardon, and S. Glagov, "Differential Transmural Distribution of Gene Expression for Collagen Types I and III Proximal to Aortic Coarctation in the Rabbit," *Journal of Vascular Research*, vol. 37, no. 3, pp. 170–182, 2000. DOI: 10.1159/000025728.

[150] K. M. Yamada, A. D. Doyle, and J. Lu, "Cell–3D matrix interactions: recent advances and opportunities," *Trends in Cell Biology*, vol. 32, no. 10, pp. 883–895, 2022. DOI: 10.1016/j.tcb.2022.03.002.

[151] K. M. Yamada and M. Sixt, "Mechanisms of 3D cell migration," *Nature Reviews Molecular Cell Biology*, vol. 20, no. 12, pp. 738–752, 2019. DOI: 10.1038/s41580-019-0172-9.

[152] H. Yamashita, T. Ichikawa, D. Matsuyama, Y. Kimura, K. Ueda, S. W. Craig, I. Harada, and N. Kioka, "Interaction of the vinculin proline-rich linker region with vinexin α in sensing extracellular matrix stiffness," *Journal of Cell Science*, 2014. DOI: 10.1242/jcs.133645.

[153] M. Yanagishita, "Function of proteoglycans in the extracellular matrix," *Acta Pathologica Japonica*, vol. 43, no. 6, pp. 283–293, 1993. DOI: 10.1111/J.1440-1827.1993.TB02569.X.

[154] P. Y. K. Yue, E. P. Y. Leung, N. K. Mak, and R. N. S. Wong, "A Simplified Method for Quantifying Cell Migration/Wound Healing in 96-Well Plates," *Journal of Biomolecular Screening*, vol. 15, no. 4, pp. 427–433, 2010. DOI: 10.1177/1087057110361772.

[155] A. Zeigler, W. Richardson, J. Holmes, and J. Saucerman, "A computational model of cardiac fibroblast signaling predicts context-dependent drivers of myofibroblast differentiation," *Journal of Molecular and Cellular Cardiology*, vol. 94, pp. 72–81, 2016. DOI: 10.1016/j.yjmcc.2016.03.008.

[156] R. Zhang, Y. Pan, V. Fanelli, S. Wu, A. A. Luo, D. Islam, B. Han, P. Mao, M. Ghazarian, W. Zeng, P. M. Spieth, D. Wang, J. Khang, H. Mo, X. Liu, S. Uhlig, M. Liu, J. Laffey, A. S. Slutsky, Y. Li, and H. Zhang, "Mechanical Stress and the Induction of Lung Fibrosis via the Midkine Signaling Pathway," *American Journal of Respiratory and Critical Care Medicine*, vol. 192, no. 3, pp. 315–323, 2015. DOI: 10.1164/rccm.201412-2326OC.

[157] W. Zhang and H. T. Liu, "MAPK signal pathways in the regulation of cell proliferation in mammalian cells.," *Cell research*, vol. 12, no. 1, pp. 9–18, 2002. DOI: 10.1038/sj.cr.7290105.

[158] D. W. Zhou, T. T. Lee, S. Weng, J. Fu, and A. J. García, "Effects of substrate stiffness and actomyosin contractility on coupling between force transmission and vinculin–paxillin recruitment at single focal adhesions," *Molecular Biology of the Cell*, vol. 28, no. 14, pp. 1901–1911, 2017. DOI: 10.1091/mbc.e17-02-0116.

[159] N. Zuela-Sopilniak and J. Lammerding, "Can't handle the stress? Mechanobiology and disease," *Trends in Molecular Medicine*, vol. 28, no. 9, pp. 710–725, 2022. DOI: 10.1016/j.molmed.2022.05.010.

Appendix A

What are the key mechanical mechanisms governing integrin-mediated cell migration in three-dimensional fiber networks?

published in

Biomechanics and Modeling in Mechanobiology, vol. 22, pp. 1177–1192, 2023. DOI: 10.1007/s10237-023-01709-2.

Biomechanics and Modeling in Mechanobiology
https://doi.org/10.1007/s10237-023-01709-2

ORIGINAL PAPER

What are the key mechanical mechanisms governing integrin-mediated cell migration in three-dimensional fiber networks?

Daniel Paukner[1,3] · Jonas F. Eichinger[1,2] · Christian J. Cyron[1,3]

Received: 3 January 2023 / Accepted: 1 March 2023

Abstract
Cell migration plays a vital role in numerous processes such as development, wound healing, or cancer. It is well known that numerous complex mechanisms are involved in cell migration. However, so far it remains poorly understood what are the key mechanisms required to produce the main characteristics of this behavior. The reason is a methodological one. In experimental studies, specific factors and mechanisms can be promoted or inhibited. However, while doing so, there can always be others in the background which play key roles but which have simply remained unattended so far. This makes it very difficult to validate any hypothesis about a minimal set of factors and mechanisms required to produce cell migration. To overcome this natural limitation of experimental studies, we developed a computational model where cells and extracellular matrix fibers are represented by discrete mechanical objects on the micrometer scale. In this model, we had exact control of the mechanisms by which cells and matrix fibers interacted with each other. This enabled us to identify the key mechanisms required to produce physiologically realistic cell migration (including advanced phenomena such as durotaxis and a biphasic relation between migration efficiency and matrix stiffness). We found that two main mechanisms are required to this end: a catch-slip bond of individual integrins and cytoskeletal actin-myosin contraction. Notably, more advanced phenomena such as cell polarization or details of mechanosensing were not necessary to qualitatively reproduce the main characteristics of cell migration observed in experiments.

Keywords Tissue engineering · Computational modeling · Cell migration · Fibrous networks · Durotaxis

1 Introduction

Cells in living soft tissues are constantly interacting with their surrounding extracellular matrix (ECM) to probe the local mechanical microenvironment. These interactions are known to regulate key processes ranging from biochemical signaling pathways (Nakazawa et al. 2016; Wells 2008) to morphology (Yeung et al. 2005; Ghibaudo et al. 2011) and differentiation (Lee et al. 2013; Yang et al. 2016; Engler et al. 2006). The local mechanical microenvironment also has a tremendous influence on cell migration; it can, for example, determine the mode (Yamada and Sixt 2019) and speed of migration (Wolf et al. 2013), which both play important roles in numerous processes such as development (Franz et al. 2002; Scarpa and Mayor 2016), wound healing (Yue et al. 2010; Gonzalez et al. 2016), and cancer (Friedl and Gilmour 2009; Tozluoğlu et al. 2013; McKenzie et al. 2018).

Cell migration has been studied extensively in two dimensions (reviewed for example in Parsons et al. (2010), Ridley

✉ Christian J. Cyron
christian.cyron@tuhh.de

Daniel Paukner
daniel.paukner@tuhh.de

Jonas F. Eichinger
jonas.eichinger@tum.de

[1] Institute for Continuum and Material Mechanics, Hamburg University of Technology, Eißendorfer Straße 42 (M), 21073 Hamburg, Hamburg, Germany

[2] Institute for Computational Mechanics, Technical University of Munich, Boltzmannstraße 15, Garching b., 85748 München, Bavaria, Germany

[3] Institute of Material Systems Modeling, Helmholtz-Zentrum Hereon, Max-Planck Straße 1, 21502 Geesthacht, Schleswig-Holstein, Germany

Published online: 15 June 2023

et al. (2003)), since it eliminates a lot of the complexity that comes with three-dimensional fibrous scaffolds such as porosity and microarchitecture (Yamada and Sixt 2019; Cukierman et al. 2001; Charras and Sahai 2014). Systematic studies of moving cells in three-dimensional fibrous networks are challenging, as they require precise control of the network architecture and properties (on the micro-*and* macroscale). Similarly, the majority of computational modeling has focused on 2D so far but more models for the three-dimensional case have been developed in recent years. For example, Moure and Gomez (2018) and Campbell and Bagchi (2021) studied amoeboid migration and Kim et al. (2018) studied adhesion mediated migration in 3D fiber networks. These studies have significantly improved our understanding of the processes underlying cell migration. However, cells in vivo usually migrate in three-dimensional fibrous tissues, and it is unclear whether findings from 2D migration experiments and computational models can simply be translated to 3D.

Another important factor complicating experiments in 3D is the discrepancy between bulk material behavior and local micromechanical properties. Recent studies have pointed out the importance of the local mechanical environment when studying three-dimensional fibrous tissues or scaffolds by showing that the local stiffness a cell perceives can be significantly different from the bulk mechanical properties of the scaffold (Carey et al. 2012; Doyle et al. 2015; Domaschke et al. 2019). For example, it is known that collagen fibers or fibrils have a Young's modulus on the order of 1 MPa (Jansen et al. 2018), whereas fibrous collagen networks or gels only have a Young's modulus on the order of 1 Pa−1kPa (Alcaraz et al. 2011; Miroshnikova et al. 2011; Joshi et al. 2018). Different local characteristics such as the mechanical properties of fibers and their arrangement can lead to the same bulk behavior (e.g., Doyle et al. (2015)), which complicates the comparison of experimental results. Influencing factors can be as simple as the source (and therefore exact composition and structure) of the collagen; Wolf et al. (2013) showed that gels made from bovine or rat-tail collagen can lead to similar mechanical behavior during AFM indentation testing (at the same collagen concentration), but to very different pore sizes, which, according to their study, is the rate limiting factor of cell migration in 3D.

In view of the aforementioned difficulties associated with studying cell migration experimentally in three-dimensional fibrous tissues, computational models that capture the mechanical properties of fibrous networks both on the macro- and microscale, can provide additional insights into the fundamentals of cellular migration that are otherwise difficult to assess.

In this paper, we use our previously introduced computational model for three-dimensional cell–matrix interactions (Eichinger et al. 2021) to study cell migration in realistic, three-dimensional fibrous networks. These networks are based on experimentally observed descriptors such as free fiber length, valency, and fiber orientation correlation. They capture the multiscale mechanical behavior of biological hydrogels with fibers having a stiffness on the order of *MPa* and the hydrogel itself a stiffness on the order of 1 Pa−1kPa. The study focuses on integrin-mediated mesenchymal (i.e., contractility-dependent) migration in non-confining networks, i.e., networks with pore sizes larger than the cell nucleus. Because of the large pore sizes and to reduce computational costs, we do not include contact interactions between the cell (nucleus) and the fibers. Additionally, since protease activity only plays a minor role in this case (Wolf et al. 2013), it is not included in the model. To further reduce complexity, biochemical signaling is neglected, and the model is reduced to the three key mechanical players of migration: cellular contractility, focal adhesions, and the transmembrane protein integrin, and the fibrous network. We first validate our model against experimentally observed cell migration speeds and their dependence on fiber stiffness and different pharmacological treatments. By placing the cell in networks with a gradient in stiffness, we identify the key mechanisms sufficient to reproduce durotaxis, the migration of a cell toward higher stiffnesses, in realistic three-dimensional fibrous networks without any prior assumptions on cell polarization making this a so far unique computational model of cell migration in 3D including durotaxis.

2 Methods

To simulate cells and their interaction with surrounding matrix fibers we use the computational framework described in detail in Eichinger et al. (2021). In the following, we briefly summarize its main characteristics.

2.1 Network generation

According to Davoodi Kermani et al. (2021), the mechanical properties of collagen gels are mainly governed by their valency, the free fiber length, and the orientation distribution of the fibers. Using stochastic optimization, we are able to match these key metrics to experimental values and therefore are able to create realistic periodic representative volume elements (RVEs) of fibrous collagen networks. For more details on the stochastic optimization algorithm, see appendix A1 in Eichinger et al. (2021). Since the individual fibers of the network experience large deformations during the simulation, we use geometrically exact nonlinear beam finite elements based on the Simo–Reissner theory which are able to capture the most important modes of deformation: axial tension, torsion, bending, and shear. The collagen fibers in our networks

are assumed to have a circular cross section with a fiber radius of 90 nm (Van Der Rijt et al. 2006) and a fiber stiffness $E = 1.1$ MPa (Jansen et al. 2018). Individual fibers are connected to form a network by coupling translational as well as rotational degrees of freedom. As was shown in Fig. 5C in Eichinger et al. (2021), this computational approach is able to capture the multiscale mechanics of fibrous networks with individual fibers having stiffnesses on the order of MPa, whereas the resulting macroscopic networks have a stiffness in the range 1 Pa−1kPa. This significant discrepancy between micro- and macroscale is an essential characteristic of fibrous networks and was shown experimentally (Doyle et al. 2015) and numerically for electrospun scaffolds by Domaschke et al. (2019).

In this study, we focus on collagen networks that do not impede migration, i.e., the pore sizes of the network are approximately as large or larger than the cell nucleus. To this end, we generate different kinds of networks which are defined by the total fiber length per volume of the RVE, i.e., line densities with units [μm^{-2}]. First, we generate homogeneous networks with a low and high line density and a constant fiber radius of 90 nm which result in line densities of 3.3×10^{-2} μm^{-2} and 4.9×10^{-2} μm^{-2}, respectively. Second, we use these same networks but with a linearly increasing fiber radius (with a an average radius of 90 nm) along one coordinate direction to introduce a stiffness gradient. Note that the resulting average collagen concentration can be computed by multiplying the total fiber length per volume with the cross-sectional area of the fibers and dividing by the density of collagen ($v_c = 0.73$ ml/g, Hulmes and Miller (1979)). Doing so, the low and high line density correspond to networks with a collagen concentration of 1.1 mg/ml and 1.7 mg/ml, respectively.

2.2 Cell–matrix interaction

Cells typically attach to the surrounding ECM through transmembrane proteins called integrins. These proteins cluster to form more stable adhesion complexes called focal adhesions which connect the intracellular cytoskeleton to extracellular fibers and allow for a two-way feedback. The cell is able to sense mechanical cues from its environment and at the same time, it is able to apply forces to the attached fibers via contraction of the cytoskeleton. To model these complex interactions, we represent the cell center by a particle which can connect to predefined binding spots (equidistantly spaced with $d_{bs} = 50$ nm (Selhuber-Unkel et al. 2010)) on fibers by creating an elastic connection with a certain probability. This connection can form once a potential binding spot enters a predefined range around the cell (particle) as illustrated in Fig. 1a. The cell radius is assumed to be $R = 10$ µm and the binding range is defined as $R \pm \Delta R$, with $\Delta R = 3$ µm. The resulting connections represent combinations of contractile stress fibers (forming part of the cytoskeleton) and focal adhesions consisting of several integrins (Fig. 1b). Based on experimental results (Kong et al. 2009; Weng et al. 2016), we assume a catch-slip bond behavior for individual integrins, i.e., the bond initially becomes more stable with increased loading and once a certain force is exceeded, bond stability decreases. We approximate the bond lifetime $T(F)$, depending on the current force F in the bond, by the combination of two Gaussian functions (Fig. 1c)

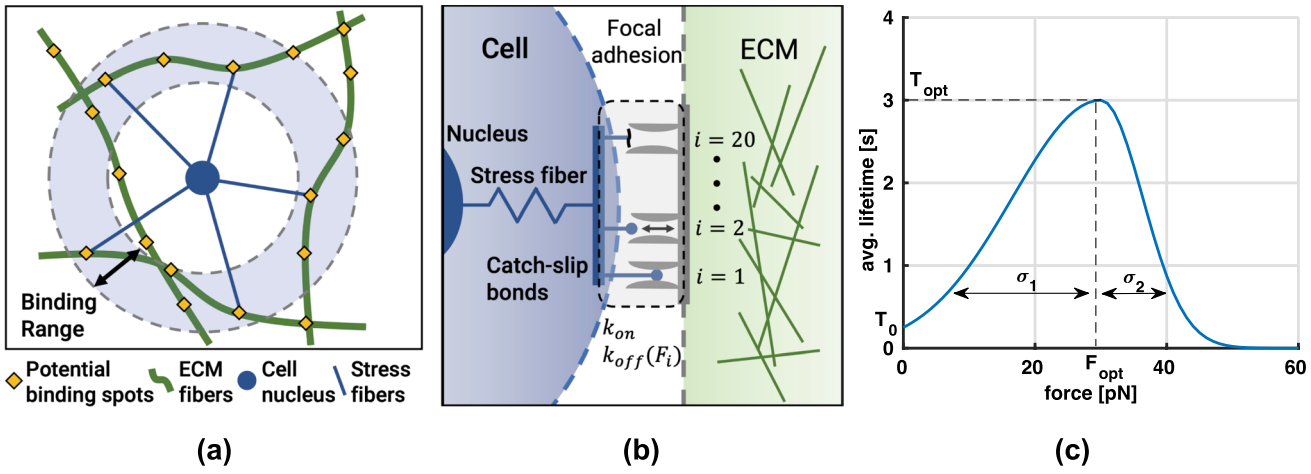

Fig. 1 **a** Cell–matrix binding. Once an ECM fiber of the extracellular matrix comes within a predefined binding range, a connection between the cell nucleus and defined binding spots on the ECM fibers can be formed through a stress fiber. **b** Focal adhesion model. A focal adhesion can consist of up to 20 integrins which bind and unbind individually according to a constant on-rate k_{on} (0.1 s^{-1}, adjusted from Elosegui-Artola et al. (2016)) and a force–dependent off-rate $k_{off}(F)$. **c** Average integrin lifetime. Experimental studies have shown that single integrins show a catch-slip bond behavior (Kong et al. 2009; Weng et al. 2016), i.e., the maximal average lifetime is assumed for tensile binding forces greater than zero

$$T(F) = \begin{cases} T_{\text{opt}} \exp\left(-\frac{(F-F_{\text{opt}})^2}{\sigma_1^2}\right) & \text{if } F \leq F_{\text{opt}} \\ T_{\text{opt}} \exp\left(-\frac{(F-F_{\text{opt}})^2}{\sigma_2^2}\right) & \text{if } F > F_{\text{opt}}. \end{cases} \tag{1}$$

They are defined by the same mean value of F_{opt} but have different spreads σ_1 and σ_2, where σ_2 is prescribed, e.g., by fitting experimental data, and σ_1 is computed such that the average lifetime at zero force equals some T_0. The force–dependent off-rate $k_{\text{off}}(F)$ is then computed as the inverse of the average bond lifetime at force F. This results in a simple, generic model for catch-slip bonds with the four parameters F_{opt}, σ_2, T_{opt}, and T_0, which are easy to interpret and identify from experimental data. For the following studies, we used $F_{\text{opt}} = 30\ pN$, $\sigma_2 = 9\ pN$, and $T_{\text{opt}} = 3s$ which is based on data from Kong et al. (2009) and Weng et al. (2016) for the average lifetimes of bonds between fibronectin and $\alpha_5\beta_1$ integrins. Note that in order to avoid infinite unbinding rates at zero force, T_0 must be set to a value larger than 0. Hence, and because of a lack of data from which T_0 could be concluded with sufficient certainty, we heuristically choose a value of $T_0 = 0.25$ s.

Cell contractility is included by allowing existing cell-ECM connections to contract at a constant rate of $\dot{c} = 0.1$ µm/s (Choquet et al. 1997; Moore et al. 2010), naturally limiting the maximum lifetime of a bond which dissolves with increase in probability as the applied load increases. Additionally, we assume that stress fiber cannot contract to a length of less than half the cell radius. Note though that this cutoff is mostly irrelevant since most stress fibers never reach this length since the associated bonds rupture first.

The stress fibers themselves are modeled as elastic springs with a stiffness k_{SF} which we assume to be 1 kPa (Gavara and Chadwick 2016). Once a stress fiber has formed, it contracts with the rate $\dot{c}$, thereby creating a tensile force F_{SF},

$$F_{SF} = k_{SF} \cdot \Delta x \tag{2}$$

with Δx the length contraction of a stress fiber since its formation. Note that the force points in the direction of the fiber in space. It acts on the cell nucleus (represented by a particle as described above) and the focal adhesion and hence the integrins in that adhesion. The force in an individual integrin, F_i is thus

$$F_i = \frac{F_{SF}}{n_{i,\text{bound}}} \tag{3}$$

where $n_{i,\text{bound}}$ is the number of currently bound integrins in the focal adhesion associated with the stress fiber. The probability of an integrin unbinding is governed by its load F_i. The unbinding of the integrins is modeled as a Poisson process yielding an unbinding probability of

$$p_{\text{off}} = 1 - \exp\left(-\frac{1}{T(F_i)} \cdot \Delta t\right) \tag{4}$$

where $T(F_i)$ is computed based on Eq. (1). Note that additional integrins can also bind during that time (further stabilizing the adhesion) with the probability

$$p_{\text{on}} = 1 - \exp\left(-k_{\text{on}} \cdot \Delta t\right). \tag{5}$$

In case all integrins of an adhesion happen to have been dissolved, the entire focal adhesion is dissolved and the stress fiber removed. However, it can form again in the next time steps. The equation of motion of the cell center is the balance between the forces of the stress fibers and a viscous drag force $\underline{\boldsymbol{F}}_{\text{drag}}$ impeding the motion of the cell through the surrounding liquid-filled space:

$$\underline{\boldsymbol{F}}_{\text{drag}} + \sum_{j}^{N} \underline{\boldsymbol{F}}_{SF,j} = \underline{\boldsymbol{0}}. \tag{6}$$

Here, $\underline{\boldsymbol{F}}_{\text{drag}} = -\gamma \cdot \underline{\boldsymbol{v}}_{\text{cell}}$ with γ the friction coefficient of a sphere in a liquid with viscosity η based on Stokes Law and $\underline{\boldsymbol{v}}_{\text{cell}}$ the velocity of the cell (center). In our case, we assumed $\gamma = 6\pi\eta R_{\text{cell}}$ and the viscosity of water $\eta = 1$ mPa·s.

The combination of contractility and force–dependent unbinding of individual integrins, which are clustered in focal adhesions, allows our model to realistically capture the distinct lifetimes of integrins (on the order of seconds) and focal adhesions (on the order of minutes). All our simulations were performed using periodic boundary conditions for the RVE (edge length 50 µm) and the entire computational framework was implemented in BACI (BACI 2021), an in-house finite element code. For more details on the periodic boundary conditions, see appendix A2 in Eichinger et al. (2021). The simulation parameters are summarized in Table 1 in the Appendix.

2.3 Quantitative characteristics of cell motion

Cells are to some extent comparable to random walkers, not moving always monotonously into a specific direction but changing their direction (or even reversing it) over time. Such a random walk-like motion can be characterized in particular by two quantities: on the one hand the velocity of the cells in the three-dimensional space (migration speed), on the other hand by the distance the cells can effectively cover in a given time, which can be characterized by the so-called mean-square displacement (MSD). In case of deterministic motions, both is directly proportional, that is, twice the speed leads to twice the distance covered in a specific period (and thus four times the mean-square displacement). By contrast, for a random motion the relation is more complex. For example,

a random walker may move through the space at a very high velocity. However, if that random walker frequently changes or even reverses the direction of motion, it may for a relatively long time remain in the same neighborhood without moving to a truly distant location.

To determine the migration speed, the position $\mathbf{x}$ of the particle representing the cell center was extracted from the raw data at (simulated) time intervals of $\Delta t = 60$ s over a total simulated time of $t_{\max} = 3600$ s. The displacement between two consecutive data points was computed, which yield the migration speed when dividing by the time interval (i.e., 1 min).

The MSD $\langle r^2(\tau)\rangle$ achieved by cell migration over a time interval τ was computed as

$$\langle r^2(\tau)\rangle = \frac{1}{N_\tau}\sum_{i=0}^{N_\tau}(\mathbf{x}(i\Delta t+\tau)-\mathbf{x}(i\Delta t))^2. \tag{7}$$

Here, $N_\tau = (t_{\max}-\tau)/\Delta t$ is the maximal number of simulated points in time from which data for the computation of the time average defining the MSD can be harvested for a given τ. To see this, consider, for example $\tau = 600$ s. In that case, the first 50 simulated points in time can be used to compute $\langle r^2(\tau)\rangle$. Because for the associated positions $\mathbf{x}(0), \mathbf{x}(60\,s), \mathbf{x}(120\,s), ..., \mathbf{x}(3000\,s)$ one has related positions $\mathbf{x}(600\,s), \mathbf{x}(660\,s), \mathbf{x}(720\,s), ..., \mathbf{x}(3600\,s)$ available in the simulation data to compute (7). By contrast, a position $\mathbf{x}(3060s)$ or a position at any later point in time, the associated position required to evaluate the MSD for $\tau = 600\,s$ would be at time $3660\,s$ or later and thus outside the simulated time interval.

2.4 Computational cost

The computational cost varies with collagen concentration, i.e., the number of fibers and thus finite elements used in the simulation. For example, using a collagen concentration of 1.7 mg/ml, there are approximately 2200 elements in the simulation domain. The average runtime of a simulation with baseline parameters is approximately 36 to 48 h on 16 cores (Intel Xeon Platinum 8160). For more details on the computational implementation, see appendix A3 in Eichinger et al. (2021).

2.5 Statistical methods

All simulations were performed with five randomly generated networks (see respective figure captions and legends for specific details). Unless stated otherwise, all data is presented as the average or average (±) standard error of the mean (SEM) of these simulations.

3 Results

3.1 Model validation

To validate our model and find its limitations, we first compared it to various experimental results. We focused on the speed of migration, a metric that is most often reported in (three-dimensional) experimental cell migration studies. Our studies were performed in homogeneous networks with a line density of 4.9×10^{-2} μm^{-2} corresponding to a collagen concentration of around 1.7 mg/ml.

3.1.1 Migration speed

Reported values of migration speeds in three-dimensional fibrous network experiments are between 0.1 and 10 μm / min (Wolf et al. 2013; Doyle et al. 2015). As can be seen in Fig. 2a, the average migration speed in our simulations (on the order of 1 μm /min) using baseline parameters motivated by experimental data are within the experimentally reported values, especially those of HT1080 and HFF cells. It is important to note that the migration speed is highly cell-type- and substrate-specific. Neutrophils, for example, are reported to migrate with a velocity of $5-10$ μm /min (Wolf et al. 2013), whereas HT1080 cells or HFFs migrate at a speed of around 0.5 μm /min (Doyle et al. 2021). Note that in order to remove any effects of the initialization phase (such as increasing numbers of integrins), we only plot the average speed in the last 30 min in Fig. 2b where migration reached a relatively steady state.

3.1.2 Cellular contractility

Through pharmacological treatment, the contractility of cells can be modified. For example, Doyle et al. (2015) and Doyle et al. (2021) used blebbistatin, a myosin II inhibitor, to partially disrupt the contractile apparatus of the cell depending on the dosage. We mimicked the influence of the drug by reducing the contraction rate of the stress fibers and observed a similar qualitative decrease in the resulting migration speeds (Fig. 2b).

3.1.3 Varying fiber stiffness

Systematically varying single parameters in a collagen network is challenging in experiments. For example, in Doyle et al. (2015) collagen gels were polymerized at different temperatures. Lower temperatures led to thicker fibers and fiber bundles. However, also the porosity of the gel, which significantly influences migration in 3D (Wolf et al. 2013; Doyle et al. 2015), was found to be temperature-dependent.

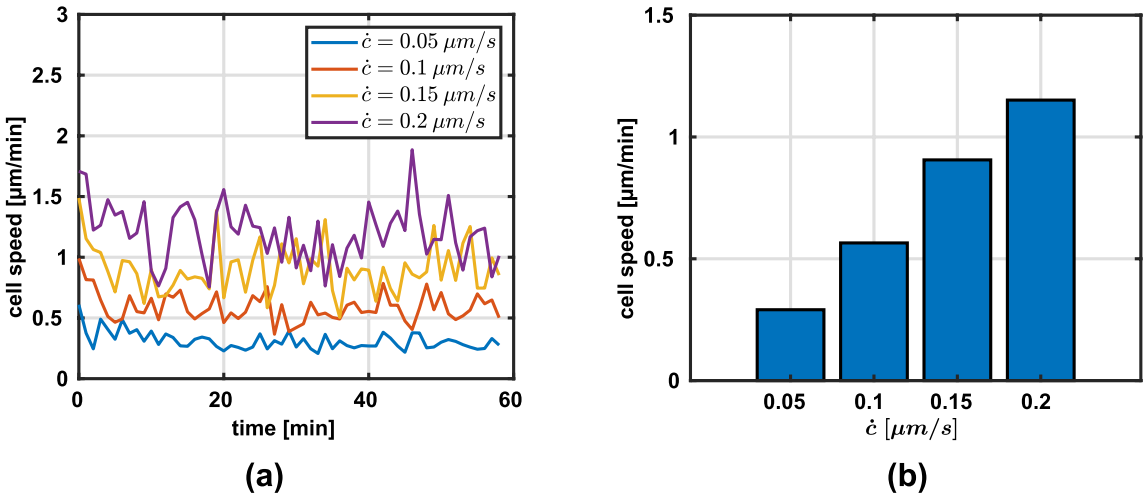

Fig. 2 Average migration speeds for varying contraction rates $\dot{c}$ in collagen networks with a line density of 4.9×10^{-2} µm^{-2}. **a** Simulated migration speed over the range of one hour ($N = 5$) **b** Migration speed during the last 30 min of the simulated time ($N = 5$, mean)

This example illustrates the difficulties associated with controlling specific mechanical characteristics of biological fiber networks. To overcome this limitation, alternative techniques such as nonelectrospinning (Nain et al. 2009) were developed. Using this technique, Meehan and Nain (2014) and Sheets et al. (2013) placed cells on synthetic fibers and demonstrated that the migration speed is negatively correlated with structural stiffness. It is important to note though that in these experiments, cells migrated along a *single* suspended fiber which limits the general transferability to three-dimensional networks.

However, since experimental data of the influence of fiber stiffness in three dimensions (without changing other network parameters) is lacking, and because (Doyle et al. 2009) found that cell migration in three dimensions has more in common with migration in one dimension than with migration on two-dimensional substrates, we used the aforementioned studies for a qualitative comparison. They found, for example, that migration on micropatterned 1D substrates and in 3D matrices was dependent on cytoskeletal contraction, whereas 2D migration speed was largely unaffected by a blebbistatin treatment which disrupts the cytoskeleton. The similarity of 1D and 3D migration might arise because migration in 3D is mainly governed by one-dimensional topological cues, the thin fibers making up the network. Based on this, we found a similar trend of decreasing migration speed with increase in stiffness in our simulations, see Fig. 3a and b, respectively. However, we would

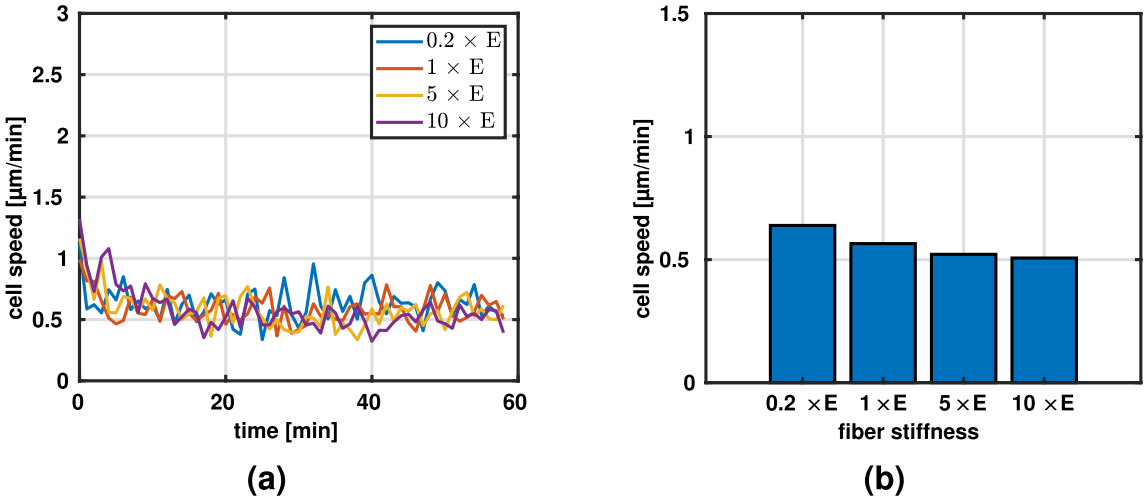

Fig. 3 Migration speeds for different fiber stiffnesses (multiples of baseline fiber stiffness $E = 1.1$ MPa). **a** Migration speed during the entire simulation. **b** Average migration speed during the last 30 min of the simulation ($N = 5$, mean)

like to emphasize that this comparison is solely intended to get an idea of how migration in 3D matrices *could* be affected by changes in fiber stiffness because of the lack of experimental data for 3D experiments with varying fiber stiffnesses. As mentioned in section 3.1.1, for Fig. 3b we only plot the average speed in the last 30 min to remove any effects of the initialization phase.

3.2 Integrin turnover

Figure 4 presents the number of bound integrins over time. This number stabilizes after an initial rapid increase. The steady state level is influenced by the collagen concentration (Fig. 4a), the contraction rate (Fig. 4b), and the fiber stiffness (Fig. 4c). Interestingly, the number of integrins seems to be insensitive to increases of the contraction rate above 0.1 $\mu m/s$.

3.3 Biphasic mean-squared displacement

Cells placed on two-dimensional substrates of varying stiffnesses have been shown to migrate most effectively on substrates of intermediate stiffness, suggesting a biphasic relationship between the stiffness of the substrate and the mean-squared displacement (Bangasser et al. 2017). The MSD can be interpreted as a measure of how effectively a random walker, in this case the cell, can explore its surroundings.

To see if we can reproduce this effect in our model, we varied the fiber stiffness at a constant contraction rate. Migration after an initialization phase of 20 min is shown in Fig. 5a. Apparently, also our model produces maximal migration rates at intermediate stiffnesses in agreement with the experimental observations of Bangasser et al. (2017).

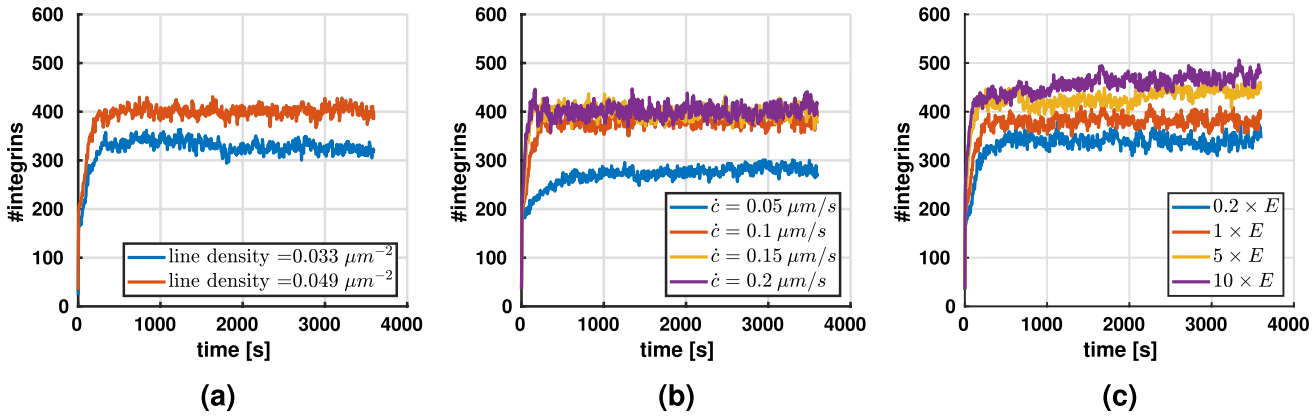

Fig. 4 Average number of integrins ($N = 5$ per condition) for varying **a** line densities (contraction rate $\dot{c} = 0.1$ µm/s, fiber stiffness $E = 1.1$ MPa), **b** contraction rates (line density of 4.9×10^{-2} µm^{-2}, fiber stiffness $E = 1.1$ MPa, and **c** fiber stiffnesses (line density of 4.9×10^{-2} µm^{-2}, contraction rate 0.1 µm/s)

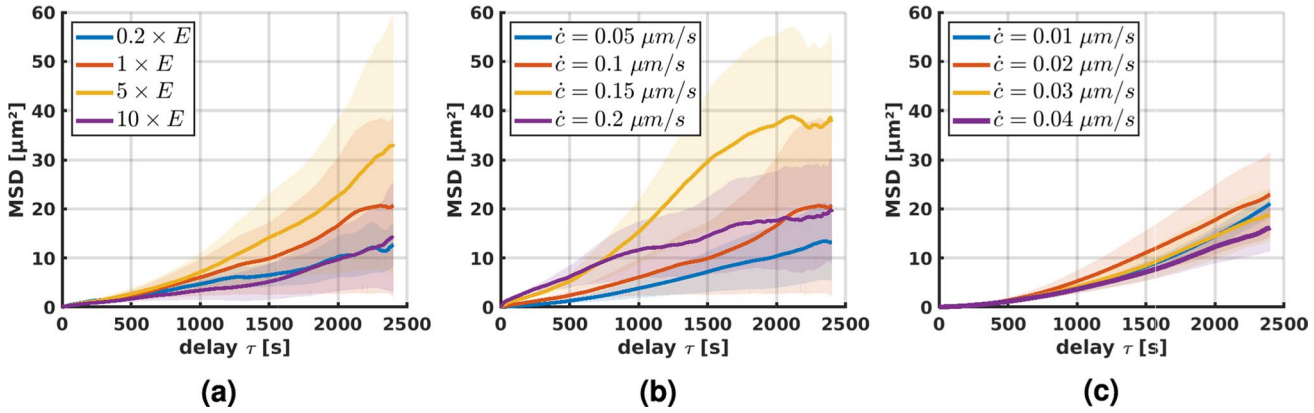

Fig. 5 Average mean-squared displacement (± SEM) during the last 40 min ($N = 5$, line density of 4.9×10^{-2} µm^{-2}): **a** different fiber stiffnesses ($E = 1.1$ MPa) at constant contraction rate $\dot{c} = 0.1$ µm/s; **b** different contraction rates at constant fiber stiffness $E = 1.1$ MPa; **c** different contraction rates at increased constant fiber stiffness $5 \times E$. Note that in this case, the contraction rates were adjusted such that the product of contraction rate and fiber stiffness remains constant compared to (**b**)

In a further set of simulations, we studied the effect of varying contraction rates at constant fiber stiffness, Fig. 5 b and c, respectively. For an intermediate fiber stiffness of $E = 1.1$ MPa (Fig. 5b), we found a biphasic relationship between MSD and contraction rate suggesting that in this regime, cells can increase their migration rate by adjusting their contraction rate (in this case to approximately 0.15 µm/s). Remarkably, increasing the fiber stiffness by a factor of 5 and adjusting the contraction in such a way that the product of fiber stiffness and contraction rate remained constant compared to the simulations in Fig. 5b, resulted in a biphasic relationship again, albeit less pronounced (5c).

3.4 Durotaxis in three-dimensional fiber networks

To study the phenomenon of durotaxis—the preference of cells to migrate toward higher stiffnesses on or in substrates with stiffness gradients—we use exactly the same networks as in the previous sections but introduce a constant gradient of the fiber radius along the *x*-axis of the simulation domain (Fig. 6). All other parameters of the network are kept constant (e.g., line density, network architecture, number of binding spots on the fibers, etc.). Thus, the only consequence of the gradient of fiber thickness is a gradient of stiffness of the fibers in the *x*-direction. We would like to note that the periodic boundary conditions lead to an inconsistency in the x-direction of the domain. However, this approach allowed us to use exactly the same five network structures as in the homogeneous networks with the only difference being the fiber radius distribution and everything else being identical. This way, we can eliminate the possibility that a favorable fiber distribution—potentially occurring at the relatively low collagen concentrations examined—caused preferred migration in the x-direction and ensure that the only factor we changed is the introduction of a stiffness gradient via the fiber radius distribution. To reduce the potential effects of this small boundary region, we adjusted the starting positions of the cells and thereby reduced the chance of the cells reaching those regions during the simulation.

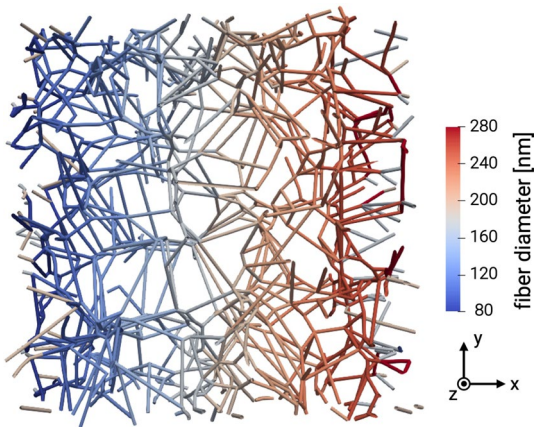

Fig. 6 Visualization of a three-dimensional fiber network used to study durotaxis

3.4.1 Influence of initial network geometry on durotaxis

In general, when placed in networks with a stiffness gradient, cells moved preferentially along the stiffness gradient, i.e., in the direction of increasing stiffness (Fig. 7). Interestingly, in a few cases, the migration of cells stagnated from the beginning. In fact, in Fig. 7 one observes for the lower collagen concentration of 1.1 mg/ml (corresponding to a line density of 3.3×10^{-2} µm^{-2}) that in two cases the cells even first moved slightly opposite to the stiffness gradient before stagnating. We hypothesized that the reason for this behavior is a statistical artifact of the distribution of binding spots around the initial position of the cell. For example, it could happen that the cells encounter in their initial position within their binding range many more binding spots on fibers in the direction of decreasing stiffness (Fig. 8). This would increase the probability of a formation of stress fibers in that direction, eventually leading to some migration against the stiffness gradient that is expected to stagnate, however, quickly because in general the structure of the network would impede such migration. To test this hypothesis, we selected one of the simulations where the cell initially migrated against the stiffness gradient (purple curve in Fig. 7a) and restarted it in a setting, where we had inverted the stiffness gradient by inverting the dependence of fiber radius on the x-coordinate. Indeed, in this reconfigured setup one observes the same cell continuing its motion in negative x-direction (i.e., the direction of the now inverted stiffness gradient) far beyond the point it could reach with a stiffness gradient in positive x-direction. This supports that the systemic driving force is indeed given by the stiffness gradient and that the initial limited motion against it in two cases in Fig. 7a is likely only a statistical artifact resulting from random binding spot availability as illustrated in Fig. 8. Note that this interpretation is supported also by the fact that initial migration against the stiffness gradient appears to happen only in the case of the lower collagen concentration in Fig. 7, where statistical artifacts are more likely. It is worth noting that in several cases in Fig. 7 and also for the reconfigured setup in Fig. 8b one observes after a prolonged period of migration in the direction of the stiffness gradient finally a stage of stagnation. Again this is likely caused by the cell entering a region where—due to a statistical artifact—sufficient binding spots for further migration in direction of the stiffness gradient are missing. Again this interpretation is supported by the fact that such stagnation appears more frequently in case of the lower collagen concentration in Fig. 7 where statistical artifacts are generally more likely than in case of high collagen concentrations. Note that a

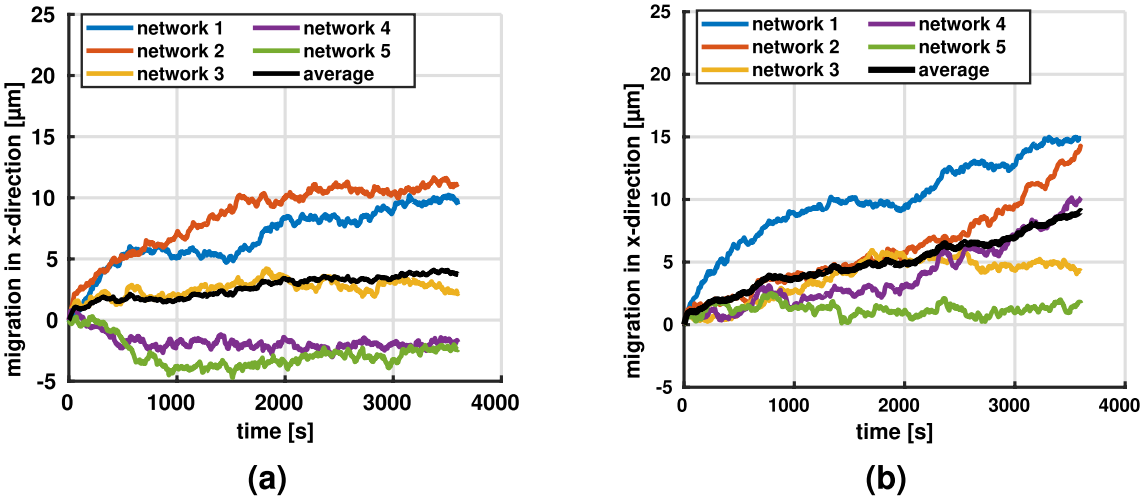

Fig. 7 Migration along stiffness gradient (x-direction) for contraction rate $\dot{c} = 0.1$ µm/s and fiber stiffness $E = 1.1$ MPa at a line density of **a** 3.3×10^{-2} µm^{-2} and **b** 4.9×10^{-2}µm^{-2}. Mean migration is plotted in black

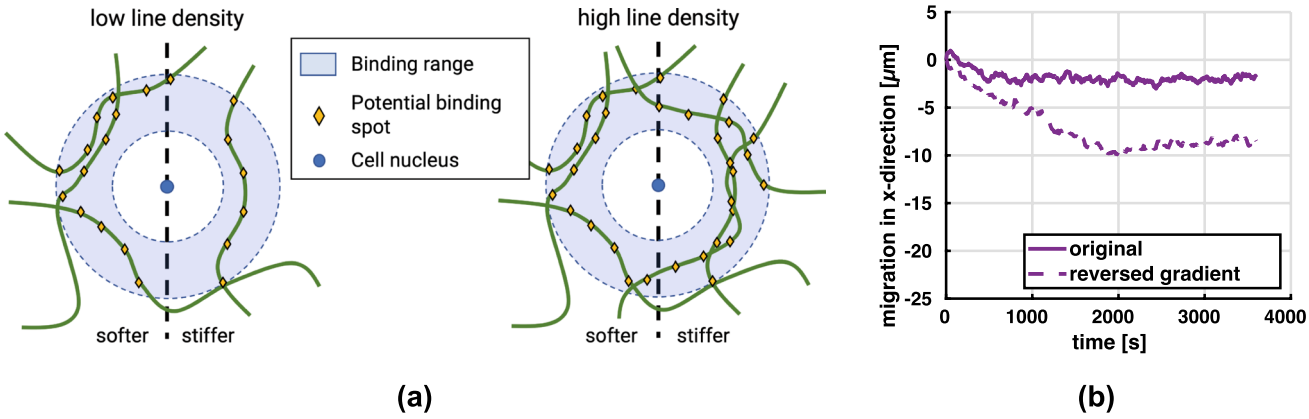

Fig. 8 **a** For low collagen concentrations, there is a considerable likelihood that—as a statistical artifact—some cells are located in an environment where they encounter many more binding spots in the direction of decreasing stiffness thus inducing migration against the stiffness gradient. For high collagen densities, the likelihood of such statistical artifacts substantially decreases. **b** The setup of the purple curve in Fig. 7a was reconfigured by inverting the stiffness gradient so that it pointed in negative x-direction. This caused a continued migration in that direction rather than a limited motion in the beginning followed by stagnation

similar observation of stagnation or slight migration against the gradient has been observed in 2D experiments (Hartman et al. 2016).

3.4.2 Influence of contraction rate on durotaxis

We studied the influence of the contraction rate $\dot{c}$, which, for example, differs for different cell types, using networks with a line density of 4.9×10^{-2} µm^{-2} to reduce random effects of the initial network geometry (see previous section). Apparently, at lower contraction rates, the cells had greater difficulties to sense and follow the direction of the stiffness gradient (Fig. 9), leading more frequently to stagnation or motion opposite to the stiffness gradient. The reason is likely that for lower contraction rates the connection between cells and matrix fibers dissolves with a higher likelihood already before substantial mechanical forces are built up because it takes longer until the regime of optimal survival time of the catch-slip bond is reached. This higher likelihood of dissolution of the cell–matrix connection before it can become mechanically effective can be interpreted as a sort of decreased effective binding spot density, translating into less pronounced directed migration of the cells.

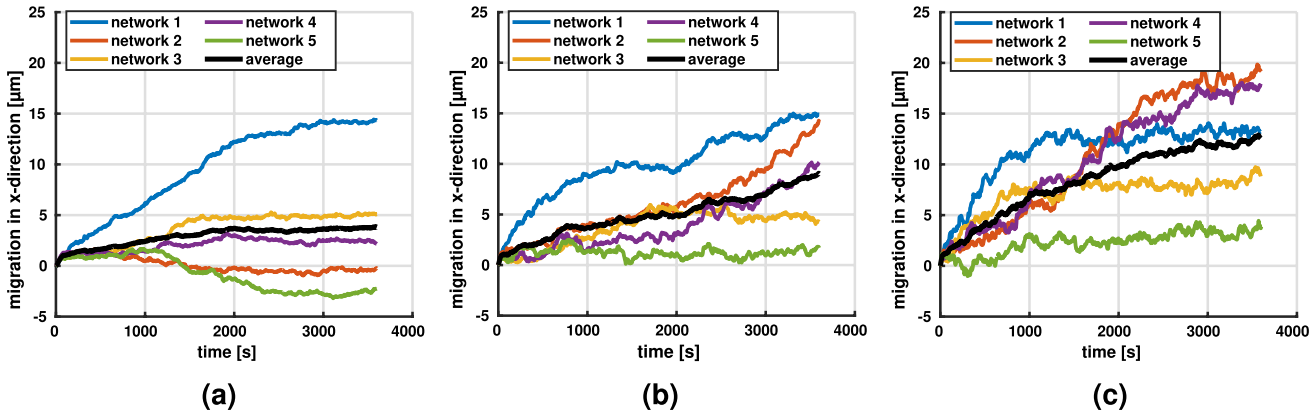

Fig. 9 Migration in networks with stiffness gradient in x-direction and a line density of 4.9×10^{-2} µm^{-2}. We studied contraction rates of **a** $\dot{c} = 0.05$µm/s. **b** $\dot{c} = 0.1$ µm/s. **c** $\dot{c} = 0.15$ µm/s with $N = 5$ realizations (different colors), respectively. The mean migration rate (black) increases with $\dot{c}$

4 Discussion

4.1 What mechanisms are sufficient to ensure a balanced adhesion turnover?

Experimental studies have argued that a balanced adhesion turnover is key for efficient cell migration (Huttenlocher and Horwitz 2011; Gupton and Waterman-Storer 2006; Webb et al. 2002). On the one hand, without the formation of stable adhesions, cells cannot attach to the matrix and are therefore unable to move the cell body by cytoskeletal actin-myosin contraction. On the other hand, if adhesions do not disengage, cells might form a large number of long-lasting adhesions resulting in impaired migration (Webb et al. 2004; Chan et al. 2009). Especially for the disengagement of integrins, the contractile apparatus of the cell has been shown to play a major role (Doyle et al. 2015; Vicente-Manzanares et al. 2007). Against this background, it is a key question what mechanisms are required to ensure the balanced adhesion turnover cells need for migration in a manner that is robust across different cellular contractile stresses and different stiffnesses of the extracellular matrix. This question is difficult to answer by experimental studies. Because in such studies it is practically impossible to ensure that not some largely unattended mechanism in the background plays an important role nobody has understood so far. By contrast, in a computational model, one has full control of the mechanisms acting. Therefore, the results shown in section 3 allow us to draw an important conclusion: the interplay of cell contractility (represented in our model by $\dot{c}$) and force–dependent unbinding of adhesions (represented in our model by Eq. (1)) is sufficient to enable the kind of balanced adhesion turnover cells need to migrate. Notably, with these two mechanisms our model robustly reproduced physiological cell migration over a range of collagen densities, fiber stiffnesses, and cell contractilities both in homogeneous collagen networks as well as in networks with a stiffness gradient.

4.2 How does the cytoskeletal contraction rate affect adhesion formation?

As shown in Fig. 10, the number of integrins through which cells connect to their environment is largely independent on whether they are embedded into a homogeneous extracellular matrix or by contrast one with a stiffness gradient. However, this number of integrins depends on the contraction rate $\dot{c}$ of the cytoskeletal stress fibers. There is some saturation value of $\dot{c}$, above which the number of integrins becomes largely independent on $\dot{c}$. However, below that threshold, the number of integrins decreases as $\dot{c}$ decreases. This can be understood from the characteristic behavior of the catch-slip bond discussed above. When new connections between cells and extracellular fibers are formed through integrins, these connections are initially nearly load-free and thus relatively unstable. The dependence of the bond stability on the transmitted force is often referred to as molecular clutch (Elosegui-Artola et al. 2014, 2018) and illustrated in Fig. 1c. Due to this molecular clutch mechanism, only as the cytoskeleton builds up more and more mechanical loading on the integrin, a more and more stable connection between cell and extracellular matrix forms that is likely to survive for a substantial time. Apparently, for very low cytoskeletal contraction rates $\dot{c}$, there is a considerable period in the beginning when a new integrin connection is established during which that connection is highly unstable and thus may disengage before becoming mechanically effective. The higher the cytoskeletal contraction rate $\dot{c}$, the shorter this critical period becomes. However, above some saturation contraction rate, one expects that nearly all integrins will

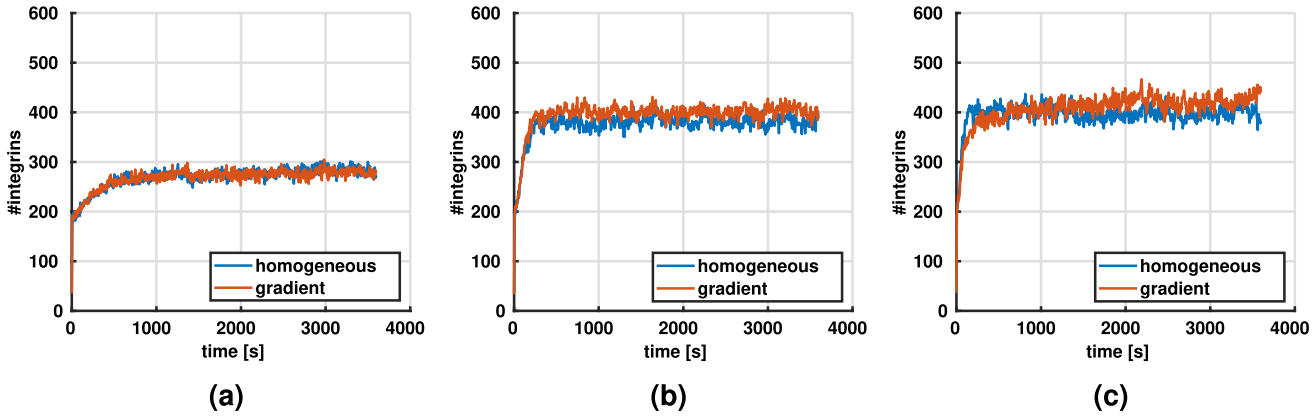

Fig. 10 Average number of integrins over time for different contraction rates $\dot{c}$ in homogeneous networks compared to networks with a stiffness gradient ($N = 5$, line density 4.9×10^{-2} µm^{-2}). **a** $\dot{c} = 0.05$ µm/s. **b** $\dot{c} = 0.1$ µm/s. **c** $\dot{c} = 0.15$ µm/s

become mechanically effective before disengaging. Above that saturation rate thus no further effect of increased $\dot{c}$ is expected.

4.3 How does fiber stiffness affect adhesion formation?

A similar argument as presented in the previous section 4.2 may also explain why the number of active integrins increases with fiber stiffness as illustrated in Fig. 4. An increased fiber stiffness may allow the integrins to stabilize more rapidly because for a given cytoskeletal contraction rate it shortens the period during which the integrin-connections are under critically low loading, highly unstable and thus likely to disengage without substantial mechanical effect. That is, increased stiffness of extracellular fibers typically extends the lifetime of integrins and of the respective integrin cluster and focal adhesion, allowing more integrins to bind. We expect that beyond a certain threshold (that generally depends on the cytoskeletal contraction rate), the number of integrins disengaging without substantial mechanical effect becomes negligible so that no benefit can be expected from a further increased fiber stiffness but the tested stiffnesses were not sufficient to show this behavior clearly.

In reality, numerous biochemical signaling pathways are involved in regulating cellular processes such as focal adhesion dynamics or cytoskeletal contractility. Moreover, cells may use several integrin types simultaneously with different binding and unbinding kinetics that will result in different turnover rates allowing a cell to adapt its migration pattern to the given surroundings (Elosegui-Artola et al. 2014). Interestingly, although our model does not capture this complexity in full, it yet reproduces the major experimental findings in cell migration, underlining that at least the fundamentals of this phenomenon can be understood from a surprisingly limited number of factors and processes.

4.4 Biphasic relation between migration efficiency and fiber stiffness

Migration speed appears to slightly decrease with stiffness of the extracellular matrix (Fig. 3). However, migration speed itself is not a good measure of how efficiently cells can explore their environment or change their position because it does not account for the fact that stochastic back-and-forth motions may limit this efficiency. Mean-squared displacement (MSD) accounts for this effect and is thus a good measure of the efficiency of cell migration. In line with (Bangasser et al. 2017), we found a biphasic relationship between fiber stiffness and MSD. This suggests that there is an optimal fiber stiffness at which cells can migrate most efficiently, i.e., explore a maximally large portion of their surroundings, given a constant contraction rate and specific integrin dynamics (Fig. 11).

The stiffness maximizing the MSD is likely cell-type dependent as different cell types may exhibit different contraction rates and properties of the integrin catch-slip bonds. It was shown that the optimal stiffness can be modulated by drugs (Bangasser et al. 2017) and potentially also by changing the integrin type and the associated dynamics (Elosegui-Artola et al. 2014).

4.5 Biphasic relation between migration efficiency and cellular contraction rate

The MSD depends not only on fiber stiffness but also on the contraction rate via a biphasic relationship as shown in Fig. 5b and Fig. 12 for a fiber stiffness of $E = 1.1$ MPa. This observation was also robust under variations of the fiber stiffness (Fig. 5c). Under such variations, the maximum MSD was achieved if cellular contraction rate and fiber stiffness were chosen such that their product was nearly equal to the one in the baseline case shown in Fig. 5b. This raises

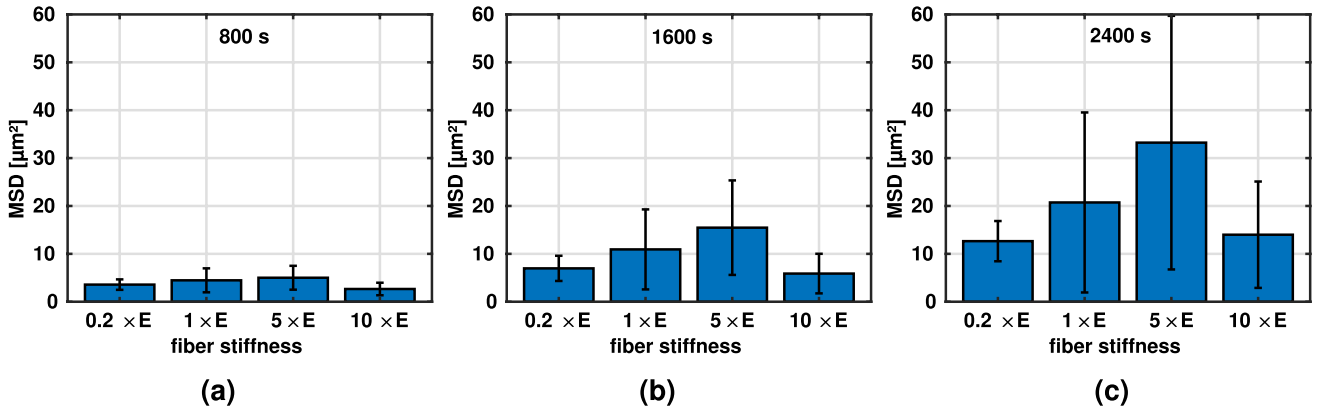

Fig. 11 Average mean-squared displacement (MSD) and SEM ($N = 5$) for varying fiber stiffnesses (in multiples of baseline stiffness $E = 1.1$ MPa) at a constant contraction rate of 0.1 µm/s after **a** 800 s, **b** 1600 s, and **c** 2400 s

the question if there is a more fundamental principle that governs this behavior. For example, there might be a preferred rate of increase of the integrin forces that maximizes the MSD. Possibly, slower rates make focal adhesions too unstable to allow effective cell-fiber interactions, and higher rates make focal adhesions too long-living to allow efficient migration through large spaces. Generally, such complex interactions between adhesion dynamics, contractility, and ECM stiffness are known from experiments (Doyle et al. 2015; Bangasser et al. 2017). Yet, exactly reproducing our computational study in a real experiment is likely challenging because in experiments it is not straightforward to vary single parameters and keep all other parameters constant.

4.6 What causes durotaxis?

One of the first computational studies of durotaxis in three dimensions was proposed by Kim et al. (2018). It relied on a very detailed and complex model where the mechanical interactions of filopodia with a three-dimensional fiber network were used to determine the local effective stiffness the cells perceive (through their filopodia). Using this perceived stiffness, a polarization of the cell was prescribed. Interestingly, our study suggests that details such as the interactions between filopodia and extracellular matrix or polarization are not required to reproduce durotaxis. Rather, the much simpler interplay between contractile stress fibers and a catch-slip integrin bond appear sufficient. To understand, how these two mechanisms alone can produce durotaxis, it is worth revisiting the literature. As was shown by Doyle et al. (2015), Domaschke et al. (2019), Kim et al. (2018), the local micromechanical environment, especially the stiffness a cell effectively perceives, has a significant influence on cellular and subcellular mechanics. Doyle et al. (2015) even showed that the local stiffness perceived by an *individual adhesion* in combination with the contractile forces of the associated stress fiber determines adhesion stability. Durotaxis could thus arise from a spatial difference in adhesion stability: adhesion sites in the direction of the stiffness gradient are loaded slightly more rapidly by cytoskeletal contraction and are therefore slightly more likely to become mechanically effective than adhesion sites in the opposite direction. At the same time, a stress fiber reaching from the cell center toward the stiffer region, i.e., in the direction of the stiffness gradient, can pull the cell slightly more in that direction than a similar stress fiber in the opposite direction because the former interacts with a stiffer matrix. In summary, we observe durotaxis in our model because cell–matrix interactions, based on catch-slip bonds, are more stable in the stiffer regions of the matrix and the contractility leads to larger movements of the cell in the direction of the stiffness gradient. That is, durotaxis can be understood from purely mechanical factors. No prior assumptions on cell polarization or on how stiffness is exactly sensed by the cells are necessary.

4.7 Limitations

Despite the qualitatively very good agreement of our computational framework with various experimental observations, it also has some limitations. As our main objective was to unravel the *mechanical* factors governing cell migration—durotaxis in particular—no biochemical signaling was included. However, it is well known that intracellular signaling pathways are intimately linked to processes such as contraction (Tozluoğlu et al. 2013; Wang et al. 2017; Moujaber and Stochaj 2020) and focal adhesion (dis-)assembly and stability (Sieg et al. 1999; Ren et al. 2000; Huttenlocher and Horwitz 2011) which are the key players according to our findings. These complex interactions were not included in our study. Therefore, when translating the results of our study to in vivo or in vitro studies, one has to keep in

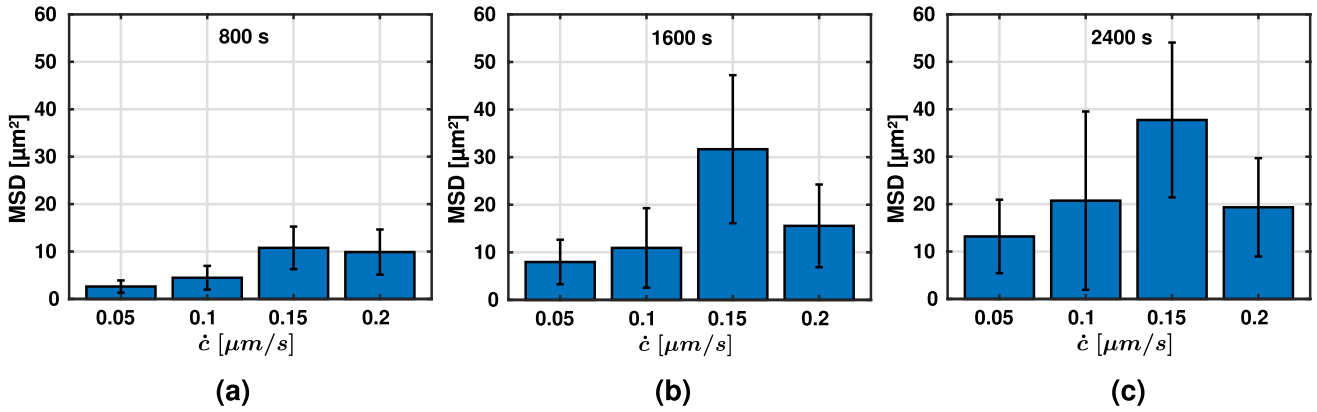

Fig. 12 Average mean-squared displacement (MSD) and SEM ($N = 5$) for varying contraction rates and a constant fiber stiffness of $E = 1.1$ MPa after **a** 800 s, **b** 1600 s, and **c** 2400 s

mind that there might be important biochemical modulators not yet accounted for in our study. Also, the model for cell–matrix adhesions is simplified and reduced to a single type of integrin. It is known that focal adhesions are made up of numerous proteins. We deliberately neglected that multitude to focus on the essential governing cell migration. However, future studies should include this complexity and examine its role in cell migration. Such studies should also account for the fact that during maturation focal adhesion can grow in size in a way that may depend on external factors such as fiber diameter or fiber alignment (Kim and Wirtz 2013).

Not only the model of cell–matrix interactions in this study was very much simplified compared to reality but also the model of the matrix itself. In our study, we focused on low concentration collagen gels. This allowed us to neglect protease activity which only has a minor influence at low collagen concentrations (Wolf et al. 2013) and would be difficult to include in the discrete beam element model. Additionally, we did not explicitly model the cell nucleus since the pore sizes in our low concentration gels were assumed to be large enough not to impede cell migration. Hence, our computational framework did not include mechanical contact and therefore was not able to capture the effects of confinement which were shown to influence cell signaling and morphology (Balzer et al. 2012) and to modulate migration (Friedl and Gilmour 2009). A further important limitation of the model is the assumed spherical geometry of the cell. In experiments, it was observed that cells have a remarkable ability to change and adjust their shape to their surroundings, see for example (Sheets et al. 2013; Yeung et al. 2005; Thiam et al. 2016). That capability, which is not captured by our model, might allow the protrusions of a cell to explore more of its immediate surrounding and potentially overcome unfavorable binding spot distributions which we observed in low concentration gradient networks, see section 3.4.1.

5 Conclusions

In our study, we used a previously developed computational model of cells and extracellular matrix. Cells and matrix were modeled as discrete objects on the micrometer scale. The structure of the matrix realistically mimicked the one of real collagen gels in terms of fiber stiffness and geometric key features (distance between and valency of network nodes, orientation correlation between fibers forming a node). The interactions between cells and matrix were represented by a very simple model relying on two corner stones, the catch-slip bond of the integrins and a contractile rate of the cytoskeletal stress fibers. We demonstrated that these two are sufficient to reproduce the main phenomena of cell migration observed experimentally, including complex phenomena such as durotaxis or the biphasic relation between the mean-squared distance covered by cell migration and the matrix stiffness. Notably, no ad hoc assumptions on cell polarization or details of the mechanical sensing of cells were required. Compared to experimental studies, the great advantage of our computational study is that the set of mechanisms acting can be exactly controlled. This makes the setup of our study particularly suitable to validate hypotheses, which mechanisms are required to produce realistic cell migration. In future work, our model could be extended to include intracellular biochemical signaling such as a dynamic feedback between the integrins and the contraction rate. Additionally, the model could be used to study additional factors known to affect cell migration such as fiber alignment (contact guidance) and the interplay of different types of integrins.

Appendix A

A.1 Simulation parameters

Table 1 Parameter values

Parameter	Description	Value	References
R	Cell radius	10 µm	Typical value
ΔR	Linking range around cell	3 µm	–
$\dot{c}$	Contraction rate of stress fiber	0.1 µm/s	Choquet et al. (1997), Moore et al. (2010)
k_{SF}	Stiffness of stress fiber	1 kPa	Gavara and Chadwick (2016)
η	Viscosity (water)	1 mPas	–
E	Young's Modulus of collagen fibers	1.1 MPa	Jansen et al. (2018)
R_f	Radius of collagen fibers	90 nm	Van Der Rijt et al. (2006)
d_{bs}	Binding spot distance on collagen fibers	50 nm	Selhuber-Unkel et al. (2010)
k_{on}	Association rate for integrin	0.1 s^{-1}	Elosegui-Artola et al. (2016)
F_{opt}	Force at which integrin lifetime is maximal	30 pN	Kong et al. (2009), Weng et al. (2016)
T_0	Lifetime of integrin at zero force	0.25 s	–
T_{opt}	Lifetime of integrin at F_{opt}	3 s	Kong et al. (2009), Weng et al. (2016)
σ_2	Spread of Gaussian distribution	pN	Kong et al. (2009), Weng et al. (2016)
$N_{FA,\mathrm{max}}$	Maximal number of focal adhesions per cell	65	Horzum et al. (2014), Kim and Wirtz (2013), Mason et al. (2019)
$N_{i,\mathrm{max}}$	Maximal number of integrins per focal adhesion	20	Changede et al. (2015), Chenget al. (2020)
L	Edge length of RVE	50 µm	–
Δt	Time step size	0.05 s	–

Funding Open Access funding enabled and organized by Projekt DEAL.

Declarations

Conflict of interest The authors declare that they have no conflict of interest.

References

Alcaraz J, Mori H, Ghajar CM, Brownfield D, Galgoczy R, Bissell MJ (2011) Collective epithelial cell invasion overcomes mechanical barriers of collagenous extracellular matrix by a narrow tube-like geometry and MMP14-dependent local softening. Integr Biol 3(12):1153. https://doi.org/10.1039/c1ib00073j

BACI (2021) BACI: A comprehensive multi-physics simulation framework

Balzer EM, Tong Z, Paul CD, Hung WC, Stroka KM, Boggs AE, Martin SS, Konstantopoulos K (2012) Physical confinement alters tumor cell adhesion and migration phenotypes. FASEB J 26(10):4045–4056. https://doi.org/10.1096/fj.12-211441

Bangasser BL, Shamsan GA, Chan CE, Opoku KN, Tüzel E, Schlichtmann BW, Kasim JA, Fuller BJ, McCullough BR, Rosenfeld SS, Odde DJ (2017) Shifting the optimal stiffness for cell migration. Nat Commun 8(1):15313. https://doi.org/10.1038/ncomms15313

Campbell EJ, Bagchi P (2021) A computational study of amoeboid motility in 3D: the role of extracellular matrix geometry, cell deformability, and cell-matrix adhesion. Biomech Model Mechanobiol 20(1):167–191. https://doi.org/10.1007/s10237-020-01376-7

Carey SP, Kraning-Rush CM, Williams RM, Reinhart-King CA (2012) Biophysical control of invasive tumor cell behavior by extracellular matrix microarchitecture. Biomaterials 33(16):4157–4165. https://doi.org/10.1016/j.biomaterials.2012.02.029

Chan KT, Cortesio CL, Huttenlocher A (2009) Fak alters invadopodia and focal adhesion composition and dynamics to regulate breast cancer invasion. J Cell Biol 185(2):357–370. https://doi.org/10.1083/jcb.200809110

Changede R, Xu X, Margadant F, Sheetz M (2015) Nascent integrin adhesions form on all matrix rigidities after integrin activation. Dev Cell 35(5):614–621. https://doi.org/10.1016/j.devcel.2015.11.001

Charras G, Sahai E (2014) Physical influences of the extracellular environment on cell migration. Nat Rev Mol Cell Biol 15(12):813–824. https://doi.org/10.1038/nrm3897

Cheng B, Wan W, Huang G, Li Y, Genin GM, Mofrad MRK, Lu TJ, Xu F, Lin M (2020) Nanoscale integrin cluster dynamics controls cellular mechanosensing via FAKY397 phosphorylation. Sci Adv. https://doi.org/10.1126/sciadv.aax1909

Choquet D, Felsenfeld DP, Sheetz MP (1997) Extracellular matrix rigidity causes strengthening of integrin-cytoskeleton linkages. Cell 88(1):39–48. https://doi.org/10.1016/S0092-8674(00)81856-5

Cukierman E, Pankov R, Stevens DR, Yamada KM (2001) Taking cell-matrix adhesions to the third dimension. Science 294(5547):1708–1712. https://doi.org/10.1126/science.1064829

Davoodi Kermani I, Schmitter M, Eichinger JF, Aydin RC, Cyron CJ (2021) Computational study of the geometric properties governing the linear mechanical behavior of fiber networks. Comput Mater Sci 199(April):110711. https://doi.org/10.1016/j.commatsci.2021.110711

Domaschke S, Zündel M, Mazza E, Ehret AE (2019) A 3D computational model of electrospun networks and its application to inform a reduced modelling approach. Int J Solids Struct 158:76–89. https://doi.org/10.1016/j.ijsolstr.2018.08.030

Doyle AD, Wang FW, Matsumoto K, Yamada KM (2009) One-dimensional topography underlies three-dimensional fibrillar cell migration. J Cell Biol 184(4):481–490. https://doi.org/10.1083/jcb.200810041

Doyle AD, Carvajal N, Jin A, Matsumoto K, Yamada KM (2015) Local 3D matrix microenvironment regulates cell migration through spatiotemporal dynamics of contractility-dependent adhesions. Nat Commun 6(1):8720. https://doi.org/10.1038/ncomms9720

Doyle AD, Sykora DJ, Pacheco GG, Kutys ML, Yamada KM (2021) 3D mesenchymal cell migration is driven by anterior cellular contraction that generates an extracellular matrix prestrain. Dev Cell 56(6):826–841. https://doi.org/10.1016/j.devcel.2021.02.017

Eichinger JF, Grill MJ, Kermani ID, Aydin RC, Wall WA, Humphrey JD, Cyron CJ (2021) A computational framework for modeling cell-matrix interactions in soft biological tissues. Biomech Model Mechanobiol 20(5):1851–1870. https://doi.org/10.1007/s10237-021-01480-2

Elosegui-Artola A, Bazellières E, Allen MD, Andreu I, Oria R, Sunyer R, Gomm JJ, Marshall JF, Jones JL, Trepat X, Roca-Cusachs P (2014) Rigidity sensing and adaptation through regulation of integrin types. Nat Mater 13(6):631–637. https://doi.org/10.1038/nmat3960

Elosegui-Artola A, Oria R, Chen Y, Kosmalska A, Pérez-González C, Castro N, Zhu C, Trepat X, Roca-Cusachs P (2016) Mechanical regulation of a molecular clutch defines force transmission and transduction in response to matrix rigidity. Nat Cell Biol 18(5):540–566. https://doi.org/10.1038/NCB3336

Elosegui-Artola A, Trepat X, Roca-Cusachs P (2018) Control of mechanotransduction by molecular clutch dynamics. Trends Cell Biol 28(5):356–367. https://doi.org/10.1016/j.tcb.2018.01.008

Engler AJ, Sen S, Sweeney HL, Discher DE (2006) Matrix elasticity directs stem cell lineage specification. Cell 126(4):677–689. https://doi.org/10.1016/j.cell.2006.06.044

Franz CM, Jones GE, Ridley AJ (2002) Cell migration in development and disease. Dev Cell 2(2):153–8. https://doi.org/10.1016/s1534-5807(02)00120-x

Friedl P, Gilmour D (2009) Collective cell migration in morphogenesis, regeneration and cancer. Nat Rev Mol Cell Biol 10(7):445–457. https://doi.org/10.1038/nrm2720

Gavara N, Chadwick RS (2016) Relationship between cell stiffness and stress fiber amount, assessed by simultaneous atomic force microscopy and live-cell fluorescence imaging. Biomech Model Mechanobiol 15(3):511–523. https://doi.org/10.1007/s10237-015-0706-9

Ghibaudo M, Di Meglio JM, Hersen P, Ladoux B (2011) Mechanics of cell spreading within 3D-micropatterned environments. Lab Chip 11(5):805–812. https://doi.org/10.1039/c0lc00221f

Gonzalez ACDO, Costa TF, Andrade ZDA, Medrado ARAP (2016) Wound healing - a literature review. An Bras Dermatol 91(5):614–620. https://doi.org/10.1590/abd1806-4841.20164741

Gupton SL, Waterman-Storer CM (2006) Spatiotemporal feedback between actomyosin and focal-adhesion systems optimizes rapid cell migration. Cell 125(7):1361–1374. https://doi.org/10.1016/j.cell.2006.05.029

Hartman CD, Isenberg BC, Chua SG, Wong JY (2016) Vascular smooth muscle cell durotaxis depends on extracellular matrix composition. Proc Natl Acad Sci 113(40):11190–11195. https://doi.org/10.1073/pnas.1611324113

Horzum U, Ozdil B, Pesen-Okvur D (2014) Step-by-step quantitative analysis of focal adhesions. MethodsX 1:56–59. https://doi.org/10.1016/j.mex.2014.06.004

Hulmes DJS, Miller A (1979) Quasi-hexagonal molecular packing in collagen fibrils. Nature 282(5741):878–880. https://doi.org/10.1038/282878a0

Huttenlocher A, Horwitz AR (2011) Integrins in cell migration. Cold Spring Harb Perspect Biol 3(9):a005074–a005074. https://doi.org/10.1101/cshperspect.a005074

Jansen KA, Licup AJ, Sharma A, Rens R, MacKintosh FC, Koenderink GH (2018) The role of network architecture in collagen mechanics. Biophys J 114(11):2665–2678. https://doi.org/10.1016/j.bpj.2018.04.043

Joshi J, Mahajan G, Kothapalli CR (2018) Three-dimensional collagenous niche and azacytidine selectively promote time-dependent cardiomyogenesis from human bone marrow-derived MSC spheroids. Biotechnol Bioeng 115(8):2013–2026. https://doi.org/10.1002/bit.26714

Kim DH, Wirtz D (2013) Focal adhesion size uniquely predicts cell migration. FASEB J 27(4):1351–1361. https://doi.org/10.1096/fj.12-220160

Kim MC, Silberberg YR, Abeyaratne R, Kamm RD, Asada HH (2018) Computational modeling of three-dimensional ECM-rigidity sensing to guide directed cell migration. Proc Natl Acad Sci 115(3):E390–E399. https://doi.org/10.1073/pnas.1717230115

Kong F, García AJ, Mould AP, Humphries MJ, Zhu C (2009) Demonstration of catch bonds between an integrin and its ligand. J Cell Biol 185(7):1275–1284. https://doi.org/10.1083/jcb.200810002

Lee J, Abdeen AA, Zhang D, Kilian KA (2013) Directing stem cell fate on hydrogel substrates by controlling cell geometry, matrix mechanics and adhesion ligand composition. Biomaterials 34(33):8140–8148. https://doi.org/10.1016/j.biomaterials.2013.07.074

Mason DE, Collins JM, Dawahare JH, Nguyen TD, Lin Y, Voytik-Harbin SL, Zorlutuna P, Yoder MC, Boerckel JD (2019) YAP and TAZ limit cytoskeletal and focal adhesion maturation to enable persistent cell motility. J Cell Biol 218(4):1369–1389. https://doi.org/10.1083/jcb.201806065

McKenzie AJ, Hicks SR, Svec KV, Naughton H, Edmunds ZL, Howe AK (2018) The mechanical microenvironment regulates ovarian cancer cell morphology, migration, and spheroid disaggregation. Sci Rep 8(1):1–20. https://doi.org/10.1038/s41598-018-25589-0

Meehan S, Nain AS (2014) Role of suspended fiber structural stiffness and curvature on single-cell migration, nucleus shape, and focal-adhesion-cluster length. Biophys J 107(11):2604–2611. https://doi.org/10.1016/j.bpj.2014.09.045

Miroshnikova YA, Jorgens DM, Spirio L, Auer M, Sarang-Sieminski AL, Weaver VM (2011) Engineering strategies to recapitulate epithelial morphogenesis within synthetic three-dimensional extracellular matrix with tunable mechanical properties. Phys Biol 8(2):026013. https://doi.org/10.1088/1478-3975/8/2/026013

Moore SW, Roca-Cusachs P, Sheetz MP (2010) Stretchy proteins on stretchy substrates: the important elements of integrin-mediated rigidity sensing. Dev Cell 19(2):194. https://doi.org/10.1016/J.DEVCEL.2010.07.018

Moujaber O, Stochaj U (2020) The cytoskeleton as regulator of cell signaling pathways. Trends Biochem Sci 45(2):96–107. https://doi.org/10.1016/j.tibs.2019.11.003

Moure A, Gomez H (2018) Three-dimensional simulation of obstacle-mediated chemotaxis. Biomech Model Mechanobiol 17(5):1243–1268. https://doi.org/10.1007/s10237-018-1023-x

Nain AS, Sitti M, Jacobson A, Kowalewski T, Amon C (2009) Dry spinning based spinneret based tunable engineered parameters (step) technique for controlled and aligned deposition of polymeric nanofibers. Macromol Rapid Commun 30(16):1406–1412. https://doi.org/10.1002/marc.200900204

Nakazawa N, Sathe AR, Shivashankar GV, Sheetz MP (2016) Matrix mechanics controls FHL2 movement to the nucleus to activate p21 expression. Proc Natl Acad Sci USA 113(44):E6813–E6822. https://doi.org/10.1073/pnas.1608210113

Parsons JT, Horwitz AR, Schwartz MA (2010) Cell adhesion: integrating cytoskeletal dynamics and cellular tension. Nat Rev Mol Cell Biol 11(9):633–643. https://doi.org/10.1038/nrm2957

Ren X, Kiosses W, Sieg D, Otey C, Schlaepfer D, Schwartz M (2000) Focal adhesion kinase suppresses Rho activity to promote focal adhesion turnover. J Cell Sci 113(20):3673–3678. https://doi.org/10.1242/jcs.113.20.3673

Ridley AJ, Schwartz MA, Burridge K, Firtel RA, Ginsberg MH, Borisy G, Parsons JT, Horwitz AR (2003) Cell migration: integrating signals from front to back. Science 302(5651):1704–1709. https://doi.org/10.1126/science.1092053

Scarpa E, Mayor R (2016) Collective cell migration in development. J Cell Biol 212(2):143–155. https://doi.org/10.1083/jcb.201508047

Selhuber-Unkel C, Erdmann T, López-García M, Kessler H, Schwarz U, Spatz J (2010) Cell adhesion strength is controlled by intermolecular spacing of adhesion receptors. Biophys J 98(4):543–551. https://doi.org/10.1016/j.bpj.2009.11.001

Sheets K, Wang J, Meehan S, Sharma PCNG, Khan M, Koons B, Behkam B, Nain AS (2013) Cell-fiber interactions on aligned and suspended nanofiber scaffolds. J Biomater Tissue Eng 3(4):355–368. https://doi.org/10.1166/jbt.2013.1105

Sheets K, Wunsch S, Ng C, Nain AS (2013) Shape-dependent cell migration and focal adhesion organization on suspended and aligned nanofiber scaffolds. Acta Biomater 9(7):7169–7177. https://doi.org/10.1016/j.actbio.2013.03.042

Sieg D, Hauck C, Schlaepfer D (1999) Required role of focal adhesion kinase (FAK) for integrin-stimulated cell migration. J Cell Sci 112(16):2677–2691. https://doi.org/10.1242/jcs.112.16.2677

Thiam HR, Vargas P, Carpi N, Crespo CL, Raab M, Terriac E, King MC, Jacobelli J, Alberts AS, Stradal T, Lennon-Dumenil AM, Piel M (2016) Perinuclear Arp2/3-driven actin polymerization enables nuclear deformation to facilitate cell migration through complex environments. Nat Commun. https://doi.org/10.1038/ncomms10997

Tozluoğlu M, Tournier AL, Jenkins RP, Hooper S, Bates PA, Sahai E (2013) Matrix geometry determines optimal cancer cell migration strategy and modulates response to interventions. Nat Cell Biol 15(7):751–762. https://doi.org/10.1038/ncb2775

Van Der Rijt JA, Van Der Werf KO, Bennink ML, Dijkstra PJ, Feijen J (2006) Micromechanical testing of individual collagen fibrils. Macromol Biosci 6(9):697–702. https://doi.org/10.1002/MABI.200600063

Vicente-Manzanares M, Zareno J, Whitmore L, Choi CK, Horwitz AF (2007) Regulation of protrusion, adhesion dynamics, and polarity by myosins IIA and IIB in migrating cells. J Cell Biol 176(5):573–580. https://doi.org/10.1083/jcb.200612043

Wang T, Hamilla S, Cam M, Aranda-Espinoza H, Mili S (2017) Extracellular matrix stiffness and cell contractility control RNA localization to promote cell migration. Nat Commun 8(1):896. https://doi.org/10.1038/s41467-017-00884-y

Webb DJ, Parsons JT, Horwitz AF (2002) Adhesion assembly, disassembly and turnover in migrating cells - over and over and over again. Nat Cell Biol 4(4):E97–E100. https://doi.org/10.1038/ncb0402-e97

Webb DJ, Donais K, Whitmore LA, Thomas SM, Turner CE, Parsons JT, Horwitz AF (2004) FAK-Src signalling through paxillin, ERK and MLCK regulates adhesion disassembly. Nat Cell Biol 6(2):154–161. https://doi.org/10.1038/ncb1094

Wells RG (2008) The role of matrix stiffness in regulating cell behavior. Hepatology 47(4):1394–1400. https://doi.org/10.1002/hep.22193

Weng S, Shao Y, Chen W, Fu J (2016) Mechanosensitive subcellular rheostasis drives emergent single-cell mechanical homeostasis. Nat Mater 15(9):961–967. https://doi.org/10.1038/nmat4654

Wolf K, te Lindert M, Krause M, Alexander S, te Riet J, Willis AL, Hoffman RM, Figdor CG, Weiss SJ, Friedl P (2013) Physical limits of cell migration: control by ECM space and nuclear deformation and tuning by proteolysis and traction force. J Cell Biol 201(7):1069–1084. https://doi.org/10.1083/jcb.201210152

Yamada KM, Sixt M (2019) Mechanisms of 3D cell migration. Nat Rev Mol Cell Biol 20(12):738–752. https://doi.org/10.1038/s41580-019-0172-9

Yang C, DelRio FW, Ma H, Killaars AR, Basta LP, Kyburz KA, Anseth KS (2016) Spatially patterned matrix elasticity directs stem cell fate. Proc Natl Acad Sci USA 113(31):E4439–E4445. https://doi.org/10.1073/pnas.1609731113

Yeung T, Georges PC, Flanagan LA, Marg B, Ortiz M, Funaki M, Zahir N, Ming W, Weaver V, Janmey PA (2005) Effects of substrate stiffness on cell morphology, cytoskeletal structure, and adhesion. Cell Motil Cytoskelet 60(1):24–34. https://doi.org/10.1002/cm.20041

Yue PYK, Leung EPY, Mak NK, Wong RNS (2010) A simplified method for quantifying cell migration/wound healing in 96-well plates. J Biomol Screen 15(4):427–433. https://doi.org/10.1177/1087057110361772

Appendix B

Dynamic biaxial loading of vascular smooth muscle cell seeded tissue equivalents

published in

Journal of the Mechanical Behavior of Biomedical Materials, vol. 157, 2024. DOI: 10.1016/j.jmbbm.2024.106639.

journal of the mechanical behavior of biomedical materials 157 (2024) 106639

Contents lists available at ScienceDirect

Journal of the Mechanical Behavior of Biomedical Materials

journal homepage: www.elsevier.com/locate/jmbbm

Research paper

Dynamic biaxial loading of vascular smooth muscle cell seeded tissue equivalents

Daniel Paukner [a,b,c,1], Isabella R. Jennings [c,1], Christian J. Cyron [a,b], Jay D. Humphrey [c,*]

[a] Institute for Continuum and Material Mechanics, Hamburg University of Technology, Hamburg, Germany
[b] Institute of Material Systems Modeling, Helmholtz-Zentrum Hereon, Geesthacht, Germany
[c] Department of Biomedical Engineering, Yale University, New Haven, CT, USA

ARTICLE INFO

Keywords:
Tissue engineering
Tensional homeostasis
Cell–matrix interaction
Biaxial testing
Cell-seeded collagen gels
Mechanobiology

ABSTRACT

An intricate reciprocal relationship exists between adherent synthetic cells and their extracellular matrix (ECM). These cells deposit, organize, and degrade the ECM, which in turn influences cell phenotype via responses that include sensitivity to changes in the mechanical state that arises from changes in external loading. Collagen-based tissue equivalents are commonly used as simple but revealing model systems to study cell–matrix interactions. Nevertheless, few quantitative studies report changes in the forces that the cells establish and maintain in such gels under dynamic loading. Moreover, most prior studies have been limited to uniaxial experiments despite many soft tissues, including arteries, experiencing multiaxial loading *in vivo*. To begin to close this gap, we use a custom biaxial bioreactor to subject collagen gels seeded with primary aortic smooth muscle cells to different biaxial loading conditions. These conditions include cyclic loading with different amplitudes as well as different mechanical constraints at the boundaries of a cruciform sample. Irrespective of loading amplitude and boundary condition, similar mean steady-state biaxial forces emerged across all tests. Additionally, stiffness-force relationships assessed via intermittent equibiaxial force–extension tests showed remarkable similarity for ranges of forces to which the cells adapted during periods of cyclic loading. Taken together, these findings are consistent with a load-mediated homeostatic response by vascular smooth muscle cells.

1. Introduction

Many cell types are embedded *in vivo* within a three-dimensional extracellular matrix (ECM), a network of constituents that often includes different fibrillar collagens and proteoglycans as well as elastic fibers (Hynes and Naba, 2012). Besides endowing tissues with overall structural support, the ECM provides biochemical and biomechanical cues to resident and infiltrating cells. Changes in the composition, properties, and mechanical state of the ECM can thus influence diverse cell behaviors (Lukashev, 1998; Wells, 2008), including differentiation (Engler et al., 2006), proliferation (Klein et al., 2009), migration (Wolf et al., 2013), and survival (Wang et al., 2000). Cell–matrix interactions are typically dictated by mechanotransduction in development, health, and disease (Humphrey et al., 2014; Yamada et al., 2022).

Reduced model systems called tissue equivalents were introduced decades ago to simplify the study of cell–matrix interactions (Bell et al., 1979). Most tissue equivalents are based on collagen hydrogels, as collagen is the predominant structural protein in mammals. Even basic unloaded and unconstrained models have proven useful for studying how cells remodel the ECM, often by compacting initially low-stress isotropic gels (Redden and Doolin, 2003; Simon et al., 2014). More complex experimental systems can subject uniaxial cell-seeded collagen gels to static (Brown et al., 1998; Ezra et al., 2010; Hu et al., 2013) or dynamic (Lee et al., 2018; Walker et al., 2020; Wille et al., 2006) loading. Some of these devices can also measure the forces generated by the embedded cells. This led to the seminal finding of tensional homeostasis, the phenomenon whereby cells appear to establish and maintain a preferred state of tension (force per length) or stress (force per area), which can be maintained even when external perturbations (displacements or forces) are imposed (Brown et al., 1998).

Yet, because most soft tissues are subjected *in vivo* to multiaxial loading or constraints, biaxial bioreactors are necessary to mimic these conditions more closely. For example, vascular smooth muscle cells (VSMCs) are crucial for ensuring proper function of the aorta through their responses to changes in mechanical loading. VSMC responses include changes in the deposition, organization, and degradation of their ECM. Under normal conditions, VSMCs in many arteries (including the

* Corresponding author.
E-mail addresses: daniel.paukner@tuhh.de (D. Paukner), jay.humphrey@yale.edu (J.D. Humphrey).
[1] These authors contributed equally.

https://doi.org/10.1016/j.jmbbm.2024.106639
Received 26 March 2024; Received in revised form 18 June 2024; Accepted 18 June 2024
Available online 22 June 2024

descending thoracic aorta and abdominal aorta) experience a cyclic circumferential stretch caused by the pulsatile distension of the vessel during each cardiac cycle but little to no cyclic axial stretch. The associated cyclic axial stress yet appears to contribute significantly to aortic homeostasis and remodeling (Humphrey et al., 2009); indeed, changes in axial loading can elicit rapid and dramatic responses (Gleason and Humphrey, 2005a).

Different types of biaxial bioreactors have been developed to mimic the multiaxial nature of the *in vivo* environment and to study effects of mechanical loading and boundary conditions by performing stress–strain tests on cell-seeded tissue equivalents. For example, Hu et al. (2013) compared effects of static equibiaxial and strip-biaxial loading on the mechanical properties of tissue equivalents whereas Lee et al. (2018) studied effects of dynamic cyclic equibiaxial loading. Other studies have quantified induced changes in the alignment of cells and ECM fibers in response to stretch (Chen et al., 2018; Gould et al., 2012) or sought to improve the mechanical properties of tissue-engineered constructs, particularly to yield better functionality (Mol et al., 2005; Seliktar et al., 2001; Shearn et al., 2007).

We previously developed a computer-controlled biaxial bioreactor that can measure cell-generated forces in response to prescribed static or dynamic boundary conditions imposed via four micro-stepper motors (Eichinger et al., 2020), with tests including uniaxial, strip-biaxial, equibiaxial, and non-equibiaxial stretching (Fig. A.10). Of importance herein, a strip biaxial protocol holds the sample at a constant overall stretch along one axis while cyclically stretching in the orthogonal axis, which resembles mechanical constraints experienced by VSMCs over a cardiac cycle in most segments of the aorta. We used this device to examine force generation by primary murine aortic SMCs subjected to dynamic loading conditions that are motivated by physiological conditions. Cruciform, VSMC-seeded collagen gels were subjected to two primary loading conditions. First, effects of increased biaxial stresses/stretches were examined using cyclic equibiaxial loading of different amplitudes. Second, effects of cyclic equibiaxial (biaxial stress and stretch) versus cyclic strip-biaxial (biaxial stress but not stretch) loading were examined while keeping the amplitude of the primary stretching the same. To the best of our knowledge, this is the first quantification and comparison of diverse types of cyclic loading of VSMC-seeded tissue equivalents, particularly using *in vivo* relevant conditions having implications to multiaxial tensional homeostasis.

2. Methods

2.1. Primary cell isolation and culture

Primary aortic SMCs of mesoderm lineage were isolated from the descending thoracic aorta, suprarenal abdominal aorta, and infrarenal abdominal aorta from ~13-week-old male C57BL/6J mice that were euthanized for a different study, with all live animal care and use approved by the Yale Institutional Animal Care and Use Committee. Toward this end, the aorta was excised from the left subclavian artery to the aorto-iliac bifurcation, cleaned, and subjected to an enzyme dispersion method to isolate the cells (Proudfoot and Shanahan, 2012). The digestion solution consisted of HBSS (with Ca^{2+} and Mg^{2+}, Gibco), collagenase type IV (1 mg/ml, Gibco), elastase (0.744 U/ml, Sigma-Aldrich), soybean trypsin inhibitor (1 mg/ml, Sigma-Aldrich), and penicillin-streptomycin (1% v/v, Gibco). Following partial digestion of the ECM for 10 min at room temperature, the aorta was transferred to a complete culture medium of 20% fetal bovine serum (FBS, Sigma-Aldrich) in DMEM (Sigma-Aldrich) for 2-3 min to neutralize the digestion solution. The adventitia was then removed using forceps, the wall was cut open, and the endothelial cell layer was denuded. The remaining medial layer was then sliced into small pieces and placed in an Eppendorf tube containing the same digestion solution. After 1 h of incubation at 37 °C to digest the ECM and disperse the cells, the cell suspension was neutralized again with complete medium before being centrifuged to collect the cell pellet for seeding onto fibronectin-coated culture plates. Aortas of five different mice were used and kept separate during the isolation and expansion process. Cells were stained for smooth muscle α-actin to confirm cell type, noting that separate adventitial-derived fibroblasts did not stain with smooth muscle α-actin.

The VSMCs were maintained in a humidified incubator at 5% CO_2 and 37 °C. Their first medium change occurred three days after seeding, then all other medium changes were performed every other day. The cells were expanded using complete medium until passage 3, when they were frozen using a freezing medium composed of 90% complete medium and 10% DMSO and transferred to liquid nitrogen for long-term storage.

2.2. Gel preparation

One week before each experiment, cells were thawed and seeded in collagen-coated (40 μg/ml) culture flasks and maintained in a humidified incubator at 5% CO_2 and 37 °C with 10% FBS in DMEM. The cells were starved 24 h prior to the experiment by reducing FBS to 2% to reduce cell proliferation and effects of growth factors and hormones.

Collagen gels were prepared following the protocol described in Eichinger et al. (2020). Briefly, 1.414 ml of 5X DMEM (Gibco), 0.676 ml of 10X reconstitution buffer (0.1 M NaOH and 20 mM HEPES, Sigma-Aldrich), and 0.852 ml of high concentration type I rat tail collagen (8.22 mg/mL, Corning) were mixed with 4.058 mL of complete medium containing 2% FBS. Gels were kept on ice during preparation to prevent premature polymerization of the collagen. In the VSMC-seeded collagen gels, the medium contained 2.45×10^6 cells, resulting in a final cell density of 0.35×10^6 cells/ml of gel. For all experiments, cells were at passage 4.

2.3. Biaxial mechanical testing

For testing in our biaxial bioreactor (Eichinger et al., 2020), the collagen gels were poured into a cruciform mold with four porous attachments to the loading system already in place (Fig. 1A). The gel polymerized for 30 min before filling the bioreactor bath with 80 mL of 2% FBS medium, after which the mold was removed. With the initially stress-free gel floating and attached to the force transducers, we initiated the computer-controlled loading protocol and began force measurement. Cell-generated forces were measured using two identical force transducers, one per stretching axis, each with a range of 0–5 mN (SI-H KG7, World Precision Instruments). Typical forces ranged from 0–1 mN. Overall displacements at the ends of the four arms of the cruciform samples were applied via four micro-stepper motors (Advanced Micro Systems), each with a resolution of approximately 1 μm. Prior and preliminary studies suggested that there was firm attachment of the gels within the porous attachments, with no slippage. See Eichinger et al. (2020) for further details on the experimental system.

All loading protocols were divided into the same three phases (see Fig. 1B). First, the gel was maintained in its original configuration for ~15 h to allow the cells to attach to the collagen matrix and establish steady-state values of biaxial force. Second, a quasi-static force–extension test was performed whereby the gel was subjected to a 10% equibiaxial stretch over 10 min and then returned to 0% stretch (the state achieved after the 15-h initialization phase) over 10 min, thus yielding a constant stretch rate of 1.67×10^{-4} s^{-1} (defined as change in overall length per reference length per time). Third, the gel was subjected to a seven-hour cycling period, with either equibiaxial or strip-biaxial stretching. These last two phases – force–extension test and cyclic loading – formed an experimental interval that was repeated seven times. Combined with the initialization phase and the force–extension tests, this results in a total computer-controlled duration of approximately 66 h per gel.

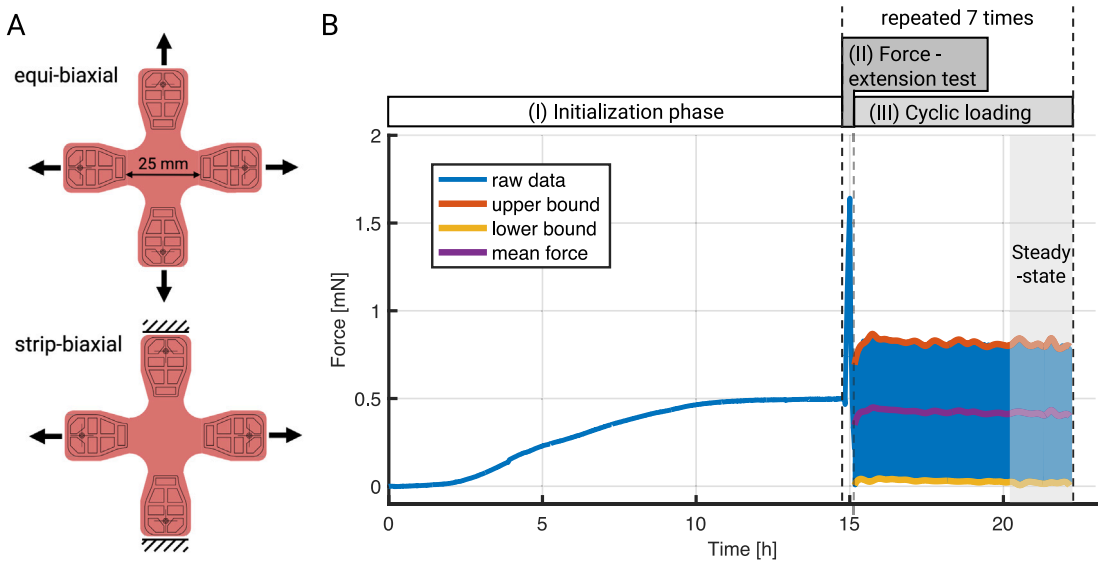

Fig. 1. Illustration of boundary conditions and loading protocols. (A) Equibiaxial (top) and strip-biaxial (bottom) loading conditions with porous fixtures at the ends of the four arms of the cruciform samples (pink) allowing the gels to be coupled easily to the four motor-controlled arms and two force transducers (one per axis). (B) The loading protocols consisted of three phases: (I) initialization, (II) force–extension testing, and (III) cyclic loading. The initialization phase lasted approximately 15 h and allowed the cells to attach to the collagen matrix and establish a steady-state biaxial force. The intermittent, quasi-static, equibiaxial force–extension tests consisted of a 10-min loading phase from 0% stretch to 10% superimposed stretch, then a 10-min unloading phase back to 0% stretch, each relative to the state established at the end of the initialization phase. The subsequent cyclic loading periods lasted seven hours each, with a force–extension test repeated after each cyclic loading period. To investigate effects of cyclic stretch amplitude, we compared 5% and 10% equibiaxial stretching; to examine the impact of different boundary conditions, a 5% strip-biaxial loading was included whereby one direction was cyclically stretched while the orthogonal direction remained at a fixed length. The last two phases – the force–extension test and cyclic loading – formed an interval that was repeated seven times. The blue line represents the preprocessed force measurements of one axis for a representative experiment; the orange, purple, and yellow curves correspond to the maximum, mean, and minimum force values during a cycling period, respectively, with force amplitude defined as the maximum minus minimum values.

Three different types of cyclic loading periods were compared. To examine effects of cycle amplitude, we performed 5% and 10% equibiaxial stretching protocols wherein both axes were stretched equally and simultaneously. Additionally, we performed strip-biaxial protocols wherein one axis was cyclically stretched 5% while the other was held at a fixed length, which allowed direct comparison to the 5% equibiaxial stretching protocol. The strip-biaxial test was chosen to mimic the mechanical conditions of the descending thoracic and abdominal aorta, in which there is little to no cyclic axial stretch but a consistent cyclic circumferential stretch due to the pulse wave originating from the heart (Bäck et al., 2013). It is important to note that both types of stretching protocols result, on average, in cyclic changes in biaxial stress while only the equibiaxial stretching protocol results, on average, in both cyclic stress and stretch (Humphrey et al., 2008). See Figs. A.11 and A.12 for additional qualitative insight into the stress and strain fields that can develop in the cruciform gels. The 5% cyclic loading was performed at a frequency of 0.5 Hz, whereas the 10% cyclic loading was performed at 0.25 Hz to maintain the stretch rate the same across protocols (0.05 s^{-1}). Albeit well less than the *in vivo* stretch rate in a mouse aorta, these rates are similar to those used in *ex vivo* studies on intact segments of the aorta (Ferruzzi et al., 2013). Control studies were repeated with acellular collagen gels under the same conditions. The loading conditions, the number of experiments performed per condition, and the abbreviations used in the following sections are summarized in Table 1.

2.4. Data (pre-)processing

The force transducers were sensitive to changes in temperature and humidity, which inevitably occur during the setup of the experiment when opening the incubator that housed the biaxial testing device. To eliminate this equilibration behavior during the initialization phase, we first computed the average forces for each transducer during the initialization phase of all acellular gels. These transducer-specific average values were then subtracted from the initialization phases of both the cellular and acellular experiments. For the time after the initialization phase, the force values were corrected with a constant value based on the last value of the transducer-specific average values. The preprocessed data were then analyzed using a custom MATLAB script. Briefly, the data were split into the three different periods: (I) initialization, (II) force–extension testing, and (III) cyclic loading. The amplitude, A_i, during each cyclic loading period, $i \in [1, 7]$, was computed using MATLAB's *envelope()* method to extract upper (f_i^{high}) and lower (f_i^{low}) values, thus yielding the difference called force amplitude $A_i = f_i^{high} - f_i^{low}$. Mean force during each cyclic loading period was computed as $f_i = f_i^{low} + 0.5 \cdot A_i$. The different quantities – upper, lower, and mean force – are illustrated in Fig. 1B.

2.5. Data and statistical analysis

To compare effects of the different loading conditions quantitatively, we focused on average steady-state values of the mean forces and

Table 1
Summary of the three loading conditions for VSMC-seeded gels (for strip-biaxial tests, cyc denotes cyclic stretching, stat denotes the static axis), two of which were also used for acellular gels.

Testing protocol	Notation Protocol (n)	Axis-specific notation (Axis 1 vs. Axis 2)
Equibiaxial (E), 5% stretch amplitude	E5 (n = 5)	E5-1, E5-2
Equibiaxial (E), 10% stretch amplitude	E10 (n = 3)	E10-1, E10-2
Strip-biaxial (S), 5% stretch amplitude	S5 (n = 4)	S5-cyc, S5-stat
Equibiaxial (E), 5% stretch amplitude, Acellular	E5A (n = 4)	E5A-1, E5A-2
Strip-biaxial (S), 5% stretch amplitude, Acellular	S5A (n = 4)	S5A-cyc, S5A-stat

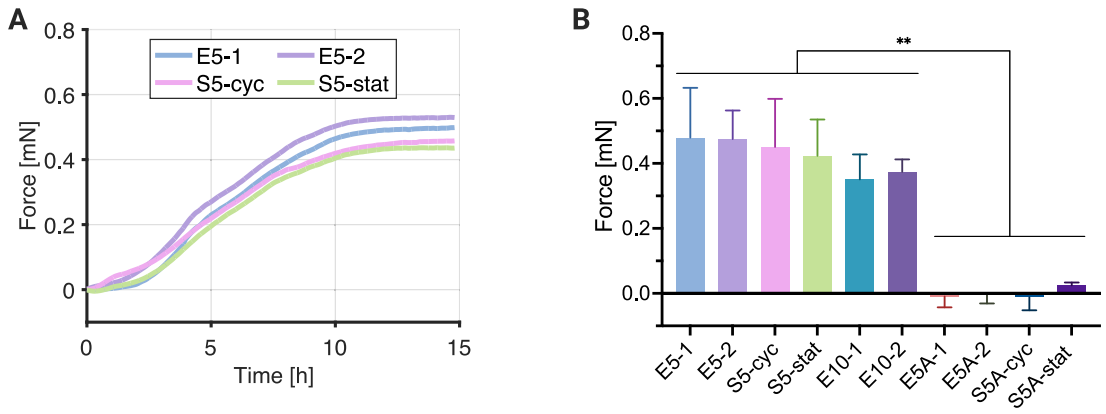

Fig. 2. Biaxial forces during and at the end of the ~15-h initialization phase. (A) Force evolution in the 1 and 2 directions for representative 5% equibiaxial (E5) and 5% strip-biaxial (S5) stretching experiments. (B) As expected, cellular gels generated significant biaxial forces during the initialization phase whereas acellular gels (denoted by A-1,2, cyc, or stat) generated negligible forces. Values of force on the ordinate represent axis-specific mean values calculated from the final two hours of initialization (**$p < 0.01$). See Table 1 for the nomenclature, with E5 or E10 denoting equibiaxial stretching of 5 or 10% and S5 denoting strip-biaxial stretching of 5% while the orthogonal direction remained static.

their amplitudes. The steady-state force at the end of the initialization phase was determined by averaging the measured values over the last two hours before beginning the first force–extension test. To compare cellular behaviors during cyclic loading, we used average values of force from the final two hours of each interval when both the mean forces and amplitudes had stabilized. A one-way or two-way repeated measures ANOVA with Tukey post-hoc testing was used for statistical comparisons of the different loading conditions. All statistical analysis was performed using GraphPad Prism 10, and results are reported as mean ± standard deviation unless noted otherwise.

3. Results

3.1. Initialization phase

Biaxial force generation was negligible in all acellular gels during the initialization phase. By contrast, there was significant force generation in all VSMC-seeded gels during this phase, with unremarkable differences between axis 1 and axis 2 across the various loading protocols (Fig. 2A). For this reason, average values of force (i.e., (axis 1 + axis 2)/2) are presented below for all equibiaxial experiments. Moreover, although these forces were slightly lower in the gels destined for 10% equibiaxial experiments (E10-1 and E10-2), these differences did not reach statistical significance when compared to all experiments involving cells (Fig. 2B). By contrast, mean forces observed in acellular gels were statistically different from those observed in cellular gels.

3.2. Cyclic loading periods

3.2.1. Consistent behavior within each loading period

Within each cyclic loading period, that is, the seven hours following each intermittent force–extension test, the cells tended to establish a new steady-state value of both force amplitude and mean force, irrespective of the cycle amplitude and boundary condition (Fig. 3). As expected, the initial force amplitude in the first interval of the E10 experiments was approximately twice as high as in the first interval of the E5 experiments (because the stretch was twice as high); it then gradually decreased and approached a value similar to the E5 experiments. Furthermore, in the E5 and S5 experiments, force amplitudes and mean forces tended to exhibit an initial increase during the first two to three hours of each cyclic loading period, suggesting further active cellular contributions. By contrast, in the E10 experiments, force amplitudes and mean forces remained largely stable over each seven-hour cyclic loading period, except during the first interval, where a decrease was observed. Compared to cellular gels, acellular gels exhibited smaller force amplitudes (Fig. B.13A) and mean forces (Fig. B.13B), each of which remained relatively constant during the experiments.

3.2.2. Steady-state force amplitudes

Analysis of the force amplitude during the final two hours of each cyclic loading period revealed that although E10 experiments tended to have the largest amplitudes, they were not statistically different from the E5 experiments (Fig. 4A). As expected, the static axis of the S5 experiment, denoted S5-stat, exhibited the smallest force amplitude and this difference was statistically significant compared with amplitudes across all intervals. A noteworthy trend observed in all VSMC-seeded gels was a decreasing amplitude from one interval to the next. In contrast, acellular amplitudes remained constant over time, albeit at a lower value (Fig. B.14A).

To assess in-plane coupling in the strip-biaxial experiments, we calculated the ratio of the force amplitude in the static axis to the amplitude in the cycled axis. In both cases, cellular and acellular, this ratio remained nearly constant over the seven intervals of study (Fig. 4B). However, the VSMC-seeded gels exhibited a significantly higher in-plane coupling compared to acellular gels.

3.2.3. Mean steady-state forces

Despite significant differences in steady-state force amplitudes in the cellular experiments (Fig. 4A), there were no statistically significant differences in steady-state mean forces across the different intervals and loading protocols (Fig. 5A). Of particular note, the force generated in the static axis of the strip-biaxial experiment closely approximated that generated in the cycled axis. The mean forces in the acellular experiments were lower than those in the VSMC-seeded gels (Fig. B.14B). Notably, both cellular and acellular experiments experienced a reduction in force from one interval to the next. This trend was more pronounced in cellular experiments, however.

To investigate whether there was a common underlying trend in the evolution of steady-state forces in the VSMC-seeded gels, we normalized the steady-state mean values by the force at the end of the initialization phase. This revealed that the behavior for all loading conditions was nearly identical (Fig. 5B), including for the E10 experiments that had a slightly lower mean force at the end of the initialization phase (Fig. 2B).

To quantify the absolute reduction in force during the experiments, we calculated the difference between the force in the initialization phase and the last interval (Fig. 6A). Cellular gels exhibited a considerably larger decrease in the average mean force when compared to acellular gels. Interestingly, the reduction in mean force appeared to be independent of the loading condition in cellular experiments, suggesting a common underlying cell-mediated mechanism. A statistically significant difference in mean force reduction became evident when comparing cellular (E5, S5) and acellular (E5A, S5A) experiments

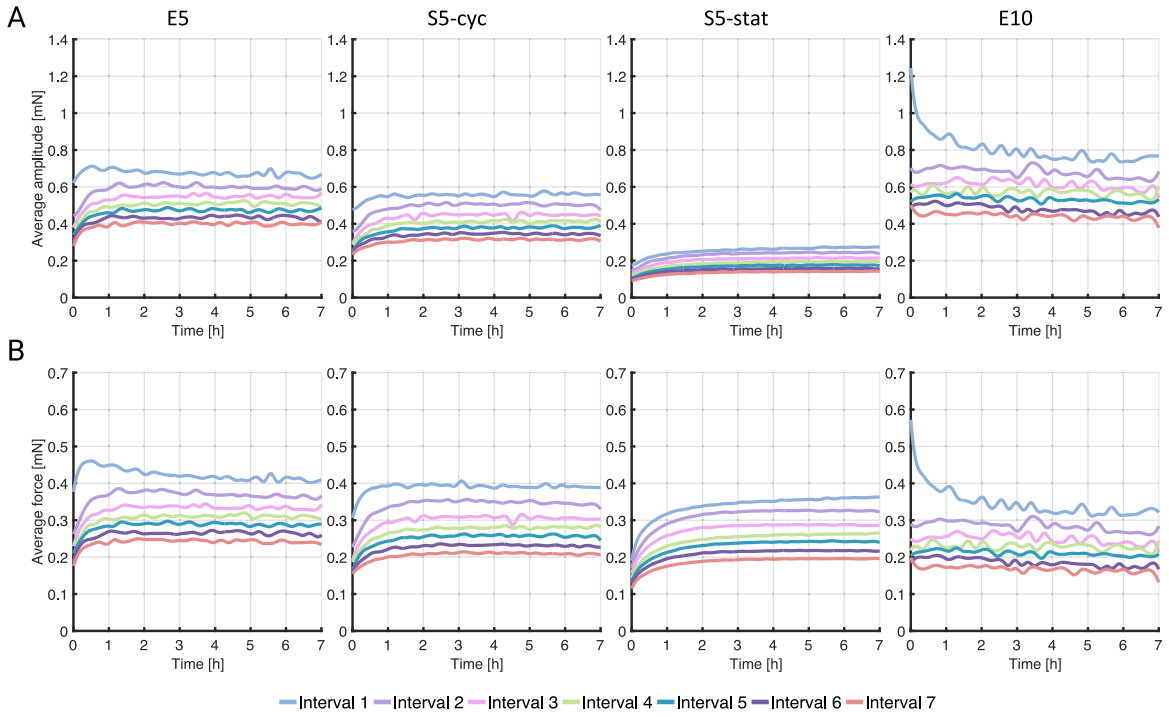

Fig. 3. Average values, that is, (axis 1 + axis 2)/2, of both force amplitude (A) and mean force (B) in VSMC-seeded gels during the seven, seven-hour cyclic loading periods. Referring to the nomenclature in Table 1, results are presented from left-to-right for the 3 experimental protocols for the VSMC-seeded gels, with periods 1–7 denoted by different colors: 1 – light blue, 2 – light purple, 3 – pink, 4 – green, 5 – blue, 6 – purple, 7 – red.

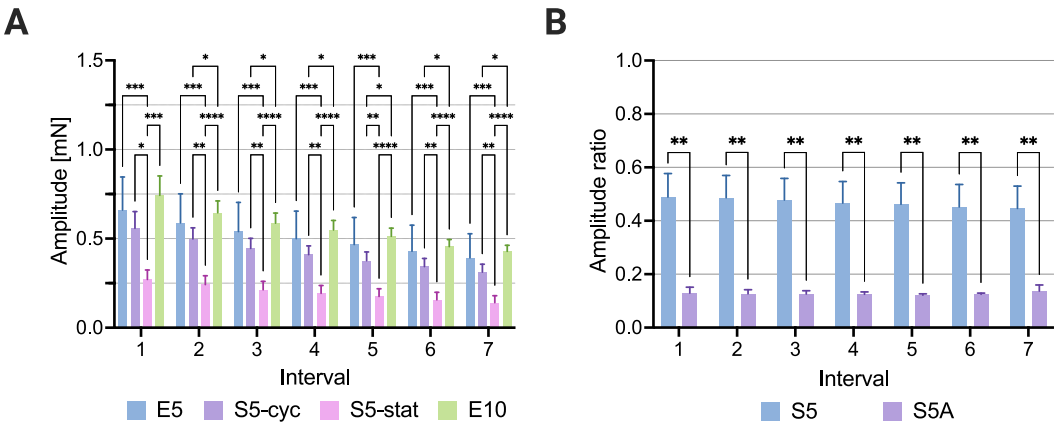

Fig. 4. Evolution of steady-state force amplitudes in VSMC-seeded collagen gels. (A) Steady-state amplitudes were calculated from the last two hours of each of the seven cyclic loading periods. Regardless of the magnitude of stretch imposed during cyclic loading, E5 and E10 showed similar steady-state amplitudes. The amplitude of the static axis in the strip-biaxial experiment was significantly different from all other amplitudes. (B) The ratio of the force amplitude in the static axis to that in the cycled axis was significantly higher in the cellular (S5) than in the acellular (S5A) strip-biaxial experiments, revealing an increased in-plane coupling in VSMC-seeded gels. The ratio remains nearly constant over time in both cases. (* $p < 0.05$, ** $p < 0.01$, *** $p < 0.001$, **** $p < 0.0001$).

(Fig. 6B). This eliminated transducer drift as the only cause as this should have affected both cellular and acellular experiments in a similar way. Additionally, transducer drift would be expected to show a continuous decrease in force, whereas the observed changes occurred in a step-like manner.

3.3. Equibiaxial force–extension tests

Before presenting results of the force–extension tests (FET), it is important to note that these tests do not necessarily begin from a stress-free configuration. Consequently, forces at zero imposed stretch are above zero for cellular gels (Fig. 7A–D) and either at or slightly below zero for acellular gels (Fig. 7E–H).

The first force–extension test in all cellular gels exhibited an almost linear relationship, though with a slight negative curvature in some cases indicating a stiffer behavior at low stretches and more compliant behavior at higher stretches (similar observations have been reported by others (Wagenseil et al., 2003; Wille et al., 2006) and is common in many elastomers). Nevertheless, the force-stretch relationship in the VSMC-seeded gels appeared nearly linear, while the acellular gels exhibited more of a nonlinear behavior. In both cases, cellular and acellular, there was no discernable difference between E5 and S5 experiments, with the static and cycled axes displaying similar behaviors during the equibiaxial force–extension tests. In the case of the E10 experiment, however, there was a notable reduction in stiffness (evidenced by the decreased slope of the curve) in the second force–extension test, which occurred after the first cyclic loading period. This

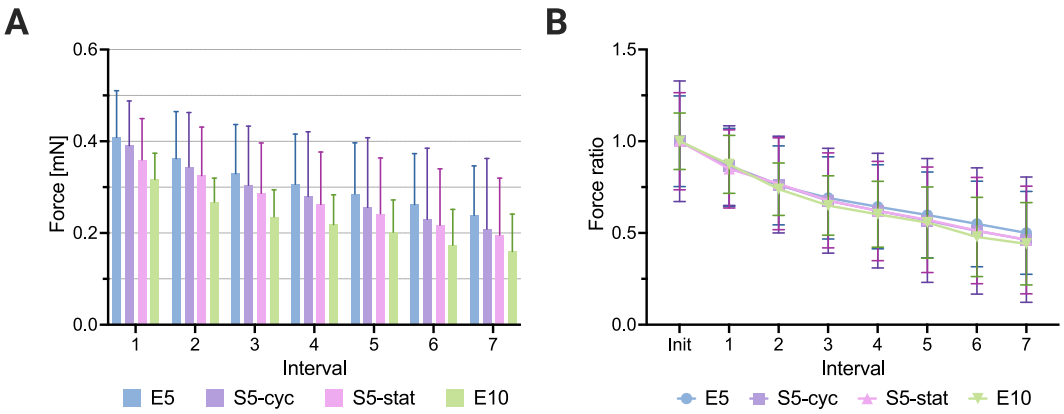

Fig. 5. Evolution of steady-state mean forces in VSMC-seeded collagen gels. (A) Average steady-state values of the mean forces were calculated from the last two hours of each loading interval. The steady-state forces decreased from interval to interval regardless of loading condition, and the forces of the static and cycled axes of the strip-biaxial experiment were comparable. (B) The force ratio was computed as the average force during the last two hours of an interval divided by the average force during the last two hours of the initialization phase. The graph reveals a similar trend for all loading conditions, potentially indicating a common underlying mechanism. Albeit not shown, a similar decrease was observed in pilot studies without intermediate force–extension testing.

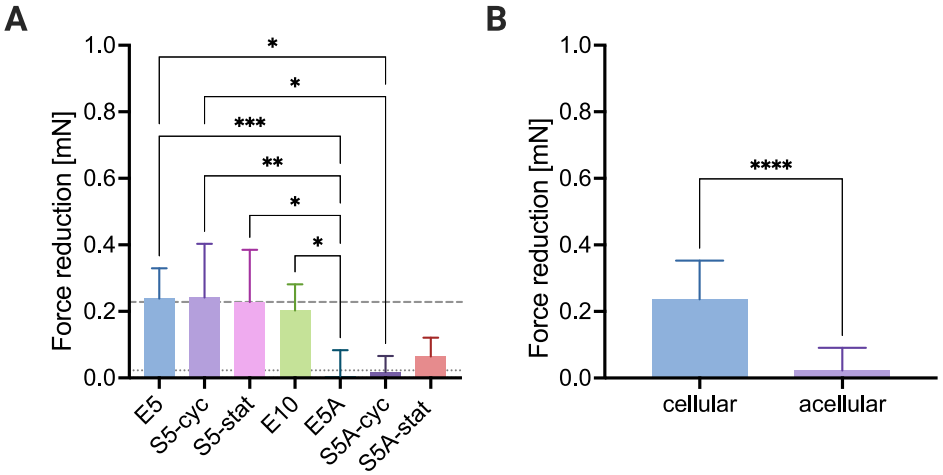

Fig. 6. Reduction in mean force from initialization phase to last cyclic loading interval. (A) Reduction in mean force between the end of the initialization phase and the end of the last (seventh) cyclic loading period for each loading condition. The dotted line represents the average value of all acellular experiments, and the dashed line represents the average value of all cellular experiments. (B) Comparing acellular (E5A, S5A) and cellular (E5, S5) experiments revealed a statistically significant difference (unpaired t-test). (*$p < 0.05$, **$p < 0.01$, *** $p < 0.001$, ****$p < 0.0001$).

reduction persisted in subsequent force–extension tests. Additionally, both acellular and cellular gels exhibited a continuous decrease in peak mean forces up to the 5th force–extension test, after which the force-stretch curves tended to stabilize.

Fig. 8A provides a visual representation of average loading and unloading curves for the second force–extension test of the E5 (blue curves) and E10 (green curves) experiments. The E10 experiment exhibited a distinct behavior compared to the other loading conditions, which is also evident from Fig. 7A–D. This was confirmed by fitting a linear relation to the loading curves to estimate the stiffness. Although the loading curves were not linear, this indicated a significant softening of the E10 gels (Fig. 8B).

Energy storage is determined as the area under the unloading curve (Fig. 8C), which remained nearly constant after the second force–extension test. Note that the E10 experiments exhibited significantly lower energy storage and dissipation than the other experiments after the first cyclic loading period. It is important to mention the difference in stored energy between the first E5 force–extension test and the first E10 force–extension test. Ideally, there should be no significant difference, but one possible explanation for this discrepancy could be the slight variation in the initialization force, which led to increased energy storage in the E5 experiments.

Dissipated energy is calculated as the area between the loading and unloading curves (Fig. 8D). This dissipation progressively decreased from one force–extension test to the next, as is common in tissue preconditioning. Experiments with a 10% cycle amplitude (E10) showed a significantly reduced energy dissipation from force–extension test 2 onward.

Fig. 9A plots mean stiffness vs. mean force generation for the first, third, fifth, and seventh force–extension tests (FET 1 through 7). Note the decreasing stiffness with increasing force in FET 1, which followed the 15-h static initialization phase. The subsequent tests, each following 7-h periods of cyclic loading, showed a marked difference: the nearly linear stiffness-force relationship changed its slope from negative (FET 1) to positive or zero (FETs 2–7) and separated into two linear regimes for the E5 and S5 experiments and one linear regime for the E10 experiment. It may be that E10 gels did not reach the same levels of force as the other loading conditions since they had already adapted to a 10% stretch during the cyclic loading periods. Regardless, the first linear regime was nearly identical for all loading conditions, whereas the second regime diverged slightly. The force at which the first linear regime transitioned into the second one coincided approximately with the maximum force that the gels had experienced during the last two hours of the previous cyclic loading period (Fig. 9B).

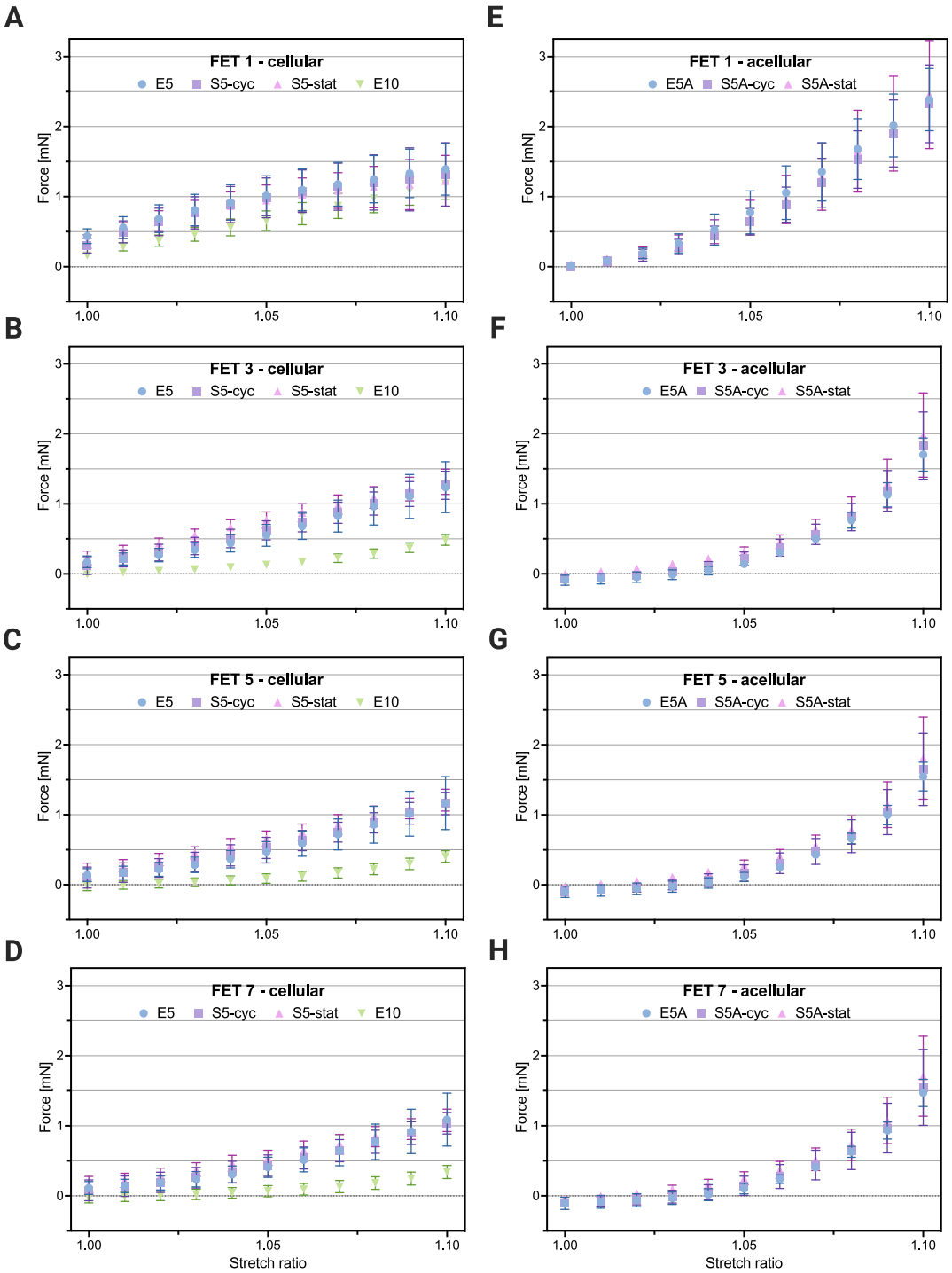

Fig. 7. Loading curves of selected intermediate force–extension tests (FETs). Shown are loading curves for FETs 1, 3, 5, and 7. The left column (A–D) shows results for VSMC-seeded gels and the right column (E–H) shows results for acellular gels. Acellular gels exhibited a more nonlinear force-stretch relationship, while VSMC-seeded gels exhibited a more linear behavior.

In contrast to the two distinct linear regimes observed in the VSMC-seeded gels, acellular gels exhibited a single nearly linear stiffness-force relationship, which did not change significantly during the course of the experiment (Fig. B.15).

4. Discussion

We quantified and compared how forces generated by primary aortic SMCs embedded within a collagenous tissue equivalent develop under different dynamic loading and boundary conditions in a biaxial setting. Whereas uniaxial tests are relatively easy to perform and interpret, they tend not to capture the complex multiaxial loading conditions that exist *in vivo*. Conversely, biaxial tests can better mimic *in vivo* conditions but are less easily performed and interpreted. Biaxial tests typically use rectangular or cruciform samples, each with associated advantages and disadvantages (Hu et al., 2009; Jhun et al., 2009; Thomopoulos et al., 2005). Important here, our measurements of overall biaxial forces in cruciform samples necessarily integrate cell-gel contributions from both the arms (which experience primarily

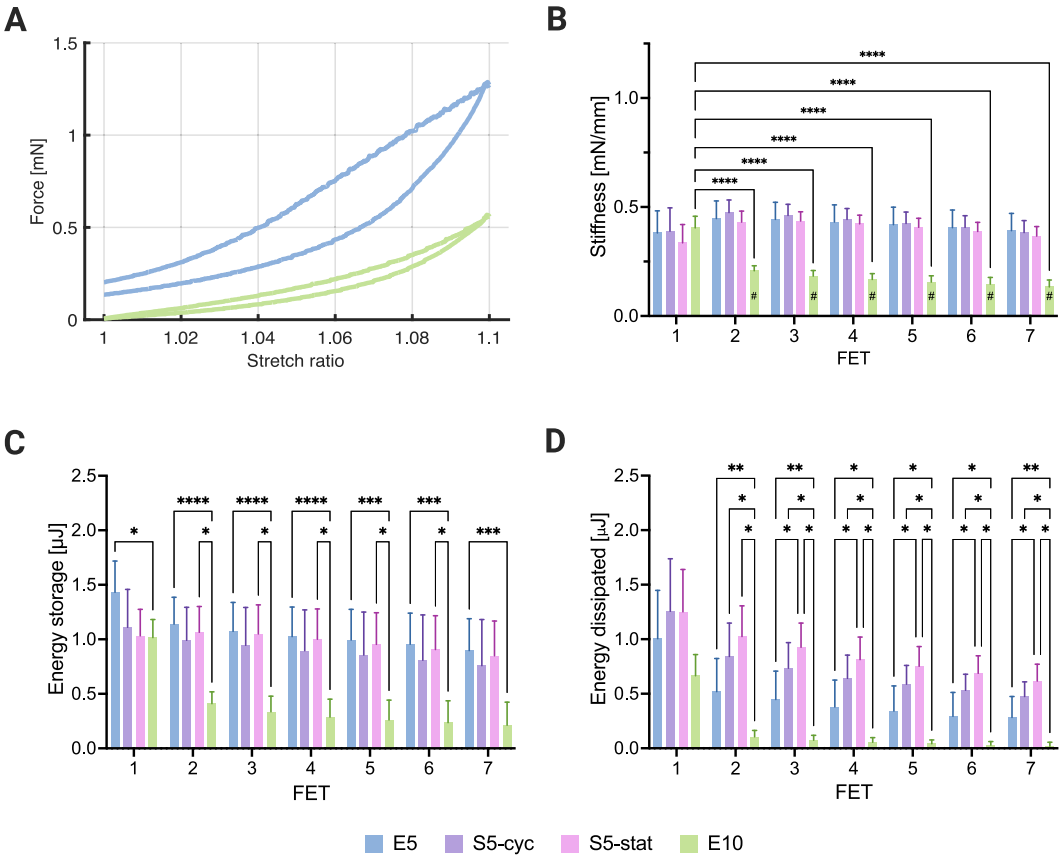

Fig. 8. Analysis of force–extension tests based on stiffness, energy storage, and energy dissipation. (A) Average loading and unloading curves of the second force–extension test (FET) for the E5 (blue) and E10 (green) experiments. (B) Stiffness estimation by simplified linear fit to loading curves. (C) The energy storage was computed as the area under the unloading curve for each loading condition. (D) The energy dissipated was computed as the area between the loading and unloading curves. (*$p < 0.05$, **$p < 0.01$, ***$p < 0.001$, ****$p < 0.0001$, #$p < 0.0001$ between E10 and all other loading conditions for the same force–extension test.)

uniaxial loading) and the central region (which experiences nonuniform biaxial stresses and strains) of the sample. Fig. A.10 shows stress–strain conditions under the relevant idealized situations, whereas Figs. A.11 and A.12 show possible nonuniform fields computed using finite elements for an illustrative initially homogeneous cruciform collagen gel. Although the evolving constitutive relation for a VSMC-seeded collagen gel is not known, similar qualitative results have been reported for simple Hookean (linear) and extended Mooney–Rivlin (mildly nonlinear) relations, that is, without superimposed cell-generated contributions. Results are shown here for the former for different values of Poisson's ratio for gels ranging from nearly incompressible ($\nu \sim 0.49$) to more compressible behaviors with less biaxial coupling ($\nu \sim 0.25$ or 0.10). Similar assumptions have been used previously (Barocas and Tranquillo, 1997; Raub et al., 2010) and likely capture qualitative trends. It is seen for a strip-biaxial case (with 1 the stretching axis and 2 the static axis) that, on average, the strains reach their target values of ~5% in the 1 direction and 0% in the 2 direction despite differences in the arms and central region. The predicted stresses were also as expected, on average, namely, overall tensile in both directions, with 1-direction stresses many-fold higher than 2-direction stresses. Yet, cell responses likely depend on local mechanical stimuli, not average states of strain and stress. The reported force measurements in our biaxial experiments necessarily represent the integrated responses by all cells, meaning cells that experienced different local stimuli. One would expect, however, that the integrated response should reflect an average of all cell responses. Given the continuing lack of understanding of how VSMCs respond to different levels and types of multiaxial stresses and strains, we also considered coordinate invariant values of the stress tensor. Spatial differences were less for the trace ($tr(\boldsymbol{\sigma})$) than for the magnitude ($\sqrt{tr(\boldsymbol{\sigma}\boldsymbol{\sigma}^T)}$) of the Cauchy stress, especially for equibiaxial stretching, remembering that the out-of-plane component of stress is zero.

Caveats notwithstanding, overall, the data suggested that, in a series of cyclic loading periods separated by force–extension tests, the cells established a new steady state level of biaxial force during each interval. This behavior is similar to prior observations in static experiments (Brown et al., 1998; Eichinger et al., 2020; Ezra et al., 2010) where cells tend to restore a preferred mechanical state when subjected to a single sustained external perturbation. It is especially interesting that the observed steady-state mean forces were similar across all protocols herein, regardless of the specific boundary conditions and amplitude of cyclic stretch over the range of 5 to 10% (Fig. 5B), and that the biaxial force generation in the two primary axes of the cruciform sample (f_1 and f_2) was similar. Conceptually, this implies that

$$\int (\sigma_{11}^{matrix} + \sigma_{11}^{cell}) dA = f_1 \approx f_2 = \int (\sigma_{22}^{matrix} + \sigma_{22}^{cell}) dA$$

where A is an appropriate cross-sectional area and we decomposed the stress into collagen gel (matrix) derived and VSMC (cell) generated contributions (cf. Barocas and Tranquillo (1997)). Since $\sigma_{11}^{matrix} \approx \sigma_{22}^{matrix}$ in an equibiaxial stretching test (which tends to preserve the original isotropy in the central region (Hu et al., 2009) and generate similar collagen fiber realignment in the uniaxial arms), this suggests that $\sigma_{11}^{cell} \approx \sigma_{22}^{cell}$ in equibiaxial stretching. By contrast, since $\sigma_{11}^{matrix} > \sigma_{22}^{matrix}$ in a strip-biaxial test, with 1 the stretching axis and 2 the static axis, this suggests that $\sigma_{22}^{cell} > \sigma_{11}^{cell}$. That is, it appears that differential cell-generated stresses were needed to yield the experimentally observed near equivalence of net force generation in the two primary directions independent of the type of loading conditions.

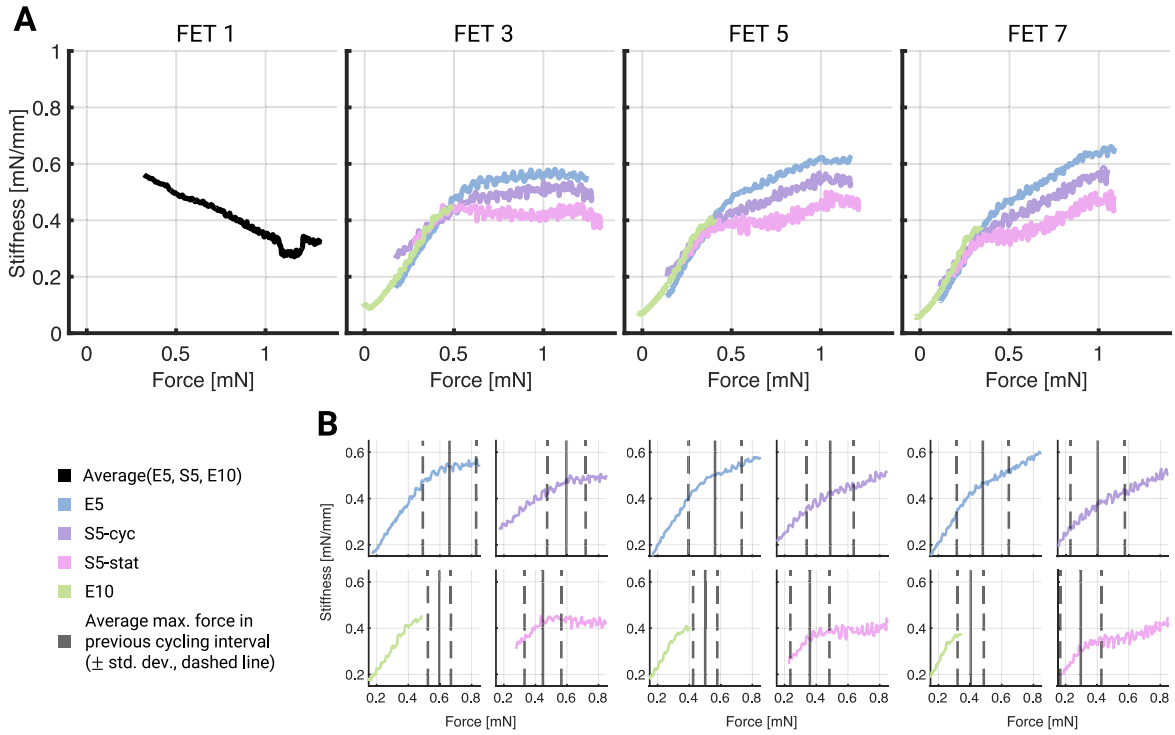

Fig. 9. Analysis of stiffness evolution for VSMC-seeded gels during consecutive force–extension tests (FETs). (A) Stiffness-force relationships for cell-seeded gels. All gels exhibited a similar behavior during the first test, which followed the initialization phase but changed significantly in the subsequent tests that followed the 7-h cyclic loading periods. Two distinct linear regimes appear to emerge for the E5 and S5 experiments, whereas one linear regime appears to hold for the E10 experiment over the forces imposed. Interestingly, there is a remarkable agreement in all loading conditions for small and medium forces. (B) Zoomed-in insets on the transition point from the first linear regime to the second one, including the average maximum force range the gels experienced during the last two hours of the previous cyclic loading interval. The transition point seems to be approximately in that range.

This experimental observation and conceptual consideration appear to be consistent with the cells seeking to establish and maintain a preferred range of forces (or tensions or stresses), irrespective of external boundary conditions. This implication also aligns with a previous observation that higher amplitude dynamic loading of uniaxial cell-seeded tissue equivalents does not lead to higher stresses after a few hours of cyclic loading (Wille et al., 2006), suggesting a cellular response aimed at maintaining a specific range of stresses. These authors hypothesized that cells achieve this regulation by adjusting their stiffness through modulation of the actin cytoskeleton. A recent study (Walker et al., 2020) confirmed this hypothesis by depolymerizing F-actin with Cytochalasin D. They proposed cytoskeletal remodeling, specifically rapid actin depolymerization, as the key mechanism by which cells adjust their stiffness and maintain a preferred mechanical state under dynamic loading defined by different strain amplitudes. Only with an intact actin cytoskeleton could cell stiffness adaptations occur, including softening. Moreover, they showed that tissue stiffness can be recovered when switching from large to small amplitudes during cyclic loading. This supports their observation that the stiffness adaptation was mainly cell-mediated, not a passive material response (such as, for example, the Mullins effect). Our experiments suggest further that, on average, cells may adapt their stiffness to maintain near-equal net steady-state forces (or tensions or stresses) despite different spatial distributions of stresses and strains.

This apparent force/tension/stress-mediated response seems to extend to the stiffness-force relationship of the cell-seeded tissue equivalents (Fig. 9). During equibiaxial force–extension tests, the average stiffness-force relationships agreed well within the force range experienced during the previous interval of cyclic loading for all tested conditions. This adaptation is not immediately apparent from force-stretch plots (Fig. 7A–D), as E10 experiments exhibited a significantly more compliant behavior. Nonetheless, this agreement diminished once forces exceeded the peak values experienced by the gels during the last two hours of the previous cyclic loading period; if stretched beyond this force, the stiffness either remained constant or increased at a lower rate. Again, the similar stiffness-force relationships for forces experienced during cyclic loading could suggest that cells not only adjust to maintain a preferred force/tension/stress but they also try to maintain a preferred stiffness or stiffness-force relationship. These two observations may not be independent, and further studies will be needed to explore and validate this relationship and find the direction of influence.

Another observation stems from the increase in force at the beginning of the cyclic loading periods in the E5 and S5 experiments (Fig. 3). The gels appeared to be initially too compliant, perhaps stimulating the cells to adjust to reach a preferred range of force/tension/stress. Interestingly, this behavior was absent in the E10 experiments. To explain this difference, we posit that these cells may have adapted to the cyclic 10% stretching by the end of the loading periods, evidenced by the steady-state mean forces and force amplitudes. Hence, during the following 10% stretch force–extension tests, the E10 cells would likely have had experienced the same forces/tensions/stresses to which they had adapted. As described before (Wille et al., 2006; Walker et al., 2020), cells can respond to higher forces by reducing their stiffness. Therefore, we hypothesize that the 10% stretch force–extension tests in the E5 and S5 experiments induced an active response by subjecting the cells to loads higher than previously experienced, triggering cellular adaptations leading to a reduced stiffness. This may also explain the reduced slope of the second linear regime for E5 and S5 experiments in the stiffness-force relationship once peak cycling forces were exceeded (Fig. 9B). For E10 experiments, perhaps there was only one linear regime in the stiffness-force relationship since the cells did not experience loads during force–extension tests that they had not experienced before. In this case, it seems reasonable that no further adaptation would occur; the cells would already be in the preferred state when cyclic loading resumed. Consequently, we suspect that the initial active

adaptation during cyclic loading might not have been present in E5 and S5 experiments if the force–extension tests did not exceed 5% stretch; alternatively, an active cell contribution might appear in E10 experiments if the force–extension tests surpass 10% strain. These and other hypotheses remain to be investigated by further studies.

Note that the static direction in the S5 experiments only experienced an imposed 10% change in strain seven times (once during each force–extension test), whereas both directions in the E10 experiments experienced an imposed 10% strain thousands of times. Despite this difference, the reduction in force was similar in all tested conditions, independent of boundary conditions. Note that such a force reduction is not limited to the experiments performed herein, as previous studies have shown that SMCs are unable to maintain a steady force for a prolonged time during static culture (Eichinger et al., 2020; Hall et al., 2007). Interestingly, pilot studies with 5% cyclic loading and no force–extension testing delayed the force reduction but did not prevent it compared to static experiments (data not shown). It thus appears that short-term, intermittent force–extension tests may have impacted the force reduction, but underlying mechanisms remain unclear.

It is important to note that comparing data from different studies can be complicated due to many factors. For example, a key difference compared to other studies is that the tissue equivalents tested herein were not mature. In multiple studies (Hu et al., 2013; Wagenseil et al., 2003; Walker et al., 2020; Wille et al., 2006), the tissue constructs were allowed to compact or incubate under dynamic loading (Lee et al., 2018) for several days before testing. This affects the mechanical properties of the gels and, hence, the measured forces. Another complicating factor is that different experimental designs are used to characterize the mechanical properties of the gels or to measure cell-generated forces. For instance, the shape of tissue-equivalents varies across different studies, with some using ring samples (Wagenseil et al., 2003; Wille et al., 2006), others uniaxial samples (Walker et al., 2020), and some biaxial samples, even with different geometries (Hu et al., 2013; Sander et al., 2011). Each testing method has advantages and disadvantages. The factors mentioned above, as well as differences in the experimental setup (cell type, serum concentration, preconditioning, applied stretch rate, etc.), must be kept in mind when comparing or translating results across different systems. We focused herein on different biaxial stretching protocols while maintaining the stretch rate fixed. Further studies should explore responses across multiple stretch rates as well as possible changes due to different degrees of hydration and levels of compressibility that would be expected to affect viscoelastic responses.

Whereas computational models should guide experimental design (Humphrey et al., 2008; Niklason et al., 2010), such modeling must be informed by relevant data. We submit that the present data will contribute to the development of new models for aortic smooth muscle cells and that additional theoretically motivated studies will be needed not only for VSMCs but also primary aortic fibroblasts. Indeed, these fibroblasts play a critical role in many cases of aortic remodeling, including in hypertension (Bersi et al., 2016). Again, notwithstanding the aforementioned caveats, biaxial testing should be used given the *in vivo* loading conditions on the aorta, which renders strip-biaxial testing at multiple fixed stretches informative for examining the critical role of axial loading on cell responses (Gleason and Humphrey, 2005b). Indeed, axial remodeling is often the earliest in many cases of aortic adaptation or maladaptation to perturbations in loading. Finally, the present study focused on mechanical homeostasis (Eichinger et al., 2021), but there will also be a need to design similar *ex vivo* studies to assess and/or test hypotheses regarding mechanobiological stability (Cyron and Humphrey, 2014).

5. Conclusion

This study sought to explore impacts of different mechanical constraints in combination with dynamic cyclic loading on possible biaxial tensional homeostasis in VSMC-seeded collagen-based tissue equivalents. It was observed that steady-state mean forces remained consistent across all tested conditions despite significant differences in boundary conditions and loading amplitudes. Additionally, the stiffness-force relationships assessed via equibiaxial force–extension tests showed remarkable similarity for ranges of loading to which the cells had adapted during previous cyclic loading periods. These results are consistent with prior findings of a critical role of force/tension/stress in the mechanical adaptation of VSMCs (Kanda and Matsuda, 1994; Karkhaneh Yousefi et al., 2023; Li and Xu, 2000). Further testing with additional cell types will be needed to determine whether this behavior is specific to VSMCs or generic mechanical homeostatic processes. Furthermore, testing cells with genetic defects in mechanosensory proteins, such as in the focal adhesion complex, could provide valuable insights into the dominant mechanisms at play in the observed behavior.

CRediT authorship contribution statement

Daniel Paukner: Writing – review & editing, Writing – original draft, Visualization, Methodology, Investigation, Formal analysis, Data curation, Conceptualization. **Isabella R. Jennings:** Writing – review & editing, Writing – original draft, Visualization, Methodology, Investigation, Formal analysis, Data curation, Conceptualization. **Christian J. Cyron:** Writing – review & editing, Supervision. **Jay D. Humphrey:** Writing – review & editing, Supervision, Resources, Conceptualization.

Declaration of competing interest

The authors declare that they have no known competing financial interests or personal relationships that could have appeared to influence the work reported in this paper.

Data availability

Data will be made available on request.

Appendix A. Loading conditions

Considering idealized mechanical tests can help build conceptual understanding and motivate experimental design (Humphrey et al., 2008). Fig. A.10 illustrates four loading conditions that have proven useful in studying planar tissue equivalents, often considered on a continuum scale to have coincident principal directions of stress and stretch with a zero out-of-plane stress.

Notwithstanding the intuition gained via idealized experimental situations, actual biaxial testing of cruciform samples results in complex stress and strain fields, potentially ranging from nearly uniaxial in the four arms of the sample to nearly homogeneous biaxial in the central-most region, with non-homogeneous fields between (Hu et al., 2014). In the absence of detailed material characterization and associated finite element studies, there is a need to interpret cautiously any associated experimental results based on the measured forces and globally prescribed stretches. Consistent with other studies (Gould et al., 2012; Hu et al., 2014; Sander et al., 2011), here we provide simple illustrative finite element simulations using ABAQUS (Dassault Systems) to appreciate better the non-homogeneous fields that can develop in a biaxially tested cruciform gel (Figs. A.11 and A.12). Because of double-symmetry, only one-quarter of the cruciform geometry was modeled with corresponding symmetry boundary conditions. The domain was discretized with 1780 finite elements (C3D8H) and described by an isotropic, linear elastic material with material parameters E (Young's modulus) and ν (Poisson's ratio). E and ν were adjusted to approximate the force amplitudes measured in acellular gels under 5% equi- and strip-biaxial loading in the steady state (Fig. B.14A), as well as the amplitude ratios of the static and perturbed axis in the strip-biaxial experiments in the steady state (Fig. 4B). This resulted in a Young's

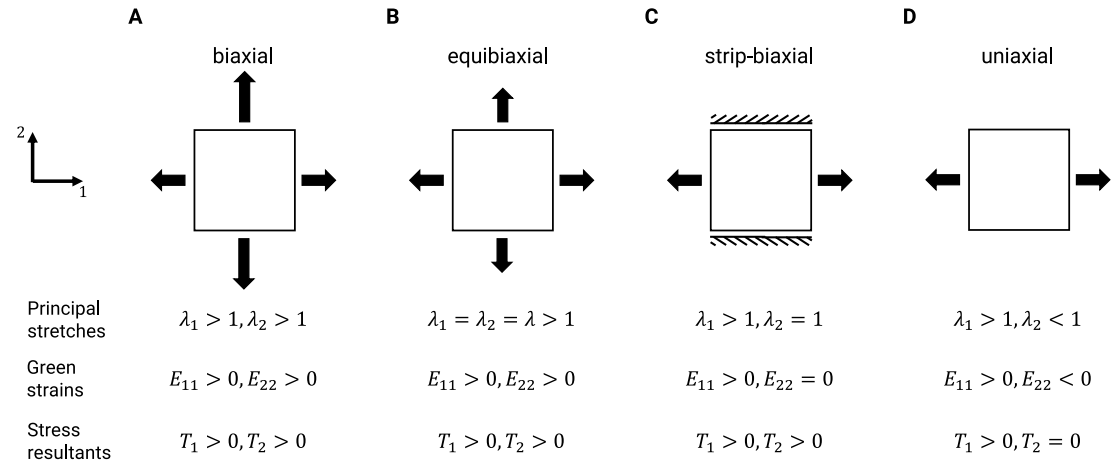

Fig. A.10. Illustration of different idealized loading conditions. (A) shows a general in-plane tensile test with biaxial stretches (λ_1, λ_2) greater than unity and associated non-negative biaxial strains and stress resultants (i.e., quantities having units of force/length that can be obtained by integrating the associated stress through the thickness). Different specializations follow in B-D. Cases (B) and (C) are relevant herein for the central region of a cruciform sample, whereas case (D) is relevant herein for the arms of a cruciform sample. It is noted further that other strip-biaxial tests could include non-zero but fixed values of E_{22}, for which the associated values of T_2 would increase further above baseline during testing.

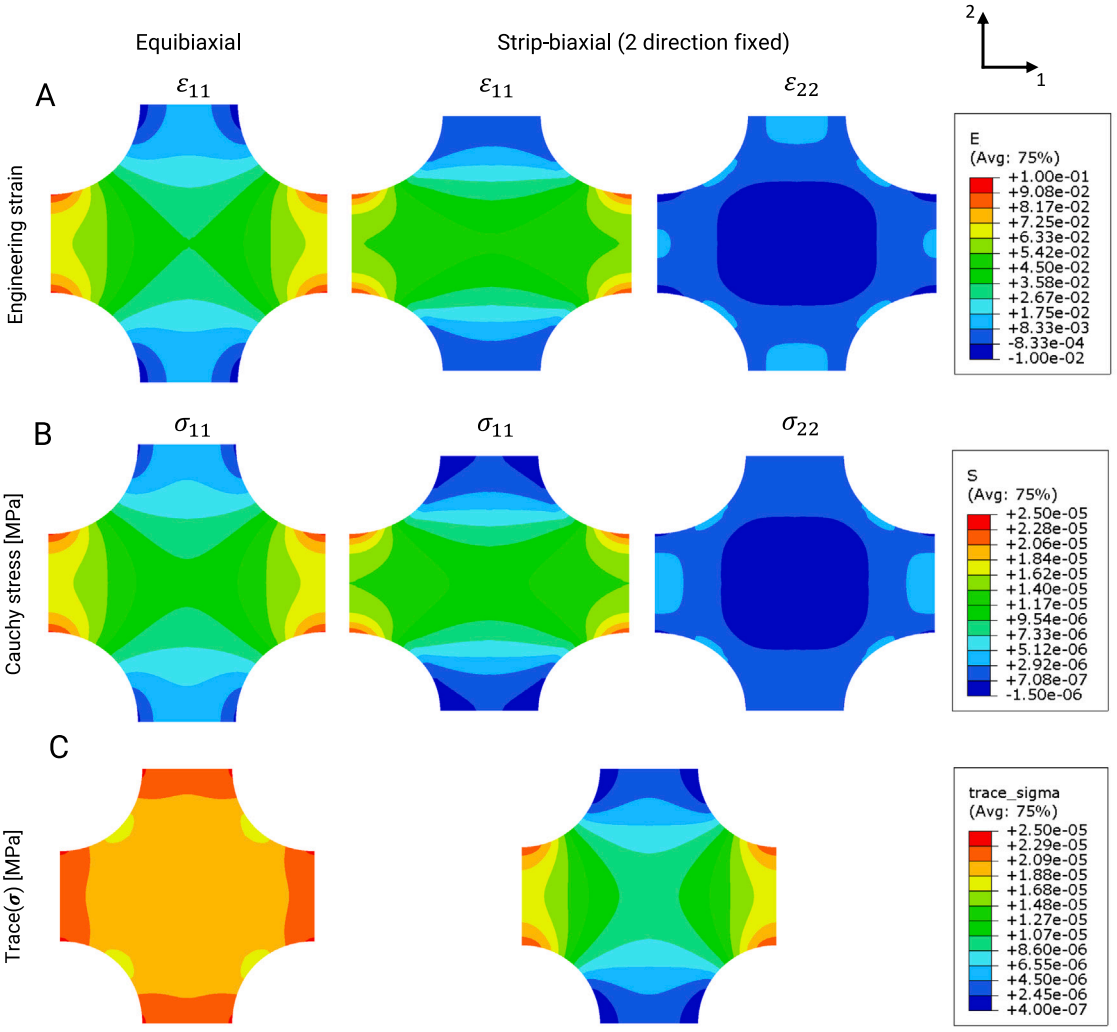

Fig. A.11. Illustrative finite element results for biaxial strains (top row) and stresses (middle and bottom rows) in a cruciform sample ($E = 250$ Pa, $\nu = 0.1$) subjected to displacement boundary conditions at the ends of the four arms. Note that, on average, the 1 and 2 directions in the equibiaxial case (left column) experience a 5% strain, while in the strip-biaxial case, the 1 direction experiences a 5% strain (middle column) and the 2 direction 0% strain (right column). Despite achieving the target levels of biaxial strain, on average, note the complex nonuniform strain and stress fields. In particular, the strain in the 2 direction yields a 2-direction stress that is both tensile (in the arms) and compressive (in the central region), though overall positive (middle row). Finally, note that coordinate invariant measures of the biaxial state of stress (bottom row), including the trace (shown) and the magnitude (not shown, but similar), reveal a more uniform distribution except for deviations in the strip-biaxial arms.

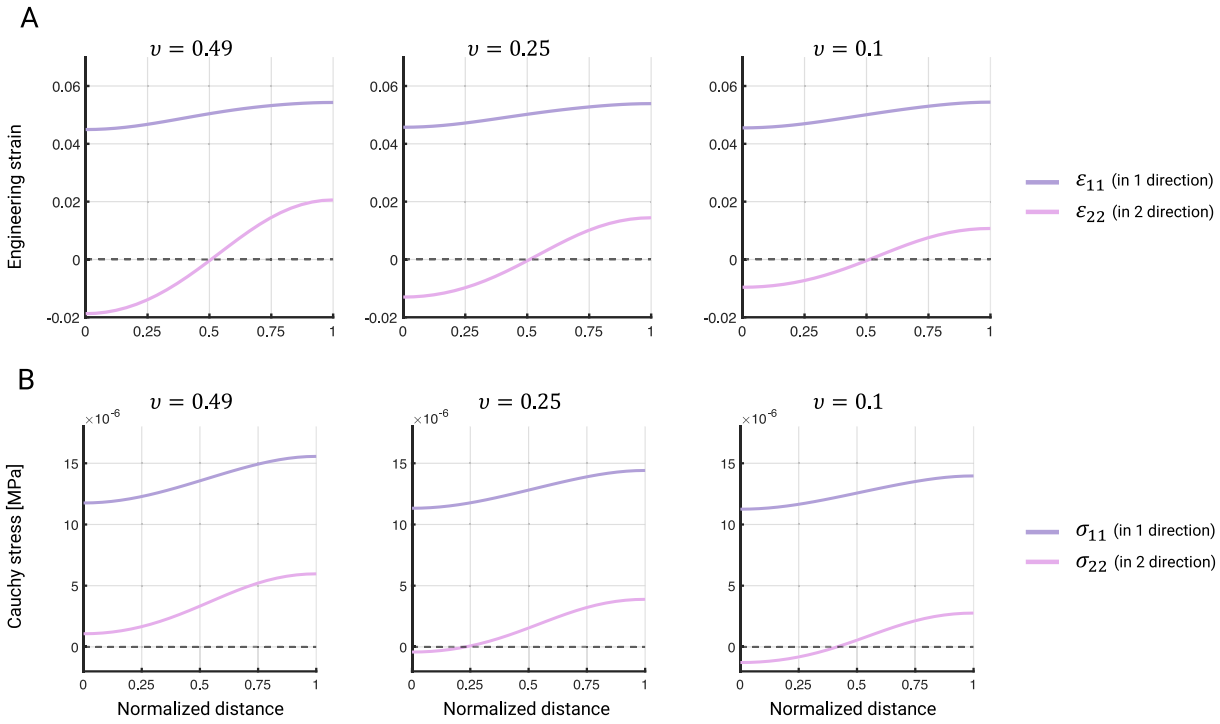

Fig. A.12. Given the idealized quarter-symmetry, illustrative biaxial strain (top) and stress (bottom) distributions along the mid-line 1 (stretched) and 2 (fixed) directions reveal that the desired strains (5% in 1 direction, 0% in 2 direction) were achieved in the strip-biaxial test, on average, when examining the full computational domain, from which the experimentally measured forces derived. Reducing the Poisson's ratio has a marked impact on the strain and stress distributions in these strip-biaxial simulations; it reduces the magnitude of the 2-direction strains, and the 2-direction stresses become slightly more compressive in the central region. Despite both tensile and compressive stresses in the 2 direction, the net stress was yet tensile in both the 1 and 2 directions as expected in a strip-biaxial test. Although cell responses likely depend on the local, not overall, state of stress and/or strain, the experimental measurement of biaxial force generation necessarily results from the integrated responses of all cells over the entire experimental domain.

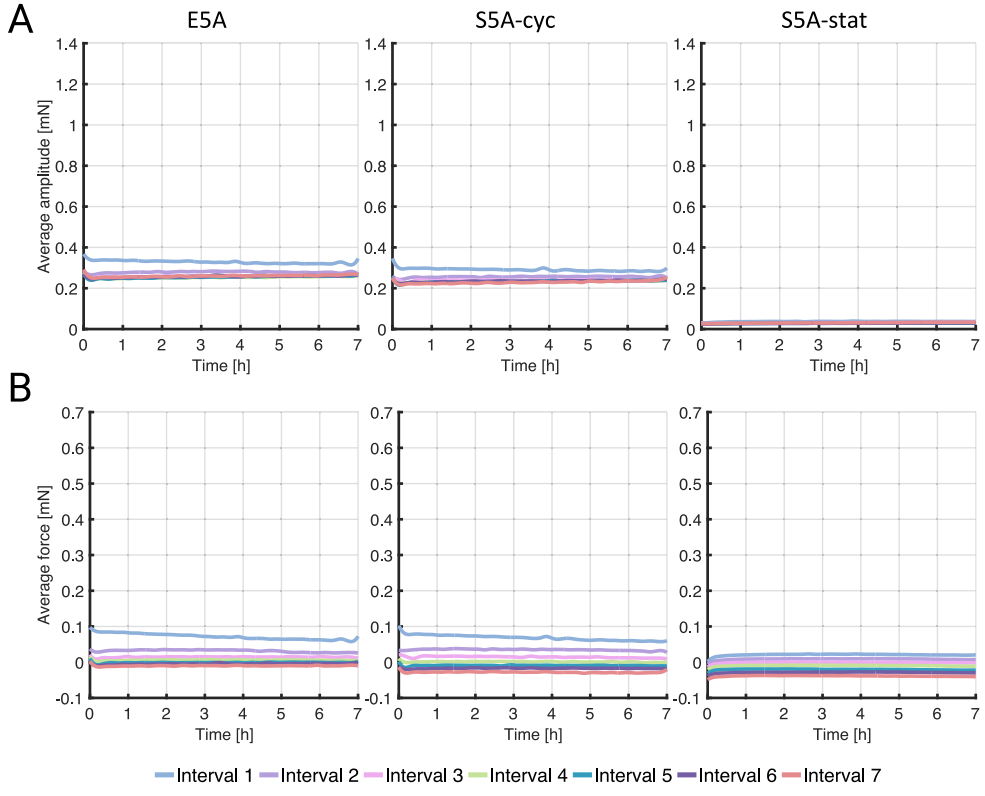

Fig. B.13. Time-averaged forces in acellular experiments during cyclic loading intervals. (A) Average force amplitude across all acellular experiments for each loading condition during the seven intervals. (B) Average mean force across all acellular experiments for each loading condition during the seven intervals. See Table 1 for the nomenclature for all testing protocols.

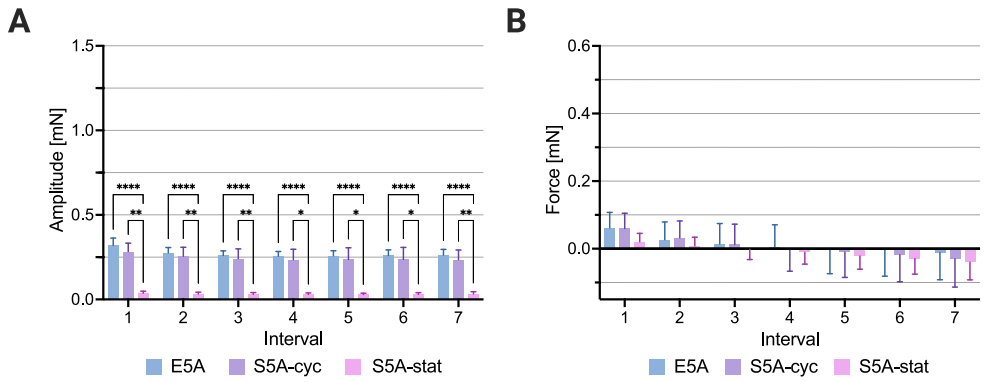

Fig. B.14. Evolution of steady-state forces in acellular experiments. (A) Force amplitudes were constant over time, with the amplitude of the static axis in the strip-biaxial being significantly different from the other amplitudes. (B) The steady-state mean forces in acellular gels were low and showed a slight decrease over time. ($*p < 0.05$, $**p < 0.01$, $***p < 0.001$, $****p < 0.0001$) See Table 1 for the nomenclature for all testing protocols.

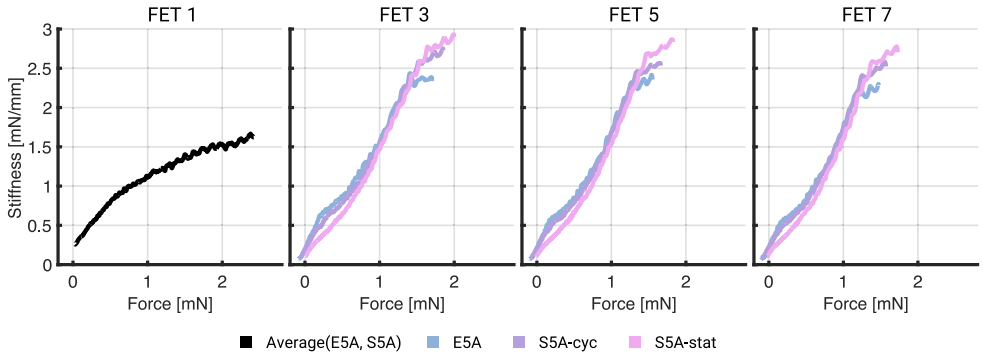

Fig. B.15. Stiffness-force relationship for acellular experiments during selected force–extension tests (FETs). All gels exhibited a similar behavior during the first test, which did not change as significantly as cell-seeded gels in the following tests. The stiffness-force relationship remained approximately linear throughout all the force–extension tests. Black – Average of the first force–extension test in E5A, S5A-cyc, and S5A-stat experiments, blue – average of E5A experiments, purple – average of S5A-cyc experiments, pink – average of S5A-stat experiments. See Table 1 for the nomenclature for all testing protocols.

modulus of 250 Pa and a Poisson's ratio of 0.1, which are comparable to previously measured values of acellular collagen gels (Raub et al., 2010). Figs. A.11 and A.12 show strain and stress distributions for the equibiaxial case (prescribed 5% strain in the 1 and 2 direction) and strip-biaxial case (prescribed 5% strain in the 1 direction, 0% strain in the 2 direction). Because of the isotropy and the symmetric loading in the equibiaxial case, only the strains and stresses in the 1 direction are shown.

Appendix B. Acellular experiments

See Figs. B.13–B.15.

References

Bäck, M., Gasser, T.C., Michel, J.-B., Caligiuri, G., 2013. Biomechanical factors in the biology of aortic wall and aortic valve diseases. Cardiovasc. Res. 99 (2), 232–241. http://dx.doi.org/10.1093/cvr/cvt040.

Barocas, V.H., Tranquillo, R.T., 1997. An anisotropic biphasic theory of tissue-equivalent mechanics: the interplay among cell traction, fibrillar network deformation, fibril alignment, and cell contact guidance. J. Biomech. Eng. 119 (2), 137–145. http://dx.doi.org/10.1115/1.2796072.

Bell, E., Ivarsson, B., Merrill, C., 1979. Production of a tissue-like structure by contraction of collagen lattices by human fibroblasts of different proliferative potential in vitro. Proc. Natl. Acad. Sci. 76 (3), 1274–1278. http://dx.doi.org/10.1073/pnas.76.3.1274.

Bersi, M.R., Bellini, C., Wu, J., Montaniel, K.R., Harrison, D.G., Humphrey, J.D., 2016. Excessive adventitial remodeling leads to early aortic maladaptation in angiotensin-induced hypertension. Hypertension 67 (5), 890–896. http://dx.doi.org/10.1161/HYPERTENSIONAHA.115.06262.

Brown, R.A., Prajapati, R., McGrouther, D.A., Yannas, I.V., Eastwood, M., 1998. Tensional homeostasis in dermal fibroblasts: Mechanical responses to mechanical loading in three-dimensional substrates. J. Cell. Physiol. 175 (3), 323–332. http://dx.doi.org/10.1002/(SICI)1097-4652(199806)175:3<323::AID-JCP10>3.0.CO;2-6.

Chen, K., Vigliotti, A., Bacca, M., McMeeking, R.M., Deshpande, V.S., Holmes, J.W., 2018. Role of boundary conditions in determining cell alignment in response to stretch. Proc. Natl. Acad. Sci. 115 (5), 986–991. http://dx.doi.org/10.1073/pnas.1715059115.

Cyron, C., Humphrey, J., 2014. Vascular homeostasis and the concept of mechanobiological stability. Internat. J. Engrg. Sci. 85, 203–223. http://dx.doi.org/10.1016/j.ijengsci.2014.08.003.

Eichinger, J.F., Haeusel, L.J., Paukner, D., Aydin, R.C., Humphrey, J.D., Cyron, C.J., 2021. Mechanical homeostasis in tissue equivalents: a review. Biomech. Model. Mechanobiol. 20 (3), 833–850. http://dx.doi.org/10.1007/s10237-021-01433-9.

Eichinger, J.F., Paukner, D., Szafron, J.M., Aydin, R.C., Humphrey, J.D., Cyron, C.J., 2020. Computer-controlled biaxial bioreactor for investigating cell-mediated homeostasis in tissue equivalents. J. Biomech. Eng. 142 (7), http://dx.doi.org/10.1115/1.4046201.

Engler, A.J., Sen, S., Sweeney, H.L., Discher, D.E., 2006. Matrix elasticity directs stem cell lineage specification. Cell 126 (4), 677–689. http://dx.doi.org/10.1016/j.cell.2006.06.044.

Ezra, D.G., Ellis, J.S., Beaconsfield, M., Collin, R., Bailly, M., 2010. Changes in fibroblast mechanostat set point and mechanosensitivity: an adaptive response to mechanical stress in floppy eyelid syndrome. Investig. Opthalmology Vis. Sci. 51 (8), 3853. http://dx.doi.org/10.1167/iovs.09-4724.

Ferruzzi, J., Bersi, M.R., Humphrey, J.D., 2013. Biomechanical phenotyping of central arteries in health and disease: advantages of and methods for murine models. Ann. Biomed. Eng. 41 (7), 1311–1330. http://dx.doi.org/10.1007/s10439-013-0799-1.

Gleason, R., Humphrey, J., 2005a. Effects of a sustained extension on arterial growth and remodeling: a theoretical study. J. Biomech. 38 (6), 1255–1261. http://dx.doi.org/10.1016/j.jbiomech.2004.06.017.

Gleason, R.L., Humphrey, J.D., 2005b. A 2D constrained mixture model for arterial adaptations to large changes in flow, pressure and axial stretch. Math. Med. Biol.: J. IMA 22 (4), 347–369. http://dx.doi.org/10.1093/imammb/dqi014.

Gould, R.A., Chin, K., Santisakultarm, T.P., Dropkin, A., Richards, J.M., Schaffer, C.B., Butcher, J.T., 2012. Cyclic strain anisotropy regulates valvular interstitial cell

phenotype and tissue remodeling in three-dimensional culture. Acta Biomater. 8 (5), 1710–1719. http://dx.doi.org/10.1016/j.actbio.2012.01.006.

Hall, S.M., Soueid, A., Smith, T., Brown, R.A., Haworth, S.G., Mudera, V., 2007. Spatial differences of cellular origins and in vivo hypoxia modify contractile properties of pulmonary artery smooth muscle cells: lessons for arterial tissue engineering. J. Tissue Eng. Regen. Med. 1 (4), 287–295. http://dx.doi.org/10.1002/term.39.

Hu, J.-J., Chen, G.-W., Liu, Y.-C., Hsu, S.-S., 2014. Influence of specimen geometry on the estimation of the planar biaxial mechanical properties of cruciform specimens. Exp. Mech. 54 (4), 615–631. http://dx.doi.org/10.1007/s11340-013-9826-2.

Hu, J.-J., Humphrey, J.D., Yeh, A.T., 2009. Characterization of engineered tissue development under biaxial stretch using nonlinear optical microscopy. Tissue Eng. Part A 15 (7), 1553–1564. http://dx.doi.org/10.1089/ten.tea.2008.0287.

Hu, J.-J., Liu, Y.-C., Chen, G.-W., Wang, M.-X., Lee, P.-Y., 2013. Development of fibroblast-seeded collagen gels under planar biaxial mechanical constraints: a biomechanical study. Biomech. Model. Mechanobiol. 12 (5), 849–868. http://dx.doi.org/10.1007/s10237-012-0448-x.

Humphrey, J.D., Dufresne, E.R., Schwartz, M.A., 2014. Mechanotransduction and extracellular matrix homeostasis. Nat. Rev. Mol. Cell Biol. 15 (12), 802–812. http://dx.doi.org/10.1038/nrm3896.

Humphrey, J.D., Eberth, J.F., Dye, W.W., Gleason, R.L., 2009. Fundamental role of axial stress in compensatory adaptations by arteries. http://dx.doi.org/10.1016/j.jbiomech.2008.11.011.

Humphrey, J.D., Wells, P.B., Baek, S., Hu, J.-J., McLeroy, K., Yeh, A.T., 2008. A theoretically-motivated biaxial tissue culture system with intravital microscopy. Biomech. Model. Mechanobiol. 7 (4), 323–334. http://dx.doi.org/10.1007/s10237-007-0099-5.

Hynes, R.O., Naba, A., 2012. Overview of the matrisome – an inventory of extracellular matrix constituents and functions. Cold Spring Harb. Perspect. Biol. 4 (1), a004903. http://dx.doi.org/10.1101/cshperspect.a004903.

Jhun, C.-S., Evans, M.C., Barocas, V.H., Tranquillo, R.T., 2009. Planar biaxial mechanical behavior of bioartificial tissues possessing prescribed fiber alignment. J. Biomech. Eng. 131 (8), http://dx.doi.org/10.1115/1.3148194.

Kanda, K., Matsuda, T., 1994. Mechanical stress-induced orientation and ultrastructural change of smooth muscle cells cultured in three-dimensional collagen lattices. Cell Transplant. 3 (6), 481–492. http://dx.doi.org/10.1177/096368979400300605.

Karkhaneh Yousefi, A.A., Petit, C., Ben Hassine, A., Avril, S., 2023. Stiffness sensing by smooth muscle cells: Continuum mechanics modeling of the acto-myosin role. J. Mech. Behav. Biomed. Mater. 144, 105990. http://dx.doi.org/10.1016/j.jmbbm.2023.105990.

Klein, E.A., Yin, L., Kothapalli, D., Castagnino, P., Byfield, F.J., Xu, T., Levental, I., Hawthorne, E., Janmey, P.A., Assoian, R.K., 2009. Cell-cycle control by physiological matrix elasticity and in vivo tissue stiffening. Curr. Biol. 19 (18), 1511–1518. http://dx.doi.org/10.1016/j.cub.2009.07.069.

Lee, P.-Y., Liu, Y.-C., Wang, M.-X., Hu, J.-J., 2018. Fibroblast-seeded collagen gels in response to dynamic equibiaxial mechanical stimuli: A biomechanical study. J. Biomech. 78, 134–142. http://dx.doi.org/10.1016/j.jbiomech.2018.07.030.

Li, C., Xu, Q., 2000. Mechanical stress-initiated signal transductions in vascular smooth muscle cells. Cell. Signal. 12 (7), 435–445. http://dx.doi.org/10.1016/S0898-6568(00)00096-6.

Lukashev, M., 1998. ECM signalling: orchestrating cell behaviour and misbehaviour. Trends Cell Biol. 8 (11), 437–441. http://dx.doi.org/10.1016/S0962-8924(98)01362-2.

Mol, A., Driessen, N.J.B., Rutten, M.C.M., Hoerstrup, S.P., Bouten, C.V.C., Baaijens, F.P.T., 2005. Tissue engineering of human heart valve leaflets: a novel bioreactor for a strain-based conditioning approach. Ann. Biomed. Eng. 33 (12), 1778–1788. http://dx.doi.org/10.1007/s10439-005-8025-4.

Niklason, L.E., Yeh, A.T., Calle, E.A., Bai, Y., Valentín, A., Humphrey, J.D., 2010. Enabling tools for engineering collagenous tissues integrating bioreactors, intravital imaging, and biomechanical modeling. Proc. Natl. Acad. Sci. 107 (8), 3335–3339. http://dx.doi.org/10.1073/pnas.0907813106.

Proudfoot, D., Shanahan, C., 2012. Human vascular smooth muscle cell culture. In: Mitry Ragai, R., Hughes, R.D. (Eds.), Human Cell Culture Protocols. Humana Press, Totowa, NJ, pp. 251–263. http://dx.doi.org/10.1007/978-1-61779-367-7{_}17.

Raub, C., Putnam, A., Tromberg, B., George, S., 2010. Predicting bulk mechanical properties of cellularized collagen gels using multiphoton microscopy. Acta Biomater. 6 (12), 4657–4665. http://dx.doi.org/10.1016/j.actbio.2010.07.004.

Redden, R.A., Doolin, E.J., 2003. Collagen crosslinking and cell density have distinct effects on fibroblast-mediated contraction of collagen gels. Skin Res. Technol. 9 (3), 290–293. http://dx.doi.org/10.1034/j.1600-0846.2003.00023.x.

Sander, E.A., Barocas, V.H., Tranquillo, R.T., 2011. Initial fiber alignment pattern alters extracellular matrix synthesis in fibroblast-populated fibrin gel cruciforms and correlates with predicted tension. Ann. Biomed. Eng. 39 (2), 714–729. http://dx.doi.org/10.1007/s10439-010-0192-2.

Seliktar, D., Nerem, R.M., Galis, Z.S., 2001. The role of matrix metalloproteinase-2 in the remodeling of cell-seeded vascular constructs subjected to cyclic strain. Ann. Biomed. Eng. 29 (11), 923–934. http://dx.doi.org/10.1114/1.1415522.

Shearn, J.T., Juncosa-Melvin, N., Boivin, G.P., Galloway, M.T., Goodwin, W., Gooch, C., Dunn, M.G., Butler, D.L., 2007. Mechanical stimulation of tendon tissue engineered constructs: effects on construct stiffness, repair biomechanics, and their correlation. J. Biomech. Eng. 129 (6), 848–854. http://dx.doi.org/10.1115/1.2800769.

Simon, D., Niklason, L., Humphrey, J., 2014. Tissue transglutaminase, not lysyl oxidase, dominates early calcium-dependent remodeling of fibroblast-populated collagen lattices. Cells Tissues Organs 200 (2), 104–117. http://dx.doi.org/10.1159/000381015.

Thomopoulos, S., Fomovsky, G.M., Holmes, J.W., 2005. The development of structural and mechanical anisotropy in fibroblast populated collagen gels. J. Biomech. Eng. 127 (5), 742–750. http://dx.doi.org/10.1115/1.1992525.

Wagenseil, J.E., Wakatsuki, T., Okamoto, R.J., Zahalak, G.I., Elson, E.L., 2003. One-dimensional viscoelastic behavior of fibroblast populated collagen matrices. J. Biomech. Eng. 125 (5), 719–725. http://dx.doi.org/10.1115/1.1614818.

Walker, M., Rizzuto, P., Godin, M., Pelling, A.E., 2020. Structural and mechanical remodeling of the cytoskeleton maintains tensional homeostasis in 3D microtissues under acute dynamic stretch. Sci. Rep. 10 (1), 7696. http://dx.doi.org/10.1038/s41598-020-64725-7.

Wang, H.-B., Dembo, M., Wang, Y.-L., 2000. Substrate flexibility regulates growth and apoptosis of normal but not transformed cells. Am. J. Physiol. Cell Physiol. 279 (5), C1345–C1350. http://dx.doi.org/10.1152/ajpcell.2000.279.5.C1345.

Wells, R.G., 2008. The role of matrix stiffness in regulating cell behavior. Hepatology 47 (4), 1394–1400. http://dx.doi.org/10.1002/hep.22193.

Wille, J.J., Elson, E.L., Okamoto, R.J., 2006. Cellular and matrix mechanics of bioartificial tissues during continuous cyclic stretch. Ann. Biomed. Eng. 34 (11), 1678–1690. http://dx.doi.org/10.1007/s10439-006-9153-1.

Wolf, K., te Lindert, M., Krause, M., Alexander, S., te Riet, J., Willis, A.L., Hoffman, R.M., Figdor, C.G., Weiss, S.J., Friedl, P., 2013. Physical limits of cell migration: control by ECM space and nuclear deformation and tuning by proteolysis and traction force. J. Cell Biol. 201 (7), 1069–1084. http://dx.doi.org/10.1083/jcb.201210152.

Yamada, K.M., Doyle, A.D., Lu, J., 2022. Cell–3D matrix interactions: recent advances and opportunities. Trends Cell Biol. 32 (10), 883–895. http://dx.doi.org/10.1016/j.tcb.2022.03.002.

Appendix C

Multiscale homogenized constrained mixture model of the bio-chemo-mechanics of soft tissue growth and remodeling

published in

Biomechanics and Modeling in Mechanobiology, vol. 23, pp. 2115–2136, 2024. DOI: 10.1007/s10237-024-01884-w.

Biomechanics and Modeling in Mechanobiology
https://doi.org/10.1007/s10237-024-01884-w

ORIGINAL PAPER

Multiscale homogenized constrained mixture model of the bio-chemo-mechanics of soft tissue growth and remodeling

Daniel Paukner[1,2] · Jay D. Humphrey[3] · Christian J. Cyron[1,2]

Received: 9 April 2024 / Accepted: 5 August 2024

Abstract
Constrained mixture models have successfully simulated many cases of growth and remodeling in soft biological tissues. So far, extensions of these models have been proposed to include either intracellular signaling or chemo-mechanical coupling on the organ-scale. However, no version of constrained mixture models currently exists that includes both aspects. Here, we propose such a version that resolves cellular signal processing by a set of logic-gated ordinary differential equations and captures chemo-mechanical interactions between cells by coupling a reaction-diffusion equation with the equations of nonlinear continuum mechanics. To demonstrate the potential of the model, we present 2 case studies within vascular solid mechanics: (i) the influence of angiotensin II on aortic growth and remodeling and (ii) the effect of communication between endothelial and intramural arterial cells via nitric oxide and endothelin-1.

Keywords Homeostasis · Constrained mixture · Cell signaling · Growth and remodeling · Soft tissue

1 Introduction

Most soft tissues consist of a collection of different cell types that communicate with each other and work together to promote tissue homeostasis under normal conditions. According to Adler et al. (2018), nearly all tissues are composed of 4 key cell types: those responsible for the primary function of the tissue plus endothelial cells, fibroblast-like stromal cells, and macrophages. This ensemble forms a remarkably robust system working reliably under different environmental conditions.

To study the response of soft tissue to changes in the mechanical environment on the macroscale, constrained mixture models (Humphrey and Rajagopal 2002) and in particular their homogenized versions (Cyron et al. 2016) have proven very successful. For example, they have been used to study the formation of aortic (Wilson et al. 2013; Mousavi and Avril 2017; Horvat et al. 2019) or cerebral (Baek et al. 2006) aneurysms, vascular adaptation to increased blood pressure (Valentín et al. 2008; Latorre et al. 2019), optimization of tissue-engineered vascular grafts (Szafron et al. 2019), inflammatory effects (Hill et al. 2018; Latorre et al. 2019; Maes et al. 2023), or cardiac growth and remodeling (Gebauer et al. 2023). In both full and homogenized models, the production of new tissue mass is usually governed by phenomenological gain parameters. While this approach allows numerically efficient organ-scale simulations, it does not allow detailed studies of subcellular processes and their effects on the organ-scale.

To study cellular signal processing, it is necessary to model the biochemical reactions within cells. These are usually triggered by signals sensed by receptors on the cell membrane (Alberts et al. 2017). One possibility is to model the reactions in detail, which requires parameters for each involved chemical reaction (Saucerman et al. 2003). This detailed approach, however, requires extensive experimental data to determine the reaction parameters. A simpler alternative is a graph representation of the signaling network (Kraeutler et al. 2010).

✉ Christian J. Cyron
christian.cyron@tuhh.de

Daniel Paukner
daniel.paukner@tuhh.de

Jay D. Humphrey
jay.humphrey@yale.edu

[1] Institute for Continuum and Material Mechanics, Hamburg University of Technology, Hamburg, Germany

[2] Institute of Material Systems Modeling, Helmholtz-Zentrum Hereon, Geesthacht, Germany

[3] Department of Biomedical Engineering, Yale University, New Haven, CT, USA

Published online: 17 October 2024

In this approach, biochemical reactions are replaced by simpler Hill-type functions, resulting in a logic-gated system of ordinary differential equations (ODEs) requiring fewer parameters. Despite its simplicity, this approach has yielded surprisingly accurate results, ranging from cardiac fibroblast signaling (Zeigler et al. 2016) to brain endothelial cells in the context of cerebral pathologies (Gorick et al. 2022). This approach also facilitates studying genetic defects, such as knockdowns or overexpression of specific proteins and pharmacological treatments (Irons and Humphrey 2020).

By combining constrained mixture models and cellular signaling models (Irons et al. 2021), one can create a scale-bridging model that captures how cell signaling affects growth and remodeling (G&R) on the organ-scale and vice versa (Karakaya et al. 2022; van Asten et al. 2022, 2023; Irons et al. 2022). Such scale-bridging models can benefit from the RNA sequencing data that are becoming more and more available. For example, this approach has been used to study effects of exogenous angiotensin II on aortic smooth muscle cells (Irons et al. 2021) and effects of notch signaling in hypertension (van Asten et al. 2023).

Whereas the above studies couple cell signaling and tissue-level constrained mixture models, others focus on chemo-mechanical coupling on the organ-scale (Marino et al. 2017; Gierig et al. 2021). That is, effects of the diffusion of paracrine signals at the tissue level were modeled by coupling reaction-diffusion equations and those for the soft tissue mechanics. Thereby, some have examined interactions of macrophages, smooth muscle cells, and endothelial cells and their effects on the mechanical properties of collagen (Marino et al. 2017); others have examined effects of matrix metalloproteinases (MMPs) and growth factors on the healing process of damaged soft tissue (Gierig et al. 2021). So far, to the authors' knowledge, no constrained mixture models of G&R include both intracellular signaling and chemo-mechanical coupling on the organ-scale.

In this paper, we introduce the first (homogenized) constrained mixture model that includes both intracellular signaling and chemo-mechanical coupling on the organ-scale for arbitrary geometries. Numerical implementation is based on open-source software packages (deal.ii (Arndt et al. 2021), Trilinos (The Trilinos Project Team 2021), SUNDIALS (Hindmarsh et al. 2005)). By making the model and the associated code available to the community, we aim to facilitate the study of how different aspects of cellular signal processing, such as (dysfunctional) intracellular signaling pathways or cell–cell communication, affect G&R on the organ-scale.

2 Mathematical model

2.1 Mechanics

Herein, we use the homogenized constrained mixture theory to describe the mechanics of soft biological tissues undergoing growth (changes in mass) and remodeling (changes in microstructure). Its main equations will be summarized in the following. For more details, the reader is referred to previous articles (Cyron et al. 2016; Braeu et al. 2017; Mousavi et al. 2019; Maes and Famaey 2023).

2.1.1 Kinematics

Using the general theory of nonlinear continuum mechanics, soft biological tissue can be modeled as a domain B_0 of material points $\boldsymbol{X}$ referred to as reference configuration. A time-dependent deformation maps the domain B_0 to its current configuration $B(s)$ at G&R time s. This means that each material point $\boldsymbol{X}$ is mapped to its current position $\boldsymbol{x}(s, \boldsymbol{X})$. Without loss of generality, we assume that the reference configuration coincides with the initial configuration, that is, $B_0 = B(s = 0)$. The so-called deformation gradient at time s is

$$\boldsymbol{F}(s) = \frac{\partial \boldsymbol{x}(s)}{\partial \boldsymbol{X}}. \tag{1}$$

The determinant of the deformation gradient, $\det(\boldsymbol{F})$, maps differential volume elements dV of the reference configuration to differential volume elements dv of the current configuration with

$$dv = \det(\boldsymbol{F}) dV. \tag{2}$$

Although we assume that each volume element is a mixture of N structurally significant constituents that are constrained to move together, each constituent has its individual stress-free reference configuration. For each constituent i, the deformation gradient $\boldsymbol{F}$ can be split into an inelastic part $\boldsymbol{F}^i_{gr}$ and an elastic part $\boldsymbol{F}^i_e$. $\boldsymbol{F}^i_{gr}$ represents the inelastic change of the tissue geometry due to G&R; it maps differential volume elements to a fictitious intermediate configuration that is not necessarily geometrically compatible. That is, neighboring volume elements in the intermediate configuration may overlap, or gaps may arise between them. The volume elements in the intermediate configuration are mapped by $\boldsymbol{F}^i_e$ to the current configuration. This happens such that the current configuration is always geometrically compatible and in mechanical equilibrium (Fig. 1).

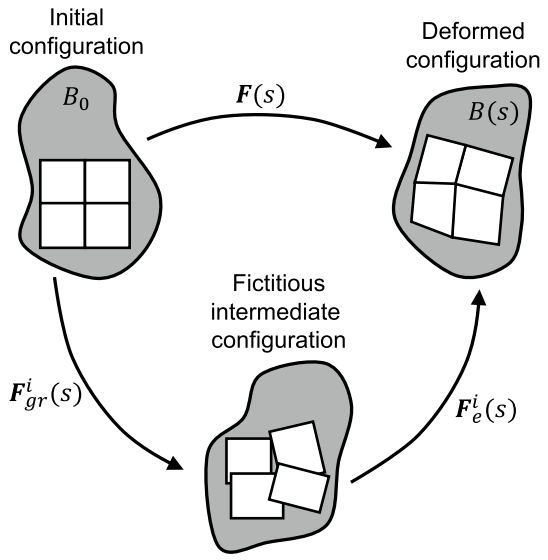

Fig. 1 Kinematics of the homogenized constrained mixture model: For each constituent i, the deformation gradient $\boldsymbol{F}$ can be split into an inelastic part $\boldsymbol{F}^i_{gr}$ and an elastic part $\boldsymbol{F}^i_e$

In the homogenized constrained mixture model, the elastic part of the deformation gradient of a constituent i at time s is given by

$$\mathbf{F}^i_e(s) = \mathbf{F}(s)\mathbf{F}_{gr}(s)^{-1} = \mathbf{F}(s)\mathbf{F}_g(s)^{-1}\mathbf{F}^i_r(s)^{-1}. \tag{3}$$

In this case, $\mathbf{F}$ is the deformation gradient of the mixture as a whole, $\mathbf{F}_g$ captures the inelastic change of geometry due to growth of all constituents together (change of tissue mass), and $\mathbf{F}^i_r$ captures the inelastic part of the deformation gradient resulting from remodeling due to mass turnover of each constituent i, where $\mathbf{F}_{gr} = \mathbf{F}^i_r\mathbf{F}_g$. Both $\mathbf{F}_g$ and $\mathbf{F}^i_r$ have to be defined via evolution equations described below.

2.1.2 Elasticity

Since growth and remodeling occur on long time scales, we solve the quasi-static equilibrium equation $div(\boldsymbol{\sigma}) = \mathbf{0}$ where $\boldsymbol{\sigma}$ is the Cauchy stress of the mixture. The strain energy of the mixture per unit reference volume is

$$\Psi = \sum_i \rho^i_0 W^i\left(\mathbf{C}^i_e\right). \tag{4}$$

Here, a superscript $i = e$ refers to elastin, $i = m$ to (circumferential) smooth muscle, and $i = c_0, c_{90}, c_{+\alpha_0}, c_{-\alpha_0}$ to 4 different collagen fiber families with the subscript indicating the angle with respect to a specific direction or axis (collectively summarized as c_j). A superscript c without an indication of an angle refers to a quantity for collagen as a whole. W^i denotes the strain energy per unit mass of constituent i, ρ^i_0 the reference apparent mass density of constituent i, and $\mathbf{C}^i_e = \mathbf{F}^{iT}_e\mathbf{F}^i_e$ the elastic part of the right Cauchy–Green tensor of constituent i. Since inelastic deformations, that is, G&R, do not contribute to the stored energy, the strain energy of the constituents only depends on the elastic part of the deformation.

The main constituents of the tissues considered herein are an isotropic elastin matrix, reinforced by several families of quasi-one-dimensional fibers of collagen and smooth muscle. The elastin matrix is modeled by the strain energy (Braeu et al. 2017; Maes and Famaey 2023)

$$W^e = \frac{\mu^e}{2}\left(\bar{I}^e_1 - 3\right) + \frac{\kappa}{2}\left(J^e_e - 1\right)^2 \tag{5}$$

where μ^e and κ are material parameters, $\bar{I}^e_1$ is the trace of the isochoric elastic Cauchy–Green tensor of elastin $\bar{\mathbf{C}}^e_e$ (including prestretch), and J^e_e is the determinant of the elastic part of the deformation gradient of elastin, $\mathbf{F}^e_e$. Note that $\bar{\mathbf{C}}^e_e = \left(J^e_e\right)^{-2/3}\mathbf{F}^{eT}_e\mathbf{F}^e_e$ (Holzapfel 2000). The quasi-one-dimensional fibers reinforcing the elastin matrix are modeled using Fung-type constitutive equations

$$W^\alpha = \frac{c^\alpha_1}{4c^\alpha_2}\left[\exp\left(c^\alpha_2\left(I^\alpha_{4e} - 1\right)^2\right) - 1\right] \tag{6}$$

with the superscript α referring to fiber constituents (i.e., $\alpha = m, c_j$), $I^\alpha_{4e} = \left(\mathbf{a}^\alpha_{gr}\right)^T\mathbf{C}^\alpha_e\mathbf{a}^\alpha_{gr}$ the fourth pseudo-invariant of the elastic Cauchy–Green tensor of constituent α and $\mathbf{a}^\alpha_{gr}$ its fiber orientation in the inelastically deformed intermediate configuration (Braeu et al. 2017; Gebauer et al. 2023). Note that $I^\alpha_{4e} = \left(\lambda^\alpha_e\right)^2$ with the elastic fiber stretch λ^α_e.

In certain cases, an additional active stress contribution of the smooth muscle cells may be considered and added in Eq. (4) as part of their strain energy. In this case, the stress of smooth muscle is the sum of the passive and active contributions. This is based on the assumption that active and passive contributions act in parallel with the contractile units embedded in a passive matrix (Murtada et al. 2010). Following Wilson et al. (2012), we model this contribution as

$$W^m_{act} = \frac{\sigma_{max}}{\rho_0(0)}y_{con}(s)\left[\lambda_{act} + \frac{\left(\lambda_{max} - \lambda_{act}\right)^3}{\left(\lambda_{max} - \lambda_0\right)^2}\right]. \tag{7}$$

Here, σ_{max} is the maximal active stress where the factor $y_{con}(s) \in [0, 1]$ modulates that stress according to intracellular signaling in a way described in Sect. 2.2. The stretches λ_{max} and λ_0 are the stretches at which force generation is maximal and minimal, respectively. The active smooth muscle stretch in the fiber direction λ_{act} is modeled as $\lambda_{act} = \lambda/\hat{\lambda}_{act}$ where λ is the total stretch in the fiber direction and $\hat{\lambda}_{act}$ represents the (evolving) reference configuration for active smooth muscle. We assume that this reference

configuration evolves due to fast muscle remodeling such that $\hat{\lambda}_{act} = \lambda$ (Wilson et al. 2012). Hence, $\lambda_{act} = \lambda/\hat{\lambda}_{act} = 1$ at all times s in the quasi-static equilibrium but $\partial\lambda_{act}/\partial\lambda = 1/\lambda$ (Braeu et al. 2017).

2.1.3 Growth

Different possibilities exist for defining the growth tensor $\mathbf{F}_g$. For simplicity, we choose an anisotropic growth tensor (Braeu et al. 2017) used in several studies (Mousavi and Avril 2017; Maes and Famaey 2023). In this case, the growth tensor in equation (3) can be written as

$$\mathbf{F}_g = \frac{\rho_0(s)}{\rho_0(0)}\mathbf{a}_g \otimes \mathbf{a}_g + \left(\mathbf{I} - \mathbf{a}_g \otimes \mathbf{a}_g\right) \tag{8}$$

with $\mathbf{a}_g$ the unit growth direction vector in the reference configuration, $\rho_0(s) = \sum_i \rho_0^i(s)$, and $J_g = \det(\mathbf{F}_g) = \rho_0(s)/\rho_0(0)$. For ease of comparison with previous studies, we chose to use transversely isotropic growth, noting that other ways of defining the growth tensor can be implemented in the model (Braeu et al. 2019).

2.1.4 Remodeling

The evolution equation for $\mathbf{F}_r^i$ in equation (3) is detailed in (Cyron et al. 2016) and (Maes and Famaey 2023); see these articles for details. Briefly, constituents are subject to continuous mass turnover where extant tissue mass is degraded and new mass is added. This process adapts the stress-free configuration of a constituent over time in a manner that is, in many respects, similar to inelastic deformations in viscoelasticity. Assuming new mass is added with a preferred stress $\boldsymbol{\sigma}_h^i$, this can effectively be captured for constituent i by an evolution equation

$$\left[\frac{\dot{\rho}_0^i}{\rho_0^i} + \frac{1}{T^i}\right]\left[\boldsymbol{\sigma}^i - \boldsymbol{\sigma}_h^i\right] = \left[\frac{\partial \boldsymbol{\sigma}^i}{\partial \mathbf{F}_e^i} : \left(\mathbf{F}_e^i \mathbf{L}_r^i\right)\right]_{\boldsymbol{F},\boldsymbol{F}_g=const.} \tag{9}$$

where $\mathbf{L}_r^i = \dot{\mathbf{F}}_r\left(\mathbf{F}_r\right)^{-1}$ represents the remodeling velocity gradient, $\dot{\rho}_0^i$ the rate of change of the referential mass density ρ_0^i, T^i the degradation time constant (Cyron et al. 2016; Maes and Famaey 2023; Gebauer et al. 2023; Braeu et al. 2017), and $\boldsymbol{\sigma}_h^i$ the assumed homeostatic target value for the Cauchy stress experienced by constituent i. We assume that only the fiber constituents representing collagen and smooth muscle ($\alpha = m, c_j$) are subject to G&R. Further assuming incompressible remodeling of the fibers, $\mathbf{F}_r^\alpha$ can be written as (Cyron et al. 2016)

$$\mathbf{F}_r^\alpha = \lambda_r^\alpha \mathbf{a}_0^\alpha \otimes \mathbf{a}_0^\alpha + \frac{1}{\sqrt{\lambda_r^\alpha}}\left(\mathbf{I} - \mathbf{a}_0^\alpha \otimes \mathbf{a}_0^\alpha\right) \tag{10}$$

with $\mathbf{a}_0^\alpha$ the fiber orientation in the reference configuration, and λ_r^α the inelastic remodeling stretch in the fiber direction, the only unknown. Hence, equation (9) can be simplified to a scalar evolution equation for $\dot{\lambda}_r^\alpha$ (see Appendix 1 in (Cyron et al. 2016) or (Maes and Famaey 2023) for a derivation)

$$\dot{\lambda}_r^\alpha = \left(\frac{\dot{\rho}_0^\alpha}{\rho_0^\alpha} + \frac{1}{T^\alpha}\right)\frac{\lambda_r^\alpha}{2I_{4e}^\alpha}\left[\frac{\partial \sigma^\alpha}{\partial I_{4e}^\alpha}\right]^{-1}\left(\sigma^\alpha - \sigma_h^\alpha\right). \tag{11}$$

This evolution equation can be integrated using standard time integration schemes; we use a forward Euler scheme. Following (Gebauer et al. 2023), the initial remodeling stretch is set to

$$\lambda_r^\alpha(0) = \frac{1}{\lambda_h^\alpha} \tag{12}$$

where λ_h^α represents the (homeostatic) deposition stretch of constituent α. This ensures a homeostatic initial state for constituents subject to G&R.

2.1.5 Initial configuration

The reference (and also initial) configuration with $\mathbf{F} = \mathbf{I}$ is typically not load-free; we assume that it is a homeostatic state. That is, the constituents subject to G&R (collagen ($\alpha = c_j$) and smooth muscle ($\alpha = m$)) are in their respective homeostatic state with an initial elastic part of the deformation gradient

$$\mathbf{F}_e^\alpha(s=0) = \lambda_h^\alpha \mathbf{a}_0^\alpha \otimes \mathbf{a}_0^\alpha + \frac{1}{\sqrt{\lambda_h^\alpha}}\left(\mathbf{I} - \mathbf{a}_0^\alpha \otimes \mathbf{a}_0^\alpha\right), \tag{13}$$

with λ_h^α the homeostatic stretch of collagen or smooth muscle, and $\mathbf{a}_0^\alpha$ the orientation of the respective fiber family in the reference configuration (Cyron et al. 2016; Braeu et al. 2019; Maes et al. 2019).

We determine the initial elastic stretch of elastin such that the constrained mixture as a whole is in mechanical equilibrium at $\mathbf{F} = \mathbf{I}$ for a given external loading (e.g., the blood pressure p_0 in a vessel) and that smooth muscle and collagen are in their respective homeostatic state (Bellini et al. 2014). An iterative approach is adopted to this end as detailed before (Mousavi and Avril 2017; Famaey et al. 2018; Maes et al. 2019). As a starting point for the iterations, an axial prestretch of elastin λ_z^e (estimated, e.g., from experimental data) is prescribed, and the initial elastin prestretch tensor is constructed assuming incompressibility (Famaey et al. 2018)

$$\mathbf{F}_{e,k=0}^e(s=0) = \begin{bmatrix} \frac{1}{\sqrt{\lambda_z^e}} & 0 & 0 \\ 0 & \frac{1}{\sqrt{\lambda_z^e}} & 0 \\ 0 & 0 & \lambda_z^e \end{bmatrix}. \tag{14}$$

At iteration step k, a mechanical equilibrium problem is solved based on an assumed elastic prestretch $\mathbf{F}_{e,k}^e(s=0)$

of elastin and yields for the constrained mixture as a whole the deformation gradient $\mathbf{F}_k$ compared to the desired initial state. The objective of the iterations is to achieve $\mathbf{F}_k = \mathbf{I}$, with k the iteration step, which indicates that the elastic prestretch of elastin has been chosen such that mechanical equilibrium is satisfied directly in the desired initial configuration. To achieve $\mathbf{F}_k = \mathbf{I}$, we compute for iteration step $k+1$ for elastin the assumed elastic prestretch $\mathbf{F}^e_{e,k+1}(s=0) = \mathbf{F}_k \mathbf{F}^e_{e,k}(s=0)$ and continue such iterations until we have found a $\mathbf{F}^e_{e,k+1}(s=0)$ which yields within a certain tolerance $\mathbf{F}_{k+1} = \mathbf{I}$ when solving the associated mechanical equilibrium problem. To facilitate the solution, external forces, predefined deposition stretches of the fiber constituents, and the axial deposition stretch of elastin are applied gradually in the first few iterations.

2.2 Intracellular signaling

As mentioned in Sect. 1, different approaches exist to model the intracellular signaling network of cells. We focus on the approach introduced by Kraeutler et al. (2010), which, despite its relative simplicity, has produced excellent results (Zeigler et al. 2016; Irons and Humphrey 2020; Gorick et al. 2022). This model uses a logic-based representation of the chemical reactions of cellular signal processing. Each chemical species is represented by a node y_i in a directed graph. Under normal conditions, the value of each node ranges in the continuous interval [0, 1] with 0 representing an inactive state and 1 a fully active state. However, diseases or pharmacological treatments might change the maximal activity level of a node to some different upper bound $y_{i,max}$, which will be discussed at the end of this section. In a graph of N nodes, the change of activation of node y_i is given by the following (nonlinear) ODE,

$$\frac{dy_i}{ds} = \frac{1}{\tau_i} f_i(y_1, \dots, y_N) y_{i,max} - y_i \tag{15}$$

where τ_i is a time constant (determining the reaction speed). To understand this model, consider the simplest case where node y_i depends only on one other node y_j. In this scenario, we distinguish 2 cases. First, y_j is assumed to have a positive (activating) effect on y_i, and $f_i(y_1, \dots, y_N)$ is assumed to reduce to

$$f_i(y_j) = f_i^+(y_j) := W_{ij} \frac{B_{ij} y_j^{n_{ij}}}{(B_{ij}-1)^{n_{ij}} + y_j^{n_{ij}}}. \tag{16}$$

This function is illustrated in Fig. 2a. Second, if y_j has a negative (inhibitory) effect on y_i, $f_i(y_1, \dots, y_N)$ is assumed to be (Kraeutler et al. 2010; Khalilimeybodi et al. 2020)

$$\begin{aligned} f_i(y_j) &= f_i^-(y_j) := 1 - f_i^+(y_j) \\ &= 1 - W_{ij} \frac{B_{ij} y_j^{n_{ij}}}{(B_{ij}-1)^{n_{ij}} + y_j^{n_{ij}}}. \end{aligned} \tag{17}$$

Activating functions of the type f_i^+ and inhibitory functions of the type f_i^- similarly form the main building blocks of a signaling network in more complex scenarios. They represent normalized Hill functions, with n_{ij} the

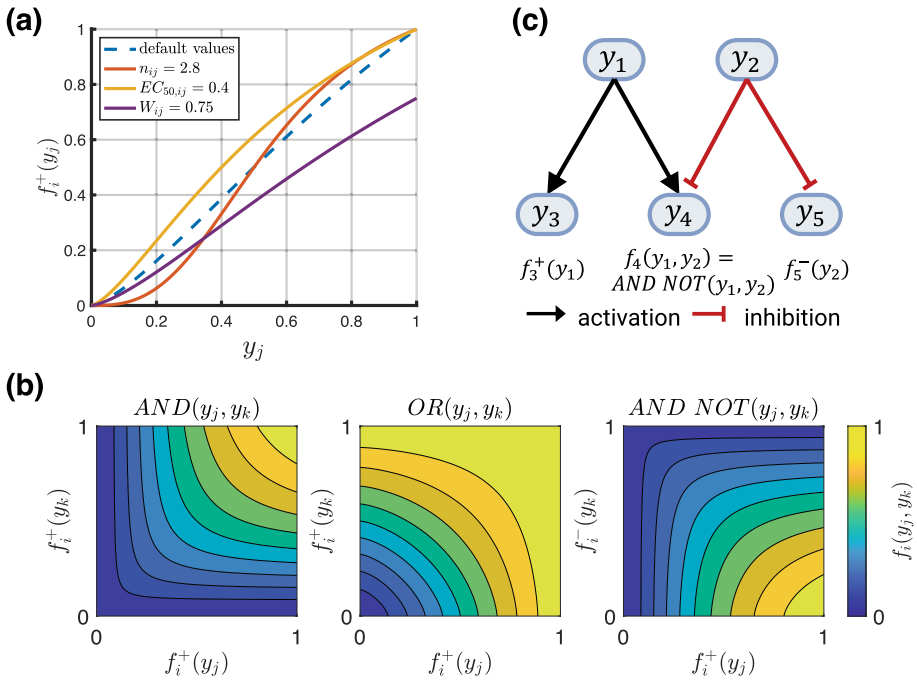

Fig. 2 **a** Dashed blue line shows activation function with default parameters $W_{ij} = 1$, $EC_{50,ij} = 0.5$, $n_{ij} = 1.4$, solid lines show variations of a single parameter (see legend) from the default case and its effect on the activation function. **b** Contour plots of logical operators described by the Eqs. (20) through (22). **c** A simple example of a signaling network with 2 input nodes (y_1, y_2) and 3 output nodes (y_3, y_4, y_5)

Hill coefficient, W_{ij} a reaction weight, and the constant B_{ij} enforcing the constraints

$$\begin{aligned} f_i^+(y_j = 0) &= 0, \\ f_i^+(y_j = 1) &= W_{ij}, \\ f_i^+(y_j = EC_{50,ij}) &= 0.5W_{ij} \end{aligned} \tag{18}$$

where $EC_{50,ij}$ is the value at which the activation function is half-maximal, i.e., $0.5W_{ij}$. Based on these constraints, B_{ij} is

$$B_{ij} = \frac{\left(EC_{50,ij}\right)^{n_{ij}} - 1}{2\left(EC_{50,ij}\right)^{n_{ij}} - 1} \tag{19}$$

with $\left(EC_{50,ij}\right)^{n_{ij}} < 0.5$ to ensure B_{ij} remains positive. If a node y_i depends on 2 nodes y_j and y_k, their combined effect is modeled by the logical operations 'AND,' 'OR,' and 'AND NOT' (Irons et al. 2022). In the first of these 3 cases, y_i is activated if both y_j and y_k are active and we have

$$f_i(y_j, y_k) = AND(y_j, y_k) := \frac{2f_i^+(y_j)f_i^+(y_k)}{f_i^+(y_j) + f_i^+(y_k)}. \tag{20}$$

In the second case, y_i is activated if y_j or y_k are active and we have

$$\begin{aligned} f_i(y_j, y_k) &= OR(y_i, y_j) \\ &:= f_i^+(y_j) + f_i^+(y_k) - f_i^+(y_j)f_i^+(y_k). \end{aligned} \tag{21}$$

In the third case, y_i is activated if y_j is active and y_k is inactive, and we have

$$\begin{aligned} f_i(y_j, y_k) &= AND\ NOT(y_i, y_j) \\ &:= \frac{2f_i^+(y_j)f_i^-(y_k)}{f_i^+(y_j) + f_i^-(y_k)} \\ &= \frac{2f_i^+(y_j)\left(1 - f_i^+(y_k)\right)}{f_i^+(y_j) + \left(1 - f_i^+(y_k)\right)}. \end{aligned} \tag{22}$$

These logical operators are illustrated in Fig. 2b. Note that Eqs. (20) and (22) deviate slightly from the original definitions (Kraeutler et al. 2010) and use a modification (Khalilimeybodi et al. 2020; Irons et al. 2022) to ensure proper scaling. This avoids issues where the classical 'AND' definition, $f_i^+(y_j)f_i^+(y_k)$, would lead to outputs that are too small if not scaled by $2/\left(f_i^+(y_j) + f_i^+(y_k)\right)$ (similar for 'AND NOT'). If a node y_i depends on several other nodes, their effect on y_i can be modeled by a recursive combination of the logical operators in Eqs. (20) through (22).

Based on the above model, the dynamics of the network are governed by a system of nonlinear ODEs. A simple example with 5 nodes is illustrated in Fig. 2c. The inputs could represent, e.g., the stress of the smooth muscle fibers (node y_1) and the nitric oxide concentration in the tissue (node y_2). The outputs could represent smooth muscle proliferation (node y_3), collagen production (node y_4), and the active contraction of smooth muscle (node y_5). By changing $y_{i,max}$, it is possible to simulate overexpression ($y_{i,max} > 1$) or knockdown ($y_{i,max} < 1$) of a species that could result from a pathogenic variant or a pharmacological treatment.

2.3 Continuum-scale biochemistry

2.3.1 Reaction-diffusion equations

One way cells communicate is by secreting signaling molecules that diffuse through the surrounding tissue and are sensed by neighboring cells (paracrine signaling) or the cell itself (autocrine signaling). We model such processes on the continuum scale by a coupled system of reaction-diffusion equations

$$\frac{\partial \rho_0^k}{\partial s} = D_0^k \nabla^2 \rho_0^k + r_0^k(\rho_0^1, ..., \rho_0^{N+M}) + s_0^k(s) \tag{23}$$

with superscript k denoting the kth species tracked by the model in the extracellular space ($k = 1, ..., N + M$). Here, ρ_0^k is the density in the reference configuration of species k, N is the number of structurally significant species (such as elastin, collagen, smooth muscle), and M is the number of relevant biochemical species, for example, signaling molecules secreted by the cells that are not structurally significant (see Fig. 3). D_0^k is the (constant) diffusion coefficient of species k, r_0^k represents possible reactions between species, and s_0^k is a potentially time-dependent source term. The source term can, for example, represent the exogenous addition of certain molecules or potential endocrine signals.

In the present coupled chemo-mechanical model (see below), the tracked species include the $N = 3$ structural constituents of the soft tissue (elastin, collagen, smooth muscle) and potentially the concentrations of M biochemical species, such that $k = e, c, m, ..., N + M$. For the 3 mechanically relevant constituents in the constrained mixture, we assume

$$\begin{aligned} D_0^c &= 0, \\ r_0^c &= \frac{1}{T^c}\frac{\rho_0^c(0)}{\rho_0^m(0)}\rho_0^m(s)(1 + \Delta\psi^c(s)) - \frac{1}{T^c}\rho_0^c(s), \\ s_0^c &= 0, \end{aligned} \tag{24}$$

$$\begin{aligned} D_0^m &= 0, \\ r_0^m &= \frac{1}{T^m}\rho_0^m(s)(1 + \Delta\psi^m(s)) - \frac{1}{T^m}\rho_0^m(s), s_0^m \quad = 0. \end{aligned} \tag{25}$$

For elastin, we assume no deposition, degradation, or diffusion, that is, $s_0^e = 0, r_0^e = 0, D_0^e = 0$. By contrast, we assume that collagen production depends on the intramural cell

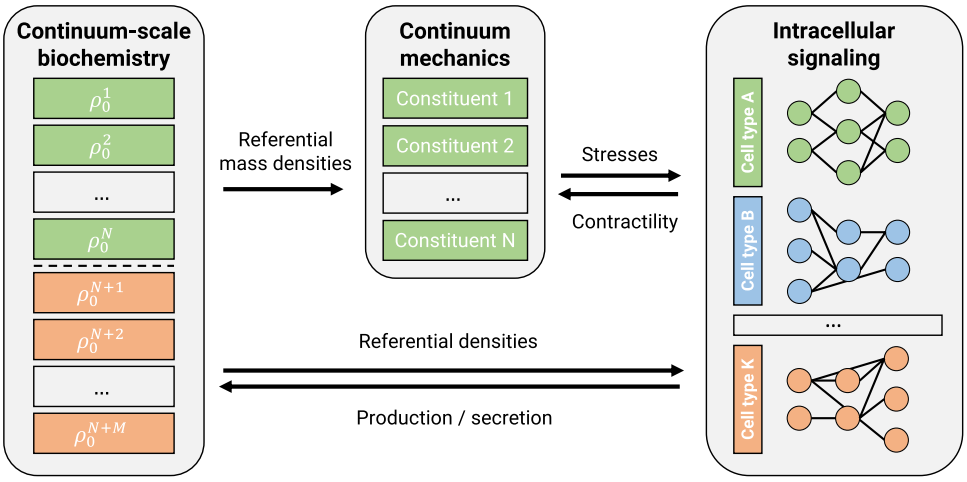

Fig. 3 Schematic coupling of mechanics, intracellular signaling, and reaction-diffusion problem (continuum-scale biochemistry). Only the first N species in the reaction-diffusion problem are assumed to be structurally significant (elastin, collagen, smooth muscle), whereas the last M species in the concentration vector are assumed to be structurally insignificant but to matter as an environment for the intracellular signaling processes

density since more cells, all producing collagen at a basal rate, leads to more collagen production. Here, the factor $\frac{\rho_0^c(0)}{\rho_0^m(0)}$ ensures a homeostatic state at G&R time $s = 0$. The T^i are degradation time constants and the $\Delta\psi^i(s)$ are normalized deviations of the relevant signaling network output of node y_i from its baseline level y_{i0} with (Irons et al. 2021)

$$\Delta\psi^i(s) = \frac{y_i(s) - y_{i0}}{y_{i0}}. \tag{26}$$

Following Irons et al. (2021, 2022), we assume a constant relative distribution of the different collagen fiber families, which leads to

$$\frac{\dot{\rho}_0^{c_j}}{\rho_0^{c_j}} = \frac{\dot{\rho}_0^c}{\rho_0^c}. \tag{27}$$

For simplicity, we assume that rates of collagen degradation and cell apoptosis are constant and $D_0^c = D_0^m = 0$.

Note that the purely mechanical homogenized constrained mixture model can be obtained by setting $D_0^\alpha = 0, s_0^\alpha = 0$ and

$$r_0^\alpha = \rho_0^\alpha(s) k^\alpha \frac{\sigma^\alpha(s) - \sigma_h^\alpha}{\sigma_h^\alpha}, \quad \alpha = m, c_j \tag{28}$$

where k^α is a rate parameter, $\sigma^\alpha(s)$ the current stress of fiber constituent α, and σ_h^α its homeostatic stress (Braeu et al. 2017; Gebauer et al. 2023). In this case, equation (27) need not hold.

2.3.2 Endothelium as a boundary condition

Endothelial cells can play important roles in sensing mechanical stimuli as well as in cell–cell communication. To include these effects, an endothelial cell layer with its own signaling network can be added to the model. For example, when modeling a blood vessel by a tube-like geometry, the endothelial cells line the inner surface. Using the current (inner) radius of the vessel, the mean wall shear stress can be computed based on

$$\tau_w = \frac{4\mu Q}{\pi a^3}, \tag{29}$$

assuming a fully developed laminar flow of a Newtonian fluid. Here, μ is the fluid viscosity, Q the flow rate, and a the current (inner) radius. Changes in wall shear stress can then serve as an input to the endothelial signaling network and trigger a response. For example, by releasing signaling molecules, which diffuse through the attached volume, the endothelial cells can communicate with intramural cells by providing potential inputs to their signaling networks. Note that the endothelial cells are assumed not to be structurally significant but instead form a (dynamic) Neumann-type boundary condition for the continuum-scale diffusion problem described in the previous section.

3 Implementation

3.1 Coupling

The equations in Sect. 2 related to mechanics, intracellular signaling, and continuum-scale biochemistry are coupled as illustrated in Fig. 3. For example, nodes in the intracellular signaling model determine mass production rates in the continuum-scale biochemistry model; these production rates govern the G&R that drives mechanical deformation; these deformations result in mechanical stress, which alters inputs for the intracellular signaling model.

Hence, the above equations must be solved as a coupled system. A geometry, for example, a tube representing a blood vessel, is discretized using the finite element method

(FEM) to solve both mechanical and continuum-scale biochemical reaction-diffusion problems. The intracellular signaling is computed at a representative selection of material points, that is, at each Gauss point in each finite element. To solve time-dependent problems, we discretize time into a finite number of times s^i with $i = 1, 2, 3, \ldots$. At each time s^i, we solve the coupled problem via the following sequence of steps:

1. FEM solution of mechanical problem based on system state at previous time s^{i-1},
2. Solution of ODE system for intracellular signaling (to steady state) at each Gauss point in the FEM discretization based on the mechanical state computed in the previous step (1) and mass concentrations from s^{i-1},
3. FEM solution of reaction-diffusion problem with mechanical state from step (1) and intracellular signaling state from step (2).

This staggered solution scheme allows a flexible combination of submodules. For example, in certain cases, only 2 of the 3 domains of the problem may actually be solved (e.g., only mechanics and diffusion or only mechanics and intracellular signaling).

3.2 Signaling network initialization

To determine normalized changes $\Delta\psi^i(s)$ of pathway output y_i in (26), its baseline pathway output y_{i0} is needed. This value can be determined by fixing all input nodes to a baseline value and simulating the dynamics of the network until a steady state at all output nodes has been reached.

3.3 Scaling of inputs for intracellular signaling

To use a continuum-level quantity q (e.g., smooth muscle stress) as an input to a node y_i in the intracellular signaling network, it has to be scaled to a suitable range. A simple way is to use a sigmoidal function

$$y_i(\Delta q) = \frac{1}{1 + e^{\beta - s_q \cdot \Delta q}}, \quad \text{with } \Delta q = \frac{q - q_h}{q_h} \tag{30}$$

where s_q determines the sensitivity to a perturbation from homeostatic, Δq represents the normalized deviation of q from its baseline (e.g., homeostatic) value, q_h, and β shifts the sigmoidal function horizontally such that $y_i(\Delta q = 0) = y_{i0}$ where y_{i0} is the baseline input at time $s = 0$. Figure 4 shows the influence of varying sensitivities on the scaling behavior.

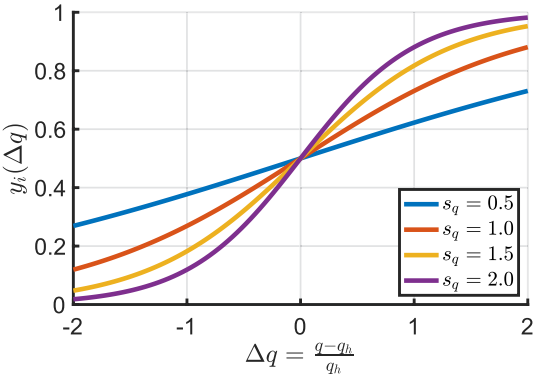

Fig. 4 Influence of sensitivity s_q on scaling behavior with $y_{i0} = 0.5$

3.4 Solvers

3.4.1 Mechanics

The nonlinear mechanical equilibrium problem was solved with a standard Newton solver from the Trilinos NOX package (The Trilinos Project Team 2021) (relative and absolute tolerances set to 10^{-12}). The linearized system was solved with a direct solver since all the problems studied were relatively small. The code was fully parallelized, supporting iterative linear solvers in case of larger problems.

3.4.2 Intracellular signaling

The system of ODEs modeling the intracellular signaling was solved using the SUNDIALS ARKode package (Hindmarsh et al. 2005; Gardner et al. 2022; Reynolds et al. 2023) with an explicit Runge–Kutta method of order 5 with relative and absolute tolerances of 10^{-10}. Because ARKode is a general-purpose ODE solver, there is no restriction on using a logic-based model of intracellular signaling.

3.4.3 Continuum-scale biochemistry

To solve the reaction-diffusion problem modeling continuum-scale biochemistry, the SUNDIALS ARKode package was used with an implicit Runge–Kutta method of order 3 in combination with a GMRES solver and an algebraic-multigrid (AMG) preconditioner. The relative and absolute tolerances of the time integration algorithm were set to 10^{-7} and 10^{-8}, respectively.

4 Numerical examples

4.1 Validation of mechanical model

To validate the implementation of the (uncoupled) homogenized constrained mixture model of G&R (Eq. (28)), we recreated the test cases presented in (Maes and Famaey 2023). See Appendix A.1 for details.

4.2 Growth and remodeling of murine aorta

In the following section, we use the coupled model to study the response of a mouse descending thoracic aorta to mild to moderate increases in pressure. To this end, we coupled the homogenized constrained mixture model to the signaling pathways introduced by Irons and Humphrey (2020) and further used and refined in (Irons et al. 2021, 2022). The network consisted of 50 nodes and 82 reactions and represents the behavior of synthetic intramural cells (SMCs and fibroblasts) as one might obtain from bulk qPCR or Western blotting. The network has 5 inputs (Angiotensin II (AngII), smooth muscle stress, flow-induced wall shear stress (WSS), integrins, stretch-activated channels (SACs)) and 4 outputs (Collagen-I, Collagen-III, cell proliferation, actomyosin activity). The outputs Collagen-I and Collagen-III were combined into one output for fibrillar collagen production by taking their average, noting that this is a simplification as collagen fiber formation is highly complex and the contribution of other matrix constituents is omitted (Kadler et al. 2008; Liu et al. 1997). For the network, we used the default parameters from (Irons and Humphrey 2020) unless noted otherwise, see Table 1. Inputs to the network were scaled using the sigmoidal function in equation (30). In Sect. 4.2.1, the only variable input to the signaling network is the smooth muscle stress, while in Sect. 4.2.2, the inputs are the smooth muscle stress, the nitric oxide, and endothelin-1 concentration.

The geometry and material parameters are based on (Irons et al. 2022; Latorre and Humphrey 2020) and represent a radially averaged single-layered arterial wall. Assuming axisymmetry, the artery was modeled as a cylindrical quarter segment similar to Sect. A.1.2 with original inner radius A, thickness H, and length L (Table 1). Axial displacements were fixed at both ends, and the growth direction defined as radial. The geometry was discretized using 216 quadratic finite elements: 2 in radial and axial directions, and 54 elements in the circumferential direction. The choice of 2 quadratic elements in the radial direction was motivated by a convergence study (Latorre and Humphrey 2020) that used 4 linear elements in radial direction. This was confirmed by a mesh convergence study. The geometry was prestressed using the algorithm described in Sect. 2.1.5 with an *in vivo* pressure of $p_0 = 14.0\ kPa$ until the average nodal displacement (normalized by the reference wall thickness) was less than 10^{-6} and a homeostatic state was (nearly) reached.

4.2.1 Cell signaling network - influence of AngII

In the first study, we compared how the presence of AngII via modification of the baseline network input $y_{AngII,0}$ influences arterial G&R when subjected to a sustained sudden increase in pressure of 15%. To quantify tissue adaption over time in response to the pressure perturbation, we computed the normalized trace of the tissue-level Cauchy stress and the normalized Cauchy stress of the smooth muscle cells at the midpoint of the vessel. Additionally, we show normalized wall thickness and inner radius. In this example, we assumed that flow rate Q remains constant at its initial value Q_0, yielding a flow rate ratio $\varepsilon = Q/Q_0 = 1$ and a pressure ratio $\gamma = p/p_0$, where p is the blood pressure after the pressure increase. It is known (Humphrey 2008) that blood vessels tend to regulate their inner radius in accordance with the flow rate (to maintain a certain wall shear stress) and their wall thickness in accordance with the inner pressure (to maintain a certain hoop stress). The markers at the right end of the graphs in the third and fourth columns represent adaptations that would be expected from these theoretical considerations. To maintain the initial wall shear stress, the (current) inner radius, a, should adapt to the limit $\varepsilon^{1/3}A$; to maintain a certain hoop stress, the (current) wall thickness, h, should adapt to the limit $\gamma\varepsilon^{1/3}H$ (Humphrey 2008).

As shown in Fig. 5a, exogenous AngII accelerated the adaptive response leading to a slight undershoot in the trace of the mixture-level Cauchy stress and the SMC stress before recovering baseline values (first 2 graphs). The adapted wall thickness was similar in both cases and close to the ideal adaptation based on the theoretical considerations (third graph). However, the adapted inner radii were different; the simulation with AngII showed a smaller radius (fourth graph). These results qualitatively aligned with experimental observations (Wu et al. 2014; Ruddy et al. 2009) that AngII increases collagen turnover, leading to accelerated remodeling. This is, for example, indicated by increased activation of the network nodes representing Col3mRNA and MMP2 (Fig. 5b). However, note that the simulations should be viewed as a proof of concept as the model still missed important aspects such as wall shear stress sensing, and the parameters were not calibrated to specific experimentally observed results.

Table 1 Parameters for coupled finite element simulations of growth and remodeling of a mouse descending thoracic aorta

Geometry and material parameters		
Mixture mass density	ρ_0	1050 kg/m^3
Initial mass fractions	ϕ^e	0.34
	ϕ^m	0.33
	ϕ^{c_0}, $\phi^{c_{90}}$, $\phi^{c_{\pm\alpha_0}}$	0.01848, 0.02211, 0.1447
Collagen fiber orientation	α_0	29.91°
Initial inner radius	A	0.647 mm
Initial wall thickness	H	0.04 mm
Initial length	L	0.04 mm
Elastin parameter	μ^e	89.71 kPa
Elastin bulk modulus	κ	$10\mu^e$
Collagen properties	c_1^c, c_2^c	234.9 kPa, 4.08
SMC properties	c_1^m, c_2^m	261.4 kPa, 0.24
Elastin axial deposition stretch	λ_z^e	1.62
Collagen deposition stretch	λ_h^c	1.25
SMC deposition stretch	λ_h^m	1.2
Mean survival times	T^m, T^c	70 $days$, 70 $days$
Initial blood pressure	p_0	14.0 kPa
Time step size	Δs	7 $days$
Continuum-scale biochemistry parameters		
SMC diffusion coefficient	D_0^m	0
Collagen diffusion coefficient	D_0^c	0
Cell signaling parameters		
SMC sensitivity to stress	s_σ	0.5
Reaction time constant	τ	1.0
Reaction edge weight	W	1.0
Half maximal activation	EC_{50}	0.55
Hill parameter	n	1.25
Maximal node activation	y_{max}	1.0
Initial input values	$y_{WSS,0}$	0.5
	$y_{integrins,0}$	0.2
	$y_{SACs,0}$	0.2
	$y_{stress,0}$	0.2
	$y_{AngII,0}$	{0.0, 0.1}

Geometry and material parameters are based on (Irons et al. 2022; Latorre and Humphrey 2020) and represent radially averaged values for a single-layered G&R model. Cell signaling parameters are based on (Irons and Humphrey 2020).

4.2.2 Endothelial cell–intramural cell communication

To ensure an adaptive response of the tissue, different cells and cell types need to communicate with each other, for example, through signaling molecules. One such example of cell–cell communication can be observed between endothelial cells (ECs) and intramural cells such as smooth muscle cells and fibroblasts. ECs in a blood vessel respond to changes in wall shear stress (WSS), τ_w, by changing their production of nitric oxide (NO) and endothelin-1 (ET1) (Sriram et al. 2016), which alter smooth muscle contractility (Hong et al. 2011) and collagen production (Hershey et al. 2012). Even though the interaction between the 2 cell types is much more complex, involving other signaling molecules and growth factors, we reduced their interaction to depend only on nitric oxide and endothelin-1. For the following simulations, we also included active SMC stresses, as NO and ET1 are potent regulators of active smooth muscle tone. The parameter regulating active cell contraction $y_{con}(s)$ used in Eq. (7) is computed via a sigmoidal scaling function (Eq. (30)) with sensitivity 1.0, $\Delta\psi^{act}(s)$ is the normalized change of the output node in the signaling network regulating actomyosin activity, and $y_{con,0} = 0.5$.

In addition to cells within the vessel wall, we included an EC layer on the inner surface as described in Sect. 2.3.2. We used the same intracellular signaling pathway as in Sect. 4.2.1 but extracted the part that represents endothelial cell behavior and assigned it to the ECs, while the remaining

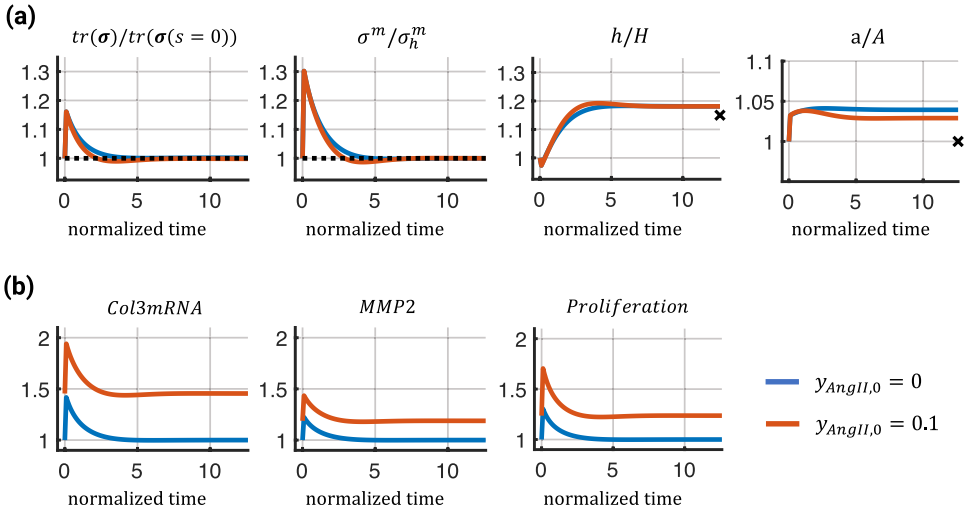

Fig. 5 Mechanical and network responses of the coupled finite element model in response to a 15% pressure increase under 2 different levels of exogenous AngII over normalized time (s/T^m). Top (**a**) shows, from left to right, the normalized trace of the mixture-level Cauchy stress, normalized Cauchy stress of the smooth muscle fibers, normalized wall thickness, and normalized inner radius. The dashed lines represent baseline values and markers represent ideal adaptations based on theoretical considerations (see text). Bottom (**b**) shows fold changes in activation levels of 3 network nodes with respect to the baseline ($y_{AngII,0} = 0$)

network was assigned to the intramural cells, which now have NO and ET1 inputs instead of wall shear stress (Fig. 6).

The ECs respond to changes in wall shear stress (WSS) by producing NO and ET1, which then diffuse through the vessel wall with diffusion coefficients D_0^{NO} and D_0^{ET1}, but are consumed or degrade with mean survival times T^{NO} and T^{ET1} assuming first-order kinetics (Vaughn et al. 1998; Liu et al. 2008). The parameter values are based on previous experimentally determined values (Malinski et al. 1993) or theoretical studies (Vaughn et al. 1998; Liu et al. 2008; Kavdia and Popel 2006) and listed in Table 2, including references where available. Compared to NO, data on ET1 are scarce. Hence, we used a generic value for the diffusion coefficient of a peptide, and the baseline production rate was assumed to be of a similar order of magnitude as NO.

One challenge in this scenario was the boundary conditions. Similar to (Vaughn et al. 1998; Kavdia and Popel 2006), we relate the NO and ET1 production rates $\dot{Q}_0^{NO}$ and $\dot{Q}_0^{ET1}$ to the influx of these 2 quantities and prescribed corresponding boundary conditions,

$$\dot{Q}_0^{NO}(1+\Delta\psi^{NO}(s)) = D_0^{NO}\frac{\partial[NO]_{lumen}}{\partial r} - D_0^{NO}\frac{\partial[NO]_{tissue}}{\partial r} \tag{31}$$

$$\dot{Q}_0^{ET1}(1+\Delta\psi^{ET1}(s)) = D_0^{ET1}\frac{\partial[ET1]_{lumen}}{\partial r} - D_0^{ET1}\frac{\partial[ET1]_{tissue}}{\partial r}. \tag{32}$$

Here, $\Delta\psi^{NO}(s)$ and $\Delta\psi^{ET1}(s)$ are outputs from the EC signaling network regulating NO and ET1 production, while $\frac{\partial[NO]}{\partial r}$ and $\frac{\partial[ET1]}{\partial r}$ represent concentration gradients in the radial direction (into the lumen or into the tissue). Some of the NO and ET1 produced by the ECs will be released into the

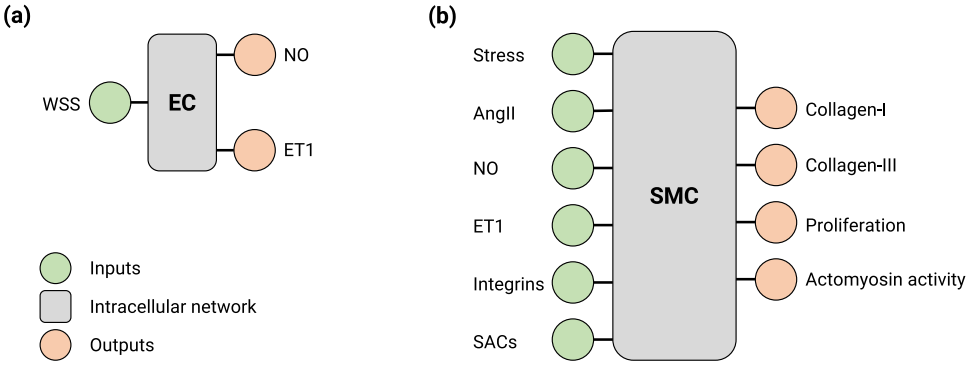

Fig. 6 Schematic illustration of the inputs and outputs of the endothelial cell signaling network (**a**) and the intramural cell signaling network (**b**). NO production by ECs increases with increases in WSS; ET1 production increases with decreases in WSS

Table 2 Additional parameters for the coupled finite element simulations including endothelial cell–intramural cell communication

Material parameters			
SMC active contribution	σ_{max}	170 kPa	Irons et al. (2022)
	λ_{max}	1.1	Irons et al. (2022)
	λ_0	0.4	Irons et al. (2022)
Continuum-scale biochemistry parameters			
Nitric oxide diffusion coefficient	D_0^{NO}	3300 $\mu m^2/s$	Malinski et al. (1993); Vaughn et al. (1998)
Nitric oxide mean survival time	T^{NO}	15s	Malinski et al. (1993); Vaughn et al. (1998)
Nitric oxide production rate	$\dot{Q}_0^{NO}$	$5.3 \cdot 10^{-14}\ \frac{\mu mol}{\mu m^2 s}$	Vaughn et al. (1998)
Endothelin-1 diffusion coefficient	D_0^{ET1}	300 $\mu m^2/s$	–
Endothelin-1 mean survival time	T^{ET1}	120s	Saleh et al. (2016)
Endothelin-1 production rate	$\dot{Q}_0^{ET1}$	$1.0 \cdot 10^{-14}\ \frac{\mu mol}{\mu m^2 s}$	see text
Fraction diffusing into tissue	η	0.2	see text
Outflux fraction	ξ	0.9	see text
Cell signaling parameters			
EC sensitivity to wall shear stress	s_τ	0.5	–
SMC sensitivity to nitric oxide	s_{NO}	0.75	–
SMC sensitivity to endothelin-1	s_{ET1}	0.75	–
SMC sensitivity to changes in acto-myosin activity	s_{con}	1.0	–

Active smooth muscle parameters are based on (Irons et al. 2022)

lumen and transported away by convection, whereas some parts will be released into the tissue and transported via diffusion. We estimate the fraction of NO and ET1 that is released into the tissue to be $\eta = 0.2$ (Vaughn et al. 1998; Liu et al. 2008; Zhang and Edwards 2006). This resulted in the following boundary conditions on the inner surface of the vessel,

$$-D_0^{NO}\frac{\partial [NO]_{tissue}}{\partial r} = \eta \dot{Q}_0^{NO}(1 + \Delta\psi^{NO}(s)) \tag{33}$$

$$-D_0^{ET1}\frac{\partial [ET1]_{tissue}}{\partial r} = \eta \dot{Q}_0^{ET1}(1 + \Delta\psi^{ET1}(s)). \tag{34}$$

Additionally, a second boundary condition is needed at the outer surface of the vessel wall. Because the outer surface of the vessel is not impermeable to NO and ET1 and the vessel is surrounded by perivascular tissue, an outflux boundary condition was prescribed. Previous studies (Vaughn et al. 1998; Liu et al. 2008; Zhang and Edwards 2006) found that the concentration profile of NO is nearly linear over short distances comparable to the wall thickness of the studied vessel. Hence, we assumed that the outflux is proportional to the influx with a proportionality factor ξ. Here, we assumed that $\xi = 0.9$, which resulted in a nearly linear concentration profile of NO and ET1 and concentrations on the order of 100-300 nM (Chen et al. 2008).

To analyze the influence of EC–transmural cell communication on tissue adaptation, we first applied a sudden 10% pressure increase that was sustained over time. The additional stimulus through NO and ET1, mediated by wall shear stress sensing of the endothelial cells, led to an almost ideal adaptation in inner radius and wall thickness (Fig. 7a). After a slight undershoot, the stress of the SMCs slowly returned back toward the baseline value while a slight offset in the trace of the tissue-level Cauchy stress remained.

With the addition of the EC layer and the NO-mediated cell–cell communication, the model could now also account for changes in blood flow rate. To study the response of the vessel to a change in (blood) flow, we increased the flow rate Q by 10% ($\varepsilon = Q/Q_0 = 1.1$) while keeping the blood pressure constant ($\gamma = p/p_0 = 1$). As illustrated in Fig. 7b, the vessel dilated to reduce the wall shear stress close to the value $\varepsilon^{1/3}A \approx 1.03A$ with $\varepsilon = Q/Q_0 = 1.1$. The stresses slowly returned toward their baseline values with a slight offset in the trace of the tissue-level Cauchy stress. After a slight decrease, the thickness of the vessel remained unchanged compared to the initial thickness, different from the idealized adaptation limit $\gamma\varepsilon^{1/3}H$.

4.3 Instabilities for high sensitivities

When analyzing the results from the previous Sects. 4.2.1 and 4.2.2, we found that simulations can exhibit instabilities at longer simulation times (normalized time > 20). These instabilities resulted in a continuous deviation of the stresses from their baseline values, ultimately leading to divergence of the simulations. To further probe this behavior, we replaced the complex intracellular signaling pathway with a highly simplified model consisting of only 3 nodes:

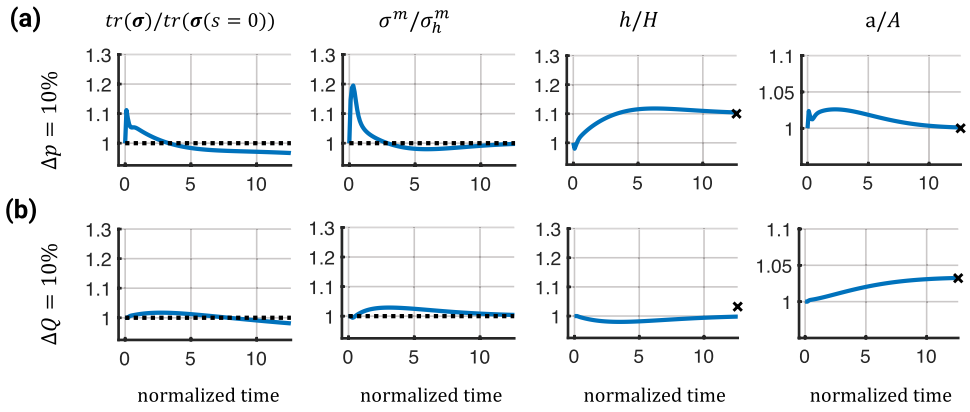

Fig. 7 Evolution of selected quantities over normalized time (s/T^m) in response to a 10% pressure increase (**a**) or a 10% flow increase (**b**). Dashed lines represent baseline values and markers indicate theoretical ideal adaptations for the different cases

one input node (smooth muscle stress) that activated 2 outputs (cell proliferation and collagen production). For this network, $\tau = 1$, $W = 1$, $EC_{50} = 0.5$, $n = 1.4$, and $y_{max} = 1$. Smooth muscle stress as an input for the intracellular signaling network was scaled to the range [0, 1] by a sigmoidal function with an adjustable sensitivity as described in Eq. (30). Five sensitivities, s_σ, ranging from 0.25 to 1.25, were tested for a 5%, 10%, and 15% pressure increase.

Figure 8 shows that low sensitivities (e.g., $s_\sigma = 0.25$) led to unbound growth and continuous distension of the vessel. This is in agreement with a prior observation (Braeu et al. 2017) for low rate parameters, k^i, using a homogenized constrained mixture model without intracellular signaling. In fact, too low sensitivities s_σ led to mechanobiological instabilities (Cyron and Humphrey 2014; Cyron et al. 2014). By contrast, higher sensitivities led to a regime of mechanobiological stability, marked by the convergence of the vessel geometry to a new stable mechanobiological equilibrium state. Higher sensitivities decreased the offset in the trace of the tissue-level Cauchy stress compared to its initial value. This is in agreement with the concept of mechanobiological adaptivity (Cyron and Humphrey 2014; Cyron et al. 2014). The response in case of corresponding pressure decreases is shown in Fig. 11 in Appendix B.1.

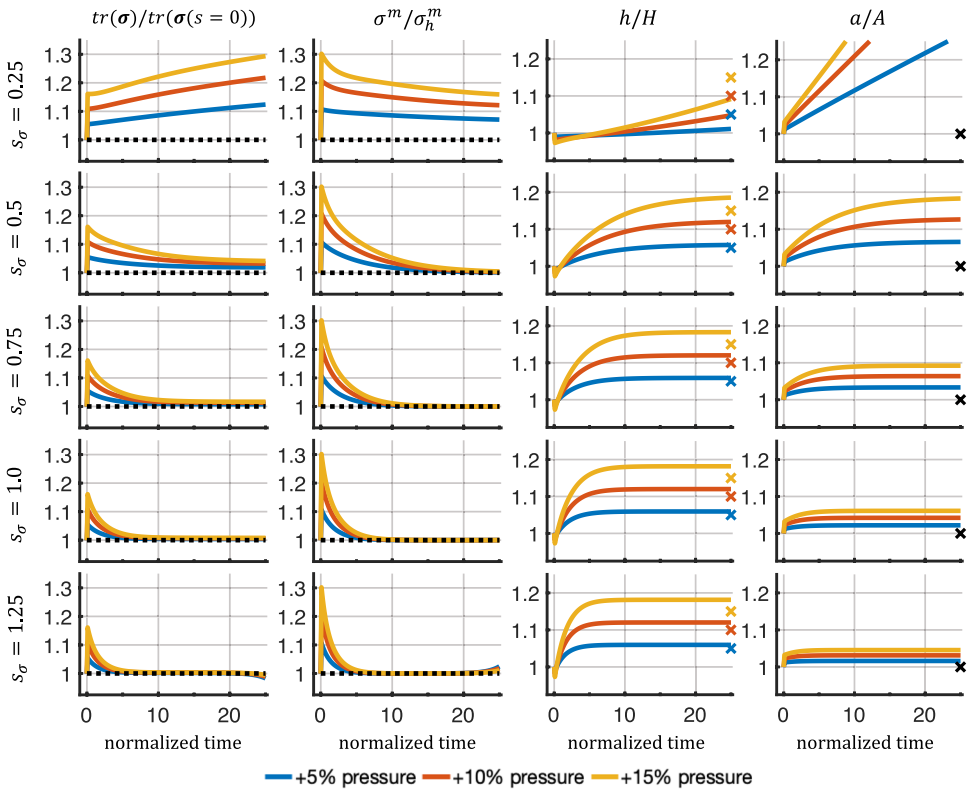

Fig. 8 Evolution of selected quantities over normalized time (s/T^m) for varying sensitivities in response to different step increases in pressure (5%, 10%, 15%). Dashed lines represent baseline values, and markers indicate ideal adaptations based on applied pressure perturbation

For the highest sensitivity ($s_\sigma = 1.25$), instabilities in the stresses were observed toward the end of the simulation. Interestingly, these instabilities seem independent of the magnitude of the applied perturbations and were not immediately visible in geometric quantities (thickness and inner radius). To ensure that the instabilities were not introduced through the coupling of the different submodules, we tested the uncoupled homogenized constrained mixture model with the same geometry, material parameters, and a pressure increase of 15%. We found similar instabilities when increasing the rate parameters, k^i, to high values, which is comparable to increasing the sensitivity s_σ (Fig. 12 in Appendix B.2). Further testing using the uncoupled homogenized constrained mixture model with the geometry and material parameters described in Braeu et al. (2017) again revealed instabilities for high rate parameters when subjected to a pressure increase of 15% (Fig. 13 in Appendix B.2).

Furthermore, we tested if the sensitivities leading to stable adaptations ($s_\sigma = \{0.5, 0.75, 1.0\}$) would show instabilities under pressure perturbations of 30% and 50% (Fig. 14 in Appendix B.3). No stress instabilities were observed in these cases. However, a sensitivity of 0.5 seemed insufficient to achieve a stable state within the observed time period. Further tests of reducing the time step size, gradual application of the pressure perturbations, or using stricter tolerances did not remove the instabilities.

5 Discussion

5.1 Intracellular signaling

Adding intracellular signaling networks to the homogenized constrained mixture model to replace phenomenological parameters for mass production with quantities rooted in intracellular signaling allows a more detailed study of how specific intracellular processes influence tissue homeostasis. While the example presented in Sect. 4.2.1 should be understood as a proof of principle, it showed how signaling networks could be used to study how G&R is affected by a different biochemical environment, in this case, the presence of AngII. In these cases, it can be difficult to know how certain chemicals influence phenomenological parameters for collagen production and cell proliferation a priori. Furthermore, the complex intracellular signaling networks can also exhibit internal feedback loops, which can lead to a more dynamic adaptation process, such as the undershoot of the stresses or the reduction in radius observed in Fig. 5.

In addition to the influence of exogenous factors, it becomes possible to study how specific defects in intracellular signaling, such as a genetic defect, change the behavior on the organ-scale. Notably, some defects in intracellular signaling may have little effect on the organ-scale due to compensatory mechanisms in the signaling networks. Generally, biological signaling networks benefit from this kind of robustness as their surrounding is inherently noisy and they have to operate under various conditions. This may explain why a unique parametrization of the (logic-gated) signaling networks is challenging to obtain but also might not be necessary to promote a stable adaptation (Irons et al. 2022).

Moreover, the intracellular signaling pathways can be created with the amount of detail necessary for the studied problem. For example, with the highly simplified signaling networks used in Sect. 4.3, we observed that a range of (stress) sensitivities can promote a stable adaptive response. Similar results were obtained with purely mechanical homogenized constrained mixture models, where a specific range of rate parameters led to stable adaptations (Appendix B.2). However, the coupled model allows a more straightforward interpretation of the physiological meaning and origin of the parameters.

5.2 Effects of cell–cell communication

It is known that different cell types collectively contribute to tissue homeostasis. In fact, 4 cell types appear to be sufficient to form a minimal tissue unit: (I) the cell type performing the core function (for example, smooth muscle cells in the aorta, hepatocytes in the liver, etc.), (II) endothelial cells, (III) fibroblast-like stromal cells, and (IV) tissue-resident macrophages. According to Adler et al. (2018), the last 3 cell types are nearly universal to all tissues and mainly support the primary cell type in their function.

In this work, we included endothelial cells in addition to the intramural cells. The combination of both cell types communicating with each other via NO and ET1 produced different results (Fig. 7a) compared to a model where only intramural cells were included (Fig. 5). The additional influence of the NO and ET1, regulated by the wall shear stress sensed by the ECs, allowed the vessel to adjust its inner radius toward ideal values. This underlines one of the many important functions of the endothelium. It also allowed the study of tissue adaptation in response to changes in flow (Fig. 7b), which, to the best of our knowledge, was so far not included in 3-dimensional simulations using the homogenized constrained mixture model.

Overall, coupled models have the potential to study different combinations of cell types forming basic tissue units. For example, including macrophages could help to elucidate their role in promoting tissue homeostasis (Zhou et al. 2018). In particular, studying dysfunctional communication between different cell types and the resulting effects on tissue adaptation could improve our understanding of when tissue can adapt and under which circumstances it cannot. This might help to identify potential pharmacological targets or treatments to improve clinical outcomes.

The flexibility of the model to include several cell types offers great potential but can also add considerable complexity. Ultimately, though, it is a trade-off between the amount of detail to include, and the resulting complexity to still generate interpretable and actionable results or hypotheses, which can then be tested experimentally.

5.3 Long-term instabilities

Long-term instabilities might arise when high rate parameters, k^i, or high sensitivities, s_σ, are used in combination with curved geometries such as the cylinder wall studied herein. Interestingly, this was independent of the magnitude of the applied pressure perturbation. We found that adding diffusion of the cells (i.e., $D_0^m > 0$ in Eq. (25)), which could represent cell migration, was able to stabilize the system for all times considered and even larger values of k^i and s_σ (not shown). However, this lacks a biological foundation, at least in the case of elastic arteries, where migration of SMCs is constrained by the elastic laminae, and fibroblasts primarily remain in the adventitia. Nevertheless, these results might indicate that the homogenized constrained mixture model is not able to homogenize the transmural stress gradients and maintain them toward the end of the adaptation process.

The question remains as to what exactly causes these instabilities potentially resulting from persistent transmural stress gradients. The instabilities might be inherent to the homogenized constrained mixture model, caused by basic assumptions, or of a purely numerical nature. For example, Taber and Humphrey (2001) showed that radially varying material parameters help to homogenize the transmural stresses. Moreover, Azeloglu et al. (2008) showed that a gradient in the proteoglycan concentration also provides a mechanism by which transmural stresses can be homogenized, and cells might modify proteoglycan synthesis and degradation in response to altered stresses. These observations are not included in current implementations. Additionally, we used a radially averaged, single-layered approach to model the arterial wall. However, the arterial wall consists of 3 distinct layers, the endothelium, media, and adventitia, the latter 2 bearing the majority of the load. This bi-layered structure can significantly influence transmural stresses. For example, Bellini et al. (2014) showed that different material properties in the medial and adventitial layer can protect the media from excessive stresses when pressure increases above normal as the adventitia carries more load at elevated pressure levels.

As evidenced by the different possibilities listed above, transmural stress gradients are important and complex, and different mechanisms have been identified that influence their distribution. More work is needed to understand this better and examine what exactly causes the long-term instabilities in the homogenized constrained mixture model when large rate parameters or sensitivities are used and how this influences transmural stress distributions.

6 Conclusion and outlook

In this paper, we proposed the first homogenized constrained mixture model of soft tissue growth and remodeling that couples mechanics, continuum-scale biochemistry, and intracellular signaling. Our model allows one to replace phenomenological growth parameters of purely mechanical homogenized constrained mixture models with models of specific intracellular processes. This allows one to relate a behavior on the organ-scale to specific intracellular processes. Moreover, it facilitates physiological interpretations of the simulations. Importantly, the continuum-scale biochemistry module in our framework also allows us to capture long-range communication between cells, e.g., the communication between endothelial cells and transmural cells via nitric oxide and endothelin-1.

The computational cost of our coupled multiphysical model was around 3–5 times higher than that of a purely mechanical homogenized constrained mixture model of soft tissue G&R. The majority of the additional cost can be attributed to the implicit time integration scheme used in the diffusion submodule and solving the intracellular signaling networks. The former could potentially be improved by using different time integration schemes. The computational cost of solving the intracellular signaling strongly depends on their size and complexity. However, the additional level of detail will always incur an additional computational cost.

In the future, the model could be used to study specific aspects of cell–cell communication or the effect of genetic defects on growth and remodeling. Moreover, it provides insights into how biochemical processes on the cell-level can translate into macroscopic changes on the tissue level. While the presented results are promising, more research is needed to make the coupled model applicable to real-world applications. Independent of the coupling to intracellular signaling networks, the instabilities in the homogenized constrained mixture model occurring during longer simulations with large rate parameters or stress sensitivities need to be addressed to find their cause.

Appendix A

A.1 Validation of mechanical model

The implementation of the (uncoupled) homogenized constrained mixture model of G&R (Eq. (28)) is validated based on test cases presented in (Maes and Famaey 2023): a unit cube with either a displacement or traction boundary

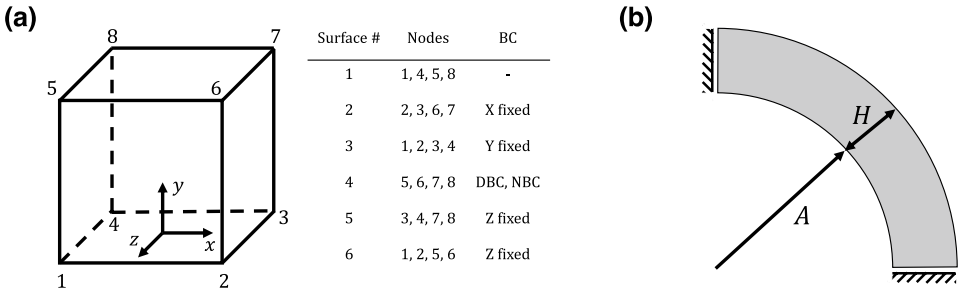

Fig. 9 Test cases used for verification based on Maes and Famaey (2023). **a** Schematic drawing of a unit cube and the corresponding boundary conditions (BC) for each surface. DBC - Dirichlet boundary condition, NBC - Neumann boundary condition. **b** Schematic of arterial growth and remodeling test case

condition and a cylindrical tube as a simplified model of arterial adaptations to a pressure increase, see Fig. 9. The material parameters for both cases are largely identical and summarized in Table 3. Note that while the elastin content is higher than *in vivo*, the material parameters suggested by Maes and Famaey (2023) fall into physiological relevant ranges and are comparable to parameters used in previous studies such as (Wilson et al. 2012) who fitted experimental data from (Vande Geest et al. 2004) or (Latorre and Humphrey 2018) who fitted experimental data from (Bersi et al. 2016).

A.1.1 Unit cube

In the first test case, a unit cube (Fig. 9a) was discretized with a single finite element. The cube consisted of a slightly compressible elastin matrix and 4 families of collagen fibers in the *yz*-plane, including angles of 0°, 90°, +22.5°, and −22.5° relative to the *y*-axis, respectively. The boundary conditions on the surfaces are as follows: Surface 1 is free, surface 2 is fixed in *x*-direction, surface 3 is fixed in *y*-direction, surface 5 is fixed in *z*-direction, and surface 6 is fixed in *z*-direction. The displacement or stress boundary condition is applied in *y*-direction to surface 4. The growth direction is defined as the *x*-direction.

Dirichlet boundary condition In the first test, a displacement of 0.5 *mm* in the *y*-direction was applied to the upper surface of the cube (surface 4), corresponding to a stretch of 1.5. In this case, no prestressing for the initial configuration was applied since the deposition stretches were assumed to be $\lambda_h^c = \lambda_z^e = 1.0$. The obtained results compared well to ones from Fig. 2(I) in (Maes and Famaey 2023), see Fig. 10a.

Neumann boundary condition In the second test, a Cauchy traction was applied to the upper surface of the cube (surface 4). Since the deposition stretches of collagen and elastin were $\lambda_h^c = 1.1$ and $\lambda_z^e = 1.2$, respectively, the iterative prestress algorithm described in Sect. 2.1.5 was used to determine the final prestretch of elastin. To this end, a homeostatic Cauchy stress, σ_0, of 0.1 *MPa* was applied in *y*-direction to surface 4, and the prestress algorithm was run for 20 iterations (equivalent to the procedure in (Maes and Famaey 2023)). In the second step, the stress was increased by 20% to 0.12 *MPa*, and the material was allowed to remodel for 100 steps, equivalent to 1000 days. The obtained results compared well with ones from Fig. 2(II) in (Maes and Famaey 2023), see Fig. 10b.

Table 3 Geometry and material parameters for the test cases based on Maes and Famaey (2023). DBC - Dirichlet boundary condition

Geometry - Cube		
Edge length	L	1 *mm*
Homeostatic Cauchy stress	σ_0	0.1 *MPa*
Geometry - Artery		
Initial inner radius	A	5 *mm*
Initial wall thickness	H	1.3 *mm*
Initial length	L	1.3 *mm*
Initial pressure	p_0	0.01 *MPa*
Material parameters		
Initial mass fractions	ϕ^e	0.8
	$\phi^{c_0}, \phi^{c_{90}}, \phi^{c_{\pm\alpha_0}}$	0.05
Collagen fiber orientation	α_0	22.5°
Elastin parameter	μ^e	0.07625 *MPa*
Elastin bulk modulus	κ	0.7625 *MPa*
Collagen properties	c_1^c, c_2^c	1.156 *MPa*, 1.23
Elastin axial deposition stretch	λ_z^e	1.0 (cube with DBC), 1.2
Collagen deposition stretch	λ_h^c	1.0 (cube with DBC), 1.1
Collagen rate parameter	k^c	$0.1/T^c$
Mean survival time	T^c	101 *days*
Time step size	Δs	10 *days*

A.1.2 Arterial wall remodeling

Next, consider an idealized model of an artery with a simple cylindrical geometry. The inner radius was $A = 5$ mm, the wall thickness $H = 1.3$ mm, and the length $L = 1.3$ mm in the reference configuration. Again, 4 families of collagen fibers were included with angles 0°, 90°, +22.5°, and −22.5° relative to the

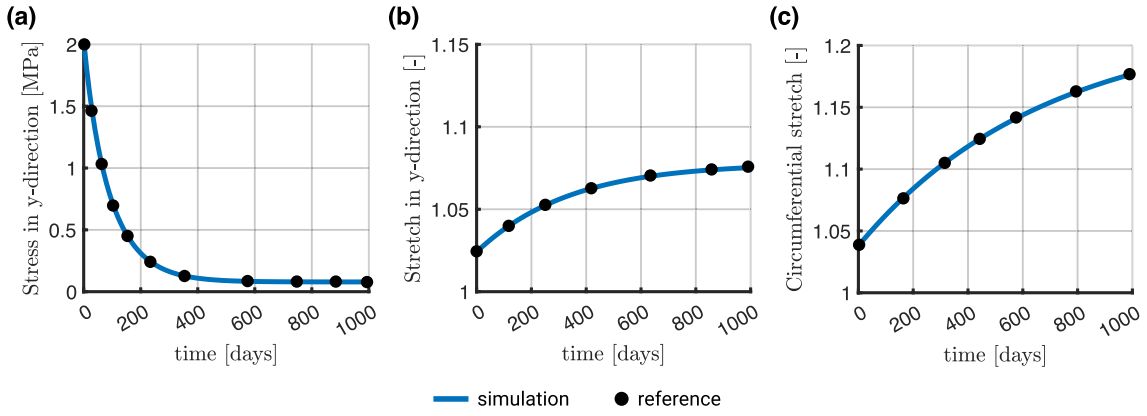

Fig. 10 Results of our simulations (continuous line) vs. reference data from Maes and Famaey (2023) (black markers). **a** Cube subjected to displacement boundary condition. **b** Cube subjected to (Cauchy) traction boundary condition. **c** Circumferential stretch at the inner surface of the cylinder wall in response to a 50% pressure increase. The reference data were obtained using WebPlotDigitizer (Rohatgi 2022)

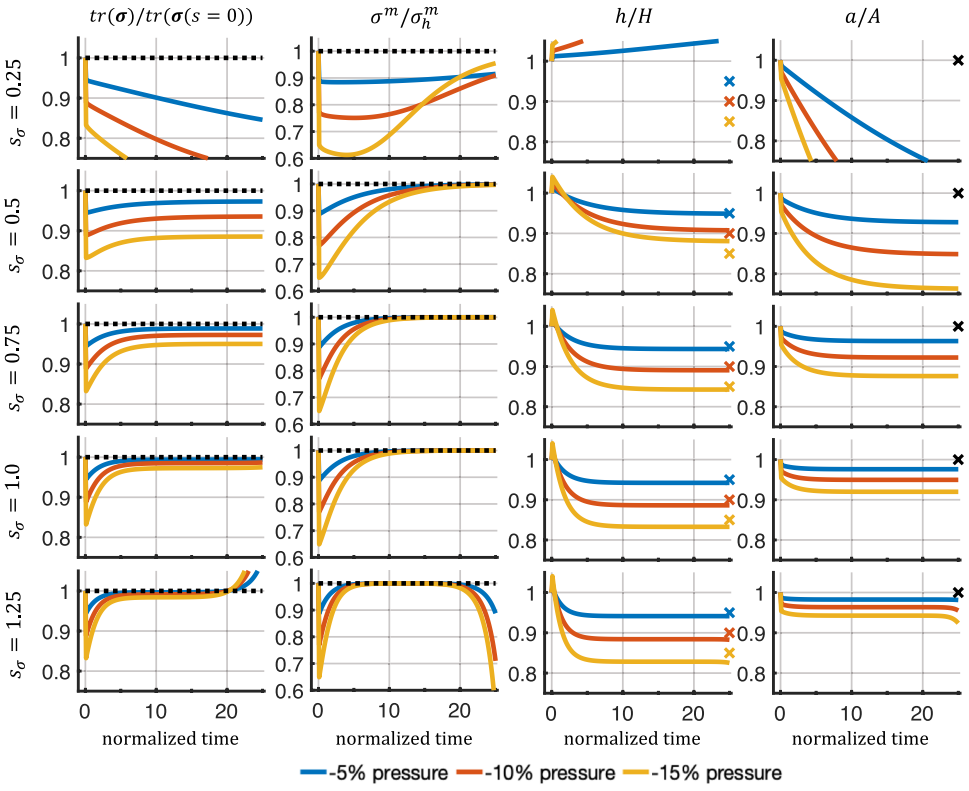

Fig. 11 Evolution of selected quantities over normalized time (s/T^m) for varying sensitivities in response to step decreases in pressure (-5%, -10%, -15%). Notably, for low sensitivities, we observed immediate instability. For very high sensitivities, we again observed long-term instabilities. Both are qualitatively similar to what was observed for pressure increases

circumferential direction. Due to axisymmetry, the geometry was reduced to a quarter cylinder (Fig. 9b) and discretized with 448 linear (hexahedral) finite elements, with 4 elements in radial and axial directions and 28 in the circumferential direction. The growth direction is defined as the radial direction. Material parameters are listed in Table 3. To obtain a prestressed configuration in equilibrium, the iterative prestress algorithm described in Sect. 2.1.5 was used with an *in vivo* pressure of 10 kPa for 20 iterations. Once this configuration was obtained, a 50% pressure increase to 15 kPa (in the current configuration) was applied, and the artery was allowed to grow and remodel over 100 time steps with a time step size of 10 days. Figure 10c depicts the circumferential stretch evolution on the cylinder's inner surface and compares the result to the one presented in (Maes and Famaey 2023) (Fig. 4(I)).

Appendix B

B.1 Response to decreased pressure

We studied how the model discussed in Sect. 4.3 responded to a decrease (rather than an increase) in internal pressure in the cylinder representing a blood vessel. Specifically, we studied pressure decreases of 5%, 10%, and 15%. Similar to the cases of pressure increases, a low sensitivity could not restore a new homeostatic state, while high sensitivities led to instabilities toward the end of the simulation.

B.2 Instabilities of purely mechanical model for large rate parameters

To examine possible reasons for the long-term instabilities observed in Sect. 4.3 for high sensitivities, we simulated comparable scenarios but with a purely mechanical homogenized constrained mixture model (based on Eq. (28)) using the geometry and material parameters listed in Table 1 and in Table 4. Figures 12 and 13 reveal that also in the case of a purely mechanical homogenized constrained mixture model, long-term instabilities arise for high rate parameters, which are comparable to high sensitivities in the model used in Sect. 4.3. This suggests that the long-term instabilities observed in Sect. 4.3 are not specific for the coupled model presented herein but are rather inherent already to the mechanical homogenized constrained mixture model (likely only in 3-dimensional geometries because they have never been reported in

Table 4 Geometry and material parameters for the simple model aorta used in Braeu et al. (2017)

Mixture mass density	ρ_0	1050 kg/m^3
Initial mass fractions	ϕ^e	0.23
	ϕ^m	0.15
	$\phi^{c_0}, \phi^{c_{90}}, \phi^{c_{\pm\alpha_0}}$	0.062, 0.062, 0.248
Collagen fiber orientation	α_0	45°
Initial inner radius	A	10 mm
Initial wall thickness	H	1.41 mm
Initial length	L	1.41 mm
Elastin parameter	μ^e	72 J/kg
Elastin bulk modulus	κ	$10\mu^e$
Collagen properties	c_1^c, c_2^c	568 J/kg, 11.2
SMC properties	c_1^m, c_2^m	7.6 J/kg, 0.8
Elastin axial deposition stretch	g_z^e	1.25
Collagen deposition stretch	λ^c	1.062
SMC deposition stretch	λ^m	1.1
Mean survival times	T^c, T^m	101 *days*, 101 *days*
Initial blood pressure	p_0	14.0 *kPa*
Time step size	Δs	10.1 *days*

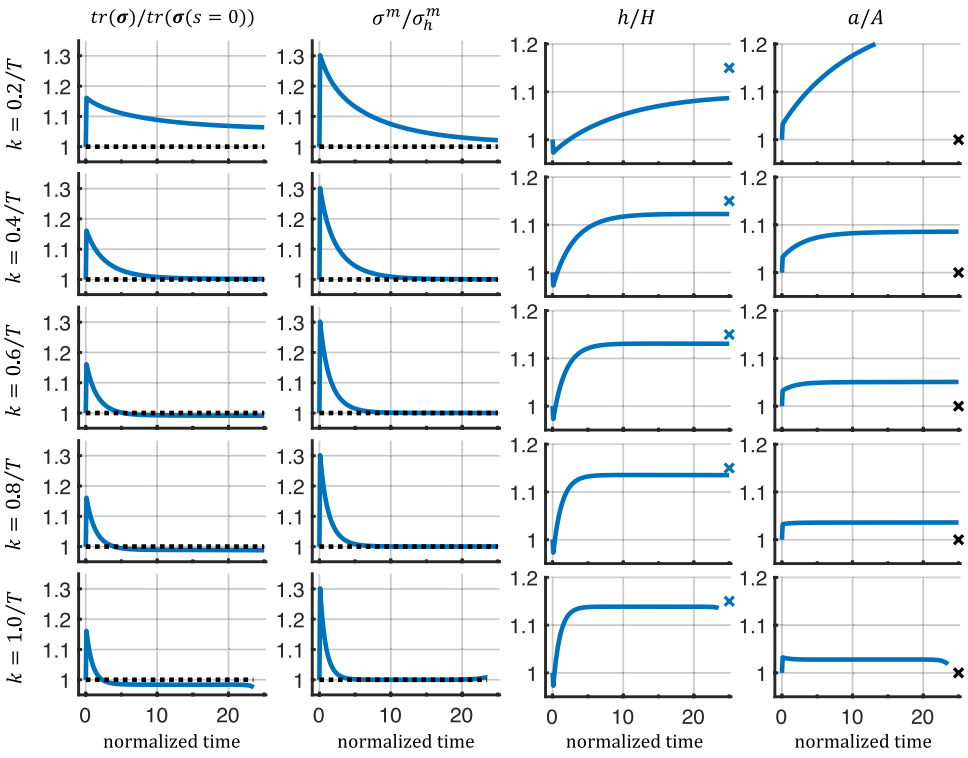

Fig. 12 Evolution of selected quantities over normalized time (s/T^m) in a purely mechanical homogenized constrained mixture model following a pressure increase of 15% with rate parameters $k = k^m = k^c$ ranging from $0.2/T$ to $1.0/T$ with $T = T^m = T^c$ the mean survival time of smooth muscle and collagen, respectively

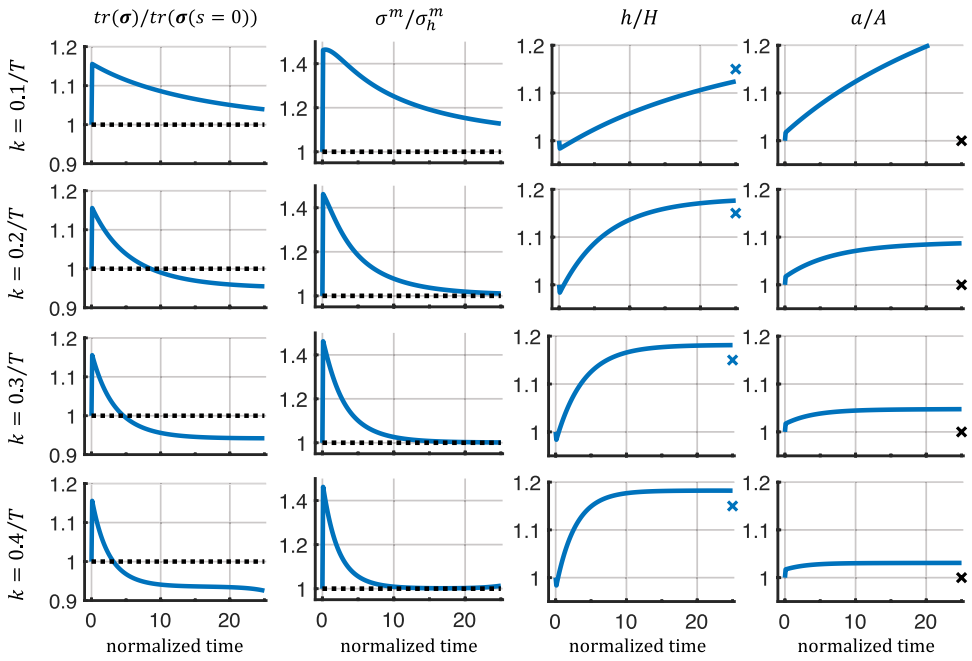

Fig. 13 Evolution of selected quantities over normalized time (s/T^m) in a purely mechanical homogenized constrained mixture model following a pressure increase of 15% with the parameters from Braeu et al. (2017) (Table 4), using rate parameters $k = k^m = k^c$ ranging from $0.1/T$ to $0.4/T$ with $T = T^m = T^c$ the mean survival time of smooth muscle and collagen, respectively

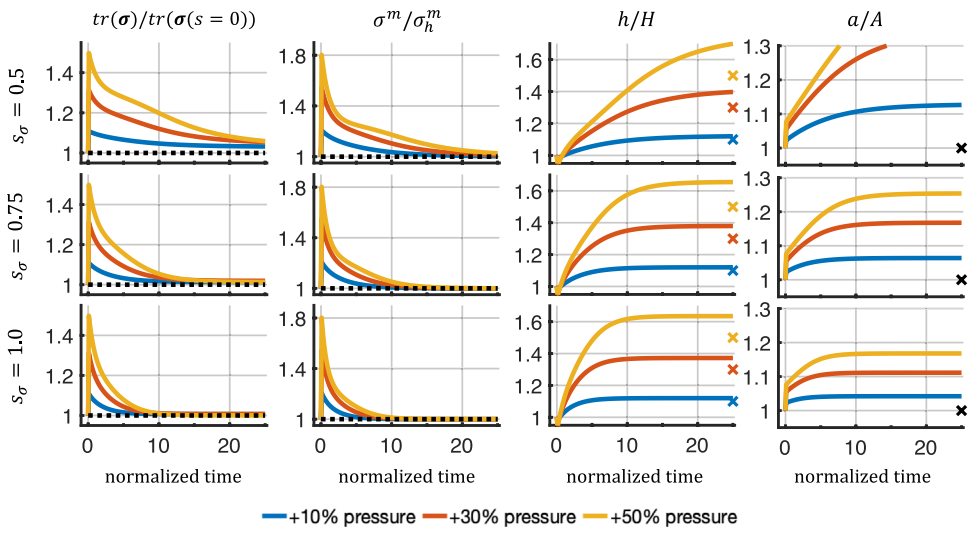

Fig. 14 Evolution of selected quantities over normalized time (s/T^m) in a coupled multiphysical model with pressure increases of 10%, 30%, and 50%. The model parameters are listed in Table 1

quasi-2-dimensional models using, e.g., membrane finite elements).

B.3 Response to higher step increases in pressure

We repeated the simulations presented in Sect. 4.3 with higher pressure increases of 30% and 50% for the previously stable (stress) sensitivities of 0.5, 0.75, and 1.0. Figure 14 shows that no long-term instabilities arise for high sensitivities (though for the sensitivity 0.5 and a pressure increase by 30% and 50%, a stable state is not reached within the observed period). Our results support the hypothesis that the magnitude of the pressure perturbation is not the decisive factor for the long-term instabilities observed in Sect. 4.3. It should be noted, of course, that *in vivo* responses to large increases in pressure are expected to elicit an inflammatory response Latorre et al. (2021), not modeled here.

Acknowledgements This work was supported by the International Graduate School for Science and Engineering (IGSSE) of the Technical University of Munich and NIH grant R01 HL155105.

Funding Open Access funding enabled and organized by Projekt DEAL. The funding was provided by National Institutes of Health having Grant No. R01 HL155105.

Code availability The code used for this article is available at https://github.com/pauknerd/multiscale_mixture.

Declarations

Conflict of interest The authors declare that they have no conflict of interest.

References

Adler M, Mayo A, Zhou X, Franklin RA, Jacox JB, Medzhitov R, Alon U (2018) Endocytosis as a stabilizing mechanism for tissue homeostasis. Proc Natl Acad Sci. https://doi.org/10.1073/pnas.1714377115

Alberts B, Johnson A, Lewis J, Morgan D, Raff M, Roberts K, Walter P (2017) Molecular biology of the cell. W.W. Norton Company: New York

Arndt D, Bangerth W, Davydov D, Heister T, Heltai L, Kronbichler M, Maier M, Pelteret JP, Turcksin B, Wells D (2021) The deal. II finite element library: design, features, and insights. Comput Math Appl 81:407–422. https://doi.org/10.1016/j.camwa.2020.02.022

Azeloglu EU, Albro MB, Thimmappa VA, Ateshian GA, Costa KD (2008) Heterogeneous transmural proteoglycan distribution provides a mechanism for regulating residual stresses in the aorta. Am J Physiol Heart Circ Physiol 294(3):H1197–H1205. https://doi.org/10.1152/ajpheart.01027.2007

Baek S, Rajagopal KR, Humphrey JD (2006) A theoretical model of enlarging intracranial fusiform aneurysms. J Biomech Eng 128(1):142–149. https://doi.org/10.1115/1.2132374

Bellini C, Ferruzzi J, Roccabianca S, Di Martino ES, Humphrey JD (2014) A microstructurally motivated model of arterial wall mechanics with mechanobiological implications. Ann Biomed Eng 42(3):488–502. https://doi.org/10.1007/s10439-013-0928-x

Bersi MR, Bellini C, Wu J, Montaniel KR, Harrison DG, Humphrey JD (2016) Excessive adventitial remodeling leads to early aortic maladaptation in angiotensin-induced hypertension. Hypertension 67(5):890–896. https://doi.org/10.1161/HYPERTENSIONAHA.115.06262

Braeu FA, Aydin RC, Cyron CJ (2019) Anisotropic stiffness and tensional homeostasis induce a natural anisotropy of volumetric growth and remodeling in soft biological tissues. Biomech Model Mechanobiol 18(2):327–345. https://doi.org/10.1007/s10237-018-1084-x

Braeu FA, Seitz A, Aydin RC, Cyron CJ (2017) Homogenized constrained mixture models for anisotropic volumetric growth and remodeling. Biomech Model Mechanobiol 16(3):889–906. https://doi.org/10.1007/s10237-016-0859-1

Chen K, Pittman RN, Popel AS (2008) Nitric oxide in the vasculature: where does it come from and where does it go? a quantitative perspective. Antioxid Redox Signal 10(7):1185–1198. https://doi.org/10.1089/ars.2007.1959

Cyron C, Humphrey J (2014) Vascular homeostasis and the concept of mechanobiological stability. Int J Eng Sci 85:203–223. https://doi.org/10.1016/j.ijengsci.2014.08.003

Cyron CJ, Aydin RC, Humphrey JD (2016) A homogenized constrained mixture (and mechanical analog) model for growth and remodeling of soft tissue. Biomech Model Mechanobiol 15(6):1389–1403. https://doi.org/10.1007/s10237-016-0770-9

Cyron CJ, Wilson JS, Humphrey JD (2014) Mechanobiological stability: a new paradigm to understand the enlargement of aneurysms? J R Soc Interface 11(100):20140680. https://doi.org/10.1098/rsif.2014.0680

Famaey N, Vastmans J, Fehervary H, Maes L, Vanderveken E, Rega F, Mousavi SJ, Avril S (2018) Numerical simulation of arterial remodeling in pulmonary autografts. ZAMM - J Appl Math Mech / Zeitschrift für Angewandte Mathematik und Mechanik 98(12):2239–2257. https://doi.org/10.1002/zamm.201700351

Gardner DJ, Reynolds DR, Woodward CS, Balos CJ (2022) Enabling new flexibility in the SUNDIALS suite of nonlinear and differential/algebraic equation solvers. ACM Trans Math Softw 48(3):1–24. https://doi.org/10.1145/3539801

Gebauer AM, Pfaller MR, Braeu FA, Cyron CJ, Wall WA (2023) A homogenized constrained mixture model of cardiac growth and remodeling: analyzing mechanobiological stability and reversal. Biomech Model Mechanobiol 22(6):1983–2002. https://doi.org/10.1007/s10237-023-01747-w

Gierig M, Wriggers P, Marino M (2021) Computational model of damage-induced growth in soft biological tissues considering the mechanobiology of healing. Biomech Model Mechanobiol 20(4):1297–1315. https://doi.org/10.1007/s10237-021-01445-5

Gorick CM, Saucerman JJ, Price RJ (2022) Computational model of brain endothelial cell signaling pathways predicts therapeutic targets for cerebral pathologies. J Mol Cell Cardiol 164:17–28. https://doi.org/10.1016/j.yjmcc.2021.11.005

Hershey JWB, Sonenberg N, Mathews MB (2012) Principles of translational control: an overview. Cold Spring Harb Perspect Biol 4(12):a011528–a011528. https://doi.org/10.1101/CSHPERSPECT.A011528

Hill MR, Philp CJ, Billington CK, Tatler AL, Johnson SR, O'Dea RD, Brook BS (2018) A theoretical model of inflammation- and mechanotransduction-driven asthmatic airway remodelling. Biomech Model Mechanobiol 17(5):1451–1470. https://doi.org/10.1007/s10237-018-1037-4

Hindmarsh AC, Brown PN, Grant KE, Lee SL, Serban R, Shumaker DE, Woodward CS (2005) SUNDIALS: suite of nonlinear and differential/algebraic equation solvers. ACM Trans Math Softw 31(3):363–396. https://doi.org/10.1145/1089014.1089020

Holzapfel GA (2000) Nonlinear solid mechanics: a continuum approach for engineering. Wiley, New York

Hong F, Haldeman BD, Jackson D, Carter M, Baker JE, Cremo CR (2011) Biochemistry of smooth muscle myosin light chain kinase. Arch Biochem Biophys 510(2):135. https://doi.org/10.1016/J.ABB.2011.04.018

Horvat N, Virag L, Holzapfel GA, Sorić J, Karšaj I (2019) A finite element implementation of a growth and remodeling model for soft biological tissues: verification and application to abdominal

aortic aneurysms. Comput Methods Appl Mech Eng 352:586–605. https://doi.org/10.1016/J.CMA.2019.04.041
Humphrey JD (2008) Mechanisms of arterial remodeling in hypertension. Hypertension 52(2):195–200. https://doi.org/10.1161/HYPERTENSIONAHA.107.103440
Humphrey JD, Rajagopal KR (2002) A constrained mixture model for growth and remodeling of soft tissues. Math Model Methods Appl Sci 12(3):407–430. https://doi.org/10.1142/S0218202502001714
Irons L, Estrada AC, Humphrey JD (2022) Intracellular signaling control of mechanical homeostasis in the aorta. Biomech Model Mechanobiol 21(5):1339–1355. https://doi.org/10.1007/s10237-022-01593-2
Irons L, Humphrey JD (2020) Cell signaling model for arterial mechanobiology. PLOS Comput Biol 16(8):e1008161. https://doi.org/10.1371/journal.pcbi.1008161
Irons L, Latorre M, Humphrey JD (2021) From transcript to tissue: multiscale modeling from cell signaling to matrix remodeling. Ann Biomed Eng 49(7):1701–1715. https://doi.org/10.1007/s10439-020-02713-8
Kadler KE, Hill A, Canty-Laird EG (2008) Collagen fibrillogenesis: fibronectin, integrins, and minor collagens as organizers and nucleators. Curr Opin Cell Biol 20(5):495–501. https://doi.org/10.1016/j.ceb.2008.06.008
Karakaya C, van Asten JGM, Ristori T, Sahlgren CM, Loerakker S (2022) Mechano-regulated cell-cell signaling in the context of cardiovascular tissue engineering. Biomech Model Mechanobiol 21(1):5–54. https://doi.org/10.1007/s10237-021-01521-w
Kavdia M, Popel AS (2006) Venular endothelium-derived NO can affect paired arteriole: a computational model. Am J Physiol Heart Circ Physiol 290(2):H716–H723. https://doi.org/10.1152/ajpheart.00776.2005
Khalilimeybodi A, Paap AM, Christiansen SLM, Saucerman JJ (2020) Context-specific network modeling identifies new crosstalk in β-adrenergic cardiac hypertrophy. PLOS Comput Biol 16(12):e1008490. https://doi.org/10.1371/journal.pcbi.1008490
Kraeutler MJ, Soltis AR, Saucerman JJ (2010) Modeling cardiac β -adrenergic signaling with normalized-Hill differential equations: comparison with a biochemical model. BMC Syst Biol 4(1):157. https://doi.org/10.1186/1752-0509-4-157
Latorre M, Bersi MR, Humphrey JD (2019) Computational modeling predicts immuno-mechanical mechanisms of maladaptive aortic remodeling in hypertension. Int J Eng Sci 141:35–46. https://doi.org/10.1016/J.IJENGSCI.2019.05.014
Latorre M, Humphrey JD (2018) Modeling mechano-driven and immuno-mediated aortic maladaptation in hypertension. Biomech Model Mechanobiol 17(5):1497–1511. https://doi.org/10.1007/s10237-018-1041-8
Latorre M, Humphrey JD (2020) Fast, rate-independent, finite element implementation of a 3D constrained mixture model of soft tissue growth and remodeling. Comput Methods Appl Mech Eng 368:113156. https://doi.org/10.1016/j.cma.2020.113156
Latorre M, Spronck B, Humphrey JD (2021) Complementary roles of mechanotransduction and inflammation in vascular homeostasis. Proc R Soc A Math Phys Eng Sci 477:2245. https://doi.org/10.1098/rspa.2020.0622
Liu X, Srinivasan P, Collard E, Grajdeanu P, Zweier JL, Friedman A (2008) Nitric oxide diffusion rate is reduced in the aortic wall. Biophys J 94(5):1880–1889. https://doi.org/10.1529/biophysj.107.120626
Liu X, Wu H, Byrne M, Krane S, Jaenisch R (1997) Type III collagen is crucial for collagen I fibrillogenesis and for normal cardiovascular development. Proc Natl Acad Sci 94(5):1852–1856. https://doi.org/10.1073/pnas.94.5.1852
Maes L, Famaey N (2023) How to implement constrained mixture growth and remodeling algorithms for soft biological tissues. J Mech Behav Biomed Mater 140:105733. https://doi.org/10.1016/j.jmbbm.2023.105733
Maes L, Fehervary H, Vastmans J, Mousavi SJ, Avril S, Famaey N (2019) Constrained mixture modeling affects material parameter identification from planar biaxial tests. J Mech Behav Biomed Mater 95:124–135. https://doi.org/10.1016/j.jmbbm.2019.03.029
Maes L, Vervenne T, Van Hoof L, Jones EAV, Rega F, Famaey N (2023) Computational modeling reveals inflammation-driven dilatation of the pulmonary autograft in aortic position. Biomech Model Mechanobiol 22(5):1555–1568. https://doi.org/10.1007/s10237-023-01694-6
Malinski T, Taha Z, Grunfeld S, Patton S, Kapturczak M, Tomboulian P (1993) Diffusion of nitric oxide in the aorta wall monitored in situ by porphyrinic microsensors. Biochem Biophys Res Commun 193(3):1076–1082. https://doi.org/10.1006/bbrc.1993.1735
Marino M, Pontrelli G, Vairo G, Wriggers P (2017) A chemo-mechano-biological formulation for the effects of biochemical alterations on arterial mechanics: the role of molecular transport and multiscale tissue remodelling. J R Soc Interface 14(136):20170615. https://doi.org/10.1098/rsif.2017.0615
Mousavi SJ, Avril S (2017) Patient-specific stress analyses in the ascending thoracic aorta using a finite-element implementation of the constrained mixture theory. Biomech Model Mechanobiol 16(5):1765–1777. https://doi.org/10.1007/s10237-017-0918-2
Mousavi SJ, Farzaneh S, Avril S (2019) Patient-specific predictions of aneurysm growth and remodeling in the ascending thoracic aorta using the homogenized constrained mixture model. Biomech Model Mechanobiol 18(6):1895–1913. https://doi.org/10.1007/s10237-019-01184-8
Murtada SI, Kroon M, Holzapfel GA (2010) A calcium-driven mechanochemical model for prediction of force generation in smooth muscle. Biomech Model Mechanobiol 9(6):749–762. https://doi.org/10.1007/s10237-010-0211-0
Reynolds DR, Gardner DJ, Woodward CS, Chinomona R (2023) ARKODE: a flexible IVP solver infrastructure for one-step methods. ACM Trans Math Softw 49(2):1–26. https://doi.org/10.1145/3594632
Rohatgi A (2022) Webplotdigitizer: version 4.6
Ruddy JM, Jones JA, Stroud RE, Mukherjee R, Spinale FG, Ikonomidis JS (2009) Differential effects of mechanical and biological stimuli on matrix metalloproteinase promoter activation in the thoracic aorta. Circulation 120(11):S262–S268. https://doi.org/10.1161/CIRCULATIONAHA.108.843581
Saleh L, Verdonk K, Visser W, van den Meiracker AH, Danser AHJ (2016) The emerging role of endothelin-1 in the pathogenesis of pre-eclampsia. Ther Adv Cardiovasc Dis 10(5):282–293. https://doi.org/10.1177/1753944715624853
Saucerman JJ, Brunton LL, Michailova AP, McCulloch AD (2003) Modeling β-adrenergic control of cardiac myocyte contractility in silico. J Biol Chem 278(48):47997–48003. https://doi.org/10.1074/jbc.M308362200
Sriram K, Laughlin J, Rangamani P, Tartakovsky D (2016) Shear-induced nitric oxide production by endothelial cells. Biophys J 111(1):208–221. https://doi.org/10.1016/j.bpj.2016.05.034
Szafron JM, Ramachandra AB, Breuer CK, Marsden AL, Humphrey JD (2019) Optimization of tissue-engineered vascular graft design using computational modeling. Tissue Eng Part C Methods 25(10):561. https://doi.org/10.1089/TEN.TEC.2019.0086
Taber LA, Humphrey JD (2001) Stress-modulated growth, residual stress, and vascular heterogeneity. J Biomech Eng 123(6):528–535. https://doi.org/10.1115/1.1412451

The Trilinos Project Team (2021) The Trilinos project website

Valentín A, Cardamone L, Baek S, Humphrey JD (2008) Complementary vasoactivity and matrix remodelling in arterial adaptations to altered flow and pressure. J R Soc Interface 6(32):293–306. https://doi.org/10.1098/RSIF.2008.0254

van Asten JG, Ristori T, Nolan DR, Lally C, Baaijens FP, Sahlgren CM, Loerakker S (2022) Computational analysis of the role of mechanosensitive Notch signaling in arterial adaptation to hypertension. J Mech Behav Biomed Mater 133(July):105325. https://doi.org/10.1016/j.jmbbm.2022.105325

van Asten JGM, Latorre M, Karakaya C, Baaijens FPT, Sahlgren CM, Ristori T, Humphrey JD, Loerakker S (2023) A multiscale computational model of arterial growth and remodeling including Notch signaling. Biomech Model Mechanobiol 22(5):1569–1588. https://doi.org/10.1007/s10237-023-01697-3

Vande Geest JP, Sacks MS, Vorp DA (2004) Age dependency of the biaxial biomechanical behavior of human abdominal aorta. J Biomech Eng 126(6):815–822. https://doi.org/10.1115/1.1824121

Vaughn MW, Kuo L, Liao JC (1998) Estimation of nitric oxide production and reactionrates in tissue by use of a mathematical model. Am J Physiol Heart Circ Physiol 274(6):H2163–H2176. https://doi.org/10.1152/ajpheart.1998.274.6.H2163

Wilson JS, Baek S, Humphrey JD (2012) Importance of initial aortic properties on the evolving regional anisotropy, stiffness and wall thickness of human abdominal aortic aneurysms. J R Soc Interface 9(74):2047–2058. https://doi.org/10.1098/rsif.2012.0097

Wilson JS, Baek S, Humphrey JD (2013) Parametric study of effects of collagen turnover on the natural history of abdominal aortic aneurysms. Proc R Soc A Math Phys Eng Sci 469(2150):20120556. https://doi.org/10.1098/rspa.2012.0556

Wu J, Thabet SR, Kirabo A, Trott DW, Saleh MA, Xiao L, Madhur MS, Chen W, Harrison DG (2014) Inflammation and mechanical stretch promote aortic stiffening in hypertension through activation of p38 mitogen-activated protein kinase. Circ Res 114(4):616–625. https://doi.org/10.1161/CIRCRESAHA.114.302157

Zeigler A, Richardson W, Holmes J, Saucerman J (2016) A computational model of cardiac fibroblast signaling predicts context-dependent drivers of myofibroblast differentiation. J Mol Cell Cardiol 94:72–81. https://doi.org/10.1016/j.yjmcc.2016.03.008

Zhang W, Edwards A (2006) Mathematical model of nitric oxide convection and diffusion in a renal medullary vas rectum. J Math Biol 53(3):385–420. https://doi.org/10.1007/s00285-006-0018-x

Zhou X, Franklin RA, Adler M, Jacox JB, Bailis W, Shyer JA, Flavell RA, Mayo A, Alon U, Medzhitov R (2018) Circuit design features of a stable two-cell system. Cell 172(4):744–757. https://doi.org/10.1016/j.cell.2018.01.015